

ARTICLE

<https://doi.org/10.1038/s42005-019-0107-y>

OPEN

Frustrated spin order and stripe fluctuations in FeSe

A. Baum^{1,2}, H.N. Ruiz^{3,4}, N. Lazarević⁵, Yao Wang^{3,6,10}, T. Böhm^{1,2,11}, R. Hosseinian Ahangharnejhad^{1,2,12}, P. Adelman⁷, T. Wolf⁷, Z.V. Popović^{5,8}, B. Moritz³, T.P. Devereaux^{3,9} & R. Hackl¹

The charge and spin dynamics of the structurally simplest iron-based superconductor, FeSe, may hold the key to understanding the physics of high temperature superconductors in general. Unlike the iron pnictides, FeSe lacks long range magnetic order in spite of a similar structural transition around 90 K. Here, we report results of Raman scattering experiments as a function of temperature and polarization and simulations based on exact diagonalization of a frustrated spin model. Both experiment and theory find a persistent low energy peak close to 500 cm⁻¹ in B_{1g} symmetry, which softens slightly around 100 K, that we assign to spin excitations. By comparing with results from neutron scattering, this study provides evidence for nearly frustrated stripe order in FeSe.

¹Walther Meissner Institut, Bayerische Akademie der Wissenschaften, 85748 Garching, Germany. ²Fakultät für Physik E23, Technische Universität München, 85748 Garching, Germany. ³Stanford Institute for Materials and Energy Sciences, SLAC National Accelerator Laboratory, 2575 Sand Hill Road, Menlo Park, CA 94025, USA. ⁴Department of Physics, Stanford University, Stanford, CA 94305, USA. ⁵Center for Solid State Physics and New Materials, Institute of Physics Belgrade, University of Belgrade, Pregrevica 118, 11080 Belgrade, Serbia. ⁶Department of Applied Physics, Stanford University, Stanford, CA 94305, USA. ⁷Karlsruher Institut für Technologie, Institut für Festkörperphysik, 76021 Karlsruhe, Germany. ⁸Serbian Academy of Sciences and Arts, Knez Mihailova 35, 11000 Belgrade, Serbia. ⁹Geballe Laboratory for Advanced Materials, Stanford University, Stanford, CA 94305, USA. ¹⁰Present address: Lyman Laboratory 336, Harvard University, 17 Oxford St. Cambridge, 02138 MA, USA. ¹¹Present address: TNG Technology Consulting GmbH, Beta-Straße, 85774 Unterföhring, Germany. ¹²Present address: School of Solar and Advanced Renewable Energy, Department of Physics and Astronomy, University of Toledo, Toledo, OH 43606, USA. Correspondence and requests for materials should be addressed to R.H. (email: hackl@wmi.badw.de)

Fe-based pnictides and chalcogenides, similar to cuprates, manganites or some heavy fermion compounds, are characterized by the proximity and competition of various phases including magnetism, charge order, and superconductivity. Specifically the magnetism of Fe-based systems has various puzzling aspects which do not straightforwardly follow from the Fe valence or changes in the Fermi surface topology^{1–4}. Some systems have a nearly ordered localized moment close to $2\mu_B$ ⁵, such as FeTe or rare-earth iron selenides, whereas the moments of AFe_2As_2 -based compounds ($A = Ba, Sr, Eu$ or Ca) are slightly below $1\mu_B$ ⁶ and display aspects of itinerant spin-density-wave (SDW) magnetism with a gap in the electronic excitation spectrum⁷. In contrast others do not order down to the lowest temperatures, such as FeSe⁸ or LaFePO⁹.

The material specific differences are a matter of intense discussion, and low- as well as high-energy electronic and structural properties determine the properties^{1,2,4,10–13}. At the Fermi energy E_F , the main fraction of the electronic density of states originates from t_{2g} Fe orbitals, but a substantial part of the Fe–Fe hopping occurs via the pnictogen or chalcogen atoms, hence via the xz , yz , and p_z orbitals. For geometrical reasons, the resulting exchange coupling energies between nearest (J_1) and next nearest neighbor (J_2) iron atoms have the same order of magnitude, and small changes in the pnictogen (chalcogen) height above the Fe plane influence the ratio J_2/J_1 , such that various orders are energetically very close¹².

The reduced overlap of the in-plane xy orbitals decreases the hopping integral t and increases the influence of the Hund's rule interactions and the correlation energy U , even though they are only in the range of 1–2 eV. Thus the electrons in the xy orbitals have a considerably higher effective mass m^* and smaller quasi-particle weight Z than those of the xz and yz orbitals. This effect was coined orbital selective Mottness^{14–16} and was observed by photoemission spectroscopy (ARPES) in Fe-based chalcogenides¹⁷. It is similar in spirit to what was found by Raman scattering in the cuprates as a function of momentum¹⁸. In either case some of the electron wave functions are more localized than others. This paradigm may explain why the description remains difficult and controversial in all cases.

Therefore we address the question as to whether systematic trends can be found across the families of the Fe-based superconductors, how the spin excitations are related to other highly correlated systems, and how they can be described appropriately.

As an experimental tool we use Raman scattering since the differences expected theoretically^{1,3} and indicated experimentally in the electronic structure⁷ can be tracked in both the charge and the spin channel. Another advantage is the large energy range of approximately 1 meV to 1 eV (8–8000 cm^{-1}) accessible by light scattering¹⁹.

Early theoretical work on Fe-based systems considered the Heisenberg model the most appropriate approach²⁰, and the high-energy maxima observed by Raman scattering in $BaFe_2As_2$ were interpreted in terms of localized spins^{21,22}. On the other hand, the low-energy spectra are reminiscent of charge density wave (CDW) or SDW formation^{22–25}. In principle, both effects can coexist if the strength of the correlations varies for electrons from different orbitals, where itinerant electrons form a SDW, while those on localized orbitals give rise to a Heisenberg-like response.

In contrast to the AFe_2As_2 -based compounds, FeSe seems to be closer to localized order with a larger mass renormalization than in the iron pnictides¹. Apart from low lying charge excitations, the remaining, presumably spin, degrees of freedom in FeSe may be adequately described by a spin-1 J_1 – J_2 – J_3 – K Heisenberg model¹² which provides also a consistent description of our results shown in this work and allows for the presence of different

spin orders. Since various types of spin order are energetically in close proximity^{12,26,27}, frustration may quench long-range order down to the lowest temperatures⁸, even though neutron scattering experiments in FeSe find large values for the exchange energies^{27,28}.

Recent experiments on FeSe focused on low-energies and B_{1g} ($x^2 - y^2$) symmetry, and the response was associated with particle-hole excitations and critical fluctuations²⁹. Here, we obtain similar experimental results below 1500 cm^{-1} . Those in the range 50–200 cm^{-1} show similarities with the other Fe-based systems while those above 200 cm^{-1} are distinctly different but display similarities with the cuprates^{30,31}. In addition to previous work, we analyze all symmetries at higher energies up to 3500 cm^{-1} , to uncover crucial information about the behavior of the spin degrees of freedom.

By comparing experimental and simulated Raman data we find a persistent low-energy peak at roughly 500 cm^{-1} in B_{1g} symmetry, which softens slightly around 100 K. We assign the B_{1g} maximum and the related structures in A_{1g} and B_{2g} symmetry to spin excitations. The theoretical simulations also aim at establishing a link between light and neutron scattering data with respect to the spin degrees of freedom and to furnish evidence for nearly frustrated stripe order at low temperature. We arrive at the conclusion that frustrated order of localized spins dominates the physics in FeSe, while critical spin and/or charge fluctuations are not the main focus of the paper.

Results

Experiments. Symmetry-resolved Raman spectra of single-crystalline FeSe (see Methods) in the energy range up to 0.45 eV (3600 cm^{-1}) are shown in Fig. 1. The spectra are linear combinations of the polarization dependent raw data (see Methods and Supplementary Fig. 1 in Supplementary Note 1). For B_{1g} symmetry (Fig. 1a) we plot only two temperatures, 40 and 300 K, to highlight the persistence of the peak at ~ 500 cm^{-1} . The full temperature dependence will be shown below. For A_{1g} , A_{2g} , and B_{2g} symmetry we show spectra at 40, 90, and 300 K (Fig. 1b–d). Out of the four symmetries, the A_{1g} , B_{1g} , and B_{2g} spectra display Raman active phonons, magnons or electron-hole excitations, while the A_{2g} spectra are weak and vanish below 500–1000 cm^{-1} . As intensity in A_{2g} symmetry appears only under certain conditions not satisfied in the present study, we ignore it here.

In the high-energy limit the intensities are smaller in all symmetries than those in other Fe-based systems such as $BaFe_2As_2$ (see Supplementary Fig. 2 in Supplementary Note 2). However, in the energy range up to ~ 3000 cm^{-1} there is a huge additional contribution to the B_{1g} cross section in FeSe (Fig. 1a). The response is strongly temperature dependent and peaks at 530 cm^{-1} in the low-temperature limit. Between 90 and 40 K the A_{1g} and B_{2g} spectra increase slightly in the range around 700 and 3000 cm^{-1} , respectively (indicated as blue shaded areas in Fig. 1b, d). The overall intensity gain in the A_{1g} and B_{2g} spectra in the shaded range is a fraction of $\sim 5\%$ of that in B_{1g} symmetry. The B_{2g} spectra exhibit a reduction in spectral weight in the range from 600 to 1900 cm^{-1} (shaded red) which is already fully developed at the structural transition at $T_s = 89.1$ K in agreement with earlier work²⁹. In contrast to A_{1g} and B_{2g} symmetry, the temperature dependence of the B_{1g} intensity is strong, whereas the peak energy changes only weakly, displaying some similarity with the cuprates³². This similarity, along with the considerations of Glasbrenner et al.¹², motivated us to explore a spin-only, Heisenberg-like model for describing the temperature evolution of the Raman scattering data.

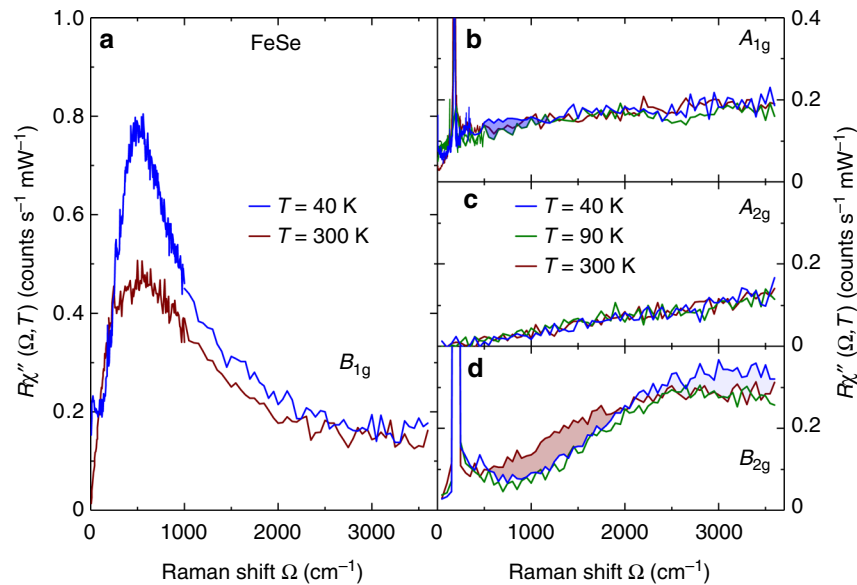


Fig. 1 Symmetry-resolved Raman spectra of FeSe at various temperatures for large energy transfers. **a** B_{1g} spectra at temperatures as indicated. The spectrum at 90 K is omitted here for clarity but is displayed in a separate figure below. The weak structure at $T = 40$ K in the range 20–25 cm^{-1} is left over from the fluctuation peak which is most pronounced right above T_s as shown below. **b** A_{1g} , **c** A_{2g} , and **d** B_{2g} spectra at temperatures as indicated. In A_{1g} and B_{2g} symmetry particle-hole excitations dominate the response. In agreement with the simulations weak additional peaks from spin excitations appear at low temperature (blue shaded areas). B_{2g} shows a loss of spectral weight (shaded red). The narrow lines close to 200 cm^{-1} are the A_{1g} and B_{1g} phonons. In the 1 Fe unit cell used here the B_{1g} phonon appears in B_{2g} symmetry since the axes are rotated by 45° with respect to the crystallographic (2 Fe) cell. The A_{2g} intensity vanishes below 500 cm^{-1} and the cross section is completely temperature independent

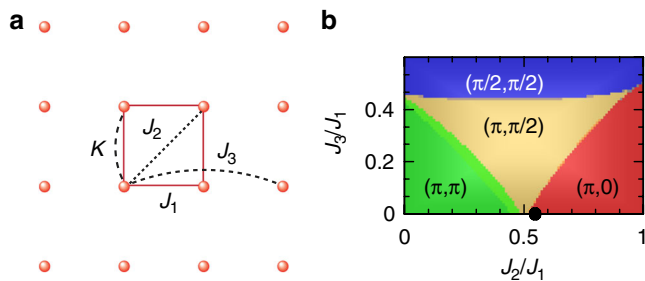


Fig. 2 Model and resulting phase diagram. **a** A 4×4 cluster was used for the simulations. The red spheres represent the Fe atoms, each of which carries localized spin \mathbf{S}_i , with $S = 1$. The nearest, next-nearest, and next-next-nearest neighbor interactions J_1 , J_2 , and J_3 , respectively, are indicated. K is the coefficient of the biquadratic term proportional to $(\mathbf{S}_i \cdot \mathbf{S}_j)^2$. **b** $J_2 - J_3$ phase diagram as obtained from our simulations at $T = 0$ and for $K = 0.1$. The black dot shows the parameters at which temperature-dependent simulations have been performed

Simulations at zero temperature. We performed numerical simulations at zero temperature for a frustrated spin-1 system on the basis of a J_1 - J_2 - J_3 - K Heisenberg model¹² on a 16-points cluster as shown in Fig. 2a and described in the Methods section. Figure 2b shows the resulting phase diagram as a function of J_2 and J_3 . K was set at 0.1 (repulsive) in order to suppress ordering tendencies on the small cluster. The parameter set for the simulations of the Raman and neutron data at finite temperature is indicated as a black dot.

In Fig. 3 we show the low-temperature data (Fig. 3a) along with the simulations (Fig. 3b). The energy scale for the simulations is given in units of J_1 which has been derived¹² to be 123 meV or 990 cm^{-1} , allowing a semi-quantitative comparison with the experiment. As already mentioned, the experimental A_{1g} and B_{2g} spectra are not dominated by spin excitations and we do not attempt to further analyze the continua extending to energies in

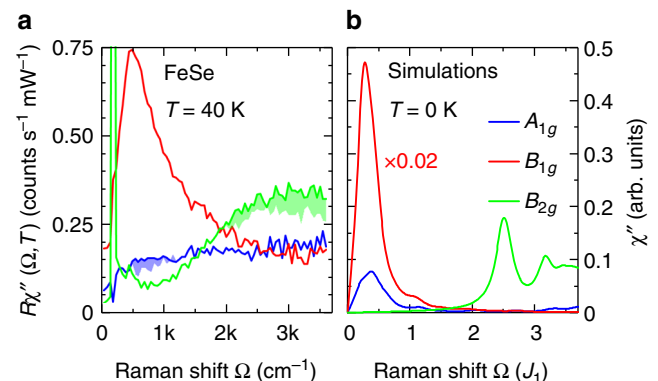


Fig. 3 Symmetry-resolved Raman spectra of FeSe for large energy shifts at low temperature. **a** Experimental results for symmetries as indicated at 40 K. The B_{1g} peak at 500 cm^{-1} dominates the spectrum. In A_{1g} and B_{2g} symmetry the electron-hole continua dominate the response, and the magnetic excitations yield only small additional contributions at approximately 700 and 3000 cm^{-1} , respectively. **b** Simulated Raman spectra at $T = 0$ K including only magnetic contributions. The A_{1g} and B_{1g} symmetries have peaks solely at low energies whereas the B_{2g} contributions are at high energies only. The B_{1g} response is multiplied by a factor of 0.02

excess of 1 eV, considering them a background. The opposite is true for B_{1g} symmetry, also borne out in the simulations. For the selected values of $J_1 = 123$ meV, $J_2 = 0.528J_1$, $J_3 = 0$, and $K = 0.1J_1$, the positions of the spin excitations in the three symmetries and the relative intensities are qualitatively reproduced. The choice of parameters is motivated by the previous use of the J_1 - J_2 Heisenberg model, with $J_1 = J_2$ to describe the stripe phase of iron pnictides²⁰. Here we use a value of J_2 smaller than J_1 to enhance competition between Néel and stripe orders when describing

FeSe. This approach and choice of parameters is strongly supported in a recent neutron scattering study²⁷.

The comparison of the different scattering symmetries, the temperature dependence, and our simulations indicate that the excitation at 500 cm^{-1} is an additional scattering channel superimposed on the particle-hole continuum and fluctuation response, as shown in Supplementary Note 3 with Supplementary Figs. 3 and 4. Here we focus on the peak centered at $\sim 500\text{ cm}^{-1}$ which, in agreement with the simulations, originates from two-magnon excitations in a highly frustrated spin system, although the features below 500 cm^{-1} also are interesting and were interpreted in terms of quadrupolar orbital fluctuations²⁹.

Temperature dependence. It is enlightening to look at the B_{1g} spectra across the whole temperature range as plotted in Fig. 4. The well-defined two-magnon peak centered at $\sim 500\text{ cm}^{-1}$ in the low temperature limit loses intensity, and becomes less well-defined with increasing temperature up to the structural transition $T_s = 89.1\text{ K}$. Above the structural transition, the spectral weight continues to decrease and the width of the two-magnon feature grows, while the peak again becomes well-defined and the energy increases slightly approaching the high temperature limit of the study. What may appear as a gap opening at low temperature is presumably just the reduction of spectral weight in a low-energy feature at $\sim 22\text{ cm}^{-1}$. The intensity of this lower energy response increases with temperature, leading to a well-formed peak at an energy around 50 cm^{-1} near the structural transition. Above the structural transition this feature rapidly loses spectral weight, hardens, and becomes indistinguishable from the two-magnon response in the high temperature limit. This low-energy feature develops in a fashion very similar to that found in $\text{Ba}(\text{Fe}_{1-x}\text{Co}_x)_2\text{As}_2$ for $x > 0$ ^{33–35}.

Now we compare the measurements with numerical simulations for the temperature dependence of the Raman B_{1g} susceptibility in Fig. 5a, b, respectively. For the simulations (Fig. 5b) we use the same parameters as at $T = 0$ (black dot in Fig. 3). At zero temperature the simulations show a single low energy B_{1g} peak around $0.3J_1$. As temperature increases, a weak shoulder forms on the low-energy side of the peak, and the whole peak softens slightly and broadens over the simulated temperature range. Except for the additional intensity at low energies, $\Omega < 200\text{ cm}^{-1}$ (Fig. 5a), there is good qualitative agreement between

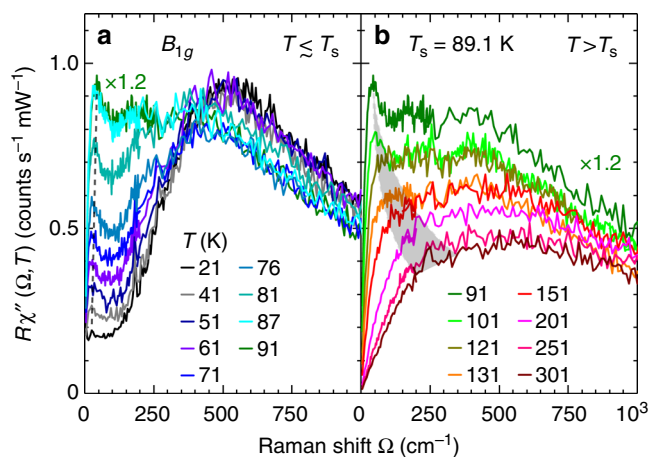


Fig. 4 Raman spectra in B_{1g} symmetry at temperatures **a** below and **b** above $T_s = 89.1\text{ K}$. The spectrum at 91 K appears in both panels for better comparison. The black dashed line in **a** and the gray shaded area in **b** indicate the approximate positions of the low-energy peak resulting from critical fluctuations. The peak centered close to 500 cm^{-1} results from excitations of neighboring spins which are studied here. A tentative decomposition is shown in Supplementary Fig. 4

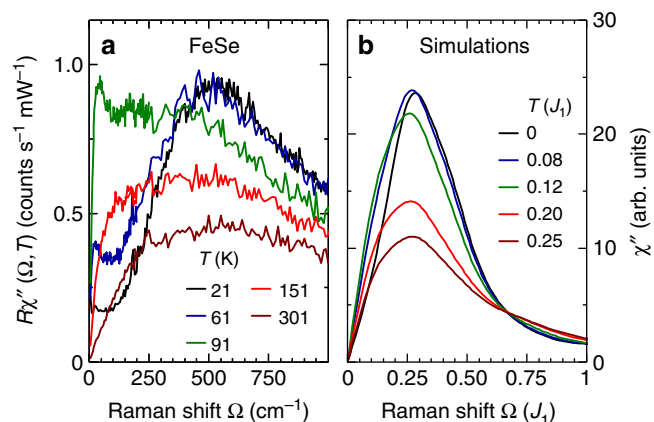


Fig. 5 Temperature dependence of the B_{1g} response. **a** Experimental spectra at selected temperatures as indicated. The spectra include several excitations the decomposition of which is shown in Supplementary Fig. 4. **b** Simulated Raman response at temperatures as indicated. Only magnetic excitations are included. The coupling constant was derived as $J_1 = 123\text{ meV}$ in ref. ¹²

theory and experiment. As shown in Supplementary Fig. 5 in Supplementary Note 4, a similar agreement between experiment and simulations is obtained for the temperature dependence in A_{1g} and B_{2g} symmetries, indicating that both the gain in intensity (blue shaded areas in Fig. 1) as well as the reduction in spectral weight in B_{2g} from 600 to 1900 cm^{-1} (shaded red in Fig. 1d) can be attributed to the frustrated localized magnetism.

Connection to the spin structure factor. To support our explanation of the Raman data, we simulated the dynamical spin structure factor $S(\mathbf{q}, \omega)$ and compared the findings to results of neutron scattering experiments²⁷. While clearly not observing long-range order, above the structural transition neutron scattering finds similar intensity at finite energy for several wave vectors along the line $(\pi, 0) - (\pi, \pi)$. Upon cooling, the spectral weight at these wave vectors shifts away from (π, π) to directions along $(\pi, 0)$, although the respective peaks remain relatively broad. In Fig. 6a, b we show the results of the simulations for two characteristic temperatures. As the temperature decreases, spectral weight shifts from (π, π) toward $(\pi, 0)$ in agreement with the experiment²⁷. In Fig. 6c we show the evolution of the spectral weights around (π, π) and $(\pi, 0)$ in an energy window of $(0.4 \pm 0.1)J_1$ as a function of temperature, similar to the results shown in ref. ²⁷. In the experiment, the temperature where the integrated dynamical spin structure factor changes most dramatically is close to the structural transition. From our simulations, the temperature where similar changes occur in comparison to neutron scattering corresponds to the temperature at which the simulated B_{1g} response (Fig. 5) shows the most pronounced shoulder, and the overall intensity begins to decrease. Not surprisingly, the low-energy peak in the Raman scattering experiment is also strongest near the structural transition.

Discussion

The agreement of experiment with theory in both neutron and Raman scattering suggests that a dominant contribution to the FeSe spectra comes from frustrated magnetism of essentially local spins. The differences between the classes of ferro-pnictides and -chalcogenides, in particular the different degrees of itineracy, may then originate in a subtle orbital differentiation across the families¹.

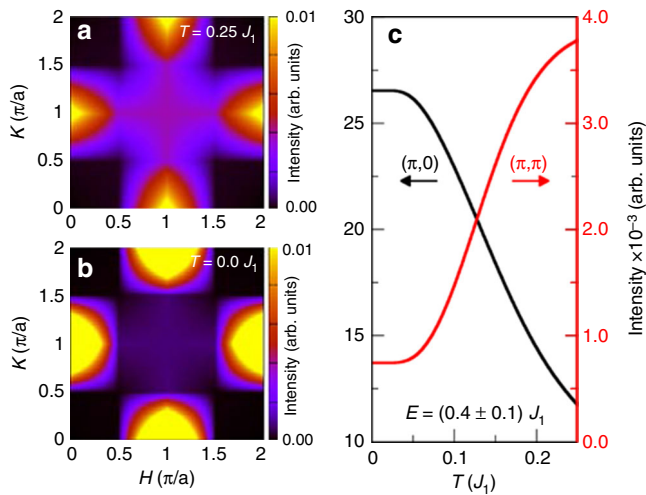


Fig. 6 Simulations of the dynamical structure factor $S(\mathbf{q}, \omega)$ of localized spin excitations integrated over an energy window of $(0.4 \pm 0.1)J_1$. **a, b** display cuts through the first Brillouin zone at $T = 0.25$ and $0J_1$, respectively. At high temperature there is intensity at (π, π) indicating a tendency toward Néel order. At low temperature the intensity at (π, π) is reduced and the stripe-like antiferromagnetism with $(\pi, 0)$ ordering wave vector becomes stronger. **c** $S(\mathbf{q}, \omega)$ integrated over an energy window $(0.4 \pm 0.1)J_1$ for fixed momenta (π, π) and $(\pi, 0)$ intensities as a function of temperature

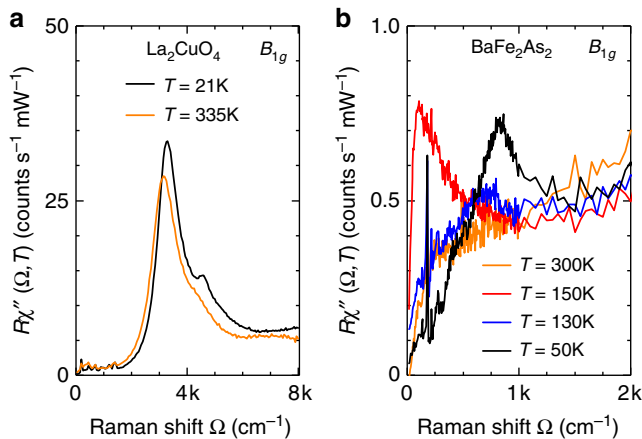


Fig. 7 Examples of localized and itinerant magnets. **a** B_{1g} Raman spectra of La_2CuO_4 . From ref. ³¹. **b** B_{1g} spectra of BaFe_2As_2 at four characteristic temperatures as indicated

If FeSe were frustrated, near such a phase boundary between magnetic states, then its behavior would be consistent with the observed sensitivity to intercalation^{36,37}, layer thickness³⁸, and pressure³⁹, which could affect the exchange interactions through the hopping. Relative to the theoretical results below 200 cm^{-1} , critical fluctuations of any origin, which are characterized by a diverging correlation length close to the transition, can neither be described nor distinguished in such a small cluster calculation. Here, only experimental arguments can be applied similar to those in ref. ³⁵, but will not be further discussed, since they are not the primary focus of the analysis. A brief summary may be found in the Supplementary Note 3.

It is remarkable how clearly the Raman spectra of an SDW state originating from a Fermi surface instability and a magnet with local moments can be distinguished. For comparison, Fig. 7

shows B_{1g} Raman spectra for La_2CuO_4 and BaFe_2As_2 at characteristic temperatures. La_2CuO_4 (Fig. 7a) is an example of a material with local moments on the Cu sites^{30,31} having a Néel temperature of $T_N = 325 \text{ K}$. The well-defined peak at $\sim 2.84J_1$ ^{40,41} possesses a weak and continuous temperature dependence across T_N ³². The origin of the scattering in La_2CuO_4 and other insulating cuprates⁴² can thus be traced back to Heisenberg-type physics of local moments⁴³, which, for simplicity, need only include the nearest-neighbor exchange interaction J_1 .

In contrast, most iron-based superconductors are metallic antiferromagnets in the parent state exhibiting rather different Raman signatures. In BaFe_2As_2 (Fig. 7b) abrupt changes are observed in B_{1g} symmetry upon entering the SDW state: the fluctuation peak below 100 cm^{-1} vanishes, a gap develops below some $500\text{--}600 \text{ cm}^{-1}$, and intensity piles up in the range $600\text{--}1500 \text{ cm}^{-1}$ (ref. ^{22,44}), the typical behavior of an SDW or CDW²⁴ in weak-coupling, resulting from Fermi surface nesting. Yet, even for itinerant systems such as these, longer range exchange interactions can become relevant and lead to magnetic frustration⁴⁵.

In summary, the Raman response of FeSe was measured in all symmetries and compared to simulations of a frustrated spin-1 system. The experimental data were decomposed in order to determine which parts of the spectra originate from particle-hole excitations, fluctuations of local spins, and low energy critical fluctuations. Comparison of the decomposed experimental data with the simulations gives evidence that the dominant contribution of the Raman spectra comes from magnetic competition between $(\pi, 0)$ and (π, π) ordering vectors. These features of the Raman spectra, which agree qualitatively with a spin-only model, consist of a dominant peak in B_{1g} symmetry around 500 cm^{-1} along with a peak at similar energy but lower intensity in A_{1g} and at higher energy in B_{2g} symmetry. These results will likely help to unravel the mechanism behind the superconducting phase found in FeSe.

Methods

Experiment. The FeSe crystals were prepared by the vapor transport technique. Details of the crystal growth and characterization are described elsewhere⁴⁶. Before the experiment the samples were cleaved in air and the exposure time was minimized. The surfaces obtained in this way have several atomically flat regions allowing us to measure spectra down to 5 cm^{-1} . At the tetragonal-to-orthorhombic transition T_s twin boundaries appear and become clearly visible in the observation optics. As described in detail by Kretzschmar et al.³⁵ the appearance of stripes can be used to determine the laser heating ΔT_L and T_s to be $(0.5 \pm 0.1) \text{ K mW}^{-1}$ and $(89.1 \pm 0.2) \text{ K}$, respectively.

Calibrated Raman scattering equipment was used for the experiment. The samples were attached to the cold finger of a He-flow cryostat having a vacuum of $\sim 5 \times 10^{-5} \text{ Pa}$ ($5 \times 10^{-7} \text{ mbar}$). For excitation we used a diode-pumped solid state laser emitting at 575 nm (Coherent GENESIS MX-SLM 577-500) and various lines of an Ar ion laser (Coherent Innova 304). The angle of incidence was close to 66° for reducing the elastic stray light entering the collection optics. Polarization and power of the incoming light were adjusted in a way that the light inside the sample had the proper polarization state and, respectively, a power of typically $P_a = 4 \text{ mW}$ independent of polarization. For the symmetry assignment we use the 1 Fe unit cell (axes x and y parallel to the Fe-Fe bonds) which has the same orientation as the magnetic unit cell in the cases of Néel or single-stripe order (4 Fe cell). The orthorhombic distortion is along these axes whereas the crystallographic cell assumes a diamond shape with the length of the tetragonal axes preserved. Because of the rotated axes in the 1 Fe unit cell the B_{1g} phonon appears in the B_{2g} spectra. Spectra at low to medium energies were measured with a resolution $\sigma \approx 5 \text{ cm}^{-1}$ in steps of $\Delta\Omega = 2.5$ or 5 cm^{-1} below 250 cm^{-1} and steps of 10 cm^{-1} above where no sharp peaks need to be resolved. Spectra covering the energy range up to $0.5\text{--}1 \text{ eV}$ were measured with a resolution $\sigma \approx 20 \text{ cm}^{-1}$ in steps of $\Delta\Omega = 50 \text{ cm}^{-1}$.

Simulations. We use exact diagonalization to study a Heisenberg-like model on a 16-site square lattice, which contains the necessary momentum points and is small enough that exact diagonalization can reach high enough temperatures to find agreement with the temperature dependence in the experiment. This was solved

using the parallel Arnoldi method⁴⁷. The Hamiltonian is given by

$$\mathcal{H} = \sum_{nn} \left[J_1 \mathbf{S}_i \cdot \mathbf{S}_j + K (\mathbf{S}_i \cdot \mathbf{S}_j)^2 \right] + \sum_{2nn} J_2 \mathbf{S}_i \cdot \mathbf{S}_j + \sum_{3nn} J_3 \mathbf{S}_i \cdot \mathbf{S}_j \quad (1)$$

where \mathbf{S}_i is a spin-1 operator reflecting the observation that the local moments of iron chalcogenides are close to $2\mu_B$ ⁴⁸. The sum over nn is over nearest neighbors, the sum over $2nn$ is over next nearest neighbors, and the sum over $3nn$ is over next next nearest neighbors.

We determine the dominant order according to the largest static spin structure factor, given by

$$S(\mathbf{q}) = \frac{1}{N} \sum_i e^{i\mathbf{q} \cdot \mathbf{R}_i} \sum_j \langle \mathbf{S}_{\mathbf{R}_i + \mathbf{R}_j} \cdot \mathbf{S}_{\mathbf{R}_i} \rangle. \quad (2)$$

Due to the possible spontaneous symmetry breaking we adjust the structure factor by the degeneracy of the momentum. To characterize the relative strength of the dominant fluctuations we project the relative intensity of the dominant static structure factor onto the range [0, 1] using the following

$$\text{Intensity} = 1 - \frac{d_{\mathbf{q}_{\text{sub}}} S(\mathbf{q}_{\text{sub}})}{d_{\mathbf{q}_{\text{max}}} S(\mathbf{q}_{\text{max}})} \quad (3)$$

where $d_{\mathbf{q}}$ is the degeneracy of momentum \mathbf{q} , \mathbf{q}_{max} is the momentum with the largest $d_{\mathbf{q}} S_{\mathbf{q}}$ and \mathbf{q}_{sub} is the momentum with the second largest (subdominant) $d_{\mathbf{q}} S_{\mathbf{q}}$.

The Raman susceptibilities for B_{1g} , B_{2g} and A_{1g} symmetries for non-zero temperatures were calculated using the Fleury-Loudon scattering operator²⁰ given by

$$\mathcal{O} = \sum_{ij} J_{ij} (\hat{\mathbf{e}}_{\text{in}} \cdot \hat{\mathbf{d}}_{ij}) (\hat{\mathbf{e}}_{\text{out}} \cdot \hat{\mathbf{d}}_{ij}) \mathbf{S}_i \cdot \mathbf{S}_j \quad (4)$$

where J_{ij} are the exchange interaction values used in the Hamiltonian, $\hat{\mathbf{d}}_{ij}$ is a unit vector connecting sites i and j and $\hat{\mathbf{e}}_{\text{in/out}}$ are the polarization vectors. For the symmetries calculated we use the polarization vectors

$$\begin{aligned} \hat{\mathbf{e}}_{\text{in}} &= \frac{1}{\sqrt{2}} (\hat{\mathbf{x}} + \hat{\mathbf{y}}), \quad \hat{\mathbf{e}}_{\text{out}} = \frac{1}{\sqrt{2}} (\hat{\mathbf{x}} - \hat{\mathbf{y}}) \text{ for } A_{1g} \oplus B_{2g}, \\ \hat{\mathbf{e}}_{\text{in}} &= \hat{\mathbf{x}}, \quad \hat{\mathbf{e}}_{\text{out}} = \hat{\mathbf{y}} \text{ for } B_{2g}, \\ \hat{\mathbf{e}}_{\text{in}} &= \frac{1}{\sqrt{2}} (\hat{\mathbf{x}} + \hat{\mathbf{y}}), \quad \hat{\mathbf{e}}_{\text{out}} = \frac{1}{\sqrt{2}} (\hat{\mathbf{x}} - \hat{\mathbf{y}}) \text{ for } B_{1g}, \end{aligned} \quad (5)$$

(where $\hat{\mathbf{x}}$ and $\hat{\mathbf{y}}$ point along the Fe-Fe directions). We use this operator to calculate the Raman response $R(\omega)$ using the continued fraction expansion⁴⁹, where $R(\omega)$ is given by

$$R(\omega) = -\frac{1}{\pi Z} \sum_n e^{-\beta E_n} \text{Im} \left(\langle \Psi_n | \mathcal{O}^\dagger \frac{1}{\omega + E_n + i\epsilon - \mathcal{H}} \mathcal{O} | \Psi_n \rangle \right) \quad (6)$$

with Z the partition function. The sum traverses over all eigenstates Ψ_n of the Hamiltonian \mathcal{H} having eigenenergies $E_n < E_0 + 2J_1$ where E_0 is the ground state energy. The Raman susceptibility is given by $\chi''(\omega) = \frac{1}{2} [R(\omega) - R(-\omega)]$. The dynamical spin structure factor was calculated using the same method with \mathcal{O} replaced with $\mathbf{S}_q^z = \frac{1}{\sqrt{N}} \sum_i e^{i\mathbf{q} \cdot \mathbf{R}_i} S_i^z$. **Note added in proof:** More details about the numerical study of the model can be found in ref. ⁵⁰.

Data availability

Data are available upon reasonable request from the corresponding author.

Received: 18 June 2018 Accepted: 21 December 2018

Published online: 04 February 2019

References

- Yin, Z. P., Haule, K. & Kotliar, G. Kinetic frustration and the nature of the magnetic and paramagnetic states in iron pnictides and iron chalcogenides. *Nat. Mater.* **10**, 932–935 (2011).
- Georges, A., de' Medici, L. & Mravlje, J. Strong correlations from Hund's coupling. *Annu. Rev. Cond. Mat. Phys.* **4**, 137–178 (2013).
- Si, Q., Yu, R. & Abrahams, E. High-temperature superconductivity in iron pnictides and chalcogenides. *Nat. Rev. Mater.* **1**, 16017 (2016).
- Skornyakov, S. L., Anisimov, V. I., Vollhardt, D. & Leonov, I. Effect of electron correlations on the electronic structure and phase stability of FeSe upon lattice expansion. *Phys. Rev. B* **96**, 035137 (2017).
- Li, S. et al. First-order magnetic and structural phase transitions in $\text{Fe}_{1+y}\text{Se}_x\text{Te}_{1-x}$. *Phys. Rev. B* **79**, 054503 (2009).
- Johnston, D. C. The puzzle of high temperature superconductivity in layered iron pnictides and chalcogenides. *Adv. Phys.* **59**, 803 (2010).
- Yi, M., Zhang, Y., Shen, Z.-X. & Lu, D. Role of the orbital degree of freedom in iron-based superconductors. *npj Quantum Mater.* **2**, 57 (2017).
- Baek, S.-H. et al. Orbital-driven nematicity in FeSe. *Nat. Mater.* **14**, 210–214 (2014).
- Taylor, A. E. et al. Absence of strong magnetic fluctuations in FeP-based systems LaFePO and $\text{Sr}_2\text{ScO}_3\text{FeP}$. *J. Phys. Condens. Matter* **25**, 425701 (2013).
- Mazin, I. I. & Johannes, M. D. A key role for unusual spin dynamics in ferropnictides. *Nat. Phys.* **5**, 141 (2009).
- Stadler, K. M., Yin, Z. P., von Delft, J., Kotliar, G. & Weichselbaum, A. Dynamical mean-field theory plus numerical renormalization-group study of spin-orbital separation in a three-band Hund metal. *Phys. Rev. Lett.* **115**, 136401 (2015).
- Glasbrenner, J. K. et al. Effect of magnetic frustration on nematicity and superconductivity in iron chalcogenides. *Nat. Phys.* **11**, 953–958 (2015).
- Baum, A. et al. Interplay of lattice, electronic, and spin degrees of freedom in detwinned BaFe_2As_2 : a Raman scattering study. *Phys. Rev. B* **98**, 075113 (2018).
- Anisimov, V. I., Nekrasov, I. A., Kondakov, D. E., Rice, T. M. & Sigrist, M. Orbital-selective Mott-insulator transition in $\text{Ca}_{2-x}\text{Sr}_x\text{RuO}_4$. *Eur. Phys. J. B* **25**, 191–201 (2002).
- de' Medici, L., Hassan, S. R., Capone, M. & Dai, X. Orbital-selective Mott transition out of band degeneracy lifting. *Phys. Rev. Lett.* **102**, 126401 (2009).
- de' Medici, L. Hund's induced fermi-liquid instabilities and enhanced quasiparticle interactions. *Phys. Rev. Lett.* **118**, 167003 (2017).
- Yi, M. et al. Observation of universal strong orbital-dependent correlation effects in iron chalcogenides. *Nat. Commun.* **6**, 7777 (2015).
- Venturini, F. et al. Observation of an unconventional metal-insulator transition in overdoped CuO_2 compounds. *Phys. Rev. Lett.* **89**, 107003 (2002).
- Devereaux, T. P. & Hackl, R. Inelastic light scattering from correlated electrons. *Rev. Mod. Phys.* **79**, 175 (2007).
- Chen, C.-C., Jia, C. J., Kemper, A. F., Singh, R. R. P. & Devereaux, T. P. Theory of Two-Magnon Raman Scattering in Iron Pnictides and Chalcogenides. *Phys. Rev. Lett.* **106**, 067002 (2011).
- Okazaki, K., Sugai, S., Niitaka, S. & Takagi, H. Phonon, two-magnon, and electronic Raman scattering of $\text{Fe}_{1+y}\text{Te}_{1-x}\text{Se}_x$. *Phys. Rev. B* **83**, 035103 (2011).
- Sugai, S. et al. Spin-density-wave gap with Dirac nodes and two-magnon Raman scattering in BaFe_2As_2 . *J. Phys. Soc. Jpn.* **81**, 024718 (2012).
- Chauvière, L. et al. Raman scattering study of spin-density-wave order and electron-phonon coupling in $\text{Ba}(\text{Fe}_{1-x}\text{Co}_x)_2\text{As}_2$. *Phys. Rev. B* **84**, 104508 (2011).
- Eiter, H.-M. et al. Alternative route to charge density wave formation in multiband systems. *Proc. Natl Acad. Sci. USA* **110**, 64–69 (2013).
- Yang, Y.-X. et al. Temperature-induced change in the Fermi surface topology in the spin density wave phase of $\text{Sr}(\text{Fe}_{1-x}\text{Co}_x)_2\text{As}_2$. *Phys. Rev. B* **89**, 125130 (2014).
- Wang, F., Kivelson, S. A. & Lee, D.-H. Nematicity and quantum paramagnetism in FeSe. *Nat. Phys.* **11**, 959–963 (2015).
- Wang, Q. et al. Magnetic ground state of FeSe. *Nat. Commun.* **7**, 12182 (2016).
- Rahn, M. C., Ewings, R. A., Sedlmaier, S. J., Clarke, S. J. & Boothroyd, A. T. Strong $(\pi, 0)$ spin fluctuations in β -FeSe observed by neutron spectroscopy. *Phys. Rev. B* **91**, 180501 (2015).
- Massat, P. et al. Charge-induced nematicity in FeSe. *Proc. Natl Acad. Sci. USA* **113**, 9177–9181 (2016).
- Sulewski, P. E., Fleury, P. A., Lyons, K. B. & Cheong, S.-W. Observation of chiral spin fluctuations in insulating planar cuprates. *Phys. Rev. Lett.* **67**, 3864 (1991).
- Muschler, B. et al. Electron interactions and charge ordering in CuO_2 compounds. *Eur. Phys. J. Spec. Top.* **188**, 131 (2010).
- Knoll, P., Thomsen, C., Cardona, M. & Murugaraj, P. Temperature-dependent lifetime of spin excitations in $\text{RBa}_2\text{Cu}_3\text{O}_6$ ($R = \text{Eu}, \text{Y}$). *Phys. Rev. B* **42**, 4842–4845 (1990).
- Choi, K.-Y. et al. Lattice and electronic anomalies of CaFe_2As_2 studied by Raman spectroscopy. *Phys. Rev. B* **78**, 212503 (2008).
- Gallais, Y. et al. Observation of incipient charge nematicity in $\text{Ba}(\text{Fe}_{1-x}\text{Co}_x)_2\text{As}_2$. *Phys. Rev. Lett.* **111**, 267001 (2013).
- Kretzschmar, F. et al. Critical spin fluctuations and the origin of nematic order in $\text{Ba}(\text{Fe}_{1-x}\text{Co}_x)_2\text{As}_2$. *Nat. Phys.* **12**, 560–563 (2016).
- Burrard-Lucas, M. et al. Enhancement of the superconducting transition temperature of fese by intercalation of a molecular spacer layer. *Nat. Mater.* **12**, 15–19 (2013).
- Zhang, A.-M. et al. Superconductivity at 44 K in K intercalated FeSe system with excess Fe. *Sci. Rep.* **3**, 1216 (2013).
- Ge, J.-F. et al. Superconductivity above 100 K in single-layer FeSe films on doped SrTiO_3 . *Nat. Mater.* **14**, 285–289 (2015).

39. Medvedev, S. et al. Electronic and magnetic phase diagram of β -Fe_{1.01}Se with superconductivity at 36.7 K under pressure. *Nat. Mater.* **8**, 630 (2009).
40. Canali, C. M. & Girvin, S. M. Theory of Raman scattering in layered cuprate materials. *Phys. Rev. B* **45**, 7127–7160 (1992).
41. Weidinger, S. A. & Zwerger, W. Higgs mode and magnon interactions in 2D quantum antiferromagnets from Raman scattering. *Eur. Phys. J. B* **88**, 237 (2015).
42. Chelwani, N. et al. Magnetic excitations and amplitude fluctuations in insulating cuprates. *Phys. Rev. B* **97**, 024407 (2018).
43. Fleury, P. A. & Loudon, R. Scattering of light by one- and two-magnon excitations. *Phys. Rev.* **166**, 514 (1968).
44. Chauvière, L. et al. Impact of the spin-density-wave order on the superconducting gap of Ba(Fe_{1-x}Co_x)₂As₂. *Phys. Rev. B* **82**, 180521 (2010).
45. Yildirim, T. Frustrated magnetic interactions, giant magneto-elastic coupling, and magnetic phonons in iron-pnictides. *Phys. C* **469**, 425 (2009).
46. Böhrer, A. E. et al. Lack of coupling between superconductivity and orthorhombic distortion in stoichiometric single-crystalline FeSe. *Phys. Rev. B* **87**, 180505 (2013).
47. Sorensen, D., Lehoucq, R. & Yang, C. *ARPACK Users' Guide: Solution of Large-Scale Eigenvalue Problems with Implicitly Restarted Arnoldi Methods*. (SIAM, Philadelphia, 1998).
48. Gretarsson, H. et al. Revealing the dual nature of magnetism in iron pnictides and iron chalcogenides using x-ray emission spectroscopy. *Phys. Rev. B* **84**, 100509 (2011).
49. Dagotto, E. Correlated electrons in high-temperature superconductors. *Rev. Mod. Phys.* **66**, 763 (1994).
50. Ruiz, H., Wang, Y., Moritz, B. & Devereaux, T. P. Frustrated magnetism from local moments in FeSe. Preprint at <https://arxiv.org/abs/1812.09609> (2018).

Acknowledgements

The work was supported by the German Research Foundation (DFG) via the Priority Program SPP 1458 (grant-no. Ha2071/7) and the Transregional Collaborative Research Center TRR80 and by the Serbian Ministry of Education, Science and Technological Development under Project III45018. We acknowledge support by the DAAD through the bilateral project between Serbia and Germany (grant numbers 57142964 and 57335339). The collaboration with Stanford University was supported by the Bavaria California Technology Center BaCaTeC (grant-no. A5 [2012-2]). Work in the SIMES at Stanford University and SLAC was supported by the U.S. Department of Energy, Office of Basic Energy Sciences, Division of Materials Sciences and Engineering, under Contract No. DE-AC02-76SF00515. Computational work was performed using the resources of

the National Energy Research Scientific Computing Center supported by the U.S. Department of Energy, Office of Science, under Contract No. DE-AC02-05CH11231.

Author contributions

A.B., T.B. and R.H. conceived the experiment. B.M. and T.P.D. conceived the ED analysis. P.A. and T.W. synthesized and characterized the samples. A.B., N.L., T.B. and R.H. A. performed the Raman scattering experiment. H.N.R. and Y.W. coded and performed the ED calculations. A.B., H.N.R., N.L., B.M. and R.H. analyzed and discussed the data. A.B., H.N.R., N.L., Z.P., B.M., T.P.D. and R.H. wrote the paper. All authors commented on the manuscript.

Additional information

Supplementary information accompanies this paper at <https://doi.org/10.1038/s42005-019-0107-y>.

Competing interests: The authors declare no competing interests.

Reprints and permission information is available online at <http://npg.nature.com/reprintsandpermissions/>

Publisher's note: Springer Nature remains neutral with regard to jurisdictional claims in published maps and institutional affiliations.



Open Access This article is licensed under a Creative Commons Attribution 4.0 International License, which permits use, sharing, adaptation, distribution and reproduction in any medium or format, as long as you give appropriate credit to the original author(s) and the source, provide a link to the Creative Commons license, and indicate if changes were made. The images or other third party material in this article are included in the article's Creative Commons license, unless indicated otherwise in a credit line to the material. If material is not included in the article's Creative Commons license and your intended use is not permitted by statutory regulation or exceeds the permitted use, you will need to obtain permission directly from the copyright holder. To view a copy of this license, visit <http://creativecommons.org/licenses/by/4.0/>.

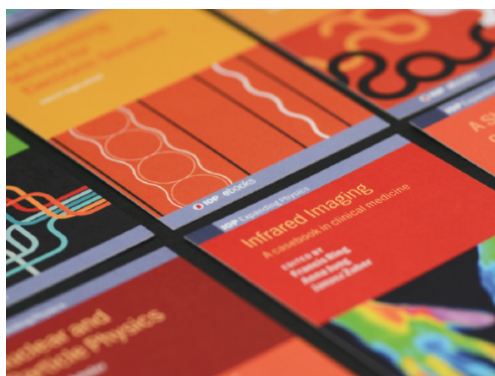
© The Author(s) 2019

TOPICAL REVIEW • **OPEN ACCESS**

Fluctuations and pairing in Fe-based superconductors: light scattering experiments

To cite this article: N Lazarevi and R Hackl 2020 *J. Phys.: Condens. Matter* **32** 413001

View the [article online](#) for updates and enhancements.



IOP | ebooks™

Bringing together innovative digital publishing with leading authors from the global scientific community.

Start exploring the collection—download the first chapter of every title for free.

Topical Review

Fluctuations and pairing in Fe-based superconductors: light scattering experiments

N Lazarević¹ and R Hackl² 

¹ Center for Solid State Physics and New Materials, Institute of Physics Belgrade, University of Belgrade, Pregrevica 118, 11080 Belgrade, Serbia

² Walther Meissner Institut, Bayerische Akademie der Wissenschaften, 85748 Garching, Germany

E-mail: nenadi@ipb.ac.rs and hackl@wmi.badw.de

Received 14 October 2019, revised 24 February 2020

Accepted for publication 9 April 2020

Published 15 July 2020



Abstract

Inelastic scattering of visible light (Raman effect) offers a window into properties of correlated metals such as spin, electron and lattice dynamics as well as their mutual interactions. In this review we focus on electronic and spin excitations in Fe-based pnictides and chalcogenides, in particular but not exclusively superconductors. After a general introduction to the basic theory including the selection rules for the various scattering processes we provide an overview over the major experimental results. In the superconducting state below the transition temperature T_c the pair-breaking effect can be observed, and the gap energies may be derived and associated with the gaps on the electron and hole bands. In spite of the similarities of the overall band structures the results are strongly dependent on the family and may even change qualitatively within one family. In some of the compounds strong collective modes appear below T_c . In $\text{Ba}_{1-x}\text{K}_x\text{Fe}_2\text{As}_2$, which has the most isotropic gap of all Fe-based superconductors, there are indications that these modes are exciton-like states appearing in the presence of a hierarchy of pairing tendencies. The strong in-gap modes observed in Co-doped NaFeAs are interpreted in terms of quadrupolar orbital excitations which become undamped in the superconducting state. The doping dependence of the scattering intensity in $\text{Ba}(\text{Fe}_{1-x}\text{Co}_x)_2\text{As}_2$ is associated with a nematic resonance above a quantum critical point and interpreted in terms of a critical enhancement at the maximal T_c . In the normal state the response from particle-hole excitations reflects the resistivity. In addition, there are strongly temperature-dependent contributions from presumably critical fluctuations in the energy range of $k_B T$ which can be compared to the elastic properties. Currently it is not settled whether the fluctuations observed by light scattering are related to spin or charge. Another controversy relates to putative two-magnon excitations, typically in the energy range below 0.5 eV. Whereas this response presumably originates from charge excitations in most of the Fe-based compounds theory and experiment suggest that the excitations in the 60 meV range in FeSe stem from localized spins in a nearly frustrated system.



Original content from this work may be used under the terms of the [Creative Commons Attribution 4.0 licence](https://creativecommons.org/licenses/by/4.0/).

Any further distribution of this work must maintain attribution to the author(s) and the title of the work, journal citation and DOI.

Keywords: superconductivity, Fe-based compounds, light scattering

(Some figures may appear in colour only in the online journal)

1. Introduction

Superconductivity in iron-based compounds (FeBCs) came as a big surprise when first reported by Kamihara and coworkers [1, 2]. The FeBCs consist of quadratically coordinated Fe planes sandwiched between layers of pnictogen (As, P) or chalcogen (S, Se, Te) atoms as shown in figure 1(a). The rest of the structure is rather variable as can be seen from the sum formulae in table 1. For this variability and the relative change in the band structures the FeBCs are a laboratory for studying the interrelation of magnetism, fluctuations and superconductivity or strong versus weak-coupling effects as summarized in excellent reviews including [3–8].

FeBCs typically have a magnetically ordered phase at zero nominal doping. Upon elemental substitution or application of pressure, magnetism can be suppressed and superconductivity (SC) may appear (figure 1(b)). In contrast to the cuprates, all phases are metallic. The order at zero doping is a stripe-like antiferromagnetic spin-density wave (SDW) and widely believed to originate from the nesting properties of the hole- and electron-like Fermi surfaces encircling the (0, 0) (Γ) and the $(\pm\pi, 0)/ (0, \pm\pi)$ (X/Y) points in the idealized 1 Fe Brillouin zone. Similarly, the topology of the Fermi surface is considered important for superconductivity [9]. Although the Fermi surfaces are always centered at Γ and X/Y there are substantial variations in shape and character across the families and as a function of doping [10]. However, this variation is not necessarily and exclusively at the origin of the differences in the superconducting ground states. Already on the level of local-density approximation (LDA) [11] a variety of nearly degenerate superconducting ground states is expected [6, 12].

In addition to the SDW and SC phase transitions, nematic order, with the rotational symmetry broken but the translational symmetry preserved, and wide temperature ranges with fluctuations are observed [14]. For studying this plethora of instabilities, a wide variety of experimental methods has been applied. Inelastic light scattering is a useful technique, since relevant information on practically all phases and their fluctuations can be obtained.

It will be the purpose of this review to present typical results, provide a snapshot of the current status of the field and outline possible future developments. First, we briefly describe the experiment and the theoretical background and then summarize the most relevant results obtained from light scattering with the focus placed on electronic and spin excitations.

2. Raman experiment

Shown in figure 2 is a schematic view of the experimental setup of a typical macro Raman experiment *in vacuo* and in a diamond anvil cell (inset) on opaque samples. In the macro

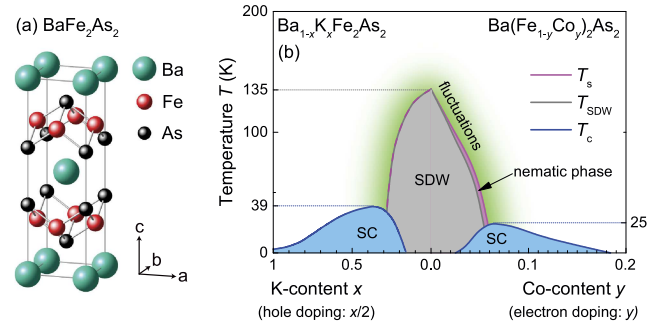


Figure 1. Crystal structure and phase diagram. (a) Crystal structure of BaFe₂As₂. Thin gray lines indicate the edges of the unit cell (2 Fe per layer), 14/mmm. Gray connecting lines between Fe and As illustrate covalent Fe-As bonds. (b) Phase diagram. The spin density wave (SDW) and the superconducting (SC) ranges are indicated in gray and blue, respectively. The dashed magenta-grey line indicates a simultaneous structural transition at T_s and SDW transition at T_{SDW}. The nematic phase is shaded magenta. The green shaded area indicates the existence of fluctuations next to the SDW transition. Note that the scales in x (hole doping) and y (electron doping) differ. Reproduced with permission from [13].

setup the incident light with polarization $\hat{\mathbf{e}}_I$ impinges on the surface at an angle of incidence $\vartheta_I \sim 70^\circ$ in order to prevent the directly reflected light from entering the optics and the spectrometer. For this ‘pseudo-Brewster’ angle the reflection is minimal for $\hat{\mathbf{e}}_I$ parallel to the plane of incidence. The scattered light is collected along the surface normal. Photons having a selected polarization state $\hat{\mathbf{e}}_S$ enter the spectrometer. A charge-coupled device (CCD) detector registers the number of transmitted photons per unit time $\dot{N}_{I,S}(\Omega)$ (‘Raman spectrum’) for a given energy shift $\Omega = \omega_I - \omega_S$ and polarization combination $(\hat{\mathbf{e}}_I, \hat{\mathbf{e}}_S)$, where $\omega_{I,S}$ are the energies of the photons. The differential light scattering cross-section is proportional to the Raman spectrum,

$$\frac{d^2\sigma_{I,S}}{d\Omega_S d\omega_S} = \hbar r_0^2 \frac{\omega_S}{\omega_I \pi} \{1 + n(\Omega, T)\} R_{I,S} \chi''_{I,S}(\mathbf{q}, \Omega, T). \quad (1)$$

Here Ω_S is the solid angle into which the photons are scattered, and $R_{I,S}$ absorbs matrix element effects and experimental factors, $\chi_{I,S}(\mathbf{q}, \Omega, T) = \chi'_{I,S} + i\chi''_{I,S}$ is the typically non-resonant response function, $n(\Omega, T) = [\exp(\hbar\Omega/k_B T) - 1]^{-1}$ is the Bose–Einstein occupation number and $r_0 = e^2/(4\pi\epsilon_0 mc^2)$ the Thomson electron radius, thus equation (1) describes the cross section per electron. From linear combinations of the spectra, pure symmetries μ can be derived (for details see section 4.9).

3. Materials

Most of the existing FeBCs were studied by Raman scattering. In the beginning the phonons were in the main focus [16–22]. With the advent of high-quality single crystals of

Table 1. Materials studied by Raman scattering. The table includes only materials for which electronic properties (spin, charge, fluctuations) were studied. In the second column typical acronyms are listed which will be used occasionally in the text. The main subject of the respective experiments are listed in the second to last column.

Material	Acronym	Substitution	Subject	Reference
BaFe ₂ As ₂	BFA/Ba122	No	SDW	[27, 32]
SrFe ₂ As ₂	Sr122	No	SDW, fluctuations	[29, 33]
EuFe ₂ As ₂	Eu122	No	SDW, fluctuations	[33, 34]
CaFe ₂ As ₂	Ca122	No	SDW	[34]
LaFeAsO	1111	No	SDW	[35]
Ba(Fe _{1-x} Co _x) ₂ As ₂	BFCA	$x = 0.061, 0.085$	SC gap	[25]
Ba(Fe _{1-x} Co _x) ₂ As ₂	BFCA	$x = 0.061$	Gap, vertex	[36]
Ba(Fe _{1-x} Co _x) ₂ As ₂	BFCA	$x = 0.08$	Gap	[37]
Ba(Fe _{1-x} Co _x) ₂ As ₂	BFCA	$0 \leq x \leq 0.045$	SDW	[26]
Ba(Fe _{1-x} Co _x) ₂ As ₂	BFCA	$0 \leq x \leq 0.20$	Fluctuations	[30]
Ba(Fe _{1-x} Co _x) ₂ As ₂	BFCA	$0.055 \leq x \leq 0.10$	SC gap	[38]
Ba(Fe _{1-x} Co _x) ₂ As ₂	BFCA	$0 \leq x \leq 0.10$	SC gap-nematicity	[39]
Ba(Fe _{1-x} Co _x) ₂ As ₂	BFCA	$x = 0, 0.025, 0.051$	Fluctuations	[40]
Ba(Fe _{1-x} Co _x) ₂ As ₂	BFCA	$0.045 \leq x \leq 0.085$	Fluctuations and SC gap	[41]
Ca(Fe _{1-x} Co _x) ₂ As ₂		$x = 0.03$	Crystal field	[42]
Sr(Fe _{1-x} Co _x) ₂ As ₂		$x = 0, 0.04, 0.20$	SDW	[43, 44]
Ba(Fe _{1-x} Au _x) ₂ As ₂		$x = 0, 0.012, 0.014, 0.031$	Fluctuations	[45]
Ba _{1-x} K _x Fe ₂ As ₂	BKFA	$x = 0.4$	SC gap and pairing	[46]
Ba _{1-x} K _x Fe ₂ As ₂	BKFA	$x = 0.4$	SC gap and pairing	[47]
Ba _{1-x} K _x Fe ₂ As ₂	BKFA	$0.22 \leq x \leq 0.70$	Fluctuations and SC gap	[41]
Ba _{1-x} K _x Fe ₂ As ₂	BKFA	$x = 0.25, 0.4, 0.6$	Fluctuations and SC gap	[48]
BaFe ₂ (As _{1-x} P _x) ₂	BFAP	$x = 0.5$	Fluctuations and SC gap	[48]
NaFe _{1-x} Co _x As	Na111	$0 \leq x \leq 0.08$	Fluctuations and SC gap	[49]
CaKFe ₄ As ₄	CKFA/1144	No	SC gap and pairing	[50, 51]
Fe _{1+δ} Te _{1-x} Se _x		$x = 0, 0.4$	SC gap, phonon, magnon	[52]
FeSe	11	No	Fluctuations	[15, 53, 54]
FeSe	11	No	2-Magnon	[55]
FeSe _{0.82}	11	No	Crystal field	[56]
FeSe _{1-x} S _x		$x = 0, 0.04, 0.08, 0.15, 0.20$	Fluctuations	[57]
K _{0.75} Fe _{1.75} Se ₂		No	Gap	[58]
Rb _{0.8} Fe _{1.6} Se ₂		No	Gap	[46]
A _{0.8} Fe _{1.6} Se ₂		$A = \text{K, Rb, Cs, Tl}$	2-Magnon	[59]

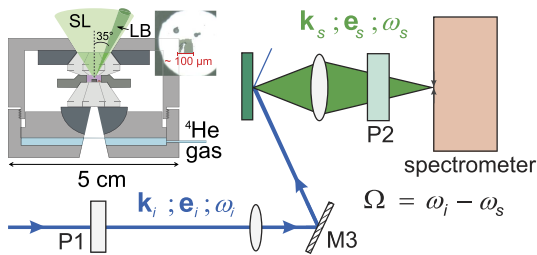


Figure 2. Schematic representation of a Raman experiment. The polarized monochromatic photons hit the sample at a large angle of incidence. The scattered photons are collected along the surface normal and pass the analyzer before entering the spectrometer. Inset: side view of a Raman pressure cell. The laser beam (LB) enters from the right, the scattered light (SL) is collected along the normal of the sample surface. Reprinted figure with permission from [15], Copyright (2018) by the American Physical Society.

the 122 family [23], being a result of FeAs self-flux growth [24], the study of electronic properties by light scattering became promising, and the superconducting gap was studied successfully in Ba(Fe_{1-x}Co_x)₂As₂ for two doping levels

[25]. Soon thereafter the redistribution of spectral weight in the SDW state of BaFe₂As₂ was reported [26, 27]. Finally, the fluctuations above the magneto-structural transformation, inferred from transport [28], were observed [29, 30]. Although there are reports on spectra in the range 1000 cm⁻¹ to 4000 cm⁻¹ (the energy range of two-magnon excitations) [31], their interpretation remains controversial.

The materials for which data on the spin, charge and orbital response exist are compiled in table 1.

4. Theoretical background

The analysis of the results in the FeBCs requires insight into the theoretical background, including both standard knowledge and modern developments. We give a brief historical summary and sketch the underlying theory with the emphasis placed on metallic systems.

4.1. Historical remarks

Raman scattering studies of excitations of localized spins started in the 1960s on insulating antiferromagnets [60] and

experienced a renaissance with the advent of the cuprates [61]. The theoretical framework was set by the seminal work of Elliot, Fleury and Loudon [62] which still represents the basis of contemporary analyses [63] even in the case of metallic systems such as the FeBCs [31, 64, 65].

Light scattering from conduction electrons was first discussed in the context of superconductors [66]. It took almost 20 years to observe the effect experimentally in the layered compound 2H-NbSe₂ [67]. In NbSe₂ superconductivity competes with a charge density wave (CDW) for area on the Fermi surface (FS), and the spectral features observed below T_c cannot directly be traced back to the superconducting energy gap in contrast to those for selected symmetries in the A15 compounds V₃Si and Nb₃Sn [68, 69] or in the cuprates [63, 70, 71]. Hence, only in special cases the Raman spectra of superconductors can be described satisfactorily in terms of lowest order weak coupling theory as developed between 1961 and 1984 [66, 72, 73]. In all other cases, including the FeBCs, lowest order is insufficient, although it still captures the plain vanilla such as the strong momentum dependence of the gap if the symmetries of the response are properly taken into account [74].

In normal metals, contributions from particle–hole excitations were observed and discussed for doped semiconductors [75, 76], but in-depth studies started only in the cuprates [77–81]. Similarly as in the superconducting state, the major contribution from Raman scattering, in addition to what was known from optical spectroscopy, was the observation of a polarization dependent relaxation of the carriers which could be mapped on the electronic momentum [74, 82].

Important new developments include the observation and analysis of critical fluctuations in both cuprates [83, 84] and FeBCs [29, 30, 49, 85–87]. In the superconducting state an anisotropic pairing potential [73, 88–92], amplitude (‘Higgs’) fluctuations of the superconducting order parameter [93, 94], number-phase fluctuations in multiband systems (Leggett modes [95]) [96–100] or a nematic resonance [39] need to be included. Whereas the interpretation of the results in NbSe₂ in terms of coupled gap excitations and amplitude fluctuations in a coupled SC-CDW system seems to converge [101, 102] the discussion of the E_g symmetry contributions in the A15 materials [68, 69, 89, 102, 103], the B_{1g} response in the cuprates [104–109] or the in-gap modes in the FeBCs [39, 41, 46, 47, 49] remains controversial. In addition to the weak-coupling description of the superconducting state at $T = 0$ a lot more work is needed to arrive at a coherent picture for the normal and superconducting states in the presence of collisions, fluctuations and strong coupling. Only a few special cases have been studied theoretically so far [77, 83, 85–87, 110–116]. More details can be found in references [63, 82] and, for recent developments, in [41, 64, 65, 85–87, 91, 92, 99, 100, 115–118].

4.2. Light scattering

Photons in the visible or x-ray range do not directly scatter off low-energy excitations. Rather, high-energy electron–hole pairs having energies of the incoming photons ($1.6 \leq \hbar\omega_I \leq$

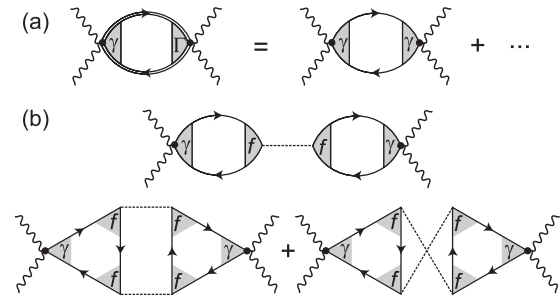


Figure 3. Feynman diagrams for (non-resonant) light scattering. (a) Raman response of particle–hole excitations in the presence of interactions and (b) scattering processes involving one and two bosonic excitations. Wavy lines represent incident and scattered photons whereas solid lines are electronic propagators. The bosonic excitation or fluctuation propagators are represented by dashed lines. The bare and renormalized Raman vertices γ and, respectively, Γ describe the interaction of light and electrons and f describes the interaction of electrons and other excitations, e.g. bosons.

3.5 eV for the visible) are created and couple to excitations in the range $\hbar\Omega = 1, \dots, 200$ meV such as phonons, fluctuations, particle–hole, gap or spin excitations [119]. After scattering, the electron–hole pairs recombine and emit photons with energies $\hbar\omega_S = \hbar\omega_I \mp \hbar\Omega$. The mechanism works whether or not the intermediate electronic states are eigenstates. If they are eigenstates the cross-section is resonantly enhanced, but most of the results were successfully analysed in terms of non-resonant scattering. In systems with a high correlation energy $U = \mathcal{O}(\hbar\omega_I)$ there are no well-defined eigenstates, and the resonances are in fact found to be mild in most of the cases.

Given these considerations, equation (1) is most naturally derived from scattering matrix elements in third order perturbation theory such as in the case of phonons or spin excitations [62, 119]. For electrons the Raman susceptibility or response function $\chi(\Omega, T)$ is almost always derived in the non-resonant limit using either diagrammatic techniques [63, 66, 73, 77] or the kinetic equation [82, 120]. Since $\chi(\Omega, T)$ is not a pure density or current correlation function there is no general sum rule such as the f -sum rule in optical conductivity [121]. Usually³ for this reason, the Raman cross section may be a superposition of independent contributions, for example particle–hole excitations (electronic continuum) and magnons or phonons. Occasionally, some of the excitations may be inter-related, for instance phonons and particle–hole excitations leading to the Fano effect (not discussed in this review) or gap formation and excitations in density-wave or superconducting states and the continuum playing an important role below.

The Raman response of all types of excitations is causal implying that $\chi_{I,S}^*(-\Omega) = \chi_{I,S}(\Omega)$ where $*$ denotes the complex conjugate. Thus $\chi_{I,S}''(\Omega)$ is anti-symmetric with respect to the origin, and its expansion contains only odd powers of Ω .

In figure 3, Feynman diagrams for Raman scattering are displayed. γ and Γ are the bare and the renormalized

³ Special cases [107, 122] are beyond the scope of this review.

vertices, respectively, for the interaction between light and electrons [63]. They depend on the light polarization and on momenta and determine the selection rules. In panel (a) particle–hole excitations are described. The bare vertex γ is an approximation where properties of the intermediate states are neglected assuming that all photon energies are smaller than any band gap, $\hbar\omega_{LS} < |\varepsilon_c - \varepsilon_\nu|$, where the subscripts c and ν refer to electrons in the conduction bands and those in other bands, respectively. Γ is a renormalized vertex in the spirit of the Bethe–Salpeter equation [123]. In panel (b) scattering from bosons via electrons is described. f is the vertex for the interaction between electrons and other excitations.

4.3. Charged systems

In general, visible light cannot transfer substantial momentum to a crystal since the lattice constant a is much smaller than the wavelengths λ_{LS} of the incoming and outgoing photons, and all unit cells are excited in phase. This is usually called the $q = 0$ selection rule of Raman scattering in crystals. In the case of (resonant) inelastic x-ray scattering [(R)IXS] with $\lambda = \mathcal{O}(a)$ most of the Brillouin zone can be accessed [124]. Metals have a small penetration depth for light $a < \delta_0 < \lambda_{LS}$. As a consequence, the momentum transfer in a metal is bigger than in an insulator, $|\mathbf{q}| = q \sim \delta_0^{-1}$, where $100 \text{ \AA} < \delta_0 < 1000 \text{ \AA}$ for typical metals, as pointed out first by Abrikosov and Fal’kovskii [66]. Yet, the available momentum is still much smaller than π/a , and for exciting a non-interacting conduction electron from an occupied (i) to an unoccupied (f) state the maximal energy is limited by $\hbar\Omega_{\max} = \epsilon_{\mathbf{k}}^{(f)} - \epsilon_{\mathbf{k}}^{(i)} \approx \hbar v_F \delta_0^{-1}$ where $\epsilon_{\mathbf{k}}$ is the electronic dispersion. In the FeBCs the relevant in-plane Fermi velocity is of order 10^6 cm s^{-1} , and the penetration depth is close to 1000 \AA yielding $\hbar\Omega_{\max} \lesssim 1 \text{ meV} \approx 8 \text{ cm}^{-1}$.

Due to charge conservation and screening all isotropic charge excitations are pushed up to the plasma frequency Ω_{pl} [125], and there is no scattering in the range of $k_B T$ in non-interacting systems with a strictly quadratic electron dispersion. What looks like a disadvantage at first glance is the origin of the selection rules for electronic Raman scattering [72]. Loosely speaking, one cannot move charges from one unit cell to another one but the charges can only be redistributed in phase inside all unit cells (quadrupolar-type of excitations). This is the origin of the form factors, and the light does not scatter from the charge density but from a weighted charge density [72, 73, 89],

$$\tilde{\rho}_{\mathbf{q}} = \frac{1}{N} \sum_n \sum_{\mathbf{k}, \sigma} \gamma_n(\mathbf{k}, \mathbf{q}) c_{n, \mathbf{k}+\mathbf{q}, \sigma}^\dagger c_{n, \mathbf{k}, \sigma}. \quad (2)$$

n is the band index, and $\gamma_n(\mathbf{k}, \mathbf{q})$ is a form factor which is related to the Raman vertex $\gamma_{\alpha, \beta}(\mathbf{k}, \mathbf{q})$ through the polarization directions $\hat{\mathbf{e}}_{LS}$,

$$\gamma_n(\mathbf{k}, \mathbf{q}) = \sum_{\alpha, \beta} e_I^\alpha \gamma_{n, \alpha, \beta}(\mathbf{k}, \mathbf{q}) e_S^\beta. \quad (3)$$

The bare response $\tilde{\chi}(\mathbf{q}, \Omega)$ is the commutator of $\tilde{\rho}_{\mathbf{q}}$,

$$\tilde{\chi}(\mathbf{q}, \Omega) = \langle\langle [\tilde{\rho}_{\mathbf{q}}(t), \tilde{\rho}_{-\mathbf{q}}(0)] \rangle\rangle_\Omega = \tilde{\chi}' + i\tilde{\chi}'', \quad (4)$$

where $\langle\langle \dots \rangle\rangle_\Omega$ denotes the thermodynamic average and the Fourier transformation, and $\tilde{\chi}'$ and $\tilde{\chi}''$ are the real and imaginary part of $\tilde{\chi}$, respectively. Equation (4) includes a sum over the Brillouin zone and the bands through equation (2), and can be recast as [82],

$$\tilde{\chi}_{a,b}(\mathbf{q}, \Omega) = \frac{1}{N} \sum_n \sum_{\mathbf{k}} a_{\mathbf{k}} b_{\mathbf{k}} \Theta_n(\mathbf{k}, \Omega). \quad (5)$$

$a = a_{\mathbf{k}}$ and $b = b_{\mathbf{k}}$ are generalized vertices that stand for either an isotropic (1) or Raman ($\gamma(\mathbf{k}, \mathbf{q})$) or renormalized Raman ($\Gamma(\mathbf{k}, \mathbf{q})$) vertex. $\Theta_n(\mathbf{k}, \Omega)$ is the response kernel, examples of which will be presented below.

The bare response is not gauge invariant, and charge conservation and screening lead to the final—exact and gauge-invariant—result for the response [89, 120, 126],

$$\chi_{\gamma, \gamma} = \tilde{\chi}_{\gamma, \gamma} - \frac{\tilde{\chi}_{1, \gamma} \tilde{\chi}_{\gamma, 1}}{\tilde{\chi}_{1, 1}} \left(1 - \frac{1}{\varepsilon} \right). \quad (6)$$

The projected structure of the first two terms is a result of charge conservation. The polarization-dependent vertex is written down explicitly as a subscript in equation (6), and ε in the third term is the dielectric function which originates from screening alone. Since a constant vertex can be pulled in front of the sum of equation (2) the first two terms of equation (6) cancel for constant γ (corresponding to lowest order A_{1g} symmetry and/or strictly parabolic dispersion), and only the last term survives but is suppressed as q^2/Ω_{pl}^2 in a charged system. In the fully symmetric channel having A_{1g} symmetry in the D_{4h} space group, applicable for most of the FeBCs, the response is at least partially screened.

4.4. Weakly interacting systems

The scattering from free electrons cuts off at $\hbar\Omega_{\max}$ [127]. In a realistic normal metal with a single conduction band either impurities or interactions can maintain the $q = 0$ selection rule and facilitate the occurrence of broad continua extending to energies well above $\hbar\Omega_{\max}$ [77, 128]. Obviously this is the case in all materials of interest with interactions including the FeBCs, the cuprates, the A15 compounds, MgB_2 and many others. However, only in the cuprates the argumentation is straightforward since there is one conduction band in the single-layer compounds with one CuO_2 plane per unit cell, for instance $\text{La}_{2-x}\text{Sr}_x\text{CuO}_4$. Somewhat surprisingly, the response is nearly identical in the double-layer compounds (two neighboring CuO_2 planes) such as $\text{YBa}_2\text{Cu}_3\text{O}_{6+y}$ to that in materials with just one CuO_2 plane. It was in fact shown that the contributions from individual bands in multi-band systems just add up to a good approximation not only in the cuprates [129] but also in the FeBC [117] allowing one, as a starting point, to treat the response in a band basis and neglect inter-band transition.

If we disregard spurious contributions to the cross section such as luminescence (being a good approximation at low energies; see, however, reference [57]) only (dynamic) interactions can produce the broad continua observed [81, 130]. Impurities are present but irrelevant in high-quality single crystals as can be seen directly below T_c since impurities reduce the effect of pair breaking in the Raman spectra. As shown by

Klein and Dierker [73] the response of a clean isotropic superconductor has a square root singularity at the gap edge 2Δ in the limit $q = 0$. In the presence of impurities (and similarly for finite q [73]) the singularity disappears and the response at 2Δ becomes finite and scales as $\Delta\tau_0$, where τ_0 is the impurity scattering time [110–112]. In all realistic cases the difference between the normal and superconducting spectra cannot be observed any further for $\hbar\tau_0^{-1} \rightarrow \Delta$. Therefore, the continuum in superconductors essentially comes from dynamical interactions between the conduction electrons and other excitations which are gapped out below T_c for $\hbar\Omega \lesssim 2\Delta$. In nearly all superconductors which have been studied by light scattering this conclusion holds. The only exception is the A_{1g} response in A15 compounds where the normal state intensity vanishes [103, 131].

Although the normal state continuum generally signals the presence of strong interactions, it is impossible to describe the superconducting response in terms of strong-coupling theory so long as the microscopic origin of the relevant interactions is unknown. Only in the case of spin fluctuations both the normal and the superconducting spectra have been modelled microscopically on equal footing [113]. In a few cases phenomenological descriptions on the basis of Eliashberg theory were applied [112, 132–134].

In the majority of cases, the weak-coupling result [73] is used since it is sufficient to capture the generic properties of the superconducting state. The response kernel is given by the Tsuneto–Maki (TM) function [135],

$$\Theta''_{\mathbf{k},\text{TM}}(\Omega, T) = \frac{\pi}{2} \frac{|2\Delta_{\mathbf{k}}|^2}{\Omega \sqrt{\Omega^2 - |2\Delta_{\mathbf{k}}|^2}}; \quad \Omega > |2\Delta_{\mathbf{k}}|. \quad (7)$$

It is the result of a superposition of particle excitations across the gap from an occupied into an unoccupied state and pair breaking. Both contributions have a square-root singularity at $|2\Delta_{\mathbf{k}}|$ and, because of the coherence factors, add constructively in the case of light scattering and destructively in the case of the (real part of the) optical (IR) conductivity $\sigma'(\Omega)$ [136].

In the case of a charge or spin density wave the functional form of the response close to the density-wave gap $|2\Delta_{\text{DW}}|$ is also described by equation (7) [137] if the material is insulating below the transition. In a metal the best way of describing the response is the superposition of a normal metallic response (see next section) and a condensate in the spirit of a two-fluid model [82]. In all metallic cases there is an incomplete redistribution of spectral weight from low to high energies starting abruptly at the transition temperature. The line shape is comparable to that of a superconductor having an anisotropic gap with BaFe_2As_2 being a prototypical example for SDW formation in the pnictides [38].

4.5. Collision limited regime

The simplest type of response in the normal state in systems with vanishingly small $\hbar v_F q$ results from the presence of (heavy) impurities. Here the electrons change only

their momentum but not their energy (Drude model). The gauge-invariant kernel was derived by Zawadowski and Cardona [77],

$$\Theta''_{\mathbf{k},\text{D}}(\Omega) = \frac{\pi}{2} \frac{\hbar\Omega\Gamma_{\mathbf{k}}^*}{(\hbar\Omega)^2 + (\Gamma_{\mathbf{k}}^*)^2}, \quad (8)$$

where $\Gamma_{\mathbf{k}}^* = \hbar(\tau_{\mathbf{k}}^*)^{-1}$. $\tau_{\mathbf{k}}^*$ is not identical to the electronic relaxation time but is renormalized by a (presumably small) channel-dependent vertex correction, similarly as in ordinary transport where the vertex corrections ensure (among other things) that forward scattering does not contribute to the resistivity. $\Gamma_{\mathbf{k}}^*$ is temperature and energy independent.

If the electrons scatter from excitations in the energy range of $k_B T$ such as phonons, spin fluctuations or among themselves they transfer both momentum and energy. As a consequence they become dressed quasi-particles, and the relaxation rate depends now on energy, momentum and temperature. Due to these interaction effects, the electron velocity gets reduced and the mass increases by the same factor $1 + \lambda_{\mathbf{k}}(\Omega, T)$, and the extended Drude response reads [81]

$$\Theta''_{\mathbf{k},\text{eD}}(\Omega, T) = \frac{\pi}{2} \frac{\hbar\Omega\Gamma_{\mathbf{k}}^*(\Omega, T)}{(\hbar\Omega[1 + \lambda_{\mathbf{k}}(\Omega, T)])^2 + [\Gamma_{\mathbf{k}}^*(\Omega, T)]^2}. \quad (9)$$

The energy and temperature dependent projected parameters $\Gamma_{\mathbf{k}}^*(\Omega, T)$ and $1 + \lambda_{\mathbf{k}}(\Omega, T)$ can be derived if $\Theta''_{\mathbf{k},\text{eD}}(\Omega, T)$ is known for a sufficiently wide energy interval [81]. The zero-energy extrapolation value of $\Gamma_0(T) = \Gamma_{\mathbf{k}}^*(\Omega \rightarrow 0, T)$ can be compared with ordinary or optical transport, for instance. Shastry and Shraiman [138] noticed that the relation between the Raman response and the real part of the optical conductivity, $\Theta''_{\mathbf{k},(\text{e})\text{D}}(\Omega, T) \propto \Omega\sigma'(\Omega, T)$, is a good approximation in many cases, in particular if the momentum dependence is weak⁴. In this sense $\Theta''_{\mathbf{k},(\text{e})\text{D}}(\Omega, T)/\Omega$ is a momentum dependent ‘Raman conductivity’.

An expression equivalent to equation (9) can be derived for the superconducting or a density-wave state in terms of Eliashberg theory. It is considerably more complicated, and the normal state continuum and the gap excitations are closely interrelated [113]. Since this analysis was not used in the case of the FeBCs so far we do not reproduce it here. The interested reader can consult references [132, 134]. Qualitatively, the continuum is gapped out below $|2\Delta|$ for zero temperature and increases continuously for $0 < T \leq T_{\text{c(DW)}}$ due to the presence of thermal excitations. In the zero-energy limit $\chi'' \propto \Omega$, and the initial slope reflects the anomalous (Nambu) Raman relaxation rate $\Gamma_{0,\mu}^{\text{SC(DW)}}$ inside the gap being similarly difficult to analyze as the relaxation rates in NMR, microwave or ultrasound absorption experiments, in particular in unconventional systems.

All results summarized here are essentially lowest-order response theory. However, the experiments in $\text{Ba}_{1-x}\text{K}_x\text{Fe}_2\text{As}_2$ and $\text{Na}(\text{Fe}_{1-x}\text{Co}_x)\text{As}_2$ show [41, 46, 47, 49] that higher order corrections may be necessary for the proper interpretation

⁴ The reason is that σ' is always an average over the entire Fermi surface whereas $\Theta''_{\mathbf{k},(\text{e})\text{D}}$ is not (see below).

and for extracting relevant information on the pairing in the superconducting state [47, 90, 91, 115, 118].

4.6. Beyond lowest order

Equation (7) is the lowest-order approximation of the response and is not gauge invariant as already pointed out by Klein and Dierker [73]. The controversy as to whether or not the resulting vertex corrections are relevant for the interpretation in the A15 materials is still not settled [73, 89, 94, 103, 139]. A similar narrow in-gap mode as in the E_g response of the A15s was observed recently in BKFA where it is well separated from the pair-breaking peak [46]. A mode in the $d_{x^2-y^2}$ channel (1 Fe unit cell) with this property was predicted by Scalapino and Devereaux [91] for a two-band model applicable to the FeBCs. Chubukov and coworkers [90] predicted an A_{1g} mode originating from the same type of mechanism for a different hierarchy of pairing instabilities.

The existence of in-gap modes in a superconductor was first noticed by Bardasis and Schrieffer (BS) [140]. They studied the effect of final state interaction in the presence of an anisotropic pairing potential $V_{\mathbf{k},\mathbf{k}'}$ and found undamped modes below the gap edge, $\hbar\Omega_{L,M} < 2\Delta$, which are characterized by quantum numbers L and M corresponding to the expansion of $V_{\mathbf{k},\mathbf{k}'}$ into spherical harmonics. These collective excitations, usually called BS modes, are similar to excitons in semiconductors with binding energy $E_{b,L,M} = 2\Delta - \hbar\Omega_{L,M}$. For simplicity they may be referred to as $E_{BS,\alpha}$ labelled by α in consecutive order. The result was adopted for light scattering in superconductors [89] and is formally similar to light scattering from roton pairs in superfluid ^4He [88, 141]. The predictions include symmetry selection rules and the dependence of $E_{BS,\alpha}$ and the strength of the pole $Z_{BS,\alpha}$ on the relative coupling strength of the sub-leading channels $\alpha > 1$ with respect to the ground state $\alpha = 1$, λ_α/λ_1 . As pointed out in references [90, 91] the analysis of these excitons would help in clarifying the so far elusive pairing mechanism in the FeBCs.

The functional form of the response additional to lowest order (equation (7)) reads [91],

$$\Delta\tilde{\chi}''(\Omega) = \frac{8}{\Omega^2} \Im \left\{ \frac{\langle \gamma(\mathbf{k})g(\mathbf{k})\Delta(\mathbf{k})\bar{P}(\Omega, \mathbf{k})^2 \rangle}{(\lambda_d^{-1} - \lambda_s^{-1}) - \langle g^2\bar{P}(\Omega, \mathbf{k}) \rangle} \right\}, \quad (10)$$

where $\gamma(\mathbf{k})$ is the usual Raman vertex, $g(\mathbf{k})$ is the d -wave-like form factor on the electron bands for making the interaction between them separable, and $\bar{P}(\Omega, \mathbf{k})$ is the complex superconducting response kernel the imaginary part of which is given in equation (7). Equation (10) was used in reference [47] for estimating the value of the sub-leading $d_{x^2-y^2}$ coupling parameter λ_d from the electronic Raman spectra of BKFA for a given s -wave coupling strength λ_s . Identical expressions with redefined coupling parameters were derived for explaining the nematic resonance [39]. Similarly as in the case of excitons, there may be more than one BS mode in the presence of several sub-leading coupling channels. This possibility was considered recently in a theoretical study [92].

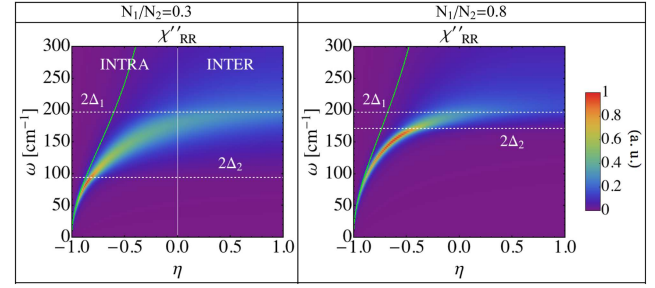


Figure 4. Response from Leggett modes in a two-gap system. N_i is the density of states on band i . η encodes the ratio of intra- to inter-band coupling with $\eta = -1$ and $\eta = 1$ representing pure intra- and inter-band coupling, respectively. The mode's energy saturates at the maximal gap. The damping starts above the smaller gap. Reprinted figure with permission from [99], Copyright (2016) by the American Physical Society.

In a system with more than one band there is an additional contribution to the response from number-phase oscillations between the bands in momentum space comparable to the Josephson effect in real space [95]. It must be included to make the response gauge invariant, as pointed out recently by Cea and Benfatto [99]. Usually, for instance in the cases studied theoretically by Suhl and coworkers [142], which is possibly realized in MgB_2 , the main contribution to superconductivity comes from coupling in the individual bands having strength $\lambda_{i,i}$. The inter-band coupling $\lambda_{i,j}$ is weaker but leads to an increase of T_c to values above the maximum of the individual bands. It is widely believed that the main contribution to pairing in the FeBC has its origin in inter-band [9] or inter-orbital [143] coupling and that the intra-band pairing is weak. The effect of weak inter-band coupling was investigated already earlier in the context of MgB_2 [96, 97] whereas strong inter-band coupling was addressed only recently in the context of the FeBCs [98–100]. The symmetry properties of the Leggett modes depend sensitively on the orbital content [98, 100].

For weak inter-band coupling, the mode related to the number-phase fluctuations is below the gap energy and increases essentially linearly with $\lambda_{i,j}$. For $\lambda_{i,i} \ll \lambda_{i,j}$ the Leggett mode is in the continuum above 2Δ and is therefore overdamped. Figure 4 shows the transition between the two coupling regimes and demonstrates the damping effect. In addition, it could be shown that the energy saturates at the maximal gap energy.

4.7. Spin excitations

For spin excitations the Elliot–Fleury–Loudon Hamiltonian [62] is the simplest nonresonant interaction operator which describes scattering in a Heisenberg model with nearest-neighbour exchange coupling J ,

$$\hat{H}_{\text{EFL}} = J \sum_{\langle i, \hat{\delta} \rangle} (\hat{\delta} \cdot \hat{\mathbf{e}}_i)(\hat{\delta} \cdot \hat{\mathbf{e}}_s)(\mathbf{S}_{\mathbf{r}(i)} \cdot \mathbf{S}_{\mathbf{r}(i) + \hat{\delta}a}). \quad (11)$$

$\mathbf{S}_{\mathbf{r}(i)}$ is a spin at site $\mathbf{r}(i)$, a is the distance between the sites and $\hat{\delta}$ is a unit vector pointing towards one of the nearest

neighbors. $\langle i, \delta \rangle$ is a restricted sum to avoid double counting. The spectral shape can either be determined in terms of spin-wave theory [62], by numerical [64] or field theoretical methods [144]. In the thermodynamic limit (infinitely large systems) of a spin-only model the low-energy limit is characterized by an Ω^3 variation of the response [144–147]. If there exist itinerant electrons in addition to localized spins, such as proposed for FeSe for instance [148–150], the spin response may be superimposed on an electronic continuum. Possible interrelation effects have not been explored yet.

In anisotropic systems two-magnon excitations may be observed well above T_N . Then the evolution of the two-magnon line is continuous over large temperature ranges below and above T_N [151]. Thus the line shape and the temperature dependence of the response allows one to clearly distinguish the scattering from localized and itinerant spins as described at the end of section 4.4.

Screening may become relevant in metallic systems such as the FeBCs in which the spins forming the SDW are itinerant as opposed to the cuprates which are Mott insulators at low doping. However, there is no analytic treatment yet dealing with the problem of light scattering from spin polarized conduction electrons beyond SDW formation or the nearly antiferromagnetic Fermi liquid [152]. Doped cuprates were studied using quantum Monte Carlo methods [153, 154]. Considerations along these lines may surface when analyzing the differences between the pnictides and chalcogenides where the magnetism is believed to be predominantly itinerant and localized, respectively, at least for some orbitals [149, 155–158]. However, this rather general problem cannot be solved here and the controversial discussion on spin excitations in the FeBCs requires additional work.

4.8. Fluctuations

In the case of fluctuations, there are three possibilities to deal with the $q = 0$ selection rule. (i) A fluctuation can have zero momentum. This case applies if all unit cells have the same excitation pattern as for the case of ferro-orbital fluctuations [49]. (ii) A fluctuation with finite critical wave vector such as $\mathbf{q}_c = (\pi, \pi)$ or $\mathbf{q}_c = (\pi, 0)$ for incipient Néel type or stripe-like antiferromagnetic order, respectively, can exchange momentum with another excitation or a defect. The case of moderately high defect concentrations was studied by Gallais and Paul [116]. The momentum transferred by the photons is certainly insufficient for large critical momenta (see section 4.3). (iii) Two fluctuations with opposite momenta are exchanged. It is exactly what happens in the case of two-magnon excitations in a system with long-ranged order [62, 159]. The same type of scattering may also occur in partially ordered systems [160] or in the presence of critical fluctuations [83]. This type of diagrams were first studied by Aslamazov and Larkin in the context of paraconductivity above the superconduction transition [161].

For the FeBCs there are various theoretical studies on the Raman response of fluctuations [85–87, 115, 118]. Although

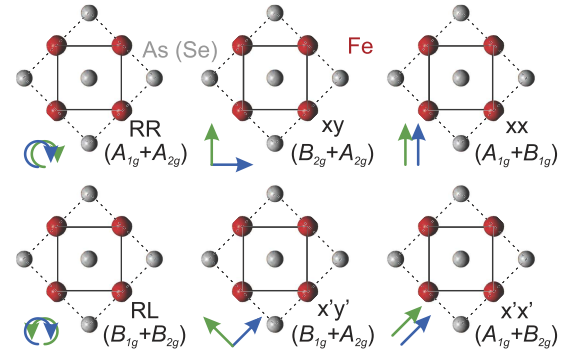


Figure 5. Scattering geometry and symmetries for the ab plane of FeBCs. Incoming and scattered photon polarizations are indicated as blue and green arrows. In backscattering configuration, the arrows corresponding to R and L polarization of the scattered light should be interchanged. The symmetries refer to the 1 Fe unit cell (full line) which is relevant (and frequently used) for electronic and spin excitations. Phonons have the right symmetry in the crystallographic or 2 Fe unit cell (broken line) where B_{1g} and B_{2g} are interchanged with respect to the 1 Fe cell.

spin, orbital, and charge degrees of freedom are not independent, the question as to the leading instability remains relevant and crucial for the understanding of the FeBCs [40, 49, 115, 116, 118, 162–166].

4.9. Selection rules

In an inelastic light scattering experiment, all selection rules must be compatible with the direct product of two dipole transitions in the relevant crystal structure [119]. Figure 5 shows the main scattering geometries and the related sums of projected symmetries μ of the D_{4h} point group relevant for FeBCs (and cuprates). The pure symmetries can only be obtained by linear combinations of the spectra measured in appropriate geometries. The symmetry selection rules are generally valid and well known for, e.g., phonons. We now consider those for spin and charge excitations.

4.9.1. Particle-hole and gap excitations. In the simplest approximation the vertices relevant for the projections in the Brillouin zone can be expanded into crystal harmonics of the respective point group [167]. Figure 6 shows the related symmetry form factors μ .

In first order approximation selection rules can be derived on the basis of symmetry alone since $\gamma_\mu(\mathbf{k}, \mathbf{q} \rightarrow 0)$ can be expanded into the set of basis functions $\Phi_\mu(\mathbf{k})$ [82]. Figure 6 shows schematic representations of the first and second order basis functions (crystal harmonics) of each symmetry to which the Raman vertices γ_μ are proportional. For particle-hole excitations, symmetry-resolved Raman vertices can be derived from the band structure within the effective mass approximation,

$$\gamma_{n,A_{1g}}(\mathbf{k}, \mathbf{q} \rightarrow 0) \propto \frac{1}{2} \left(\frac{\partial^2 \varepsilon_n(\mathbf{k})}{\partial k_x^2} + \frac{\partial^2 \varepsilon_n(\mathbf{k})}{\partial k_y^2} \right) \quad (12)$$

$$\gamma_{n,B_{1g}}(\mathbf{k}, \mathbf{q} \rightarrow 0) \propto \frac{1}{2} \left(\frac{\partial^2 \varepsilon_n(\mathbf{k})}{\partial k_x^2} - \frac{\partial^2 \varepsilon_n(\mathbf{k})}{\partial k_y^2} \right) \quad (13)$$

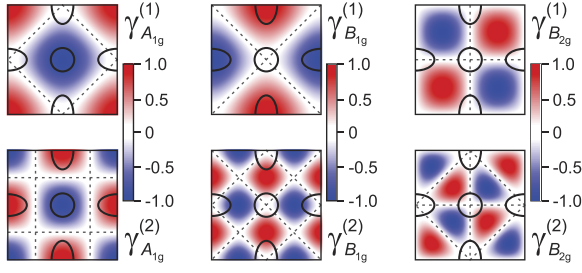


Figure 6. Symmetry properties and momentum dependences of the Raman vertices γ_μ . Shown are the first and second order vertices (form factors) for the symmetries $\mu = A_{1g}, B_{1g}$ and B_{2g} of the D_{4h} point group. The zeroth order A_{1g} vertex is just a constant and is entirely screened. Higher order A_{1g} vertices are only partially screened. The solid lines represent an idealized two-band Fermi surface of FeSCs in the 1Fe unit cell. For the symmetry properties of the band structure in the FeBCs the screening in A_{1g} symmetry is almost negligible [117].

$$\gamma_{n,B_{2g}}(\mathbf{k}, \mathbf{q} \rightarrow 0) \propto \left(\frac{\partial^2 \varepsilon_n(\mathbf{k})}{\partial k_x \partial k_y} \right), \quad (14)$$

where n is the band index. The vertex for each symmetry μ is obtained by summing over all bands crossing E_F .

The first-order diagram on the right-hand side of figure 3(a) describes particle–hole excitations above and below T_c upon using the propagators for either the normal or the superconducting state. The evaluation yields the Raman response which depends quadratically on $\gamma_\mu(\mathbf{k})$. The vertices for $\text{Ba}(\text{Fe}_{1-x}\text{Co}_x)_2\text{As}_2$ and $\text{Ba}_{1-x}\text{K}_x\text{Fe}_2\text{As}_2$ were calculated in references [36, 47] yielding $\gamma_{A_{1g}}^{(2)}$ rather than $\gamma_{A_{1g}}^{(1)}$ to be relevant for presumably most of the FeBCs. As can be seen from figure 6, in the B_{1g} symmetry ($\gamma_{B_{1g}}^{(1)}$) one may expect to probe electron pockets, whereas both electron and hole pockets may be probed in A_{1g} symmetry ($\gamma_{A_{1g}}^{(2)}$). The dependence of the Raman response on $\gamma_\mu^2(\mathbf{k})$ directly explains the selectivity in k -space.

4.9.2. Bardasis-Schrieffer modes. The selection rules for BS modes depend on the symmetry of the sub-leading interaction. The first proposals considered a ground state being driven by spin fluctuations thus having an s_\pm -wave gap with opposite sign on the electron and hole bands. Then, if the sub-leading channel originates from orbital fluctuations, predominantly along the $(\pi, 0)$ direction [143], the BS mode is expected in the A_{1g} channel [90]. Alternatively, the next strongest pairing interactions can have the same origin as the ground state resulting from spin fluctuations between the electron bands along (π, π) thus entailing a BS mode in B_{1g} symmetry.

4.9.3. Leggett modes. The symmetry selection rules for the Leggett modes depend on the interactions included and thus on the band structure and the coupling. If two concentric bands or interactions with wave-vector $(\pi, 0)$ are included the Leggett mode appears in the fully symmetric A_{1g} channel [99]. In the case when (π, π) interactions have to be considered, in particular if the central hole band is missing, the Leggett modes appear in B_{1g} symmetry [100]. In the case of fluctuations

between the d_{xz} and d_{yz} orbitals Leggett modes may also appear in B_{1g} symmetry so long as they are not overdamped [98].

4.9.4. Fluctuations. Fluctuation contributions to the Raman response may arise from one and/or two fluctuations (see figure 3(b)). As can be seen from the diagrams, the first order term is non-vanishing only if the symmetry of the fluctuation is that of the Raman vertex. On the other hand, second order diagrams include electronic loops $\Lambda_\mu^0(\mathbf{q})$ which depend linearly on γ and quadratically on f . Consequently, for a given critical vector \mathbf{q}_c and a set of FS hot spots \mathbf{k}_0 which are connected by \mathbf{q}_c , the selection rules for the second order term read $\Lambda_\mu^0(\mathbf{q}_c) \propto \sum_{\mathbf{k}_0} \gamma_\mu(\mathbf{q}_c)$ [83]. It states that a finite response in symmetry channel μ is expected only if \mathbf{q}_c connects hot-spots in which γ_μ does not change sign. As opposed to the first order term, γ_μ does not necessarily reflect the symmetry of the fluctuation for second order processes.

5. Instabilities beyond superconductivity

The phase diagram (figure 1) shows that the FeBCs have a multitude of instabilities beyond superconductivity. Their interrelation amongst each other and with superconductivity is a main focus of research. For certain ranges of doping and/or applied pressure all FeBCs exhibit long range magnetism while remaining metallic in contrast to undoped cuprates. Some of the FeBCs like FeSe display only short-ranged magnetic order at finite temperature [157, 168]. Not surprisingly, the nature of the magnetism is still under discussion. It was shown recently that the degree of localization of electrons and thus spins may depend on the orbital and varies between the materials [149].

Above the magnetic ordering temperature there are various structural transitions which typically go along with electronic anisotropies such as substantial differences in the resistivities measured along inequivalent directions [28] or orbital order, specifically of the d_{xz} and d_{yz} orbitals [169]. Yet, how can the origin of these differences be pinned down?

5.1. Excitations from localized spins

While itinerant and localized magnetism cannot easily be distinguished by neutron scattering, Raman scattering offers clear criteria [55] which are outlined in sections 4.4 and 4.7. The main arguments are the temperature, doping and symmetry dependences and line shapes.

Early experiments on Fe chalcogenides and pnictides reported excitations in the range 2000–4000 cm^{-1} in all symmetries. The results were interpreted in terms of local spins [27, 31], and the energies are in fact compatible with the exchange coupling $J \approx 120$ meV found by neutron scattering or density functional theory (DFT) [170]. With the improvement of the sample quality, the peaks in this range faded away and may be traced back to luminescence with high probability [43].

Recent experiments in FeSe support scattering from localized spins. The B_{1g} spectra at high (300 K) and low (20 K)

temperature are dominated by a broad peak centered at approximately 500 cm^{-1} , whereas near T_S an additional sharp peak appears in the range $100\text{--}200 \text{ cm}^{-1}$ [53, 55, 57] which we disregard here but discuss in detail below in the context of fluctuations. The main peak in B_{1g} symmetry at 500 cm^{-1} depends continuously on temperature [55] and survives low doping with sulfur [57]. For FeS the excitation is completely gone. In contrast to Massat *et al* [53] and Zhang *et al* [57], Baum and coworkers [55] assign this peak to a two-magnon excitation of nearly frustrated spins.

There are experimental and theoretical arguments for this assessment. Very generally, antiferromagnetically ordered local spins give rise to two-magnon excitations close to $3J$ [62] whereas SDW order in a metallic system leads to instantaneously appearing coherence effects close to the gap energy in the electronic excitation spectrum similar to those in a superconductor (see section 4.4). In FeSe, the pronounced excitation in B_{1g} symmetry on top of the particle-hole continuum builds up gradually [53, 55]. Thus the temperature dependence of the scattering intensity is compatible with that of a quasi two-dimensional Néel antiferromagnet, e.g., $\text{YBa}_2\text{Cu}_3\text{O}_6$ [151]. However, the energy of the B_{1g} peak is too small by approximately a factor of five, suggesting frustrated magnetism, as studied theoretically already in pnictides and chalcogenides [64], expected from LDA results [170], and explored recently for FeSe using exact diagonalization [171].

On a square lattice, frustration can occur in the presence of interactions beyond nearest-neighbour coupling. In this case, a variety of ordering patterns or wave vectors may be realized. A possible model is the $J_1\text{--}J_2\text{--}J_3\text{--}K$ Heisenberg model [170] where nearest, next-nearest and next-next-nearest neighbor exchange couplings are taken into account. K is the coefficient of the bilinear interaction proportional to $(\mathbf{S}_i \cdot \mathbf{S}_j)^2$ which, depending on the sign (de)stabilizes long-range order. For $J_2 \approx 0.5J_1$ Néel (π, π) and stripe $(\pi, 0)$ order occur with similar probability for $J_3 \rightarrow 0$ and are separated by a $(\pi, \pi/2)$ phase for $J_3 > 0$ [170]. In all cases, little energy is required for flipping a spin, and the maximum of the two-magnon excitation moves to zero energy in the classical limit ($S \rightarrow \infty$) and to approximately $0.5J_1$ for $S = 1/2$ as opposed to $2.84J_1$ when J_1 dominates [144]. The near degeneracy of the Néel and the stripe state going along with short range order in FeSe was not only predicted by LDA studies [170] but also observed recently by neutron scattering [157].

The B_{1g} response in FeSe was studied theoretically for zero and finite temperature by diagonalizing a 4×4 cluster carrying spin 1 using $J_2 = 0.528J_1$ and $J_3 = 0$ [55, 171]. The observed agreement between theory and experiment is semi-quantitative for all symmetries. The conclusions are in agreement with those of the neutron scattering experiments [157] and support the existence of local spins. How are local spins compatible with metallic transport in FeSe and why is FeSe different from the pnictides? Before discussing this question in section 5.4 the SDW systems and fluctuations will be reviewed.

5.2. Spin density wave order

Signatures of the SDW in the Raman spectra of BFA were first discussed by Chauvière *et al* [26]. Figure 7 compares the low

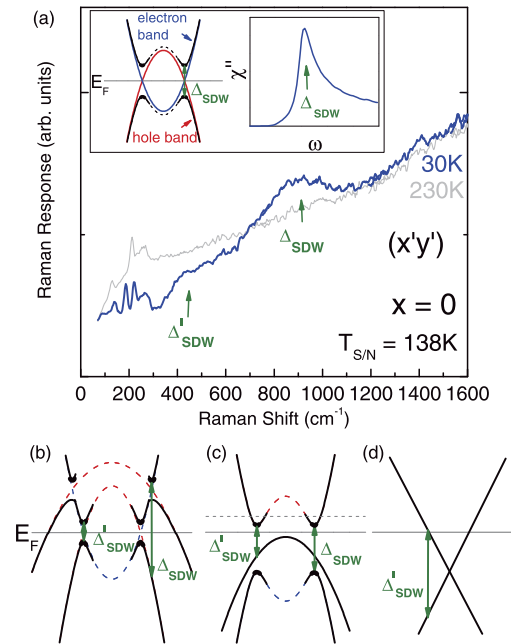


Figure 7. Effect of SDW formation on the Raman response of BFA. (a) High- and low-temperature Raman response in $x'y'$ configuration. The spectra show two spectral features at Δ_{SDW} and Δ'_{SDW} . The inset shows the anti-crossing of the hole and electron band and the related opening of Δ_{SDW} . The Raman response (right) is given by Equation (7). (b) If one electron band and two hole bands anti-cross Δ_{SDW} is much larger than Δ'_{SDW} . (c) If one of the hole bands does not reach the Fermi level the two gaps are expected to have similar magnitude. For phase-space reasons the response at Δ'_{SDW} has higher spectral weight than that at Δ_{SDW} in case (b) in comparison to case (c). (d) In the presence of a Dirac cone (non-interacting bands) Δ'_{SDW} should be characterized by very small spectral weight, and Δ_{SDW} is not expected to be observable. Reprinted figure with permission from [26], Copyright (2011) by the American Physical Society.

and high temperature B_{1g} Raman response. Spectral weight is redistributed from energies below to above the SDW gap upon entering the SDW state. The Raman spectra exhibit two distinct features: A peak at about 900 cm^{-1} appearing only in B_{1g} symmetry and a step-like increase at about 400 cm^{-1} in all channels [26].

The B_{1g} selection rules for inter-orbital transitions would be compatible with a transition $d_{x^2-y^2} \leftrightarrow d_{z^2}$ to correspond to the peak at 900 cm^{-1} . Yet, this straightforward explanation is in conflict with band-structure calculations which find the dominant contribution to the states at the Fermi surface to originate from d_{xz} , d_{yz} , and d_{xy} orbitals. Thus intensity can only be redistributed among these orbitals. Consequently, a band-folding picture was suggested with two types of electronic transitions in the SDW state: (a) a high-energy transition between electron and hole bands anti-crossing after back-folding and (b) a low-energy transition involving either interacting or noninteracting bands. Upon Co substitution, the peak observed in B_{1g} symmetry disappears due to the increase of the Fermi energy and the related filling of the unoccupied states at the anti-crossing points [26].

A much more pronounced redistribution of spectral weight was reported for Sr122 [43] with a suppression at low

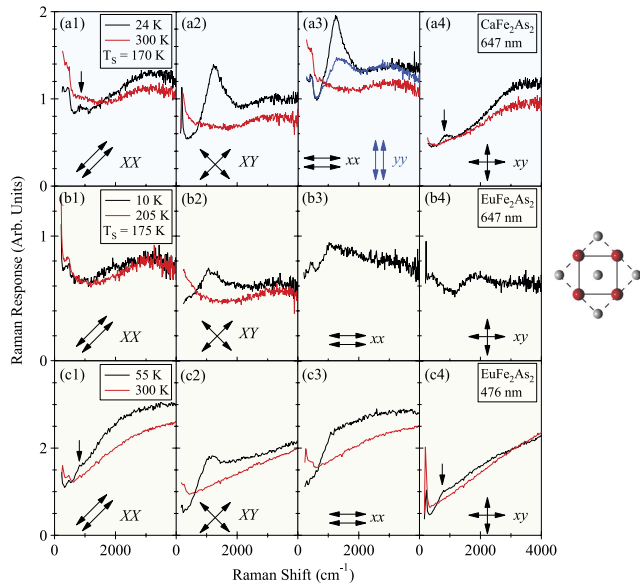


Figure 8. Effect of SDW order in the Raman spectra of CaFe_2As_2 and EuFe_2As_2 . The unit cell on the right which the polarizations in the panels refer to is added to the original figure for clarity. Note the notations $X \equiv x'$ and $Y \equiv y'$. (a1)–(a4) Spectra of CaFe_2As_2 measured with 647 nm laser excitation in the normal state (300 K, red) and in the SDW phase (24 K, black/blue) of a twin-free sample. (b1)–(b4) Raman response of EuFe_2As_2 in the normal state (205 K, red) and the SDW state (10 K, black) of a twinned sample. (c1)–(c4) Same as (b1)–(b4) with 476 nm laser excitation. Reprinted figure with permission from [34], Copyright (2016) by the American Physical Society.

energies and three distinct peaks at 820 cm^{-1} , 1140 cm^{-1} and 1420 cm^{-1} appearing in B_{1g} symmetry. The peak at 820 cm^{-1} is also present in B_{2g} symmetry. In A_{1g} symmetry no peaks can be resolved. On the basis of the symmetry selection rules the authors argue that the peaks at 1140 cm^{-1} and 1420 cm^{-1} originate from anti-crossing bands in the presence of imperfect nesting rendering the X and Y points inequivalent. The peak at 1420 cm^{-1} appears only well below T_{SDW} and was explained in terms of a temperature dependent Fermi surface topology and the disappearance of a hole-like Fermi surface pocket very close to the chemical potential in the reconstructed SDW electronic structure. The peak at 820 cm^{-1} is assigned to an optical transition between folded bands away from the Γ – X and Γ – Y directions which are probed in xy configuration.

Recently Zhang *et al* [34] reported spectral weight redistribution in twinned Eu122 and detwinned mono-domain Ca122 single-crystals in the SDW phase, as shown in figure 8. In the $x'y'[\equiv XY]$ configuration, spectral weight is transferred from low energy to above 800 cm^{-1} with the development of a peak at 1220 cm^{-1} and 1060 cm^{-1} for Ca122 and Eu122, respectively (see panels (a2) and (b2) in figure 8). For de-twinned Ca122 a large intensity anisotropy of the 1220 cm^{-1} peak is observed in xx and yy scattering configurations (see panel (a3) in figure 8). In addition, a weak spectral feature is observed at 830 cm^{-1} in $x'x'[\equiv XX]$ and xy scattering configurations as indicated by arrows. The authors derive the selection rules for inter- and intra-orbital transitions on the basis of the D_{2h}

group for the high symmetry points in the Brillouin zone. The symmetry analysis, augmented by an orbital-resolved DFT + DMFT study [34], suggests that the peak at 1200 cm^{-1} in the A_g symmetry channel originates from an intra-orbital transition at the Z point induced by the SDW band folding, whereas the peak at 830 cm^{-1} in the B_{1g} channel arises from the $d_{xz} \leftrightarrow d_{yz}$ transition at the Γ point.

The analysis of the Raman spectra in the SDW state shows that the typical gaps induced by ordering of the magnetic moments of itinerant electrons are in the range of 100 – 150 meV or $8 k_B T_{\text{SDW}}$. This ratio is in the same range as that of the superconducting gap, and one cannot conclude that T_{SDW} is suppressed by fluctuations as, for instance, in the tritellurides [137]. Rather, the large value may indicate strong coupling. Whether or not the $a - b$ anisotropy of the gap energy found in Ca122 [34] is a generic feature of all pnictides cannot be decided on the basis of the material at hand. However, a strong electronic anisotropy was also found in the energy range of 2 – 3 eV in Ba122 below T_{SDW} when studying resonance effects of the A_g arsenic phonon [172]. Thus, anisotropies in the electronic structure were identified by Raman scattering at low and high energies in the magnetically ordered phase.

5.3. Fluctuations above the ordering transitions

There are various types of instabilities in the FeSCs which can drive the phase transitions. While some groups consider magnetic ordering the dominant interaction [9, 173], Kontani *et al* see orbital ordering in the driver's seat [174]. These basic considerations were studied in some detail and refined recently. A tendency towards charge-driven or Pomeranchuk-type order was found for FeSe using either Hubbard models with strong coupling between spin and orbitals [163] or renormalization group (RG) schemes on model band structures [164, 165] or orbital-dependent nesting properties [166]. For the pnictides these studies favor spin-driven nematicity and explain, on a qualitative basis, the proximity of the nematic and the magnetic transitions and the absence of magnetism in the chalcogenides. This rather incomplete selection of theoretical work already highlights the importance of experimental studies for clarifying the issue.

Since strong fluctuations precede the structural transitions in many compounds, experimental access to the fluctuations is highly desirable. Raman spectroscopy is among the handful of techniques available but does not probe the fluctuations alone. Rather, since the FeBCs are metals the contribution is always superimposed on the particle–hole continuum which needs to be taken into account for quantitative analyses.

A contribution from fluctuations to the Raman spectra of FeBCs were first reported by Choi *et al* [29]. They observed a pronounced build up of the low energy Raman response in Sr122 upon cooling towards T_S and suggested a magnetic nature of the fluctuations. The similar build up of the low-energy signal in the B_{1g} channel was also observed for Ba122 by Sugai *et al* [27, 32] as presented in figure 9. The authors attributed the low-energy $x'x'[\equiv aa]$ and xy spectra to excitations near Dirac nodes where the bands intersect without interacting (circles in figure 9(b)) and the xx and $x'y'[\equiv ab]$ spectra to the ‘anti-nodal’ excitations where the back-folded

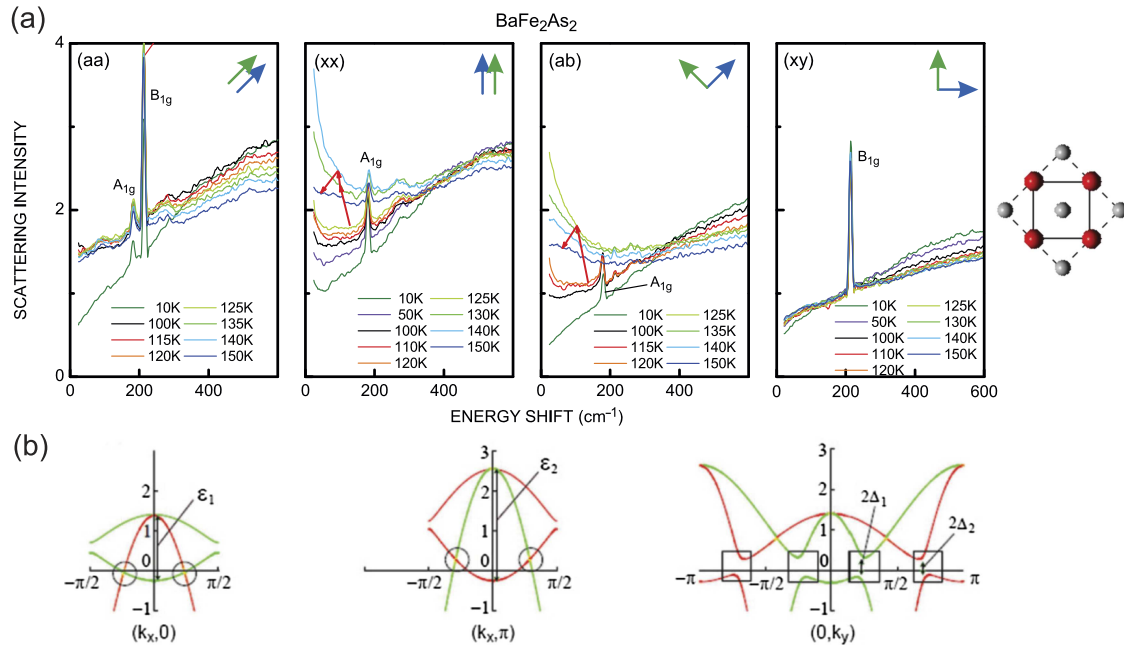


Figure 9. (a) Low-energy Raman spectra of BaFe₂As₂ at temperatures as indicated. The pictograms displaying the unit cell and the polarizations are added to the original figure for clarity. The two central panels (*xx*) and (*ab*) [$\equiv x'y'$] show contributions from fluctuations at low energy and the redistribution of spectral weight from below to above 350 cm⁻¹ upon cooling through $T_{\text{SDW}} \approx 135$ K as indicated by red arrows. Reprinted from [27], with the permission of AIP Publishing. (b) Electron dispersions in ($k_x, 0$), (k_x, π), and ($0, k_y$) direction. The circles denote the Dirac nodes, and the squares denote the ‘anti-nodes’ where the electrons interact. Reprinted by permission from Springer Nature Customer Service Centre GmbH: Springer, Journal of Superconductivity and Novel Magnetism, [32] (2019).

bands interact (squares in figure 9(b)). The increase of the low-energy scattering intensity was interpreted in terms of critical fluctuations related to the opening of the anti-nodal gap.

Several detailed studies of fluctuations in both pnictides and chalcogenides were presented more recently in references [30, 33, 35, 40, 44, 49, 53, 116, 175, 176]. As discussed in section 4.8, one and/or two fluctuations may contribute to the Raman spectra via distinct scattering processes. Gallais and Paul [116] and Thorsmølle *et al* [49] point out that the first order term has a non-zero contribution only in the presence of momentum scattering processes (or, equivalently, finite $v_F q$). On the other hand, the second order AL diagrams may include contributions having $q \gg 0$.

Gallais and coworkers suggested to use the static limit of the real part of the response, $\chi'_{B1g}(\Omega = 0, T)$, for analyzing the Raman data and comparing them to the results of other quasi-static methods such as NMR or elasticity. $\chi'_{B1g}(\Omega = 0, T)$ was directly extracted from $\chi''_{B1g}(\Omega, T)$ via Kramers–Kronig transformation, $\chi'_{B1g}(\Omega = 0, T) = \pi^{-1} \int d\Omega \chi''_{B1g}(\Omega, T)/\Omega$, where $\chi''_{\mu}(\Omega, T)/\Omega$ has the meaning of a channel dependent Raman conductivity. This procedure requires an extrapolation of $\chi''_{B1g}(\Omega, T)$ to zero energy and the selection of a high-energy cutoff since $\chi''_{B1g}(\Omega \rightarrow \infty, T) \approx c$ where c is a constant. The method was applied to the analysis of the data of BFCA [30, 116] (see next paragraph) and subsequently of Eu/Sr122 [33, 44], BKFA [176], and Na111 [49]. Thorsmølle *et al* demonstrated the scaling of the static susceptibility obtained from Raman scattering and NMR data for Na111. Consequently, low energy quasi-elastic scattering was related to d^{\pm} quadrupolar nematic fluctuations which became critical on

approaching a Pomeranchuk instability with a deformation of the Fermi surface [177, 178].

The low-energy Raman response in differently doped BFCA was extensively studied by Gallais *et al* [30, 116]. The authors argue that the nematic susceptibility is observable in the B_{1g} channel and originates from charge fluctuations for symmetry reasons since inelastic light scattering couples preferably to the charge. They observe a strong enhancement of the B_{1g} response $\chi''_{B1g}(\Omega \approx k_B T, T)$ upon cooling towards T_S and a collapse thereof in the orthorhombic/SDW state, whereas the B_{2g} response is essentially temperature independent. First, $\chi'_{B1g}(\Omega = 0, T)$ was determined. Second, it is shown that this quantity is equal to the quasi-static nematic susceptibility and, in fact, compares well to the Young modulus $c_{66}(T)$ derived from thermal expansion [116, 179]. Interestingly, neither $c_{66}(T)$ nor $\chi'_{B1g}(\Omega = 0, T)$ diverge at T_S due to the coupling of the electronic/spin degrees of freedom to the lattice [30, 116, 180]. As a consequence, the divergence of $\chi'_{B1g}(\Omega = 0, T)$ derived from a Curie–Weiss fit occurs always below the structural transition, $T_0 < T_S$.

Kretzschmar *et al* [40] focused their attention on BFCA at finite doping where the magnetic ordering temperature and the structural transition are separated ($T_{\text{SDW}} < T_S$) as shown in figure 10. The memory function method [81] was used for extracting the static Raman relaxation rates $\Gamma_0(T)$ in A_{1g} and B_{1g} symmetry and for facilitating the identification of the cross-over temperature T_f below which the contributions from fluctuations become detectable in the B_{1g} channel.

The fluctuations and the particle–hole continuum can only be considered additive if they get excited through independent

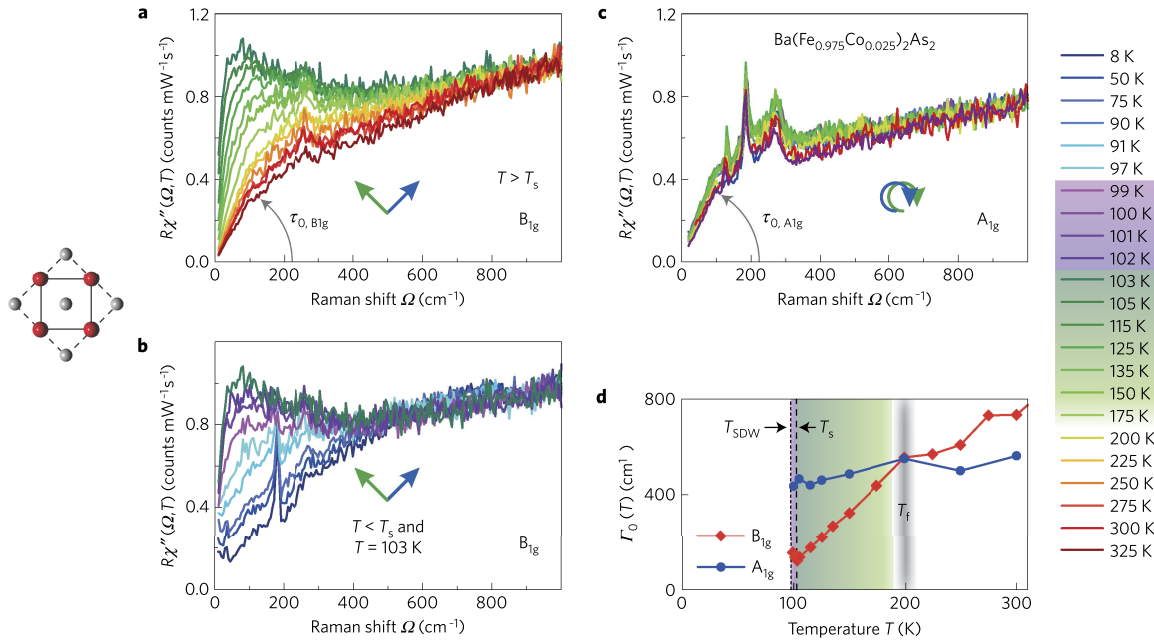


Figure 10. Polarization-resolved Raman results for $\text{Ba}(\text{Fe}_{0.975}\text{Co}_{0.025})_2\text{As}_2$. (a)–(c) Response $R\chi''(\Omega, T)$ at temperatures as indicated. The pictograms for the polarizations were added. (a) B_{1g} spectra above and (b) below T_S . (c) A_{1g} response. The initial slopes defined in (a) and (c) by gray arrows are proportional to the static two-particle lifetime $\tau_{0,\mu}$ in symmetry $\mu = A_{1g}, B_{1g}$. (d) Raman relaxation rates $\Gamma_{0,\mu}(T) = \hbar/\tau_{0,\mu}(T)$, in A_{1g} (blue circles) and B_{1g} (red diamonds) symmetry as a function of temperature. The A_{1g} and B_{1g} data above T_f closely follow the resistivity. The fluctuation range $T_S < T < T_f$ and the nematic phase $T_{SDW} < T < T_S$ are shaded green and magenta, respectively. Reprinted by permission from Macmillan Publishers Ltd: [Nature Physics] [40], Copyright (2016).

scattering channels such as, e.g., phonons and charge excitations. If two fluctuations are excited simultaneously (AL mechanism) the response from fluctuations exists independent of other excitations, otherwise the excitations are entangled. In order to separate the fluctuation contribution, the high temperature particle–hole continuum ($T > T_f$) was extrapolated down to low temperatures by varying $\Gamma_0(T)$ in a way that the initial slope of the spectra matches the transport results and was subtracted from the respective total Raman response.

It is considered the key observation of that paper that the fluctuations do not disappear directly below T_S but continuously lose spectral weight with the peak maximum staying pinned. This indicates a nearly constant correlation length between T_S and T_{SDW} . The persistence of the fluctuations down to T_{SDW} and their immediate disappearance below T_{SDW} favors their magnetic origin.

For LaFeAsO and $\text{Sr}(\text{Fe}_{1-x}\text{Co}_x)_2\text{As}_2$ the analysis arrives at slightly different conclusions for the temperature dependence but similar ones for the origin of the fluctuations [35, 44]. In both compounds the maxima of the fluctuation response do not coincide with the structural transition temperature, and in $\text{Sr}(\text{Fe}_{0.8}\text{Co}_{0.2})_2\text{As}_2$ the fluctuations do not disappear right below the magnetic ordering temperature. Some of the discrepancies may be related to the time scale of the fluctuations relative to that of the phonons. In fact, the peak positions indicate much slower dynamics in $\text{Sr}(\text{Fe}_{0.8}\text{Co}_{0.2})_2\text{As}_2$ than in the other materials. In addition, inhomogeneities in the Co content may contribute. It is certainly necessary to study more doping levels before concluding finally.

The spectral shape of the fluctuations can be described quantitatively in terms AL-type of diagrams if electron–phonon interaction is included [83]. Otherwise the decay on the high-energy side is too slow [115, 118]. The corresponding selection rules (see section 4.9) yield $\mathbf{q}_c = (\pi, 0)$ as the wave vector of the critical fluctuations. Furthermore, it was demonstrated that the initial slope of the fluctuation response χ''_{fluct} exhibits qualitative agreement with the temperature dependence of the nematic susceptibility in the tetragonal and the nematic phase, as expected from a Ginzburg–Landau type of consideration. A comparison of BFCA and BKFA and details of the analysis are further discussed in reference [181].

In FeSe, having a structural transition at $T_S \approx 90$ K and short-ranged but no long-ranged magnetic order above 4 K [157, 168], the fluctuations survive down to temperatures right above $T_c \approx 9$ K [53, 55, 57]. The experimental results, of the three groups of authors agree with each other in the energy and temperature range where they can be compared. We show the results of Massat *et al* in figure 11 and describe those in B_{1g} symmetry in detail. At 295 K (upper part of panel (a)) a broad peak at 50 meV is observed which is unique for FeSe (and $\text{FeSe}_{1-x}\text{S}_x$ for $x \leq 0.2$). In the pnictides or in pure FeS it is absent, the spectra are nearly flat and the overall intensity in all symmetry projections is similar. Upon cooling, this peak first gains intensity. Below 200 K an additional structure starts to appear at some 20 meV which becomes clearly discernible in the yellow spectrum at 142 K (see also and panel (b)). At $T_S = 90$ K (black) it peaks at 4–5 meV and has maximal intensity. The peak at 50 meV stays nearly pinned and has

now almost twice the intensity as at 295 K. Below 90 K (panel (c)) the low energy peak survives down to at least 45 K (Baum *et al* [55] can resolve it even at 20 K) and moves to lower energies reaching some 2 meV directly above T_c while losing most of its intensity. The redistribution of spectral weight in the superconducting state shows directly that the remaining intensity below 15 meV originates from particle–hole excitations as in the pnictides. Concomitantly, the peak at 50 meV hardens slightly and increases further. Baum *et al* [55] argue that the persistence of the fluctuations well below T_S is supportive of spin fluctuations similar to those in BFCA, whereas Massat *et al* [53] assign the fluctuations to charge and/or orbital physics and the peak at 50 meV to interband transitions. Zhang *et al* [57] interpret the quasi-elastic peak at low-energy in terms of ferro-quadrupole fluctuations of a d -wave Pomeranchuk instability at $q = 0$ and assign the reduction of the intensity below 50 meV and T_S to the opening of a gap in the electronic excitation spectrum following the lattice distortion.

In a recent preprint [87] Udina *et al* present a detailed gauge-invariant study of the charge part of the low-energy Raman response in FeSe and assign the temperature dependence of the spectra to the relative shift of the Fe $3d_{xz}$ and $3d_{yz}$ orbitals in the nematic phase. The authors predict the variation of the spectral shape below T_S and find that the energy of the quasi-elastic peak increases with decreasing temperature if an order-parameter-like variation of the orbital splitting is assumed (see figure 3 of reference [87]). This variation leads to a gap-like suppression of the intensity at low energies and resembles the temperature dependent intensity of the fluctuation peak, whereas the energy of the quasi-elastic peak increases below T_S at variance with the experimental findings (see last preceding paragraph).

Massat and coworkers apply an analysis similar to that in BFCA for studying FeSe at ambient [53] and applied pressure [15], as shown in figure 11. The spectra for $P = 0$ exhibit a pronounced temperature dependence in the B_{1g} channel (figure 11(a)–(c)). The real part of the static Raman susceptibility $\chi'_{B_{1g}}(\Omega = 0, T)$, as derived from the ‘Raman conductivity’ $\chi''_{B_{1g}}(\Omega, T)/\Omega$, follows a Curie–Weiss law with T_0 significantly lower than T_S for reasons discussed above in agreement with the stiffness data. With increasing pressure (figure 11(e)) T_S decreases, and above 2 GPa the SDW is the dominating phase with T_{SDW} reaching 45 K at approximately 5 GPa (figure 11(d)) [182]. With the appearance of the SDW phase above 2 GPa the Curie–Weiss-type variation of $\chi'_{B_{1g}}(\Omega = 0, T)$, as determined from the spectra in figure 11(f), disappears as opposed to the observations in BFCA. Apparently, the magnetism in FeSe has aspects different from those in the pnictides.

5.4. Origin of the excitations: spin or charge?

There is no consensus yet on the leading instability in the FeBCs, and there are arguments in favor of both orbital and spin ordering. This controversy characterizes also the interpretation of the Raman data, in particular those of the fluctuation response. It is true that photons couple to the charge, and if

the vertex has the same symmetry as the fluctuations, there is coupling. However, this does not exclude other types of fluctuations to couple to the light; in other words, the selection rules and the coupling argument are not sufficient for deciding between spin and charge⁵.

Selection rules similar to those of charge excitations can also be derived for spin fluctuations owing to the specific band structure of the FeBCs [40, 83]. Given the issue with the selection rules, the temperature dependence may be used as another criterion, since critical fluctuations are expected to disappear immediately at the corresponding ordering temperature. This disappearance is observed directly at $T_S \approx T_{SDW}$ in BFA [39, 40], at $T_{SDW} < T_S$ in BFCA [40], and not at all in FeSe without long-ranged order [53, 55]. $\chi'_{B_{1g}}(\Omega = 0, T)$ as an energy-integrated quantity possibly obscures this important detail to some extent. Therefore, we argue that spin fluctuations dominate the low-energy Raman spectra in most of the FeBCs but would not go so far as to say that there is evidence beyond reasonable doubt. However, we believe that the issue can be settled, presumably by light scattering, using a wide range of excitation energies in the visible range for tracking the resonance behavior or by resonant inelastic x-ray scattering (RIXS) [183].

The second open question pertains to the nature of the short- or long-ranged spin ordering (which exists beyond any doubt): in the pnictides the spins of itinerant electrons order because of a Fermi surface instability [9, 184, 185], whereas the spins or at least some of the spins in the chalcogenides are more localized than in the pnictides [149, 186]. The signatures of these different types of order in the Raman spectra are relatively clear as can be directly seen by comparing the Raman response in cuprates to that in Ba122, for instance. However, it was argued that the band at 500 cm^{-1} in FeSe originates from incoherent intra-band scattering [53] rather than spin excitations [55]. Yet, there are two considerations which are hard to reconcile with charge (particle–hole) excitations: (i) since the energy of the band does not vary significantly upon cooling from 300 to 4 K, only momentum scattering having a scattering rate of approximately 500 cm^{-1} and a temperature independent intensity [77] can be at its origin. (ii) With the scattering rate being an order of magnitude larger than the superconducting gap the gap excitations would be entirely suppressed [110, 111] as opposed to the experimental results [53, 55, 57].

On the other hand, the semi-quantitative agreement of the spectra in all symmetries with simulations [55, 171] provides an attractive explanation for the observed spectra. While the dependence (or independence) of the B_{1g} peak on S substitution [57] still needs to be clarified it does not seem to be a killer argument [187]. The orbital dependent localization [149, 156] provides the necessary explanation for the differences between

⁵ Coupling to the charge does not mean that the photons couple directly to low-energy charge excitations. Rather, the effective scattering Hamiltonian for particle–hole excitations close to E_F is an approximation derived for photon energies much smaller than the gaps in the band structure [63]. Why this approximation works quite well in the FeBCs and in the cuprates in the presence of low-lying bands is not entirely clear. It may have its origin in strong correlation effects which broaden all electronic states away from E_F and thus reduce resonances.

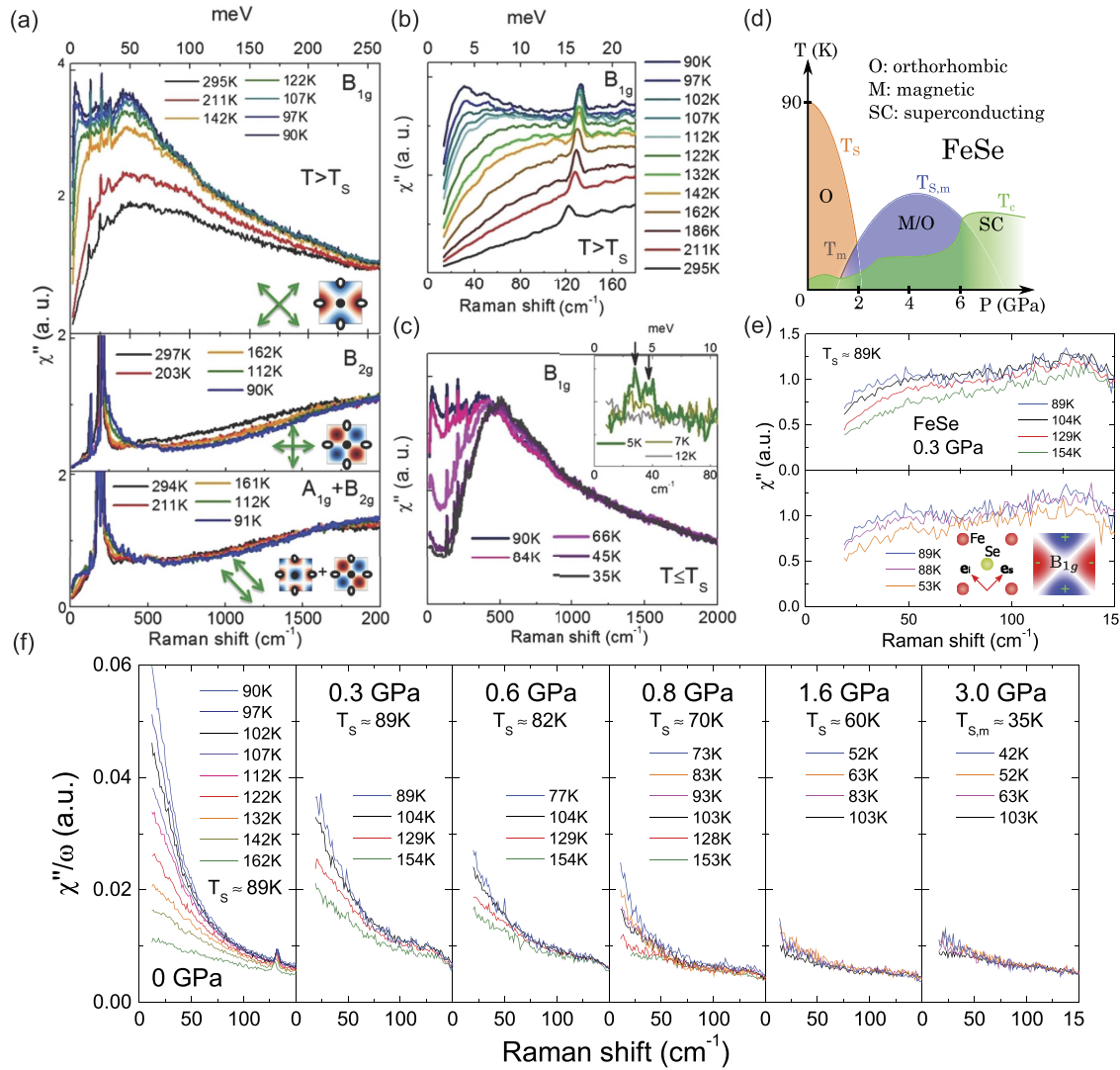


Figure 11. Light scattering in FeSe. (a)–(c) Symmetry-dependent Raman spectra of FeSe above $T_S = 87$ K using photons at 2.33 eV. The sharp peaks superimposed on the electronic continuum are due to Raman active optical phonons. The insets display the Raman form factors in different symmetries (blue and red colors indicate positive and negative amplitudes, respectively), and the polarization configurations used to select them. (b) Temperature dependence of the low energy B_{1g} spectra above T_S . (c) Evolution of the B_{1g} spectra across T_S . The inset shows the spectra across the superconducting transition at $T_c = 8.5$ K. The arrows indicate the peaks associated with 2Δ . Panels (a)–(c) reproduced with permission from [53]. (d) Pressure–temperature phase diagram of FeSe. (e) B_{1g} response at $P = 0.3$ GPa and temperatures as indicated. (f) $\chi''(\omega)/\omega$ in B_{1g} symmetry for pressure values and temperatures as indicated. Panels (d)–(f) reprinted with permission from [15], Copyright (2018) by the American Physical Society.

the pnictides and chalcogenides, including the experimentally observed near localization of the electrons in the d_{xy} orbitals in FeSe as opposed to the by and large orbital-independent itinerancy of the electrons in all bands in the pnictides [188]. RIXS as a rapidly developing technique may help to pin down the orbital character of the differently localized electrons [189].

In spite of all these arguments the problem is not settled, and the type of fluctuations and the leading instability may be different in the pnictides and chalcogenides as outlined in the beginning of section 5.3. Thus further criteria for the analysis of the B_{1g} Raman data were proposed recently including scaling arguments for the slope of the spectra in the zero-energy limit and for the real part of the static susceptibility [86]. Klein *et al* analyzed data of FeSe, Ba122 and $\text{NaFe}_{1-x}\text{Co}_x\text{As}$ and found support for a Pomeranchuk-type charge instability in

FeSe and for spin fluctuations in the pnictides. Close to a quantum critical point being ubiquitous in the pnictides and chalcogenides energy power laws for the response were derived but were not tested yet against experiments [85].

6. Superconductivity

The identification of the pairing mechanism remains one of the major challenges in all unconventional superconductors. The momentum dependence of the gap magnitude (and phase, if possible) is among the important observables for addressing this question since $\Delta_{\mathbf{k}}$ and the pairing potential $V_{\mathbf{k},\mathbf{k}'}$ are interrelated via the BCS gap equation [190]. Therefore, a large variety of methods has been applied to derive properties of the energy gap in the iron-based materials with the goal to

understand $V_{\mathbf{k},\mathbf{k}'}$ and the coupling [7]. Raman spectroscopy allows access to the magnitude of the gap [66, 73, 74], its number-phase fluctuations [95–97] and bound in-gap states encoding the anisotropy of $V_{\mathbf{k},\mathbf{k}'}$ [89–91, 140].

6.1. Gap spectroscopy

6.1.1. Results from canonical methods. From the beginning, a substantial band and momentum dependence of the energy gap was observed. Yet, sign changes of the gap on individual bands or between the bands could not be pinned down unambiguously although tunneling experiments with an applied magnetic field [191] and neutron scattering experiments [192] supported unconventional order parameters in Fe(Se,Te) and BKFA, respectively. More pieces need to be added to solve the puzzle and clarify the type of pairing in the ground state.

Further complication arises since the gaps vary strongly between the families and with elemental substitution [12, 210, 211]. In BKFA at optimal doping band dependent gaps with little variation on the individual Fermi surfaces are observed by angle-resolved photoemission spectroscopy (ARPES) [201, 212], while the gaps vary rather strongly around the electron and hole pockets and along the k_z reciprocal axis in BFCA and overdoped BKFA [196, 199, 213, 214]. As a general feature, the maximal gaps observed across the families are in the range 6–8 in units of $k_B T_c$ similar to those in cuprates.

In table 2 we compile characteristic results found by ARPES, specific heat (c_{el}), neutron scattering (INS) and tunneling spectroscopy (STS) and compare them to Raman results. It is instructive to have this overview in addition to the light scattering results which are usually more subject to controversy than the canonical methods, since data analysis is more difficult due to the appearance of additional electronic excitations close to or below the gap energy (cf section 4.6).

6.1.2. Raman results. Momentum- and band-resolved Raman results for the energy gap were first presented and discussed by Muschler *et al* [25] and are shown in figure 12. They reported data of a complete symmetry analysis in the normal and superconducting states of optimally doped $\text{Ba}(\text{Fe}_{1-x}\text{Co}_x)_2\text{As}_2$ ($x = 0.061$). For the symmetry analysis the 2 Fe unit cell was used, and the related projections in the Brillouin zone were discussed subsequently on the basis of an LDA band structure [36]. For comparison with figure 5 the B_{1g} and B_{2g} symmetries must be interchanged. The effect of superconductivity is best seen by comparing spectra taken well below and slightly above T_c similarly as in the case of an SDW (see figure 7).

In $\text{Ba}(\text{Fe}_{1-x}\text{Co}_x)_2\text{As}_2$, differences between the spectra above and below T_c which are associated with the opening of the superconducting gap are observed only in A_{1g} and B_{1g} symmetry. In A_{2g} the intensity is generally low for the absence of excitations having the right symmetry. In B_{2g} symmetry little spectral weight is expected since the vertices are small close to the Fermi surface crossings of the bands. Surprisingly, the intensity becomes comparable to that in A_{1g} and B_{1g} symmetry at approximately 300 cm^{-1} but there are no indications of an energy gap. There are essentially three explanations for the absence of gap structures: (a) The intensity originates from

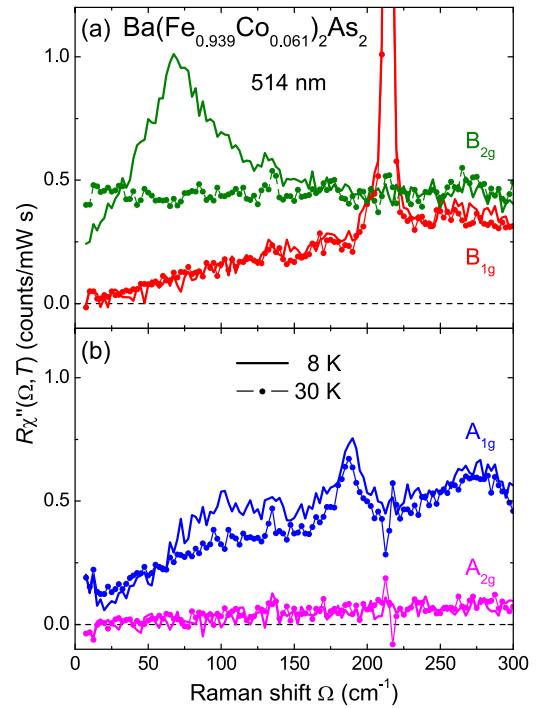


Figure 12. Symmetry-resolved Raman response of $\text{Ba}(\text{Fe}_{1-x}\text{Co}_x)_2\text{As}_2$ ($x = 0.061$) for in-plane light polarizations right above (points) and well below T_c (full lines). The redistribution of intensity typical for superconductivity is observed only in (a) B_{2g} and (b) A_{1g} symmetry. (a) In this study, the 2 Fe unit cell was used for the symmetry assignment implying that the out-of-phase Fe phonon at 214 cm^{-1} is observed in the proper B_{1g} symmetry. (b) In A_{1g} symmetry there is a small increase for $\Omega \rightarrow 0$ from insufficient rejection of the laser light. The A_{2g} signal can safely be neglected at low energies. Reprinted with permission from [25], Copyright (2009) by the American Physical Society.

excitations other than electron–hole pairs such as spins. The slow increase of the B_{2g} intensity indicates either that (b) states far away from the Fermi surface are projected consistent with the vertices or that (c) the relaxation rate is much higher than expected from transport. Such an anisotropy may occur if the quasi-particle relaxation is strongly momentum dependent for the presence of Co scatterers in the Fe plane. Then the gap excitations are suppressed for specific symmetry projections [112]. We consider (c) the most likely explanation since spin excitations are already very weak at optimal doping and B_{2g} gap features indeed appear in $\text{Ba}_{1-x}\text{K}_x\text{Fe}_2\text{As}_2$ where the substitution generates only out-of-plane defects [46].

In superconducting BFCA [25], the broad maximum close to 100 cm^{-1} and the well-defined peak at around 70 cm^{-1} in A_{1g} and B_{1g} symmetry, respectively, correspond to gap excitations in the hole and the electron band. Finite spectral weight observed down to very small energies indicates vanishingly small gaps. The $\sqrt{\Omega}$ dependence in B_{1g} symmetry suggests accidental nodes [215].

Similar spectra were reported for doping levels in the range $0.045 \leq x \leq 0.10$ [37, 38, 181, 216] where broad pair-breaking peaks appear in A_{1g} symmetry between 50 cm^{-1} and 160 cm^{-1} . The B_{1g} spectra generally peak at lower energy than those in A_{1g} symmetry. In both symmetries the spectral changes upon entering the superconducting state become less

pronounced below and above optimal doping [38, 181, 216]. In A_{1g} symmetry the peak maxima scale approximately as $6k_B T_c$ in agreement with $2\Delta_{\max}$ from other methods. The B_{1g} spectra peak at $4k_B T_c$ at optimal doping and at $3k_B T_c$ for $x < 0.055$.

The discussion about the details of the interpretation of the spectral shape in superconducting BFCA is not finally settled although the data agree and the basic features are clear. Chauvière *et al* [38] interpret their B_{1g} results for optimally doped and underdoped samples in terms of a two-gap scenario with a maximal gap $2\Delta_{\max} \approx 75\text{cm}^{-1}$ and a small but finite gap $2\Delta_{\min} \approx 15\text{cm}^{-1}$ (see table 2). The maximal superconducting gap appears in the same location in momentum space as the SDW gap and is thus suppressed rapidly below optimal doping by the opening of the larger SDW gap, $2\Delta_{\text{SDW}} > 2\Delta_{\max}$, and only the feature related to $2\Delta_{\min}$ survives. The spectral shape in B_{1g} symmetry may also be reproduced with a strong k_z dependence of $\Delta_{\mathbf{k}}$ but the disappearance of the structure at $2\Delta_{\max}$ in underdoped samples can only be explained with an in-plane anisotropy.

Muschler *et al* [25] argue that the \sqrt{N} variation of the low-energy B_{1g} spectra can be explained with accidental nodes or near-nodes on the outer electron band. This would be in agreement with the results from heat transport [217] and theoretical considerations [36]. Sugai *et al* find support from band structure calculations for the B_{1g} intensity (1 Fe cell) to originate from the hole bands [37]. The latter conclusion is at variance with symmetry arguments (cf figure 5) and the LDA results of Mazin *et al* [36]. As a matter of fact, the gap in BFCA is very anisotropic at all doping levels and may even vanish for certain momenta. The maximum is in the range $2\Delta_{\max} \approx 6k_B T_c$. Below optimal doping there is an interaction with the SDW gap.

The observation of gap features in other pnictides and in chalcogenides was delayed by sample and surface issues. In chalcogenides the observation of pair breaking succeeded first in $\text{Rb}_{0.8}\text{Fe}_{1.6}\text{Se}_2$ after cleaving the sample *in situ* at low temperature [46]. Differences between normal and superconducting spectra were only found in B_{1g} symmetry. Since $\text{Rb}_{0.8}\text{Fe}_{1.6}\text{Se}_2$ has presumably no hole pockets, the B_{1g} selection rule supports the symmetry assignment of references [25, 36] as reproduced in section 4.9. The observed gap appears to be almost constant on the electron pockets, being compatible with either a simple s - or a d -wave state without nodes on the Fermi surface and a sign change between the pockets. From what we shall see below d -wave symmetry is more likely but cannot be distinguished from an s -wave gap on the basis of the light scattering experiment. As in the case of BFCA, it is difficult to explain the intensities in other symmetries which do not show features induced by superconductivity. As a hypothesis which needs to be worked out in more detail we assign the continua in A_{1g} and B_{2g} symmetry to excitations in lower lying bands and/or the tails of the numerous phonon lines.

In $\text{Ba}_{0.6}\text{K}_{0.4}\text{Fe}_2\text{As}_2$ continua and gap structures are observed in all symmetries and are by and large in agreement with the results from other methods [46] as shown in table 2. Since the hole-like Fermi surfaces are more extended in the Brillouin zone, the relevant electronic states are well

sampled by all vertices. Second, the simulations using the effective mass approximation arrive at a semi-quantitative explanation of the spectra [47]. Third, the effect of defects induced by K doping in the Ba layer is expected to be weak. Finally, resonance effects may contribute [41, 49, 65] although they were found to be mild in BFCA [36].

The spectra of $\text{Ba}_{0.6}\text{K}_{0.4}\text{Fe}_2\text{As}_2$ clearly show a small but true gap of approximately 30cm^{-1} indicating, among other things, that the contributions from luminescence are negligible here. The largest gaps reside on the middle hole band and on the electron bands and are rather sharp as opposed to BFCA. The gap maximum $2\Delta_{\max}$ reaches almost 10 in units of $k_B T_c$ [46, 47]. This large ratio exceeds the ARPES results and, in particular, the gap ratio derived from the electronic specific heat as a typical bulk method [199]. However, thermally activated behavior is generally sensitive to the small gaps on the individual bands. These minimal gap energies are typically 180cm^{-1} or 6.8 in units of $k_B T_c$ in the phenomenological analysis [41, 47] thus reconciling Raman scattering and thermodynamic measurements.

In addition to the pair-breaking features, the B_{1g} spectra show unexpected structures below $2\Delta_{\max}$ which, as opposed to the pair-breaking features, have a nearly resolution limited width and will be discussed in detail in the following section. Here we first wrap up observations of the energy gaps by Raman scattering in other compounds.

A pair-breaking peak was also observed in the A_{1g} spectrum of $\text{BaFe}_2(\text{As}_{0.5}\text{P}_{0.5})_2$ [48] with the spectral weight decreasing linearly towards low frequencies indicating the presence of nodes in agreement with recent ARPES results for optimally doped $\text{BaFe}_2(\text{As}_{0.65}\text{P}_{0.35})_2$ [207] but, at first glance, not with thermodynamic results on a material with comparable doping [208] (see table 2). However, the small value of the thermodynamically derived gap indicates a substantial anisotropy also for $\text{BaFe}_2(\text{As}_{0.5}\text{P}_{0.5})_2$ which may be concealed by the notion of a single (average) gap.

Very recently, pair-breaking features were observed in $\text{CaKFe}_4\text{As}_4$ [50, 51]. Depending on the incoming photon energy, gap features are observed either in all symmetries [50] or only in B_{1g} symmetry (1 Fe unit cell corresponding to B_{2g} in the 2 Fe cell used by Zhang *et al* [51]). The gap energies derived from the A_{1g} and B_{2g} (1 Fe) Raman data are compatible with those determined by ARPES [205] if the entire energy range given by Mou *et al* is considered (see also table 2). The B_{1g} maximum (1 Fe) appears at a substantially smaller energy, has a sharp onset and is clearly peaked [50]. Zhang *et al* [51] identify all features observed in B_{1g} symmetry with pair breaking while Jost *et al* [50], based on the results in three symmetries, propose that the B_{1g} peak at 134cm^{-1} originates from a collective mode similar to that in slightly underdoped BKFA [41]. This—controversial—point of view would indicate a sub-leading interaction having $d_{x^2-y^2}$ symmetry which is to be discussed in more detail now.

6.2. Collective modes

The lowest order gap excitations in the electronic Raman spectra essentially reflect the magnitude of the energy gap.

Table 2. Compilation of gap energies in Fe-based superconductors as observed by angle-resolved photoemission (ARPES), tunneling (STS), optical (IR) and Raman spectroscopy. For selected cases we show also the results of thermodynamic measurements (c_{el}) and neutron scattering (INS) revealing local gap minima and, respectively, the spin resonance energy which are typically below the maximal gap. In the third last column the maximal gap of each method is given in units of $k_B T_c$. A similar compilation of the results and a discussion may be found in references [8, 193]. In particular in the case of ARPES but also for some of the thermodynamic and Raman measurements the entries are not exhaustive and display only typical values. In some Raman studies the data of B_{1g} symmetry were fitted using one, two or three gap scenarios as indicated. For four samples of BKFA the data of all symmetries were fitted simultaneously using a phenomenology including collective modes [41, 47]. In some cases the peak frequencies alone are reproduced. For the analysis of the IR spectra the theory by Mattis and Bardeen [136] was applied. The BFCA sample used for STS [194] had a nominal doping of $x = 0.10$ but the T_c is more compatible with optimal doping.

Material	T_c (K)	Method	$2\Delta_i$ (meV)	$2\Delta_i$ (cm^{-1})	$2\Delta_{\text{max}}$ ($k_B T_c$)	Ref.	Comment
Ba(Fe_{1-x}Co_x)₂As₂							
$x = 0.051$	19	ARPES	8.0/11.6		7.1	[195]	el/h band
$x = 0.051$	18	Raman	3.7...7.4/9.9	40...60/80	6.4	[181]	B_{1g}/A_{1g} peaks
$x = 0.052$	20	c_{el}	3.1/7.1		4.1	[196]	Min/max gap
$x = 0.055$	20.5	Raman	5.0	41		[38]	B_{1g} ; 1-gap
$x = 0.055$	23	Raman	8.7/12.4	65/105	5.9	[181]	B_{1g}/A_{1g} peaks
$x = 0.060$	24	Raman	4.1/9.3	33/75	4.5	[38]	B_{1g} ; 2-gaps
$x = 0.061$	24	Raman	8.7/12.4	70/100	5.9	[25]	B_{1g}/A_{1g} ; aniso.
$x = 0.060$	25	c_{el}	4.3/10.8		5.0	[196]	Min/max gap
$x = 0.065$	24.5	Raman	1.9/8.9	15/72	4.2	[38]	B_{1g} ; 2-gaps
$x = 0.067$	25	INS	8.0 ± 1			[195]	Spin resonance
$x = 0.067$	25	ARPES	9.2/13.0		6.0	[195]	el/h band
$x = 0.075$	25.5	ARPES	10/13.8		6.2	[197]	el/h band; isotropic
$x = 0.075$	23.5	Raman	9.7	78	4.8	[38]	B_{1g} ; 1-gap
$x = 0.085$	23	c_{el}	4.0/8.7		4.4	[196]	Min/max gap
$x = 0.085$	22	Raman	9.3/11.8	75/95	6.2	[25]	B_{1g}/A_{1g} peaks
$x = 0.095$	19	ARPES	9.2/11.2		6.8	[195]	el/h band
$x = 0.100$	25.3	STS	12.5 ± 3.0		5.7	[194]	Average; OPT?
$x = 0.100$	20	Raman	9.8	79	5.7	[38]	B_{1g} ; 1-gap
Ba_{1-x}K_xFe₂As₂							
$x = 0.22$	24.6	Raman	3.1...13.7	25...110	6.5	[41]	Only B_{1g} peaks
$x = 0.25$	26	ARPES	7.8/15.7		7.0	[198]	el/h bands
$x = 0.25$	31	c_{el}	1.9/16.0		6.0	[199]	Min/max gap
$x = 0.25$	31	Raman	6.0, 20.0	48, 161	7.5	[48]	B_{1g} peaks
$x = 0.25$	30.9	Raman	7.4, 18.6	60, 150 ± 20	7.0	[41]	B_{1g} peaks
$x = 0.27$	31	IR	13.7/27.1	110/218	10.1	[200]	Mattis–Bardeen
$x = 0.35$	38.9	Raman	9.9...31.8	80...256	9.5	[41]	Phenomenology
$x = 0.40$	38	INS	14			[192]	Spin resonance
$x = 0.40$	38	ARPES	12/24		7.5	[201]	Min/max gap
$x = 0.40$	38	ARPES	8/24		7.5	[202]	Min/max gap; k_z
$x = 0.40$	38	ARPES	7.2/20.4		6.2	[203]	Min/max gap; k_z
$x = 0.40$	37	STS	30		≈ 9.4	[204]	
$x = 0.40$	39.0	IR	18.6/31.0	157/263	9.7	[200]	Mattis–Bardeen
$x = 0.40$	38.5	Raman	8.4...32.0	68...258	9.6	[46, 47]	Phenomenology
$x = 0.42$	38.5	c_{el}	2.3/24.2		7.3	[199]	Min/max gap
$x = 0.43$	36.7	Raman	6.2...31.0	50...250	9.8	[41]	Phenomenology
$x = 0.48$	34.3	Raman	4.0...20.0	32...161	6.8	[41]	Phenomenology
$x = 0.51$	34.2	c_{el}	2.1/17.7		6.0	[199]	Min/max gap
$x = 0.62$	26.6	Raman	7.4...13.7	60...110 \pm 10	6.0	[41]	Peak energies
$x = 0.70$	22	c_{el}	2.1/9.1		4.8	[199]	Min/max gap
$x = 0.70$	21.6	Raman	6.2...11.2	50...90 \pm 10	6.0	[41]	Peak energies
CaKFe ₄ As ₄	35	ARPES	16/24		8.0	[205]	el/h band
CaKFe ₄ As ₄	35	Raman	15.5/26.7	125/215	8.8	[50]	All symmetries
CaKFe ₄ As ₄	35	Raman	13.6/16.8/20.2	110/135/162	6.7	[51]	B_{1g} ; 3-gaps
BaFe ₂ (As _{0.65} P _{0.35}) ₂	30	ARPES	4		3	[206]	Isotropic
BaFe ₂ (As _{0.7} P _{0.3}) ₂	30	ARPES	12/15.2		5.9	[207]	Nodal gap
BaFe ₂ (As _{0.5} P _{0.5}) ₂	18.2	c_{el}	4.8		3.1	[208]	Average gap
BaFe ₂ (P _{0.5} As _{0.5}) ₂	16	Raman	6.7	54	4.9	[176]	B_{1g}
FeSe	9	STS	5.0/7.0		9.0	[209]	
FeSe	8.5	Raman	3.6/4.7	29...38	6.4	[53]	B_{1g}
FeSe	8.9	Raman	3.0...4.6	24...37	6.0	[57, 55]	B_{1g}

Yet, some caution is appropriate when numbers are to be derived (see table 2). Similar as in the ARPES or tunneling spectra neither the onset of the enhanced intensity nor the peak maxima are directly related to the gap 2Δ . Only in the clean limit, for $q = 0$, and an isotropic superconductor a square-root singularity is expected at 2Δ [73]. In all other cases the maximum is at higher energies [73, 74, 110, 112], and numbers can only be extracted via theoretical models. Specifically in multiband systems, such as the FeBCs or in the presence of higher order corrections (final state interactions), only a model analysis leads to useful conclusions as outlined in section 4.6. Yet, since a host of additional information can in principle be derived from the spectra in general and from higher order contributions specifically it is worth the effort.

There is general consensus that collective modes exist in at least some of the pnictides having sufficiently clean gaps [41, 46, 47, 49, 50]. Indications of collective modes were also reported for the chalcogenide $\text{K}_{0.75}\text{Fe}_{1.75}\text{Se}_2$ and discussed along with a theoretical model [58] but we are not aware of a comprehensive symmetry analysis or an in-depth study. Including this report, collective modes were observed mainly in B_{1g} (1 Fe) or B_{2g} (2 Fe) symmetry (which are equivalent). An A_{1g} collective mode, as predicted by Chubukov *et al* [90], was observed as part of a broad spectrum but not as an isolated line [49].

There is a lively discussion on how the collective modes are to be explained in terms of one of the essentially four possibilities (see also section 6.4): (i) amplitude (Higgs) fluctuations of the order parameter (ii) Leggett modes, (iii) fluctuation modes which become undamped in the presence of a gap and (vi) BS modes. Here, the distinction between particle–particle and particle–hole modes [49] was introduced only recently, and both of them were actually coined excitons in the original paper of Bardasis and Schrieffer [140]. We adopt this nomenclature in the following. The essential difference is that particle–particle and particle–hole bound states are expected for attractive and, respectively, repulsive contributions to an attractive pairing potential and vice versa. From an experimental point of view a distinction is difficult or impossible.

6.2.1. Amplitude fluctuations of the order parameter. Were discussed mainly for systems where superconductivity competes with other ordering phenomena such as a CDW [67, 94, 101] which break the particle–hole symmetry. Otherwise the coupling to the amplitude mode is weak [218]. Currently it is not clear whether or not amplitude fluctuations can be observed in the FeSCs. The only chance would be in $\text{Ba}_{1-x}\text{K}_x\text{Fe}_2\text{As}_2$ below $x < 0.25$ where the gap is sufficiently clean and $T_{\text{SDW}} > T_c$. So far we are not aware of related reports.

6.2.2. Leggett modes. [95] were first discussed for MgB_2 [96, 97] where the intra-band interaction dominates and the Leggett modes are below the gap edge. In FeBCs there is a wide agreement that the intra-band interaction is weaker than the inter-band interaction [9, 219], and the Leggett modes are expected to be pushed towards the continuum and overdamped. They may contribute to the Raman intensity at the

gap edge and are thus indistinguishable from the pair-breaking effect [98, 99]. Consequently, they are unlikely to augment the information derived from gap spectroscopies, although interesting conclusions about the pairing symmetry could be derived in special cases of chalcogenides without a central Fermi surface [100]. Here the Leggett modes are predicted to appear in B_{1g} symmetry, whereas, in the presence of a Fermi surface encircling the Γ point, as in all pnictides and in bulk FeSe, the Leggett modes are expected to be observed in A_{1g} symmetry [99]. This argument needs to be qualified if the orbital content of the bands is taken into account [98]. An experimental study thereof does not exist and seems difficult. Only resonance effects may be a viable approach.

6.2.3. Quadrupole modes. In $\text{NaFe}_{1-x}\text{Co}_x\text{As}$, when excited with blue light (476 nm), a very strong and narrow B_{2g} mode (B_{1g} in the 1 Fe unit cell) appears below T_c at approximately 56 cm^{-1} close to the gap edge derived from ARPES [49]. As shown in figure 13, 56 cm^{-1} is close to the maximum of the fluctuation peak observed above T_c . The continuous temperature dependence across T_c , the narrowing below T_c and the independence of the mode energy of T_c support the interpretation in terms of a quadrupolar fluctuation of charges between the electron and hole bands which becomes undamped inside the superconducting gap.

In A_{1g} symmetry a broad peak is observed which cuts off softly below the maximum located at approximately 70 cm^{-1} thus indicating a finite density of states inside the gap. The maximum—as an integral part of the peak—is interpreted in terms of the particle–hole collective Bardasis–Schrieffer mode predicted by Chubukov, Eremin, and Korshunov [90] for the case of an s_{\pm} ground state, where the gap has opposite sign on the electron and hole bands and an s_{++} subleading instability without a sign change induced by orbital fluctuations [143]. Since the relatively broad peak includes several excitations, the gap energy can be extracted only with difficulties from the smoothed A_{1g} spectra. For $x = 0.0175$ and 0.05 the humps on the high-energy side are close to the ARPES gaps.

The authors also used red photons (646 nm) for excitation but show only B_{2g} spectra, making a comparison with the spectra obtained for blue light less stringent. For 646 nm, the B_{2g} excitation at 56 cm^{-1} becomes much weaker in the underdoped range, $x \leq 0.0175$, and two new modes appear. These modes are compared to the BS mode in the A_{1g} spectrum measured with excitation at 476 nm and are tentatively assigned to p–h and p–p collective modes without experimental substantiation or a phenomenological theory. Therefore, more work is needed to disentangle the complex but very interesting Raman spectra of $\text{NaFe}_{1-x}\text{Co}_x\text{As}$.

Whereas the normal-state data of $\text{NaFe}_{1-x}\text{Co}_x\text{As}$ are rather similar to those of BFCA several differences are observed below T_c . For instance, the gap anisotropy on the individual bands is larger in BFCA than in $\text{NaFe}_{1-x}\text{Co}_x$ as can be inferred from the Raman spectra [25, 38, 49] or, similarly, from other experiments [213, 220, 221]. Given the rather anisotropic gap in BFCA, it is not surprising that no sharp in-gap modes comparable to those in $\text{NaFe}_{1-x}\text{Co}_x\text{As}$ are observed. On the other

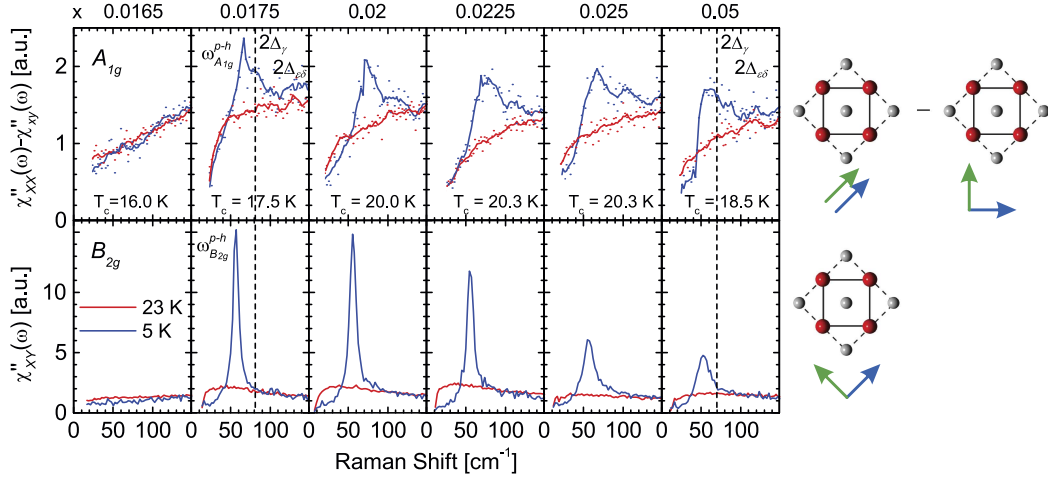


Figure 13. Raman susceptibilities of $\text{Na}(\text{Fe}_{1-x}\text{Co}_x)\text{As}_2$ in the normal (red) and superconducting (blue) states for excitation with blue photons (476 nm). Reprinted with permission from [49], Copyright (2016) by the American Physical Society. The pictograms were added by the authors for clarity. (a) $\chi''_{XX}(\omega) - \chi''_{YY}(\omega)$ (top row) and $\chi''_{XY}(\omega)$ (bottom row) in the superconducting (5 K) and normal (23 K) states at doping levels as indicated. The vertical dashed lines, shown for $x = 0.0175$ and 0.05 , indicate the lowest superconducting gaps $2\Delta_{\gamma} \approx 10$ meV and 9 meV, respectively, determined by ARPES. B_{2g} symmetry in the figure corresponds to B_{1g} used in this review.

hand, the peak maximum in B_{1g} symmetry is quite sharp in optimally doped BFCA and may be interpreted alternatively in terms of a nematic resonance near a quantum critical point [39, 116]. In BFCA, both the enhancement of the spectral weight of the B_{1g} pair-breaking peak upon approaching optimal doping, $x \approx 0.065$, and its scaling with the nematic response above T_c (figure 14) argue in favor of the nematic resonance. Yet, a similar doping dependence is also observed in A_{1g} symmetry and qualifies this conclusion [181].

Na111 and BFCA seem to be the two material classes with the strongest interaction between superconductivity and nematic fluctuations. In contrast, the fluctuations can hardly be observed in BKFA [48, 181] or CKFA [51], and a detailed comparison of these material classes seems highly desirable.

6.2.4. BS modes. Finally, we discuss the possibility of sub-leading pairing interactions having $d_{x^2-y^2}$ symmetry and the related BS modes inside the gap in the B_{1g} Raman spectra. The BS modes display various properties which distinguish them from other collective modes (see Equation (10)).

(a) In a clean gap the BS modes are resolution limited. The energy, $\Omega_{BS}(T)$, is directly linked to the gap parameter [89], as opposed to the maximum of the pair-breaking peak $\Omega_{pb}(T)$ which depends on both the gap $\Delta_{\max}(T)$ and the quasi-particle relaxation rate $\Gamma_{qp}(T)$ as $\Omega_{pb}(T) \approx 2\sqrt{|\Delta_{\max}(T)|^2 + \Gamma_{qp}^2(T)}$ [110–113]. Thus the temperature dependence of the BS modes rather than that of $\Omega_{pb}(T)$ is expected to be determined by that of the single particle gap, $\Omega_{BS} \propto \Delta_{\max}(T)$.

(b) The BS mode drains spectral weight from the pair-breaking peak, but there is no sum rule. Rather, the intensity in the pair-breaking maximum is reduced rapidly, whereas the spectral weight in the BS mode increases first with increasing interaction strength λ_{α} , with α

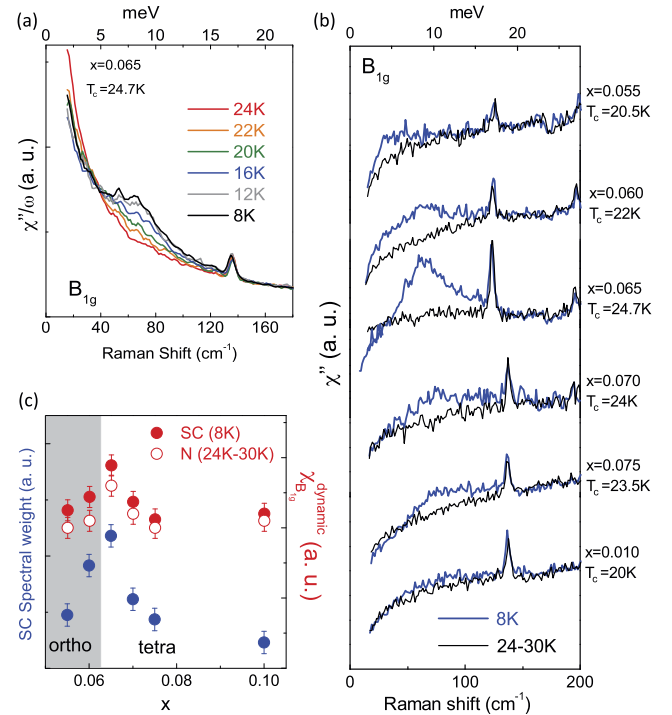


Figure 14. Doping dependence of the Raman spectra of $\text{Ba}(\text{Fe}_{1-x}\text{Co}_x)_2\text{As}_2$. (a) Evolution of the B_{1g} Raman conductivity χ''/ω across T_c for $x = 0.065$. (b) B_{1g} Raman response well below (blue) and right above T_c (black) as a function of Co doping as indicated. (c) Integrated SC spectral weight of the Raman response χ'' (blue) as a function of Co doping. The corresponding nematic susceptibilities $\chi_{B_{1g}}^{\text{dynamic}}$ both slightly above T_c (N) and well below T_c (SC) are also shown (open and, respectively, full red symbols). Reproduced from [116]. CC BY 4.0.

indexing the eigenvalues (see section 6.3), and then decreases towards zero [41]. In isotropic systems the intensity in the pair-breaking maximum is reduced in the entire energy range. In systems with anisotropic

interactions $V_{\mathbf{k},\mathbf{k}'}$ only parts of the pair-breaking peak are depleted depending on the channel-specific components of $V_{\mathbf{k},\mathbf{k}'}$. This behavior can be modeled phenomenologically [47] or on the basis of the eigenvectors $g_\alpha(\mathbf{k})$ which determine the momentum dependence of the gap $\Delta_\alpha(\mathbf{k})$ and, to some extent, reflect the variation of $V_{\mathbf{k},\mathbf{k}'}$ by virtue of the BCS gap equation [41, 92].

- (c) The binding energies of the BS modes, $E_{\text{BS},\alpha} = 2\Delta_{\text{max}} - \Omega_{\text{BS},\alpha}$, are related to the coupling strengths of the sub-leading channels λ_α ($\alpha > 1$) with respect to that of the ground state λ_1 . For $\lambda_1 \approx 1$ the relationship is given by $\sqrt{E_{\text{BS},\alpha}/2\Delta_{\text{max}}} \approx \lambda_\alpha/\lambda_1$ and is thus much simpler than that of the intensities [41].

All B_{1g} peaks observed in $\text{Ba}_{0.6}\text{K}_{0.4}\text{Fe}_2\text{As}_2$ were suggested to be BS modes [46] following the phenomenology for anisotropic gaps proposed by Scalapino and Devereaux [91]. The detailed study of the temperature dependence performed later [47] is shown in figure 15 and requires this assignment to be revisited. The inset demonstrates the scaling of $\Omega_{\text{BS}}(T)$ at 140 cm^{-1} and $\Delta_{\text{max}}(T)$ as directly observed by ARPES [212], while the maximum at 170 cm^{-1} stays pinned. Apparently, the two strongest modes depend distinctly differently on temperature suggesting the mode at 170 cm^{-1} to be related to pair breaking and that at 140 cm^{-1} to a sub-leading channel. The comparison of all symmetries shows that intensity is in fact drained from the B_{1g} pair-breaking maximum although part of the peak survives indicating highly anisotropic interactions.

Maiti *et al* [92] pointed out that there may be more than one BS mode in the presence of a hierarchy of sub-leading coupling channels in addition to the s_\pm -wave ground state. Although there is a candidate peak at 70 cm^{-1} (see figure 15), this proposal can only be addressed by studying differently doped samples.

6.3. Doping

Doping x or pressure P can be used as non-thermal control parameters in the context of quantum phase transitions. Here, doping x proves useful for the assignment of the in-gap modes and for scrutinizing the anisotropy of the pairing potential $V_{\mathbf{k},\mathbf{k}'}$ through the evolution with x of the related in-gap modes in BKFA. This will be the main focus of this subsection, but prior to this discussion the results on BFCA and BFAP will be summarized. For Na111 the reader is referred to section 6.2.

The parent compound Ba122 can be driven superconducting in various ways. Both chemical substitution, using isovalent phosphorus substitution for arsenic, and applied pressure lead to T_c values in the 30 K range [222, 223]. Currently there are no Raman studies of pressure-induced superconductivity in BFA. However, BFAP can be considered to fill this gap at least as a proxy [176]. For $x = 0.5$ BFAP has a T_c of 16 K and displays a broad pair-breaking peak in A_{1g} symmetry having a maximum at $\Omega_{\text{pb}}(T) \approx 2\Delta_{\text{max}} = 6.7 \text{ meV}$ or $4.9 k_B T_c$ (see table 2 and section 6.1). The nearly linear energy dependence of the spectra below the peak maximum indicates a much broader gap distribution than in BKFA and suggests

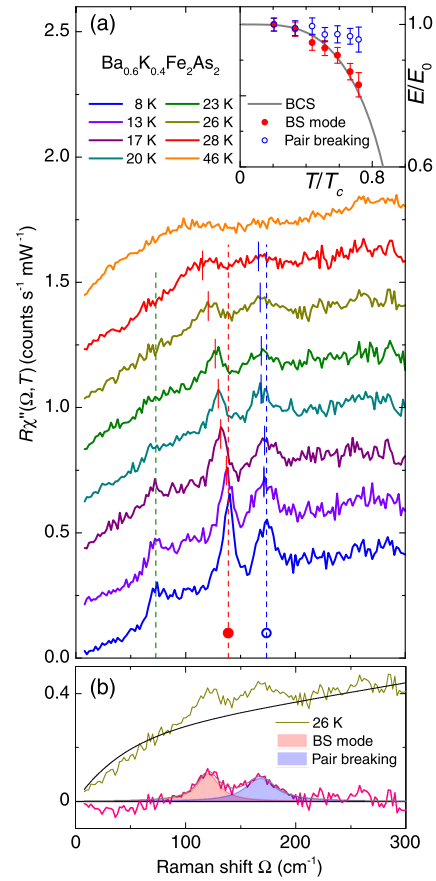


Figure 15. Temperature dependence of the Raman spectra of $\text{Ba}_{0.6}\text{K}_{0.4}\text{Fe}_2\text{As}_2$ in B_{1g} symmetry. (a) The spectra measured above 8 K are consecutively shifted up by 0.2 units. The pair-breaking features (open symbols) and the collective mode (full circles) depend differently on temperature, as shown in the inset (where zero energy is suppressed). The pair-breaking maximum exhibits a temperature dependence which is different from the BCS prediction due to interaction effects. (b) The peak energies are determined by fitting the spectra with two Lorentzians and a smooth phenomenological background (black curve). Reproduced from [47]. CC BY 4.0.

line nodes of the gap. If the peak is identified with the gap maximum of $4.9 k_B T_c$, it falls below the ratio in the range of $6\text{--}8 k_B T_c$ for other compounds [8]. There are no gap structures in the other symmetries and no collective modes in any symmetry. Thus from all aspects BFAP is closer to BFCA than BKFA.

Due to the doping dependent changes of the band structure, (π, π) scattering is expected to gain strength in BFCA in comparison to BKFA, and one would expect enhanced sub-dominant coupling channels. Rather, the anisotropy of the gaps grows, and the resulting density of states below the gap maximum leads to overdamping of potential in-gap modes similar to what has theoretically been shown to happen for d -wave gaps [120]. Therefore no collective modes can be resolved in BFCA, and the doping dependence is limited to intensity variations of the pair-breaking features described above. Consequently, only BKFA and the related CKFA [50] facilitate the study of changes of $V_{\mathbf{k},\mathbf{k}'}$ as a function of doping or, more appropriately, of the Fermi surface topology.

In what follows we assume that the modes observed below the maximal gap in BKFA are excitonic in origin [140]. This interpretation is not entirely accepted, although many criteria were tested experimentally (see above) and found to be in agreement with the theoretical prediction whereas counterarguments have not been presented yet. The doping dependence adds another piece of evidence to this assignment.

Although BKFA is superconducting for $0.1 < x \leq 1$ the range without magnetic order or changes of the Fermi surface topology is rather small, $0.25 < x < 0.6$. For $x < 0.25$ BKFA develops an SDW which gaps out part of the Fermi surface. For $x > 0.6$ the Fermi energy dives below the bottom of the inner electron band and for $x > 0.7$ hole-like bands appear around the X points [224]. It is still under debate which doping level should be associated with the Lifshitz transition but, as a matter of fact, one electron band is lost at $x \approx 0.6$.

The doping dependence of the Raman spectra in superconducting BKFA was studied by two groups. Wu and coworkers [48] looked at three doping levels, $x = 0.25, 0.4$, and 0.6 and, for $x = 0.4$, reproduced earlier results [46]. Three peaks were observed in B_{1g} symmetry at 50, 120, and 168 cm^{-1} and at 70, 140, and 172 cm^{-1} for the first and the second cleave, respectively, of the same crystal. Sample-dependent differences at optimal doping were also observed by Kretzschmar and collaborators [46] but the variations were much smaller, in particular the peak energies were nearly and the overall intensities entirely identical. We find it difficult to explain that the results obtained from two successive cleaves of the same crystal differ substantially, while the local T_c values or doping concentrations x are not reported to be different. For $x = 0.25$ Wu *et al* observe spectra which are qualitatively different from those at optimal doping and similar to what was found later by Böhm *et al* [41] in comparable samples. The spectra of Wu's over-doped BKFA, having nominally $x = 0.6$ and $T_c = 25$ K, are closer to the results found for $x = 0.43, \dots, 0.48$ in reference [41] although the T_c values differ by at least 10 K. An explanation of these discrepancies without directly comparing the magnetization measurements of the samples studied cannot be a subject of this review.

Regarding the experiments in the doping range $0.35 \leq x \leq 0.48$ studied in reference [41] only samples without indications of secondary transitions and with $\Delta T_c < 1.3$ K were selected. In this relatively small doping range which is sufficiently far away from the SDW and from changes in the Fermi surface topology the Raman spectra of all symmetries depend continuously on x . The highest peak energies in all symmetries follow T_c to within $\pm 12\%$. In general, the A_{1g} and B_{2g} energies are close to $(8 \pm 1)k_B T_c$ (see table 2) and thus higher than those in B_{1g} symmetry which scale roughly as $6.2k_B T_c$ as shown in figure 16 which displays raw and difference spectra in B_{1g} symmetry. There are two other maxima in B_{1g} symmetry at lower energy which are clearly resolved in all data sets and scale as $1 - x$ rather than T_c (figure 16(e)). The comparison of all symmetries and doping levels demonstrates that there are only very weak or no maxima in A_{1g} and B_{2g} symmetry in the range of the low-energy B_{1g} peaks. In addition, the low-energy peaks are nearly resolution limited and depend on temperature as $\Delta(T)$ [47].

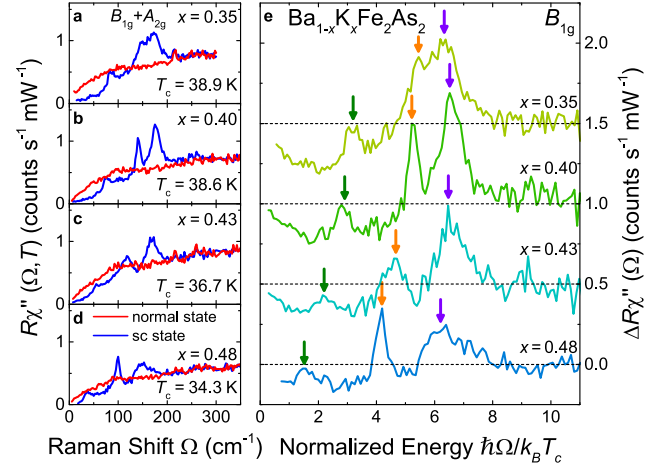


Figure 16. B_{1g} Raman spectra of BKFA for doping levels as indicated. (a)–(d) Raw data (after division by the Bose–Einstein factor) slightly above (red) and well below T_c (blue). (e) Difference spectra $\Delta R\chi''(\Omega) = R\chi''(\Omega, T \approx 8\text{ K}) - R\chi''(\Omega, T \gtrsim T_c)$. Here all temperature independent features drop out. Apparently, there are no temperature-dependent phonons. As an artifact, the intensity becomes negative inside the gap. Zero-intensity is indicated by horizontal lines (dashes). Reproduced from [41]. CC BY 4.0.

For $0.35 \leq x \leq 0.48$ the spectra of all symmetries can be described consistently [41] in terms of the phenomenology outlined in reference [91] and further elaborated on by Böhm *et al* [47] for $x = 0.4$. This approach starts from a realistic electronic structure [11], and the doping is accounted for by a shift of the Fermi energy. The Raman vertices are derived from the band structure (see equation (12)–(14)). The A_{1g} and B_{2g} spectra are used for determining the band and momentum dependent gap values compatible with ARPES studies. After some iterations the bare B_{1g} spectra (without final state interaction) become consistent with the experimental B_{1g} spectra. Here, consistent does not mean that the entire B_{1g} spectra can be reproduced. Rather, there are three features which by no combination of gaps can be explained: the two sharp lines below the gap edge and the missing intensity above the B_{1g} pair-breaking maximum which is expected according to the A_{1g} and B_{2g} spectra. With the final state interaction ‘switched on’ this part of the calculated B_{1g} spectrum is suppressed and reappears in the narrow modes. An explicit calculation was performed only for the stronger mode which was then found to acquire too much spectral weight for the coupling strength λ_d derived from the energy position (see equation (10)).

This discrepancy was solved later when theoretical considerations suggested the existence of two sub-leading channels rather than one [41, 92]. The two sub-leading channels ($\alpha = 2, 3$ ordered by strength) were derived from two independent microscopic approaches and were found to have second and first order $d_{x^2-y^2}$ (B_{1g}) symmetry (see figure 6 center). Having the higher binding energy $E_{BS(2)} > E_{BS(3)}$ the intensity of the BS mode at lower absolute energy (higher binding energy) is much smaller but still high enough for being the strongest spectral feature in the respective energy range. Unfortunately, the gap energies of the outer hole bands are in

the same range [199], motivating Wu *et al* to assign the mode to that gap at $x = 0.4$ [176]. Yet, both the phenomenology and the experimental results in A_{1g} and B_{2g} symmetry show that the B_{1g} mode is at least an order of magnitude too strong for justifying an explanation in terms of direct gap excitations [41] thus furnishing further evidence for the excitonic character of the two narrow in-gap modes.

Very recently, CKFA was studied. CKFA is a stoichiometric version of BKFA since the Ca and K layers alternate in a regular fashion for the substantial size difference of the Ca and K ions. From the viewpoint of valence count CKFA should be slightly overdoped, and the T_c values are indeed close to the maximum found for BKFA. The ARPES [205] and Raman experiments [50, 51] find gaps similar to those of BKFA. The features appearing below T_c are relatively strong in B_{1g} symmetry. In A_{1g} and B_{2g} symmetry they are weak and can only be observed for $\hbar\omega_I = 2.16$ eV [50] but not for $\hbar\omega_I = 1.92$ eV [51]. The weak structures in A_{1g} and B_{2g} symmetry are compatible with the gaps derived from ARPES. The B_{1g} spectra have substructures similar to those found for $x = 0.35$ in BKFA. There is agreement that the mode at 134 cm^{-1} may be a collective excitation and that the hump at 160 cm^{-1} is a remainder from pair breaking. The very weak structure at 50 cm^{-1} , tentatively assigned to a second BS mode in reference [50], remains controversial.

Even though there is no full agreement among the experimental groups about the details of the interpretation and, in particular, the doping dependence in BKFA, the question arises as to whether or not the idea of competing pairing channels may be a relevant contribution from Raman scattering to directly support the microscopic considerations. For addressing this question the hierarchy of pairing interactions was studied.

6.4. Possible conclusions for Cooper pairing

In conventional superconductors, the ground state has a much lower energy than potential competing pairing tendencies. Unconventional superconductors have typically various instabilities in close proximity, all of which may be intertwined with Cooper pairing. The ways to study the related phase diagrams include Hubbard-like models [143], the spin-fluctuation scenario which is studied in the random phase approximation (RPA) [9, 225], and the functional renormalization group (fRG) scheme [12, 210, 226, 227] which, as opposed to RPA, treats all possible interactions on equal footing.

In contrast to the Hubbard–Holstein model, which predicts an s_{++} ground state [143], both RPA and fRG find an s_{\pm} ground state for the specific band structure of the FeBCs where the energy gap has the same magnitude on the electron and hole bands but opposite sign [9, 12, 210, 226, 227]. Upon using a realistic band structure [11] and a rigid band model for simulating the doping, the hierarchy of pairing interactions was studied with RPA and fRG schemes. The results are similar in both cases and show that the ground state has s_{\pm} symmetry followed by two $d_{x^2-y^2}$ pairing tendencies. The solution of the eigenvalue equations yields the eigenvectors $g_{\alpha}(\mathbf{k})$ and

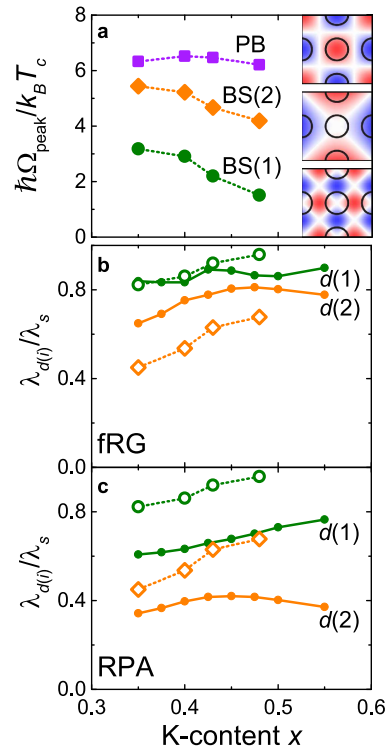


Figure 17. Doping dependence of the pairing strength in BKFA.

(a) The positions of the pair-breaking maxima scale approximately as T_c whereas the energies of the BS modes decrease monotonously with increasing doping in the range $0.35 \leq x \leq 0.48$ indicating increasing coupling in the sub-leading channels. The insets show the eigenvectors $g_{\alpha}(\mathbf{k})$ of the three channels. (b) and (c) The coupling strength of the two sub-leading $d_{x^2-y^2}$ -wave channels relative to the s_{\pm} -wave ground state, $\lambda_{d(i)}/\lambda_s$ (s , $d(1)$, and $d(2)$ correspond to $\alpha = 1, 2$, and 3 , respectively), is predicted to increase with doping (full symbols) in qualitative agreement with experiment (open symbols). $\lambda_{d(i)}/\lambda_s$ is derived from the binding energies in (a) as described in section 6.2. The results on the basis of fRG and RPA are similar. Reproduced from [41]. CC BY 4.0.

eigenvalues λ_{α} in channel α . $g_{\alpha}(\mathbf{k})$ and λ_{α} describe the variation with \mathbf{k} of the energy gap and, respectively, the coupling strength in channel α . On this basis the positions of the BS modes can be predicted and compared with the experiments as shown in figure 17.

The agreement of experiment and theory is remarkable in the case of fRG and still qualitative for RPA. The RPA results are offset to lower coupling strengths by 10%–20%. Since RPA neglects contributions other than spin-fluctuations, the observed discrepancy may indicate the existence of weak contributions from other coupling mechanisms such as charge fluctuations [41]. Yet, the similarity of the fRG and RPA results for the hierarchy of pairing channels supports spin-fluctuation-induced superconductivity in BKFA in the doping range studied. CKFA appears to fit into this picture although the weakness of the putative low-energy BS mode, the proximity of the second BS mode to the pair-breaking maximum [50], and the resulting controversy in the interpretation [51] qualify this conclusion and call for further experiments.

Whereas the recent RPA and fRG studies favor spin fluctuations, an s_{\pm} -wave gap and two sub-leading pairing channels having $d_{x^2-y^2}$ symmetry, the Hubbard–Holstein model leads to different conclusions and finds an s_{++} ground state driven by electron–phonon coupling and orbital fluctuations [143]. For the construction of the model sub-leading channels were not identified. However, if the sub-leading interactions in this model would be identified to have $d_{x^2-y^2}$ symmetry the resulting Raman spectra would be indistinguishable from those observed in BKFA and CKFA. Thus the case for spin fluctuation induced pairing depends crucially on the reliability of the hierarchy of pairing tendencies derived from fRG and RPA. Other experimental probes such as the study of quasi-particle interference effects in magnetic fields [191] or in the presence of impurities [228, 229] by scanning tunneling spectroscopy may help to clarify the symmetry of the ground state.

7. Conclusions

Raman scattering in iron pnictides and chalcogenides has provided a host of information on the electronic, magnetic and lattice properties of these systems. We focused on the spin and charge degrees of freedom in this review.

In all cases the spectra consist of a superposition of several types of excitations. To which extent *luminescence* (as an *a priori* undesired contribution) plays a role is not entirely clear, but the comparison of a large amount of results shows that luminescence decreases substantially with improved sample quality and may be neglected at least at low energies.

Particle–hole excitations are important in all compounds and for all doping levels. They are partially gapped out in the SDW state (section 5.2) where the materials remain metallic and are fully gapped out, for instance, in superconducting BKFA when the surfaces are sufficiently clean (see section 6.1 and reference [46]). In the normal state, the particle–hole excitations in A_{1g} symmetry depend on temperature as expected from the static resistivity (cf figure 10(d)).

In B_{1g} symmetry, a strong contribution from *fluctuations* (see section 5.3) is observed below room temperature at energies of order $k_B T$ which softens with decreasing temperature, has the strongest spectral weight directly at the structural transition T_S , and loses intensity below T_S without, however vanishing so long as the material does not order magnetically. Raman scattering is particularly useful here since other spectroscopies have generic difficulties in observing the fluctuations: in the case of neutron scattering, the fluctuations appear only in the notoriously weak four-particle correlation, and NMR spectroscopy covers only a small energy range well below $k_B T$. The same holds true for thermodynamic methods [230] or transport measurements [231] both of which probe fluctuations only indirectly. We argue that the temperature dependence identifies the Raman response as critical fluctuations which are expected to vanish at the related transition temperature. The persistence of the excitations below T_S is therefore considered an indication of spin rather than charge fluctuations. Yet, there is no consensus in the published literature on this point. However, if the controversy was

settled the driving force behind the phase transitions could be identified.

In all pnictides, the response of the spin density wave (SDW) is clearly observed (section 5.2). Although the gap energies are in the range $6\text{--}8\ k_B T_{SDW}$, the spectra are by and large described by weak-coupling physics including band reconstruction in the ordered state. This indicates that the magnetism here results from a Fermi surface instability of itinerant electrons. The relevant gap energies are in the range $100\text{--}150\text{ meV}$ in the parent compounds and decrease with doping or substitution along with the gradual suppression of the magnetically ordered phase.

In the chalcogenide $\text{Fe}(\text{Se}_{1-x}\text{S}_x)$ the B_{1g} response is distinctly different from that in the pnictides at all temperatures [55, 57]. In the range 60 meV , a broad excitation is observed for $x \lesssim 0.2$ which gains spectral weight by a factor of approximately two upon cooling without moving by more than a few percent. This temperature (and doping) dependence is not expected for quasi-particle scattering from impurities. Rather, the peak was associated with *two-magnon excitations of nearly localized moments in a frustrated magnet* (see sections 5.1 and 5.4) in agreement with neutron scattering experiments [157], LDA predictions for the exchange parameters J_1 and J_2 [170], and simulations using exact diagonalization [55, 171]. The response from fluctuations entirely fills the gap below 60 meV in the temperature range around T_S and persists down to $T \approx 20\text{ K}$. Indications of an SDW were not found. It is argued that orbital dependent localization of electrons as expected in Hund’s metals with $J \sim U$ may be at the origin of this dichotomy between the pnictides and chalcogenides [149, 156].

In the *superconducting state* gap excitations are observed in all sufficiently clean systems independent of the concentration of substitutional atoms (see section 6.1). Only Co substitution gradually suppresses the pair-breaking features. In all FeBCs there is a strong band dependence of the gaps. In FeSe the gap can be resolved in the Raman spectra but its small magnitude prevents a reliable analysis. In BFCA, the gaps on the electron bands exhibit a strong modulation with momentum and may even have accidental nodes at optimal doping. Here, Raman scattering and transport measurements arrive at similar conclusions [25, 36, 217]. In BKFA and presumably CKFA, the gaps on the individual bands are nearly constant. This fact, first derived from ARPES [205, 212], manifests itself in sharp gap edges in the Raman spectra.

Below the gap edges narrow, nearly *resolution-limited lines* are observed in the B_{1g} spectra of BKFA [47] (see sections 6.2 and 6.3). These lines display a BCS-like temperature dependence, vary as $1 - x$ with doping and steal spectral weight from the pair-breaking features. The pair-breaking features scale with T_c and barely depend on temperature. These criteria are predicted only for BS modes that result from sub-leading pairing interactions competing with the ground state.

Microscopic model calculations using fRG and RPA (see section 6.4) show that the pnictides have indeed a hierarchy of pairing channels with very similar eigenvalues, an s_{\pm} ground state, and two sub-leading $d_{x^2-y^2}$ instabilities of different order [41]. The Raman experiments agree semi-quantitatively with

these predictions concerning doping dependence but cannot pin down the sign change of the ground state. Tunneling experiments in samples with different impurity concentration [232] and with applied field [191] or RIXS experiments [233] may settle this point. Yet, the doping dependence of the sub-leading channels in BKFA and presumably the results in CKFA as well make a strong case for spin fluctuations to contribute partially or predominantly to the Cooper pairing in the pnictides.

In summary, the most significant contributions from light scattering experiments to the physics of the FeBCs pertain to the analysis of fluctuations and of the superconducting pairing states. The fluctuations can be compared to the evolution of the elasticity [116, 181] and of the spin-lattice relaxation as obtained from NMR studies [49]. While the interrelation of the various methods is obvious several aspects of the interpretation remain controversial, in particular the origin of the fluctuations. Concerning superconductivity the derivation of the gap energies is of specific relevance. Table 2 shows that the results from light scattering fit very well into the concert of the other methods if the data are read properly. Reading properly means, in particular, understanding the respective observables and including collective excitations which reveal details of the pairing potential $V_{\mathbf{k},\mathbf{k}'}$. In many cases the Raman response contributes information which cannot easily or not at all be obtained by other methods. Thus, part of the understanding of the pnictides and chalcogenides may rest on light scattering results, in particular if the remaining challenges in the interpretation can be settled. Additional insight is expected from novel x-ray techniques [124] which may help to settle, e.g., the sign problem of the order parameter [233] and from experiments under extreme conditions, specifically pressure. Here, the problem of the luminescence in the diamond anvils is a particular challenge if continuous spectra rather than narrow phonon lines have to be analyzed quantitatively.

Acknowledgments

We gratefully acknowledge discussions with A Baum, L Benfatto, G Blumberg, A Chubukov, T P Devereaux, Y Gallais, M Grilli, W Hanke, F Hardy, P Hirschfeld, D Jost, M Khodas, S Lederer, S Maiti, C Meingast, B Moritz, Z V Popović, R Thomale, and I Tüttő. Financial support came from the German Research Foundation (DFG) via the Priority Program SPP1458 (Grant-no Ha2071/7), the Transregional Collaborative Research Center TRR80 (Project ID 107745057), from the Serbian Ministry of Education, Science and Technological Development under Project III45018 and by the Science Fund of the Republic of Serbia (Project ‘StrainedFe’). We acknowledge support by the DAAD through the bilateral project between Serbia and Germany (Grant Numbers 57335339 and 57449106).

ORCID iDs

R Hackl  <https://orcid.org/0000-0002-6751-0879>

References

- [1] Kamihara Y, Hiramatsu H, Hirano M, Kawamura R, Yanagi H, Kamiya T and Hosono H 2006 *J. Am. Chem. Soc.* **128** 10012
- [2] Kamihara Y, Watanabe T, Hirano M and Hosono H 2008 *J. Am. Chem. Soc.* **130** 3296
- [3] Paglione J and Greene R L 2010 *Nat. Phys.* **6** 645
- [4] Johnston D C 2010 *Adv. Phys.* **59** 803
- [5] Stewart G R 2011 *Rev. Mod. Phys.* **83** 1589
- [6] Hirschfeld P J, Korshunov M M and Mazin I I 2011 *Rep. Prog. Phys.* **74** 125508
- [7] Hirschfeld P J 2016 *Compt. Rendus Phys.* **17** 197
- [8] Korshunov M M 2018 *Phys. Rev. B* **98** 104510
- [9] Mazin I I, Singh D J, Johannes M D and Du M H 2008 *Phys. Rev. Lett.* **101** 057003
- [10] Kordyuk A A, Zabolotnyy V B, Evtushinsky D V, Yaresko A N, Büchner B and Borisenko S V 2013 *J. Supercond. Nov. Magnetism* **26** 2837
- [11] Graser S, Maier T, Hirschfeld P and Scalapino D 2009 *New J. Phys.* **11** 025016
- [12] Thomale R, Platt C, Hanke W and Bernevig B A 2011 *Phys. Rev. Lett.* **106** 187003
- [13] Böhm T 2017 The case for spin-fluctuation induced pairing in $\text{Ba}_{1-x}\text{K}_x\text{Fe}_2\text{As}_2$ *PhD Thesis* (Technische Universität München)
- [14] Fernandes R M, Chubukov A V and Schmalian J 2014 *Nat. Phys.* **10** 97
- [15] Massat P, Quan Y, Grasset R, Méasson M A, Cazayous M, Sacuto A, Karlsson S, Strobel P, Toulemonde P, Yin Z and Gallais Y 2018 *Phys. Rev. Lett.* **121** 077001
- [16] Hadjiev V G, Iliev M N, Sasmal K, Sun Y Y and Chu C W 2008 *Phys. Rev. B* **77** 220505
- [17] Litvinchuk A P, Hadjiev V G, Iliev M N, Lv B, Guloy A M and Chu C W 2008 *Phys. Rev. B* **78** 060503
- [18] Rahlenbeck M, Sun G L, Sun D L, Lin C T, Keimer B and Ulrich C 2009 *Phys. Rev. B* **80** 064509
- [19] Um Y J, Park J T, Min B H, Song Y J, Kwon Y S, Keimer B and Le Tacon M 2012 *Phys. Rev. B* **85** 012501
- [20] Lazarević N, Popović Z V, Hu R and Petrovic C 2011 *Phys. Rev. B* **83** 024302
- [21] Lazarević N, Abeykoon M, Stephens P W, Lei H, Bozin E S, Petrovic C and Popović Z V 2012 *Phys. Rev. B* **86** 054503
- [22] Zhang A M, Liu K, Xiao J H, He J B, Wang D M, Chen G F, Normand B and Zhang Q M 2012 *Phys. Rev. B* **85** 024518
- [23] Rotter M, Tegel M and Johrendt D 2008 *Phys. Rev. Lett.* **101** 107006
- [24] Sefat A S, Jin R, McGuire M A, Sales B C, Singh D J and Mandrus D 2008 *Phys. Rev. Lett.* **101** 117004
- [25] Muschler B, Prestel W, Hackl R, Devereaux T P, Analytis J G, Chu J H and Fisher I R 2009 *Phys. Rev. B* **80** 180510
- [26] Chauvière L, Gallais Y, Cazayous M, Méasson M A, Sacuto A, Colson D and Forget A 2011 *Phys. Rev. B* **84** 104508
- [27] Sugai S, Mizuno Y, Watanabe R, Kawaguchi T, Takenaka K, Ikuta H, Takayanagi Y, Hayamizu N and Sone Y 2012 *J. Phys. Soc. Japan* **81** 024718
- [28] Chu J H, Analytis J G, Greve K D, McMahon P L, Islam Z, Yamamoto Y and Fisher I R 2010 *Science* **329** 824
- [29] Choi K Y, Lemmens P, Eremin I, Zwicknagl G, Berger H, Sun G L, Sun D L and Lin C T 2010 *J. Phys.: Condens. Matter* **22** 115802
- [30] Gallais Y, Fernandes R M, Paul I, Chauvière L, Yang Y X, Méasson M A, Cazayous M, Sacuto A, Colson D and Forget A 2013 *Phys. Rev. Lett.* **111** 267001
- [31] Okazaki K, Sugai S, Niitaka S and Takagi H 2011 *Phys. Rev. B* **83** 035103
- [32] Sugai S, Mizuno Y, Watanabe R, Kawaguchi T, Takenaka K, Ikuta H, Kiho K, Nakajima M, Lee C H, Iyo A, Eisaki H and Uchida S 2013 *J. Supercond. Nov. Magnetism* **26** 1179

- [33] Zhang W L, Richard P, Ding H, Sefat A S, Gillett J, Sebastian S E, Khodas M and Blumberg G 2014 On the origin of the electronic anisotropy in iron pnictide superconductors (arXiv: [1410.6452](#))
- [34] Zhang W L, Yin Z P, Ignatov A, Bukowski Z, Karpinski J, Sefat A S, Ding H, Richard P and Blumberg G 2016 *Phys. Rev. B* **93** 205106
- [35] Kaneko U F, Gomes P F, García-Flores A F, Yan J Q, Lograsso T A, Barberis G E, Vaknin D and Granado E 2017 *Phys. Rev. B* **96** 014506
- [36] Mazin I I, Devereaux T P, Analytis J G, Chu J H, Fisher I R, Muschler B and Hackl R 2010 *Phys. Rev. B* **82** 180502
- [37] Sugai S, Mizuno Y, Kiho K, Nakajima M, Lee C H, Iyo A, Eisaki H and Uchida S 2010 *Phys. Rev. B* **82** 140504
- [38] Chauvière L, Gallais Y, Cazayous M, Méasson M A, Sacuto A, Colson D and Forget A 2010 *Phys. Rev. B* **82** 180521
- [39] Gallais Y, Paul I, Chauvière L and Schmalian J 2016 *Phys. Rev. Lett.* **116** 017001
- [40] Kretzschmar F, Böhm T, Karahasanović U, Muschler B, Baum A, Jost D, Schmalian J, Caprara S, Grilli M, Di Castro C, Analytis J H, Chu J H, Fisher I R and Hackl R 2016 *Nat. Phys.* **12** 560
- [41] Böhm T, Kretzschmar F, Baum A, Rehm M, Jost D, Hosseinian Ahangharnejhad R, Thomale R, Platt C, Maier T A, Hanke W, Moritz B, Devereaux T P, Scalapino D J, Maiti S, Hirschfeld P J, Adelman P, Wolf T, Wen H H and Hackl R 2018 *npj Quant. Mater.* **3** 48
- [42] Kumar P, Muthu D V S, Harnagea L, Wurmehl S, Buchner B and Sood A K 2014 *J. Phys.: Condens. Matter* **26** 305403
- [43] Yang Y X, Gallais Y, Rullier-Albenque F, Méasson M A, Cazayous M, Sacuto A, Shi J, Colson D and Forget A 2014 *Phys. Rev. B* **89** 125130
- [44] Kaneko U F, Piva M M, Jesus C, Saleta M, Urbano R, Pagliuso P G and Granado E 2019 *J. Phys.: Condens. Matter* **31** 495402
- [45] Wu S F, Zhang W L, Li L, Cao H, Kung H H, Sefat A, Ding H, Richard P and Blumberg G 2017 On the origin of critical nematic fluctuations in pnictide superconductors (arXiv: [1712.06066](#))
- [46] Kretzschmar F, Muschler B, Böhm T, Baum A, Hackl R, Wen H H, Tsurkan V, Deisenhofer J and Loidl A 2013 *Phys. Rev. Lett.* **110** 187002
- [47] Böhm T, Kemper A F, Moritz B, Kretzschmar F, Muschler B, Eiter H M, Hackl R, Devereaux T P, Scalapino D J and Wen H H 2014 *Phys. Rev. X* **4** 041046
- [48] Wu S F, Richard P, Ding H, Wen H H, Tan G, Wang M, Zhang C, Dai P and Blumberg G 2017 *Phys. Rev. B* **95** 085125
- [49] Thorsmølle V K, Khodas M, Yin Z P, Zhang C, Carr S V, Dai P and Blumberg G 2016 *Phys. Rev. B* **93** 054515
- [50] Jost D, Scholz J R, Zweck U, Meier W R, Böhrer A E, Canfield P C, Lazarević N and Hackl R 2018 *Phys. Rev. B* **98** 020504
- [51] Zhang W L, Meier W R, Kong T, Canfield P C and Blumberg G 2018 *Phys. Rev. B* **98** 140501
- [52] Okazaki K, Sugai S, Niitaka S and Takagi H 2011 *Phys. Rev. B* **83** 035103
- [53] Massat P, Farina D, Paul I, Karlsson S, Strobel P, Toulemonde P, Méasson M A, Cazayous M, Sacuto A, Kasahara S, Shibauchi T, Matsuda Y and Gallais Y 2016 *Proc. Natl Acad. Sci.* **113** 9177
- [54] Glamazda A, Lemmens P, Ok J M, Kim J S and Choi K Y 2019 *Phys. Rev. B* **99** 075142
- [55] Baum A, Ruiz H N, Lazarević N, Wang Y, Böhm T, Hosseinian Ahangharnejhad R, Adelman P, Wolf T, Popović Z V, Moritz B, Devereaux T P and Hackl R 2019 *Commun. Phys.* **2** 14
- [56] Kumar P, Kumar A, Saha S, Muthu D, Prakash J, Patnaik S, Waghmare U, Ganguli A and Sood A 2010 *Solid State Commun.* **150** 557
- [57] Zhang W L, Wu S F, Kasahara S, Shibauchi T, Matsuda Y and Blumberg G 2017 Stripe quadrupole order in the nematic phase of $\text{FeSe}_{1-x}\text{S}_x$ (arXiv: [1710.09892](#))
- [58] Khodas M, Chubukov A V and Blumberg G 2014 *Phys. Rev. B* **89** 245134
- [59] Zhang A M, Xiao J H, Li Y S, He J B, Wang D M, Chen G F, Normand B, Zhang Q M and Xiang T 2012 *Phys. Rev. B* **85** 214508
- [60] Fleury P A, Porto S P S, Cheesman L E and Guggenheim H J 1966 *Phys. Rev. Lett.* **17** 84
- [61] Lyons K B, Sulewski P E, Fleury P A, Carter H L, Cooper A S, Espinosa G P, Fisk Z and Cheong S W 1989 *Phys. Rev. B* **39** 9693
- [62] Fleury P A and Loudon R 1968 *Phys. Rev.* **166** 514
- [63] Devereaux T P and Hackl R 2007 *Rev. Mod. Phys.* **79** 175
- [64] Chen C C, Jia C J, Kemper A F, Singh R R P and Devereaux T P 2011 *Phys. Rev. Lett.* **106** 067002
- [65] Baum A, Milosavljević A, Lazarević N, Radonjić M M, Nikolić B, Mitschek M, Maranloo Z I, Šćepanović M, Grujić-Brojčin M, Stojilović N, Opel M, Wang A, Petrović C, Popović Z V and Hackl R 2018 *Phys. Rev. B* **97** 054306
- [66] Abrikosov A A and Fal'kovskii L A 1961 *Zh. Eksp. Teor. Fiz.* **40** 262
Abrikosov A A and Fal'kovskii L A 1961 *Sov. Phys. - JETP* **13** 179
- [67] Sooryakumar R and Klein M V 1980 *Phys. Rev. Lett.* **45** 660
- [68] Dierker S B, Klein M V, Webb G W and Fisk Z 1983 *Phys. Rev. Lett.* **50** 853
- [69] Hackl R, Kaiser R and Schick Tanz S 1983 *J. Phys. C: Solid State Phys.* **16** 1729
- [70] Cooper S L, Klein M V, Pazol B G, Rice J P and Ginsberg D M 1988 *Phys. Rev. B* **37** 5920
- [71] Hackl R, Gläser W, Müller P, Einzel D and Andres K 1988 *Phys. Rev. B* **38** 7133
- [72] Abrikosov A and Genkin V 1973 *Zh. Eksp. Teor. Fiz.* **65** 842
Abrikosov A and Genkin V 1974 *Sov. Phys. - JETP* **38** 417
- [73] Klein M V and Dierker S B 1984 *Phys. Rev. B* **29** 4976
- [74] Devereaux T P, Einzel D, Stadlober B, Hackl R, Leach D H and Neumeier J J 1994 *Phys. Rev. Lett.* **72** 396
- [75] Chandrasekhar M, Cardona M and Kane E O 1977 *Phys. Rev. B* **16** 3579–95
- [76] Ipatova I, Subashiev A and Voitenko V 1981 *Solid State Commun.* **37** 893
- [77] Zawadowski A and Cardona M 1990 *Phys. Rev. B* **42** 10732
- [78] Stauffer T, Hackl R and Müller P 1990 *Solid State Commun.* **75** 975
- [79] Slakey F, Klein M V, Rice J P and Ginsberg D M 1991 *Phys. Rev. B* **43** 3764
- [80] Hackl R, Opel M, Müller P F, Krug G, Stadlober B, Nemetschek R, Berger H and Forró L 1996 *J. Low Temp. Phys.* **105** 733
- [81] Opel M, Nemetschek R, Hoffmann C, Philipp R, Müller P F, Hackl R, Tütt I, Erb A, Revaz B, Walker E, Berger H and Forró L 2000 *Phys. Rev. B* **61** 9752
- [82] Einzel D and Hackl R 1996 *J. Raman Spectrosc.* **27** 307
- [83] Caprara S, Di Castro C, Grilli M and Suppa D 2005 *Phys. Rev. Lett.* **95** 117004
- [84] Tassini L, Venturini F, Zhang Q M, Hackl R, Kikugawa N and Fujita T 2005 *Phys. Rev. Lett.* **95** 117002
- [85] Klein A, Lederer S, Chowdhury D, Berg E and Chubukov A 2018 *Phys. Rev. B* **97** 155115
- [86] Klein A, Lederer S, Chowdhury D, Berg E and Chubukov A 2018 *Phys. Rev. B* **98** 041101
- [87] Udina M, Grilli M, Benfatto L and Chubukov A V 2020 *Phys. Rev. Lett.* **120** 197602
- [88] Zawadowski A, Ruvalds J and Solana J 1972 *Phys. Rev. A* **5** 399
- [89] Monien H and Zawadowski A 1990 *Phys. Rev. B* **41** 8798–810
- [90] Chubukov A V, Eremin I and Korshunov M M 2009 *Phys. Rev. B* **79** 220501
- [91] Scalapino D J and Devereaux T P 2009 *Phys. Rev. B* **80** 140512

- [92] Maiti S, Maier T A, Böhm T, Hackl R and Hirschfeld P J 2016 *Phys. Rev. Lett.* **117** 257001
- [93] Littlewood P B and Varma C M 1981 *Phys. Rev. Lett.* **47** 811
- [94] Littlewood P B and Varma C M 1982 *Phys. Rev. B* **26** 4883
- [95] Leggett A J 1966 *Prog. Theor. Phys.* **36** 901
- [96] Blumberg G, Mialitsin A, Dennis B S, Klein M V, Zhigadlo N D and Karpinski J 2007 *Phys. Rev. Lett.* **99** 227002
- [97] Klein M V 2010 *Phys. Rev. B* **82** 014507
- [98] Burnell F J, Hu J, Parish M M and Bernevig B A 2010 *Phys. Rev. B* **82** 144506
- [99] Cea T and Benfatto L 2016 *Phys. Rev. B* **94** 064512
- [100] Huang W, Sigrist M and Weng Z Y 2018 *Phys. Rev. B* **97** 144507
- [101] Méasson M A, Gallais Y, Cazayous M, Clair B, Rodière P, Cario L and Sacuto A 2014 *Phys. Rev. B* **89** 060503
- [102] Pekker D and Varma C 2015 *Annu. Rev. Condens. Matter Phys.* **6** 269
- [103] Hackl R, Kaiser R and Gläser W 1989 *Physica C* **162-164** 431
- [104] Kendziora C and Rosenberg A 1995 *Phys. Rev. B* **52** 9867
- [105] Chen X K, Naeini J G, Hewitt K C, Irwin J C, Liang R and Hardy W N 1997 *Phys. Rev. B* **56** R513
- [106] Sugai S and Hosokawa T 2000 *Phys. Rev. Lett.* **85** 1112
- [107] Le Tacon M, Sacuto A, Georges A, Kotliar G, Gallais Y, Colson D and Forget A 2006 *Nat. Phys.* **2** 537
- [108] Munnikes N, Muschler B, Venturini F, Tassini L, Prestel W, Ono S, Ando Y, Peets D C, Hardy W N, Liang R, Bonn D A, Damascelli A, Eisaki H, Greven M, Erb A and Hackl R 2011 *Phys. Rev. B* **84** 144523
- [109] Li Y, Le Tacon M, Matiks Y, Boris A V, Loew T, Lin C T, Chen L, Chan M K, Dorow C, Ji L, Barišić N, Zhao X, Greven M and Keimer B 2013 *Phys. Rev. Lett.* **111** 187001
- [110] Devereaux T P 1992 *Phys. Rev. B* **45** 12965
- [111] Devereaux T P 1993 *Phys. Rev. B* **47** 5230
- [112] Devereaux T P 1995 *Phys. Rev. Lett.* **74** 4313
- [113] Manske D 2004 *Theory of Unconventional Superconductors* (Springer Tracts in Modern Physics 202) (Heidelberg: Springer)
- [114] Caprara S, Colonna M, Di Castro C, Hackl R, Muschler B, Tassini L and Grilli M 2015 *Phys. Rev. B* **91** 205115
- [115] Karahasanovic U, Kretzschmar F, Böhm T, Hackl R, Paul I, Gallais Y and Schmalian J 2015 *Phys. Rev. B* **92** 075134
- [116] Gallais Y and Paul I 2016 *Compt. Rendus Phys.* **17** 113
- [117] Boyd G R, Devereaux T P, Hirschfeld P J, Mishra V and Scalapino D J 2009 *Phys. Rev. B* **79** 174521
- [118] Khodas M and Levchenko A 2015 *Phys. Rev. B* **91** 235119
- [119] Hayes W and Loudon R 2005 *Scattering of Light by Crystals* (New York: Dover)
- [120] Devereaux T P and Einzel D 1995 *Phys. Rev. B* **51** 16336
- [121] Kosztin J and Zawadowski A 1991 *Solid State Commun.* **78** 1029
- [122] Freericks J K, Devereaux T P, Moraghebi M and Cooper S L 2005 *Phys. Rev. Lett.* **94** 216401
- [123] Salpeter E E and Bethe H A 1951 *Phys. Rev.* **84** 1232–42
- [124] Ament L J P, van Veenendaal M, Devereaux T P, Hill J P and van den Brink J 2011 *Rev. Mod. Phys.* **83** 705–67
- [125] Pines D and Nozières P 1966 *The Theory of Quantum Liquids: Normal Fermi Liquids* (Reading, MA: Benjamin)
- [126] Maiti S, Chubukov A V and Hirschfeld P J 2017 *Phys. Rev. B* **96** 014503
- [127] Platzman P M 1965 *Phys. Rev.* **139** A379
- [128] Kostur V N 1992 *Z. Phys. B Condens. Matter* **89** 149–59
- [129] Devereaux T P, Virostek A and Zawadowski A 1996 *Phys. Rev. B* **54** 12523
- [130] Muschler B, Prestel W, Tassini L, Hackl R, Lambacher M, Erb A, Komiya S, Ando Y, Peets D, Hardy W, Liang R and Bonn D 2010 *Eur. Phys. J. Spec. Top.* **188** 131
- [131] Hackl R and Kaiser R 1988 *J. Phys. C: Solid State Phys.* **21** L453
- [132] Cuk T, Lu D H, Zhou X J, Shen Z X, Devereaux T P and Nagaosa N 2005 *Phys. Status Solidi b* **242** 11
- [133] Inosov D S, Borisenko S V, Eremin I, Kordyuk A A, Zabolotnyy V B, Geck J, Koitzsch A, Fink J, Knupfer M, Büchner B, Berger H and Follath R 2007 *Phys. Rev. B* **75** 172505
- [134] Prestel W, Venturini F, Muschler B, Tüttel, Hackl R, Lambacher M, Erb A, Komiya S, Ono S, Ando Y, Inosov D, Zabolotnyy V B and Borisenko S V 2010 *Eur. Phys. J. Spec. Top.* **188** 163
- [135] Tsuneto T 1960 *Phys. Rev.* **118** 1029–35
- [136] Mattis D C and Bardeen J 1958 *Phys. Rev.* **111** 412
- [137] Eiter H M, Lavagnini M, Hackl R, Nowadnick E A, Kemper A F, Devereaux T P, Chu J H, Analytis J G, Fisher I R and Degiorgi L 2013 *Proc. Natl. Acad. Sci.* **110** 64
- [138] Shastry B S and Shraiman B I 1990 *Phys. Rev. Lett.* **65** 1068
- [139] Varma C M 2002 *J. Low Temp. Phys.* **126** 901
- [140] Bardasis A and Schrieffer J R 1961 *Phys. Rev.* **121** 1050–62
- [141] Greytak T J and Yan J 1969 *Phys. Rev. Lett.* **22** 987
- [142] Suhl H, Matthias B T and Walker L R 1959 *Phys. Rev. Lett.* **3** 552
- [143] Kontani H and Onari S 2010 *Phys. Rev. Lett.* **104** 157001
- [144] Weidinger S A and Zwerger W 2015 *Eur. Phys. J. B* **88** 237
- [145] Podolsky D, Auerbach A and Arovas D P 2011 *Phys. Rev. B* **84** 174522
- [146] Gazit S, Podolsky D and Auerbach A 2013 *Phys. Rev. Lett.* **110** 140401
- [147] Chelwani N, Baum A, Böhm T, Opel M, Venturini F, Tassini L, Erb A, Berger H, Forró L and Hackl R 2018 *Phys. Rev. B* **97** 024407
- [148] de' Medici L, Hassan S R, Capone M and Dai X 2009 *Phys. Rev. Lett.* **102** 126401
- [149] Yin Z P, Haule K and Kotliar G 2011 *Nat. Mater.* **10** 932
- [150] Leonov I, Skornyakov S L, Anisimov V I and Vollhardt D 2015 *Phys. Rev. Lett.* **115** 106402
- [151] Knoll P, Thomsen C, Cardona M and Murugaraj P 1990 *Phys. Rev. B* **42** 4842
- [152] Devereaux T P and Kampf A P 1999 *Phys. Rev. B* **59** 6411
- [153] Moritz B, Johnston S, Devereaux T P, Muschler B, Prestel W, Hackl R, Lambacher M, Erb A, Komiya S and Ando Y 2011 *Phys. Rev. B* **84** 235114
- [154] Jia C J, Nowadnick E A, Wohlfeld K, Kung Y F, Chen C C, Johnston S, Tohyama T, Moritz B and Devereaux T P 2014 *Nat. Commun.* **5** 3314
- [155] Georges A, de' Medici L and Mravlje J 2013 *Annu. Rev. Condens. Matter Phys.* **4** 137
- [156] Si Q, Yu R and Abrahams E 2016 *Nat. Rev. Mater.* **1** 16017
- [157] Wang Q, Shen Y, Pan B, Zhang X, Ikeuchi K, Iida K, Christianson A D, Walker H C, Adroja D T, Abdel-Hafiez M, Chen X, Chareev D A, Vasiliev A N and Zhao J 2016 *Nat. Commun.* **7** 12182
- [158] Skornyakov S L, Anisimov V I, Vollhardt D and Leonov I 2017 *Phys. Rev. B* **96** 035137
- [159] Sulewski P E, Fleury P A, Lyons K B and Cheong S W 1991 *Phys. Rev. Lett.* **67** 3864
- [160] Venturini F, Michelucci U, Devereaux T P and Kampf A P 2000 *Phys. Rev. B* **62** 15204
- [161] Aslamasov L G and Larkin A I 1968 *Sov. Phys. Solid State* **10** 875
- [162] Fernandes R M and Schmalian J 2012 *Supercond. Sci. Technol.* **25** 084005
- [163] Yamakawa Y, Onari S and Kontani H 2016 *Phys. Rev. X* **6** 021032
- [164] Chubukov A V, Khodas M and Fernandes R M 2016 *Phys. Rev. X* **6** 041045
- [165] Classen L, Xing R Q, Khodas M and Chubukov A V 2017 *Phys. Rev. Lett.* **118** 037001
- [166] Fanfarillo L, Benfatto L and Valenzuela B 2018 *Phys. Rev. B* **97** 121109
- [167] Allen P B 1976 *Phys. Rev. B* **13** 1416
- [168] Baek S H, Efremov D V, Ok J M, Kim J S, van den Brink J and Büchner B 2014 *Nat. Mater.* **14** 210

- [169] Yi M, Lu D, Chu J H, Analytis J G, Sorini A P, Kemper A F, Moritz B, Mo S K, Moore R G, Hashimoto M, Lee W S, Hussain Z, Devereaux T P, Fisher I R and Shen Z X 2011 *Proc. Natl Acad. Sci.* **108** 6878
- [170] Glasbrenner J K, Mazin I I, Jeschke H O, Hirschfeld P J, Fernandes R M and Valentí R 2015 *Nat. Phys.* **11** 953
- [171] Ruiz H, Wang Y, Moritz B, Baum A, Hackl R and Devereaux T P 2019 *Phys. Rev. B* **99** 125130
- [172] Baum A, Li Y, Tomić M, Lazarević N, Jost D, Löffler F, Muschler B, Böhm T, Chu J H, Fisher I R, Valentí R, Mazin I I and Hackl R 2018 *Phys. Rev. B* **98** 075113
- [173] Fernandes R M, Chubukov A V, Knolle J, Eremin I and Schmalian J 2012 *Phys. Rev. B* **85** 024534
- [174] Kontani H, Saito T and Onari S 2011 *Phys. Rev. B* **84** 024528
- [175] Gnezdilov V, Pashkevich Y G, Lemmens P, Wulferding D, Shevtsova T, Gusev A, Chareev D and Vasiliev A 2013 *Phys. Rev. B* **87** 144508
- [176] Wu S F, Zhang W L, Hu D, Kung H H, Lee A, Mao H C, Dai P C, Ding H, Richard P and Blumberg G 2016 Collective excitations of dynamic Fermi surface deformations in $\text{BaFe}_2(\text{As}_{0.5}\text{P}_{0.5})_2$ (arXiv:1607.06575)
- [177] Yamase H and Zeyher R 2011 *Phys. Rev. B* **83** 115116
- [178] Yamase H and Zeyher R 2013 *Phys. Rev. B* **88** 125120
- [179] Yoshizawa M, Kimura D, Chiba T, Simayi S, Nakanishi Y, Kihou K, Lee C H, Iyo A, Eisaki H, Nakajima M and Uchida S i 2012 *J. Phys. Soc. Japan* **81** 024604
- [180] Kontani H and Yamakawa Y 2014 *Phys. Rev. Lett.* **113** 047001
- [181] Böhm T, Hosseinian Ahangharnejhad R, Jost D, Baum A, Muschler B, Kretzschmar F, Adelmann P, Wolf T, Wen H H, Chu J H, Fisher I R and Hackl R 2017 *Phys. Status Solidi b* **254** 1600308
- [182] Sun J P, Matsuura K, Ye G Z, Mizukami Y, Shimozaawa M, Matsubayashi K, Yamashita M, Watashige T, Kasahara S, Matsuda Y, Yan J Q, Sales B C, Uwatoko Y, Cheng J G and Shibauchi T 2016 *Nat. Commun.* **7** 12146
- [183] Jia C, Wohlfeld K, Wang Y, Moritz B and Devereaux T P 2016 *Phys. Rev. X* **6** 021020
- [184] de la Cruz C, Huang Q, Lynn J W, Li J, Ratcliff II W, Zarestky J L, Mook H A, Chen G F, Luo J L, Wang N L and Dai P 2008 *Nature* **453** 899
- [185] Chu J H, Analytis J G, Kucharczyk C and Fisher I R 2009 *Phys. Rev. B* **79** 014506
- [186] Yi M, Liu Z K, Zhang Y, Yu R, Zhu J X, Lee J, Moore R, Schmitt F, Li W, Riggs S, Chu J H, Lv B, Hu J, Hashimoto M, Mo S K, Hussain Z, Mao Z, Chu C, Fisher I, Si Q, Shen Z X and Lu D 2015 *Nat. Commun.* **6** 7777
- [187] Coldea A I, Blake S F, Kasahara S, Haghighirad A A, Watson M D, Knafo W, Choi E S, McCollam A, Reiss P, Yamashita T, Bruma M, Speller S C, Matsuda Y, Wolf T, Shibauchi T and Schofield A J 2019 *npj Quant. Mater.* **4** 2
- [188] Yi M, Zhang Y, Shen Z X and Lu D 2017 *npj Quant. Mater.* **2** 57
- [189] Yao D W and Li T 2019 *Europhys. Lett.* **125** 37002
- [190] Bardeen J, Cooper L N and Schrieffer J R 1957 *Phys. Rev.* **106** 162
- [191] Hanaguri T, Niitaka S, Kuroki K and Takagi H 2010 *Science* **328** 474
- [192] Christianson A D, Goremychkin E A, Osborn R, Rosenkranz S, Lumsden M D, Malliakas C D, Todorov I S, Claus H, Chung D Y, Kanatzidis M G, Bewley R I and Guidi T 2008 *Nature* **456** 930
- [193] Korshunov M M, Shestakov V A and Togushova Y N 2017 *J. Magn. Magn. Mater.* **440** 133
- [194] Yin Y, Zech M, Williams T L, Wang X F, Wu G, Chen X H and Hoffman J E 2009 *Phys. Rev. Lett.* **102** 097002
- [195] Wang M, Yi M, Sun H L, Valdivia P, Kim M G, Xu Z J, Berlijn T, Christianson A D, Chi S, Hashimoto M, Lu D H, Li X D, Bourret-Courchesne E, Dai P, Lee D H, Maier T A and Birgeneau R J 2016 *Phys. Rev. B* **93** 205149
- [196] Hardy F, Burger P, Wolf T, Fisher R A, Schweiss P, Adelmann P, Heid R, Fromknecht R, Eder R, Ernst D, von Löhneysen H and Meingast C 2010 *Europhys. Lett.* **91** 47008
- [197] Terashima K, Sekiba Y, Bowen J H, Nakayama K, Kawahara T, Sato T, Richard P, Xu Y M, Li L J, Cao G H, Xu Z A, Ding H and Takahashi T 2009 *Proc. Natl Acad. Sci.* **106** 7330
- [198] Nakayama K, Sato T, Richard P, Xu Y M, Kawahara T, Umezawa K, Qian T, Neupane M, Chen G F, Ding H and Takahashi T 2011 *Phys. Rev. B* **83** 020501
- [199] Hardy F, Böhrer A E, de' Medici L, Capone M, Giovannetti G, Eder R, Wang L, He M, Wolf T, Schweiss P, Heid R, Herbig A, Adelmann P, Fisher R A and Meingast C 2016 *Phys. Rev. B* **94** 205113
- [200] Xu B, Dai Y M, Xiao H, Shen B, Wen H H, Qiu X G and Lobo R P S M 2017 *Phys. Rev. B* **96** 115125
- [201] Ding H, Richard P, Nakayama K, Sugawara K, Arakane T, Sekiba Y, Takayama A, Souma S, Sato T, Takahashi T, Wang Z, Dai X, Fang Z, Chen G F, Luo J L and Wang N L 2008 *Europhys. Lett.* **83** 47001
- [202] Zhang Y, Yang L X, Chen F, Zhou B, Wang X F, Chen X H, Arita M, Shimada K, Namatame H, Taniguchi M, Hu J P, Xie B P and Feng D L 2010 *Phys. Rev. Lett.* **105** 117003
- [203] Evtushinsky D V, Zabolotnyy V B, Kim T K, Kordyuk A A, Yaresko A N, Maletz J, Aswartham S, Wurmehl S, Boris A V, Sun D L, Lin C T, Shen B, Wen H H, Varykhalov A, Follath R, Büchner B and Borisenko S V 2014 *Phys. Rev. B* **89** 064514
- [204] Wray L, Qian D, Hsieh D, Xia Y, Li L, Checkelsky J G, Pasupathy A, Gomes K K, Parker C V, Fedorov A V, Chen G F, Luo J L, Yazdani A, Ong N P, Wang N L and Hasan M Z 2008 *Phys. Rev. B* **78** 184508
- [205] Mou D, Kong T, Meier W R, Lochner F, Wang L L, Lin Q, Wu Y, Bud'ko S L, Eremin I, Johnson D D, Canfield P C and Kaminski A 2016 *Phys. Rev. Lett.* **117** 277001
- [206] Shimojima T, Sakaguchi F, Ishizaka K, Ishida Y, Kiss T, Okawa M, Togashi T, Chen C T, Watanabe S, Arita M, Shimada K, Namatame H, Taniguchi M, Ohgushi K, Kasahara S, Terashima T, Shibauchi T, Matsuda Y, Chainani A and Shin S 2011 *Science* **332** 564
- [207] Zhang Y, Ye Z R, Ge Q Q, Chen F, Jiang J, Xu M, Xie B P and Feng D L 2012 *Nat. Phys.* **8** 371
- [208] Diao Z, Campanini D, Fang L, Kwok W K, Welp U and Rydh A 2016 *Phys. Rev. B* **93** 014509
- [209] Kasahara S, Watashige T, Hanaguri T, Kohsaka Y, Yamashita T, Shimoyama Y, Mizukami Y, Endo R, Ikeda H, Aoyama K, Terashima T, Uji S, Wolf T, von Löhneysen H, Shibauchi T and Matsuda Y 2014 *Proc. Natl Acad. Sci.* **111** 16309
- [210] Thomale R, Platt C, Hu J, Honerkamp C and Bernevig B A 2009 *Phys. Rev. B* **80** 180505
- [211] Thomale R, Platt C, Hanke W, Hu J and Bernevig B A 2011 *Phys. Rev. Lett.* **107** 117001
- [212] Evtushinsky D V, Inosov D S, Zabolotnyy V B, Koitzsch A, Knupfer M, Büchner B, Viazovska M S, Sun G L, Hinkov V, Boris A V, Lin C T, Keimer B, Varykhalov A, Kordyuk A A and Borisenko S V 2009 *Phys. Rev. B* **79** 054517
- [213] Tanatar M A, Ni N, Martin C, Gordon R T, Kim H, Kogan V G, Samolyuk G D, Bud'ko S L, Canfield P C and Prozorov R 2009 *Phys. Rev. B* **79** 094507
- [214] Tanatar M A, Ni N, Thaler A, Bud'ko S L, Canfield P C and Prozorov R 2010 *Phys. Rev. B* **82** 134528
- [215] Hirschfeld P 2009 *J. Phys.* **2** 100
- [216] Muschler B 2012 Carrier dynamics of $\text{Ba}(\text{Fe}_{1-x}\text{Co}_x)_2\text{As}_2$ as a function of doping *PhD Thesis* (Technical University Munich)
- [217] Tanatar M A, Reid J P, Shakeripour H, Luo X G, Doiron-Leyraud N, Ni N, Bud'ko S L, Canfield P C, Prozorov R and Taillefer L 2010 *Phys. Rev. Lett.* **104** 067002

- [218] Cea T, Castellani C and Benfatto L 2016 *Phys. Rev. B* **93** 180507
- [219] Boeri L, Dolgov O V and Golubov A A 2008 *Phys. Rev. Lett.* **101** 026403
- [220] Liu C, Palczewski A D, Dhaka R S, Kondo T, Fernandes R M, Mun E D, Hodovanets H, Thaler A N, Schmalian J, Bud'ko S L, Canfield P C and Kaminski A 2011 *Phys. Rev. B* **84** 020509
- [221] Ge Q Q, Ye Z R, Xu M, Zhang Y, Jiang J, Xie B P, Song Y, Zhang C L, Dai P and Feng D L 2013 *Phys. Rev. X* **3** 011020
- [222] Colombier E, Bud'ko S L, Ni N and Canfield P C 2009 *Phys. Rev. B* **79** 224518
- [223] Analytis J G, Kuo H H, McDonald R D, Wartenbe M, Rourke P M C, Hussey N E and Fisher I R 2014 *Nat. Phys.* **10** 194
- [224] Xu N, Richard P, Shi X, van Roekeghem A, Qian T, Razzoli E, Rienks E, Chen G F, Ieki E, Nakayama K, Sato T, Takahashi T, Shi M and Ding H 2013 *Phys. Rev. B* **88** 220508
- [225] Maier T A, Graser S, Scalapino D J and Hirschfeld P J 2009 *Phys. Rev. B* **79** 224510
- [226] Chubukov A V, Efremov D V and Eremin I 2008 *Phys. Rev. B* **78** 134512
- [227] Platt C, Hanke W and Thomale R 2014 *Adv. Phys.* **62** 453–562
- [228] Hirschfeld P J, Altenfeld D, Eremin I and Mazin I I 2015 *Phys. Rev. B* **92** 184513
- [229] Böker J, Volkov P A, Hirschfeld P J and Eremin I 2019 *New J. Phys.* **21** 083021
- [230] Böhmer A E and Meingast C 2016 *Compt. Rendus Phys.* **17** 90
- [231] Chu J H, Kuo H H, Analytis J G and Fisher I R 2012 *Science* **337** 710–2
- [232] Martiny J H J, Kreisel A, Hirschfeld P J and Andersen B M 2017 *Phys. Rev. B* **95** 184507
- [233] Marra P, van den Brink J and Sykora S 2016 *Sci. Rep.* **6** 25386

Phonon anomalies and magnetic excitations in BaFe₂Se₂O

Feng Jin,¹ Nenad Lazarević,² Changle Liu,³ Jianting Ji,⁴ Yimeng Wang,¹ Shuna He,¹ Hechang Lei,¹ Cedimir Petrovic,⁵ Rong Yu,¹ Zoran V. Popović,^{2,6} and Qingming Zhang^{4,7,*}

¹*Department of Physics and Beijing Key Laboratory of Opto-electronic Functional Materials & Micro-nano Devices, Renmin University of China, Beijing 100872, China*

²*Center for Solid State Physics and New Materials, Institute of Physics Belgrade, University of Belgrade, Pregrevica 118, 11080 Belgrade, Serbia*

³*State Key Laboratory of Surface Physics and Department of Physics, Fudan University, Shanghai 200433, China*

⁴*Beijing National Laboratory for Condensed Matter Physics, Institute of Physics, Chinese Academy of Sciences, Beijing 100190, China*

⁵*Condensed Matter Physics and Materials Science Department, Brookhaven National Laboratory, Upton, New York 11973-5000, USA*

⁶*Serbian Academy of Sciences and Arts, Knez Mihailova 35, Belgrade 11000, Serbia*

⁷*School of Physical Science and Technology, Lanzhou University, Lanzhou 730000, China*



(Received 6 March 2019; revised manuscript received 4 April 2019; published 22 April 2019)

We report a temperature- and magnetic-field-dependent Raman-scattering study of the spin-ladder compound BaFe₂Se₂O. Temperature evolution of the B_{1g} mode self-energies revealed anomalous behavior at about 100 and 240 K with strong temperature-dependent Fano asymmetry. Furthermore, the A_g modes integrated intensity exhibits an additional change in tendency at about 50 K. All the observed anomalies can be traced back to spin-phonon interaction contributions as well as multiple magnetic phase transitions present in BaFe₂Se₂O also detected in the Raman continuum induced by the spin fluctuations. Moreover, the absence of magnetic-field dependence of the magnetic mode observed at 436 cm⁻¹ and the small linewidth and high intensity are different from the magnetic modes at about 650 cm⁻¹. This suggests a two-magnon continuum and a two-magnon bound state resonance for this mode.

DOI: [10.1103/PhysRevB.99.144419](https://doi.org/10.1103/PhysRevB.99.144419)

I. INTRODUCTION

Quantum spin ladders have attracted much interest because of their fascinating properties and their possible relevance to the phase diagram of high-temperature superconducting cuprates [1–4]. The ground-state properties and the quasiparticle spectrum of the two-leg spin ladder have been studied theoretically [5–9] and experimentally [10–14]. Generally these systems may host various competing magnetic phases that are in close proximity.

Raman scattering offers a unique and powerful tool for probing lattice, spin, and charge excitations as well as interplay between them [4]. In the undoped spin ladder compound La₆Ca₈Cu₂₄O₄₁, the ladders contribute to a very broad triplet Raman line shape whose position is slightly different for leg-leg and rung-rung polarizations [15] in accordance with theoretical models [16]. However, in the spin-ladder and charge-ordered compound Sr₁₄Cu₂₄O₄₁, only a particularly sharp peak is observed at the same frequency for both polarizations [12,15]. Here, the spin-ladder (antiferromagnetic dimer) structure magnon related modes appear in the form of singularities of one-dimensional density of two-magnon states [11].

The iron-based compound BaFe₂Se₂O is an experimental realization of a two-leg ladder structure [17–19]. In this compound, all iron ions are in the Fe²⁺ oxidation state with

a high spin $S = 2$. The Fe₂Se₂O planes containing weakly coupled ladders are stacked along the c crystallographic axis. The ladder legs and rungs are along the b and a crystallographic axis, respectively. The basic magnetic properties of BaFe₂Se₂O have been characterized by magnetic susceptibility and specific-heat measurements [17,18]. The magnetic susceptibility shows a broad maximum at $T_{\max} \approx 450$ K and three successive magnetic phase transitions at $T \approx 240$, 115, and 43 K with T_{\max} explained as due to the short-range correlation of the local moments [17] and the three magnetic phase transitions explained as either due to the antiferromagnetic phase transition (240 K) or due to the formation of spin-singlet dimers (115 and 43 K) [18]. Surprisingly, the specific-heat measurements indicate that the magnetic entropy up to 300 K is much smaller than the expected value. Local-spin-density-approximation calculations [17] suggest that the interaction along the rungs J is more than three times stronger than the interladder interaction J' , whereas the interaction along the legs J'' can be neglected. A lattice dynamics study of BaFe₂Se₂O was recently reported by Popović *et al.* [19]. They also observed a magnetic excitation related structure in the form of a magnon continuum with peaks corresponding to the singularities in the one-dimensional density of magnon states. In order to clarify the unusually large intensity of the lower-energy (magnon) peak and the origin of the B_{1g} modes line-shape asymmetry, a systematic Raman study, particularly in magnetic fields, is highly required.

In this paper, we report temperature- and field-dependent Raman-scattering measurements on BaFe₂Se₂O. The

*Corresponding author: qmzhang@ruc.edu.cn

temperature-dependent Raman spectra indicate the absence of a structural phase transition between 10 and 300 K, consistent with a moderate spin-phonon coupling. The Raman continuum observed only in the parallel polarization suggests strong spin fluctuations, and allows us to identify magnetic phase transitions at about 50, 100, and 240 K. The intensity of the sharp magnetic mode at 436 cm^{-1} exhibits a strong nonmonotonic field-dependent behavior with no observable energy shift with external magnetic fields up to 9 T. It is interpreted in terms of the two-magnon continuum and a two-magnon bound state resonance. The present study provides the fundamental lattice and spin dynamics information on $\text{BaFe}_2\text{Se}_2\text{O}$ and deepens the understanding of magnetic excitations in low-dimensional spin systems.

II. EXPERIMENTS

The $\text{BaFe}_2\text{Se}_2\text{O}$ single crystals used in this study were grown using the self-flux method. The details of crystal growth can be found elsewhere [18]. The average stoichiometry was checked using energy-dispersive x-ray spectroscopy (EDS; Oxford X-Max 50). The average atomic ratios determined from EDS are $\text{Ba:Fe:Se} = 1.0:1.9(2):2.0(2)$, close to the ratio of stoichiometric $\text{BaFe}_2\text{Se}_2\text{O}$. The presence of oxygen was confirmed for $\text{BaFe}_2\text{Se}_2\text{O}$, but the exact amount could not be quantified because of experimental limitations.

Freshly cleaved samples of (001) orientation were transferred into a UHV cryostat with a vacuum of better than 10^{-8} mbar. Temperature-dependent Raman spectra were collected with a Jobin Yvon LabRam HR800 spectrometer equipped with a volume Bragg grating low-wave-number suite, a liquid-nitrogen-cooled back-illuminated charge-coupled device detector, and a 633-nm laser (Melles Griot) with $\Gamma_\sigma < 0.1 \text{ cm}^{-1}$. The laser was focused into a spot of $\sim 5 \mu\text{m}$ in diameter on the sample surface, with a power $< 100 \mu\text{W}$, to avoid overheating. Magnetic-field-dependent Raman spectra were collected with a Jobin Yvon T64000 spectrometer also equipped with a liquid-nitrogen-cooled back-illuminated CCD. A 532-nm diode-pumped solid-state laser (Torus 532; Laser Quantum) was used as an excitation source. The laser was focused onto the samples with a spot size of $5\text{--}10 \mu\text{m}$ in diameter. The laser power was maintained at a level of $300 \mu\text{W}$ and monitored with a power meter (Coherent Inc.). Magnetic fields were generated up to 9 T using a superconducting magnet (Cryomagnetics) that has a room-temperature bore that is suitable for a microscope lens. The magnetic-field direction was perpendicular to the (001) plane of the sample.

In this paper, the Porto notation $i(jk)l$ is used for the scattering geometry, where i and l denote the direction and j and k the polarization of the incident and scattered light, respectively, and u stands for unpolarized light.

III. RESULTS AND DISCUSSION

A. Lattice dynamics and spin-phonon coupling

$\text{BaFe}_2\text{Se}_2\text{O}$ crystallizes in the orthorhombic crystal structure, described with space group $Pmmm$, with Ba and O atoms having C_{2v} site symmetry, whereas Fe and Se atoms have C_s site symmetry [19]. The symmetry analysis yields a total of 18 Raman-active modes $\Gamma_{\text{Raman}} = 6A_g + 2B_{1g} + 6B_{2g} +$

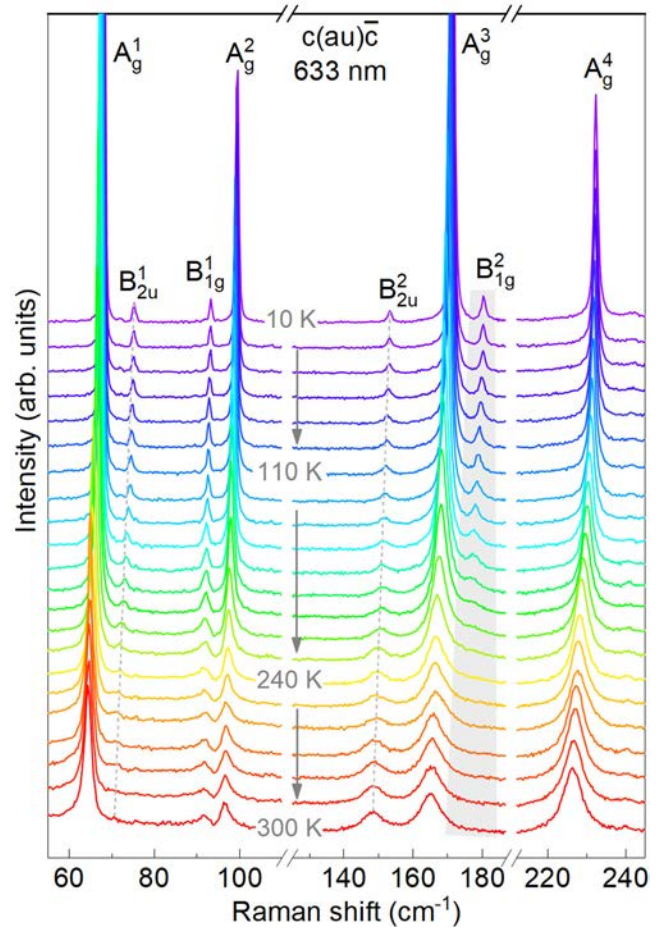


FIG. 1. Identification and temperature dependence of phonon modes in $\text{BaFe}_2\text{Se}_2\text{O}$. No change of crystal structure fingerprint was observed in the phonon spectra down to 10 K.

$4B_{3g}$, out of which, according to the Raman tensors below and the selection rules, only eight ($6A_g + 2B_{1g}$) are observable for our scattering geometry.

$$A_g = \begin{pmatrix} a & 0 & 0 \\ 0 & b & 0 \\ 0 & 0 & c \end{pmatrix}, \quad B_{1g} = \begin{pmatrix} 0 & d & 0 \\ d & 0 & 0 \\ 0 & 0 & 0 \end{pmatrix},$$

$$B_{2g} = \begin{pmatrix} 0 & 0 & e \\ 0 & 0 & 0 \\ e & 0 & 0 \end{pmatrix}, \quad B_{3g} = \begin{pmatrix} 0 & 0 & 0 \\ 0 & 0 & f \\ 0 & f & 0 \end{pmatrix}.$$

Figure 1 shows the temperature evolution of the $\text{BaFe}_2\text{Se}_2\text{O}$ Raman spectra in the temperature range between 10 and 300 K, in which eight phonon modes are observed. According to the lattice dynamical calculations [19], four A_g and two B_{1g} modes can be well assigned, as shown in Fig. 1. In addition to the A_g and B_{1g} symmetry modes, two peaks at about 75.2 and 153.3 cm^{-1} were also observed, which we previously attributed to new phonon modes due to the possible change of crystal symmetry accompanying the magnetic phase transition at $T_N = 240 \text{ K}$ [19]. As can be seen in Fig. 1, these peaks are also observable in our data even above T_N , indicating different origin. Energies are consistent with B_{2u}^1 and B_{2u}^2 infrared-active phonon modes, theoretically

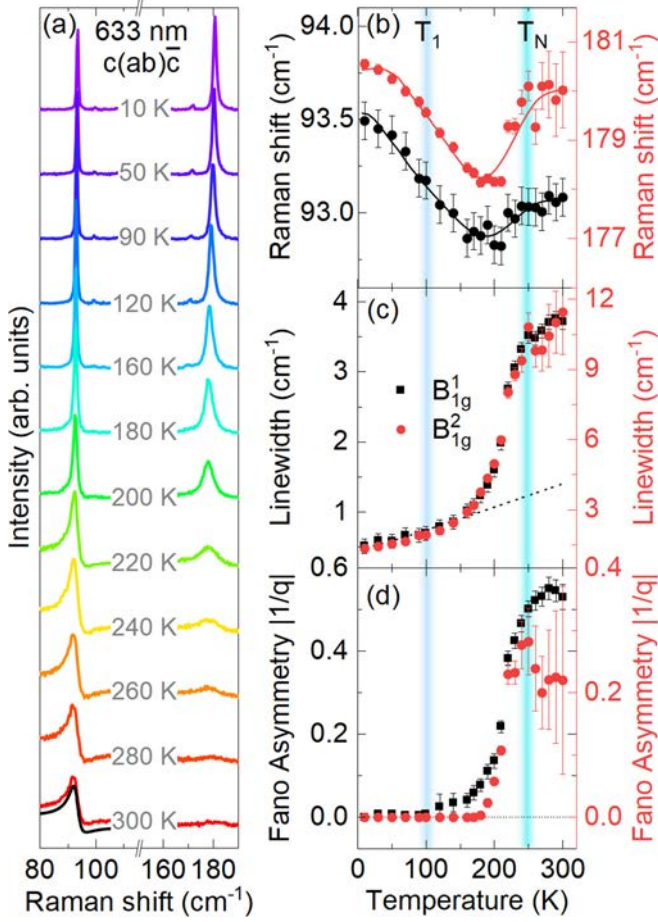


FIG. 2. Anomalies of B_{1g} modes induced by spin-lattice coupling. (a) Temperature dependence of Raman spectra for the $c(ab)\bar{c}$ polarization configuration, in which only the B_{1g} modes can be observed. The solid black line is a fit to a Fano line shape. Temperature dependence of the (b) frequency shift, (c) linewidth, and (d) Fano asymmetry parameters $|1/q|$ of B_{1g} (left axis, black) and B_{2g} (right axis, red) modes. The solid lines in (b) represent a fit to Eq. (1) and the dotted line in (c) represents the behavior expected from anharmonicity.

predicted by density functional theory calculations [19], and we assign them accordingly. Their observability in Raman data may stem from the release of symmetry selection rule by the structural imperfections. In our previous paper [18], Mössbauer data suggested oxygen deficiency, i.e., O_{1-x} composition for $BaFe_2Se_2O$. This might be the source of structural imperfections.

First, we focus on B_{1g} phonon modes, which display a pronounced asymmetry at high temperatures ($T > T_N$) that is suppressed at low temperatures ($T \ll T_N$), as can be seen in Fig. 2(a). Having in mind small instrumental broadening, the analysis of the line shape was preformed by using Fano function alone [20,21]: $I(\omega) = I_0(q + \varepsilon)^2/(1 + \varepsilon^2)$, where $\varepsilon = (\omega - \omega_0)/\Gamma$, ω_0 is the bare phonon frequency, Γ is the linewidth, and q is the asymmetry parameter [22]. Frequency shift, linewidth, and Fano asymmetry parameter $|1/q|$ for both modes as a function of temperature are presented in Figs. 2(b), 2(c), and 2(d), respectively. Whereas they exhibit very similar

temperature dependence, upon heating from 10 K a small deviation from the “standard” anharmonic type of behavior can be noticed at about $T_1 = 100$ K accompanied by the appearance of the line-shape asymmetry. Further heating results in a significant renormalization of the phonon self-energies around T_N with the Fano asymmetry parameters reaching maximum value in the same temperature region.

The pronounced Fano asymmetry observed for the B_{1g} modes above T_N [Fig. 2(d)] indicates strong coupling to a continuum of excitations. Here we attribute the continuum to the magnetic scattering stemming from the spin fluctuation, which will be further discussed below. In comparison, an electronic mechanism for the continuum is unlikely as $BaFe_2Se_2O$ is electrically insulating with a transport gap of 1.86 eV [17]. According to the lattice dynamical calculations [19], the B_{1g} modes are mainly due to the vibration of Fe and Se atoms along the b axis which mediate the magnetic interaction. Therefore, one could expect B_{1g} modes to couple to the magnetic scattering.

The coupling of B_{1g} modes to the spin system is also reflected in the abnormal behaviors of their linewidth. To demonstrate this, we have included in Fig. 2(c) plots of the behavior expected from anharmonicity, $\Gamma(T) = \Gamma_0[1 + 2/(e^{\hbar\omega/2k_B T} - 1)]$. The fit strongly deviates already around 170 K, implying an additional relaxation mechanism which we ascribe to spin-phonon coupling. Such coupling is very pronounced in low-dimensional spin dimer systems, as well as in two- and three-dimensional frustrated spin systems [23–25].

In order to estimate the spin-phonon coupling constant in $BaFe_2Se_2O$, we may approximate phonon frequency temperature dependence as

$$\omega(T) = \omega(0) - C \left(1 + \frac{2}{e^x - 1} \right) + \lambda \langle S_i S_j \rangle, \quad (1)$$

where $\omega(0)$ is the harmonic frequency of an optical mode at zero temperature, $x = \hbar\omega(0)/2k_B T$, λ is the spin-phonon coupling constant, $\langle S_i S_j \rangle$ represents the spin-spin correlation function, and C is an anharmonic constant. The second term in Eq. (1) describes the anharmonic phonon contribution based on symmetrical optical phonon decay into acoustic phonons [26], whereas the third term represents the contribution from the spin-phonon coupling based on the Baltensperger and Helman model [27,28]. If we take into account only the nearest-neighbor interactions, the spin-spin correlation function $\langle S_i S_j \rangle_\chi$ can be written as [25]

$$\langle S_i S_j \rangle_\chi = \frac{k_B T \chi_m(T)}{N_A g^2 \mu_B^2} - \frac{S(S+1)}{3}, \quad (2)$$

where $g = 2$, $S = 2$, and the magnetic susceptibility $\chi_m(T)$ is given in Ref. [18]. We can now analyze the B_{1g} symmetry modes frequency temperature dependence within Eq. (1) [see solid lines in Fig. 2(b)]. This yields the spin-phonon coupling constants $\lambda(B_{1g}^1) = 1.8 \text{ cm}^{-1}$, $\lambda(B_{1g}^2) = 12.8 \text{ cm}^{-1}$, and the anharmonic constant $C(B_{1g}^1) = 0.33 \text{ cm}^{-1}$, $C(B_{1g}^2) = 4.76 \text{ cm}^{-1}$. The individual contribution due to anharmonic and spin-phonon coupling can be found in Fig. 5 in Appendix A. Obtained spin-phonon coupling constants are smaller than those in the spin-Peierls system $CuGeO_3$, where spin-phonon

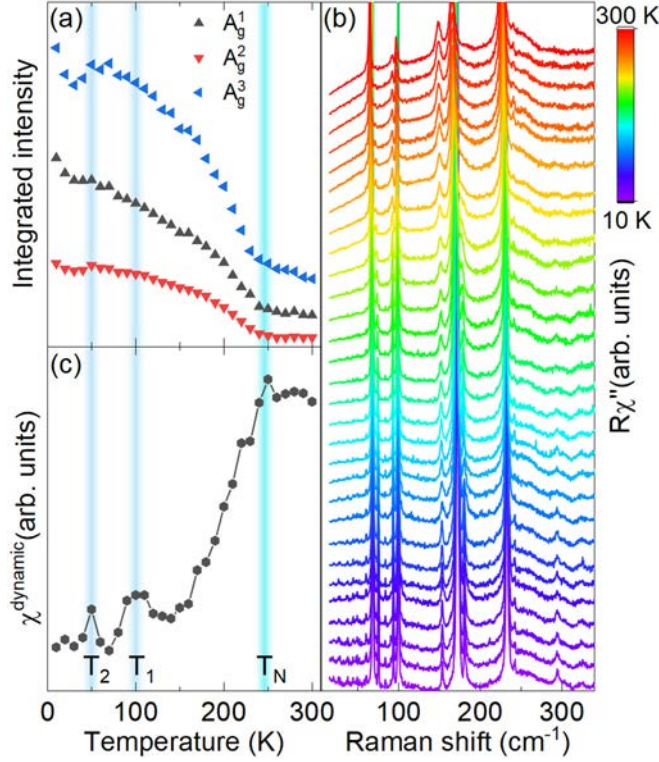


FIG. 3. (a) Integrated intensity of the A_g^1 , A_g^2 , and A_g^3 symmetry modes as a function of temperature. (b) Temperature evolution of Raman susceptibility data for BaFe₂Se₂O obtained in parallel scattering configuration. The pronounced Raman continuum evolution is observable only in parallel [i.e., (aa) or (bb)] and absent in cross polarization configurations [i.e., (ab) or (ba)] (not shown). (c) Temperature dependence of dynamical susceptibility $\chi^{\text{dynamic}}(T)$ obtained from the Raman data.

coupling constants of $\lambda_{103} = -10 \text{ cm}^{-1}$, $\lambda_{215} = 40 \text{ cm}^{-1}$, $\lambda_{366} = -21 \text{ cm}^{-1}$, and $\lambda_{812} = -8 \text{ cm}^{-1}$ were found [29]. Thus moderate spin-phonon coupling constants in BaFe₂Se₂O may account for the absence of a structural phase transition at the magnetic phase transition.

Now we turn our attention to the A_g symmetry modes. As can be seen from Fig. 3(a), the integrated intensity temperature dependence of the analyzed A_g modes exhibits clear discontinuity at T_N . In addition, another change in tendency has been observed at about $T_2 = 50 \text{ K}$.

Whereas the phonon anomalies at T_N can be directly traced back to the spin dynamics, the origin of the phonon anomalies at T_1 and T_2 is not clear. To clarify this, we analyze the Raman continuum that nonmonotonically develops in the A_{1g} channel with temperature [see Fig. 3(a)], as expected for the (quasi-) one-dimensional spin systems [30–32]. Directly from the Raman data, dynamic Raman susceptibility [33] can be calculated using the Kramers-Kronig relation $\chi^{\text{dynamic}} = \lim_{\omega \rightarrow 0} \chi(q=0, \omega) \propto \int_0^\infty \frac{\chi''}{\omega} d\omega$. Since we do not attempt to quantitatively analyze the spin-fluctuation contributions, which falls beyond the scope of our work, but to pinpoint possible magnetic phase transition, we approximate $\chi^{\text{dynamic}}(T)$ as an integral of the Raman conductivity data after excluding the contributions from phonons. As can be seen in Fig. 3(c),

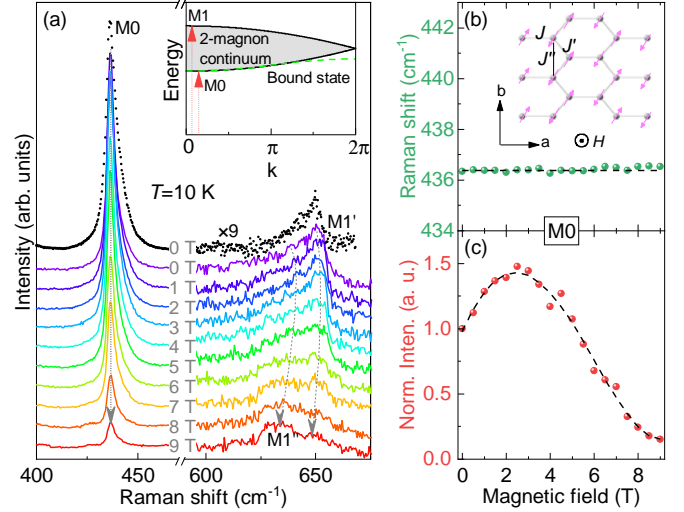


FIG. 4. Identification of magnetic excitations in BaFe₂Se₂O. (a) Field-dependent Raman spectra, measured at 10 K with 532-nm laser line (solid lines). The spectrum (dotted line) collected at 0 T with a 633-nm laser are also shown for comparison. Inset: Schematic spin excitation spectrum of BaFe₂Se₂O. The green dashed line represents a possible two-magnon bound state. Field dependence of the (b) energy and (c) intensity of the $M0$ mode. Inset of (b): Schematic representation of the periodic magnetic structure in the (ab) plane. J represents Fe-O-Fe antiferromagnetic (AFM) exchange interaction along the rungs; J' is the interladder Fe-Se-Fe AFM exchange interaction. J'' is the ferromagnetic Fe-Se-Fe exchange interaction along the ladder legs and can be neglected.

$\chi^{\text{dynamic}}(T)$ strongly increases upon approaching T_N after which it saturates in the paramagnetic phase where the spins are not correlated. At low temperatures it develops two peak-like features coinciding with observed anomalies in the lattice dynamic thus indicating their spin dynamics related origin. Furthermore, $\chi^{\text{dynamic}}(T)$ exhibits good agreement with the previously reported magnetic susceptibility data [18], indicating additional magnetic phase transitions in BaFe₂Se₂O at low temperatures.

B. Two-magnon Raman scattering

The two asymmetric peaks at 436 and 653 cm⁻¹ (see Fig. 4) have been reported before and assigned as a magnetic excitation related structure due to their special polarization and temperature-dependent characterizations [19]. However, the extremely high intensity of the 436 cm⁻¹ ($M0$) mode suggests an additional mechanism that comes into play, other than those manifested with the 653 cm⁻¹ mode. In particular, compared with the linewidth of two-magnon modes in other two-dimensional (2D) spin systems, the $M0$ linewidth of only $\sim 5 \text{ cm}^{-1}$ at 15 K is quite unusual for a 2D spin-ladder system. For example, the linewidth of the two-magnon mode is $\sim 800 \text{ cm}^{-1}$ for Sr₂Cu₂O₂Cl₂ [34], whereas it is $\sim 500 \text{ cm}^{-1}$ in La₆Ca₈Cu₂₄O₄₁ [13]. To the best of our knowledge, the sharpest two-magnon mode so far was found in CaV₂O₅ with a width of more than 50 cm⁻¹ [10], still one order of magnitude larger than that in BaFe₂Se₂O.

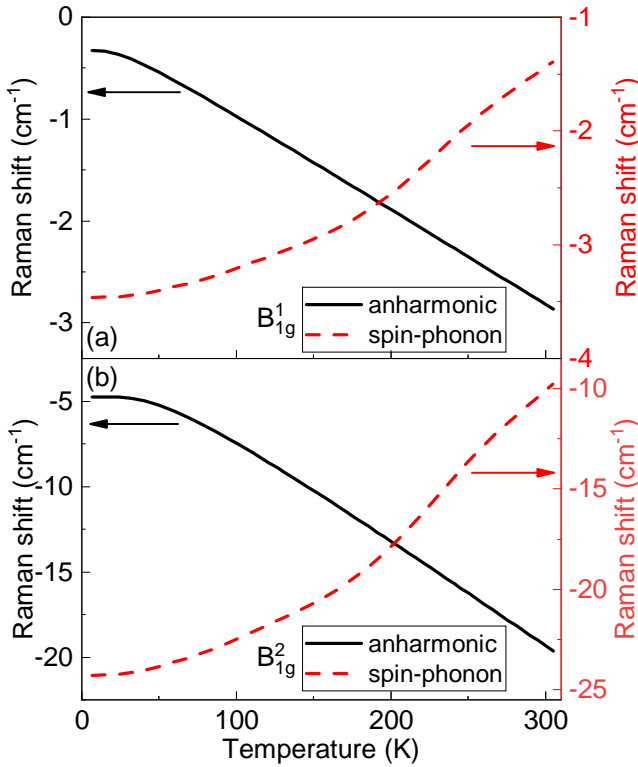


FIG. 5. Anharmonic (solid line) and spin-phonon (dashed line) contribution to the temperature dependence of the energy of (a) B_{1g} and (b) B_{2g} phonon modes obtained by fitting Eq. (1) to the experimental data.

To clarify the origin of the unusual $M0$ mode, the magnetic-field- and temperature-dependent Raman experiments have been performed on $\text{BaFe}_2\text{Se}_2\text{O}$ crystals [Fig. 4(a) and Fig. 6 in Appendix B]. The field dependence of the energy and intensity of the $M0$ mode are summarized in Figs. 4(b) and 4(c). It can be seen that both the $M0$ energy and the linewidth are nearly field independent, whereas the intensity exhibits a strong nonmonotonic field dependence. The intensity slightly increases with magnetic fields below 3 T, but quickly drops down above 3 T and almost vanishes for $B = 9$ T. A closer inspection of the 653-cm^{-1} peak magnetic-field-dependent spectra reveals its two-peak nature ($M1'$ and $M1''$; see Fig. 4). Both peaks harden up to 3 T after which they soften. Whereas the $M1'$ intensity follows the $M0$ mode behavior, $M1''$ experiences a constant gain of intensity. The strong field dependence of $M0$, $M1'$, and $M1''$ as well as their special polarization and temperature-dependent characterizations [19] confirms that these modes are indeed magnon related, but not due to some structural imperfections.

In general, several theoretical scenarios can be considered to account for the strength and sharpness of the magnon modes in the 2D system: (i) backfolding of the triplet dispersion due to charge ordering [13]; (ii) large anisotropy of the magnetic exchanges along rung and leg directions [35]; and (iii) the resonance between the two-magnon continuum and a two-magnon bound state [16,36]. In $\text{BaFe}_2\text{Se}_2\text{O}$, the origin of dispersion backfolding can be excluded because of its electrically insulating nature. Although the large anisotropy between J'' and J explains the observation of the $M0$ mode

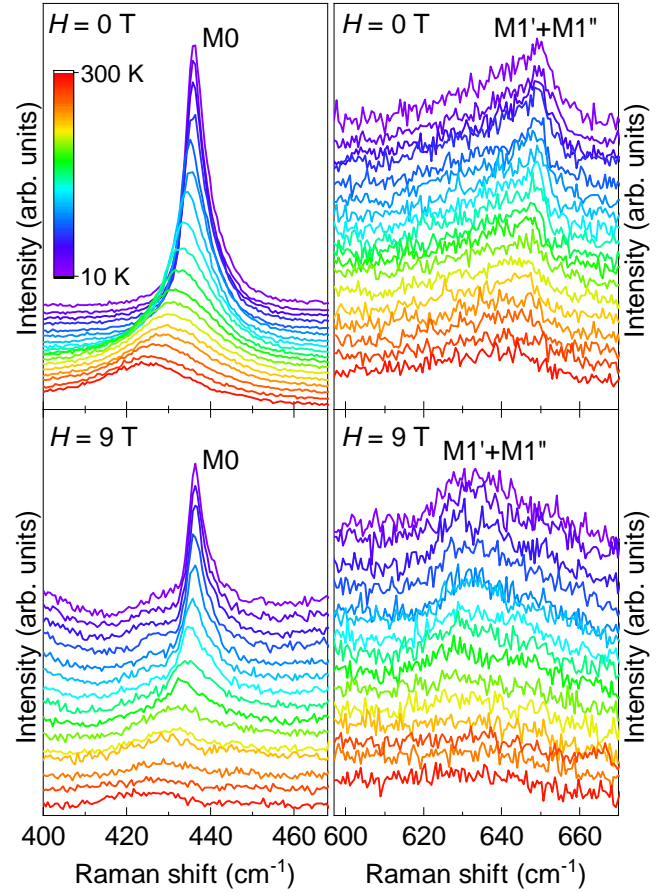


FIG. 6. Temperature-dependent spectra of the $M0$, $M1'$, and $M1''$ modes at 0 and 9 T.

at the given energy, it alone cannot account for the intensity and its magnetic-field dependence. This kind of behavior can be observed in the presence of the resonance between the two-magnon continuum and a two-magnon bound state.

In low-dimensional antiferromagnets, a strong magnon-magnon interaction induces a magnetic bound state [31,37–40] that merges with the two-magnon continuum at zero momentum (schematically shown in Fig. 4). This allows a resonance at the bottom of the continuum and contributes to the asymmetric line shape [36]. Such a resonance can well explain the strength, sharpness, and asymmetry of the $M0$ mode. The field dependence of the $M0$ mode intensity provides further support for the picture. External magnetic fields usually lead to a spin canting or even a spin flop/flip transition [41] and consequently modulate the magnon excitation spectrum. In $\text{BaFe}_2\text{Se}_2\text{O}$, the modulation of the magnon excitation spectrum is evidenced by the energy shift of the $M1'$ and $M1''$ modes (Fig. 4). A quantitative understanding of the $M0$, $M1'$, and $M1''$ modes magnetic-field dependence requires more theoretical work in the future and goes beyond the scope of this paper.

IV. SUMMARY

In summary, a $\text{BaFe}_2\text{Se}_2\text{O}$ temperature- and field-dependent Raman-scattering study has been performed. The

temperature evolution of the Raman-active modes indicates that there is no structural phase transition accompanying the magnetic phase transitions. Observed anomalies in the phonon spectra can be traced back to moderate spin-phonon interaction contributions as well as multiple magnetic phase transitions present in $\text{BaFe}_2\text{Se}_2\text{O}$ also detected in the Raman continuum induced by the spin fluctuations. The anomalous intensity of the $M0$ peak is attributed to the contribution from the two-magnon continuum and a two-magnon bound state resonance. The present study provides the fundamental lattice and spin dynamics information on $\text{BaFe}_2\text{Se}_2\text{O}$ and is of significance for the understanding of magnetic excitations in low-dimensional spin systems.

ACKNOWLEDGMENTS

This work was supported by the National Natural Science Foundation of China, the Ministry of Science and Technology of China, the Fundamental Research Funds for the Central Universities, the Research Funds of Renmin University of China and Serbian Ministry of Education, Science and Technological Development under Project III45018. The work at Brookhaven National Laboratory was supported by the

U.S. DOE under Contract No. DE-SC0012704 (material synthesis).

APPENDIX A: ANHARMONIC AND SPIN-PHONON CONTRIBUTIONS TO PHONON MODE ENERGIES

In this Appendix, we show the individual contribution of anharmonic and spin-phonon terms to the temperature dependence of the energy of the two B1g modes (Fig. 5), which are obtained by fitting Eq. (1) to the experimental data.

APPENDIX B: TEMPERATURE- AND FIELD-DEPENDENT RAMAN SPECTRA

To explore the origin of the magnetic scattering modes, we performed temperature-dependent Raman experiments and the collected spectra of the $M0$ $M1'$ and $M1''$ modes at 0 and 9 T are shown in Fig. 6. One can see that these modes exhibit distinctive temperature dependent behaviors, namely, a characteristic decrease in energy and intensity, and an increase in linewidth, with increasing temperature, reflecting the renormalization of magnon energies and lifetimes by thermally excited carriers.

-
- [1] P. W. Anderson, *Science* **235**, 1196 (1987).
 - [2] E. Dagotto and T. M. Rice, *Science* **271**, 618 (1996).
 - [3] E. Dagotto, *Rep. Prog. Phys.* **62**, 1525 (1999).
 - [4] P. Lemmens, G. Güntherodt, and C. Gros, *Phys. Rep.* **375**, 1 (2003).
 - [5] T. Barnes, E. Dagotto, J. Riera, and E. S. Swanson, *Phys. Rev. B* **47**, 3196 (1993).
 - [6] T. Barnes and J. Riera, *Phys. Rev. B* **50**, 6817 (1994).
 - [7] S. R. White, R. M. Noack, and D. J. Scalapino, *Phys. Rev. Lett.* **73**, 886 (1994).
 - [8] S. Gopalan, T. M. Rice, and M. Sigrist, *Phys. Rev. B* **49**, 8901 (1994).
 - [9] D. G. Shelton, A. A. Nersisyan, and A. M. Tsvelik, *Phys. Rev. B* **53**, 8521 (1996).
 - [10] M. J. Konstantinović, Z. V. Popović, M. Isobe, and Y. Ueda, *Phys. Rev. B* **61**, 15185 (2000).
 - [11] Z. V. Popović, M. J. Konstantinović, V. A. Ivanov, O. P. Khuong, R. Gajić, A. Vietkin, and V. V. Moshchalkov, *Phys. Rev. B* **62**, 4963 (2000).
 - [12] A. Gozar, G. Blumberg, B. S. Dennis, B. S. Shastry, N. Motoyama, H. Eisaki, and S. Uchida, *Phys. Rev. Lett.* **87**, 197202 (2001).
 - [13] K. P. Schmidt, C. Knetter, M. Grüninger, and G. S. Uhrig, *Phys. Rev. Lett.* **90**, 167201 (2003).
 - [14] A. Gößling, U. Kuhlmann, C. Thomsen, A. Löffert, C. Gross, and W. Assmus, *Phys. Rev. B* **67**, 052403 (2003).
 - [15] S. Sugai and M. Suzuki, *Phys. Status Solidi B* **215**, 653 (1999).
 - [16] K. P. Schmidt, C. Knetter, and G. S. Uhrig, *Europhys. Lett.* **56**, 877 (2001).
 - [17] F. Han, X. Wan, B. Shen, and H.-H. Wen, *Phys. Rev. B* **86**, 014411 (2012).
 - [18] H. Lei, H. Ryu, V. Ivanovski, J. B. Warren, A. I. Frenkel, B. Cekic, W.-G. Yin, and C. Petrovic, *Phys. Rev. B* **86**, 195133 (2012).
 - [19] Z. V. Popović, M. Šćepanović, N. Lazarević, M. M. Radonjić, D. Tanasković, H. Lei, and C. Petrovic, *Phys. Rev. B* **89**, 014301 (2014).
 - [20] A. Baum, A. Milosavljević, N. Lazarević, M. M. Radonjić, B. Nikolić, M. Mitschek, Z. I. Maranloo, M. Šćepanović, M. Grujić-Brojčin, N. Stojilović, M. Opel, A. Wang, C. Petrovic, Z. V. Popović, and R. Hackl, *Phys. Rev. B* **97**, 054306 (2018).
 - [21] A. Milosavljević, A. Šolajić, J. Pešić, Y. Liu, C. Petrovic, N. Lazarević, and Z. V. Popović, *Phys. Rev. B* **98**, 104306 (2018).
 - [22] U. Fano, *Phys. Rev.* **124**, 1866 (1961).
 - [23] M. Braden, B. Hennion, W. Reichardt, G. Dhalenne, and A. Revcolevschi, *Phys. Rev. Lett.* **80**, 3634 (1998).
 - [24] K.-Y. Choi, Y. G. Pashkevich, K. V. Lamonova, H. Kageyama, Y. Ueda, and P. Lemmens, *Phys. Rev. B* **68**, 104418 (2003).
 - [25] C. Kant, J. Deisenhofer, T. Rudolf, F. Mayr, F. Schrettle, A. Loidl, V. Gnezdilov, D. Wulferding, P. Lemmens, and V. Tsurkan, *Phys. Rev. B* **80**, 214417 (2009).
 - [26] J. Menéndez and M. Cardona, *Phys. Rev. B* **29**, 2051 (1984).
 - [27] W. Baltensperger and J. S. Helman, *Helv. Phys. Acta* **41**, 668 (1968).
 - [28] W. Baltensperger, *J. Appl. Phys.* **41**, 1052 (1970).
 - [29] R. Werner, C. Gros, and M. Braden, *Phys. Rev. B* **59**, 14356 (1999).
 - [30] T. Sekine, M. Jouanne, C. Julien, and M. Balkanski, *Phys. Rev. B* **42**, 8382 (1990).
 - [31] P. Lemmens, M. Grove, M. Fischer, G. Güntherodt, V. N. Kotov, H. Kageyama, K. Onizuka, and Y. Ueda, *Phys. Rev. Lett.* **85**, 2605 (2000).

- [32] K. Y. Choi, J. W. Hwang, P. Lemmens, D. Wulferding, G. J. Shu, and F. C. Chou, *Phys. Rev. Lett.* **110**, 117204 (2013).
- [33] A. Glamazda, P. Lemmens, S. H. Do, Y. S. Choi, and K. Y. Choi, *Nat. Commun.* **7**, 12286 (2016).
- [34] G. Blumberg, P. Abbamonte, M. V. Klein, W. C. Lee, D. M. Ginsberg, L. L. Miller, and A. Zibold, *Phys. Rev. B* **53**, R11930 (1996).
- [35] K. P. Schmidt, A. Gössling, U. Kuhlmann, C. Thomsen, A. Löffert, C. Gross, and W. Assmus, *Phys. Rev. B* **72**, 094419 (2005).
- [36] C. Jurecka, V. Grützun, A. Friedrich, and W. Brenig, *Eur. Phys. J. B* **21**, 469 (2001).
- [37] O. P. Sushkov and V. N. Kotov, *Phys. Rev. Lett.* **81**, 1941 (1998).
- [38] G. Bouzerar, A. P. Kampf, and G. I. Japaridze, *Phys. Rev. B* **58**, 3117 (1998).
- [39] M. Windt, M. Grüninger, T. Nunner, C. Knetter, K. P. Schmidt, G. S. Uhrig, T. Kopp, A. Freimuth, U. Ammerahl, B. Büchner, and A. Revcolevschi, *Phys. Rev. Lett.* **87**, 127002 (2001).
- [40] C. Knetter, K. P. Schmidt, M. Grüninger, and G. S. Uhrig, *Phys. Rev. Lett.* **87**, 167204 (2001).
- [41] S. Blundell, in *Magnetism in Condensed Matter* (Oxford University Press, New York, 2001).

Short-Range Order in VI_3

Sanja Djurdjić Mijin, A. M. Milinda Abeykoon, Andrijana Šolajić, Ana Milosavljević, Jelena Pešić, Yu Liu, Cedimir Petrovic, Zoran V. Popović, and Nenad Lazarević*

Cite This: <https://dx.doi.org/10.1021/acs.inorgchem.0c02060>

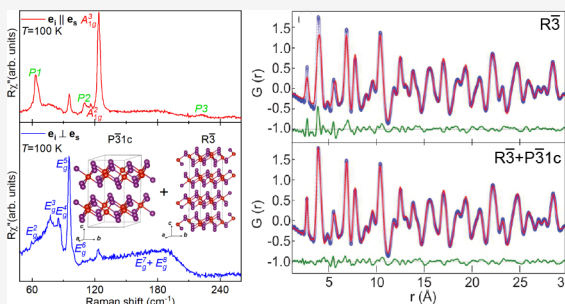
Read Online

ACCESS |

Metrics & More

Article Recommendations

ABSTRACT: We present a detailed investigation of the crystal structure of VI_3 , a two-dimensional van der Waals material of interest for studies of low-dimensional magnetism. As opposed to the average crystal structure that features $R\bar{3}$ symmetry of the unit cell, our Raman scattering and X-ray atomic pair distribution function analysis supported by density functional theory calculations point to the coexistence of short-range ordered $P\bar{3}1c$ and long-range ordered $R\bar{3}$ phases. The highest-intensity peak, A_{1g} , exhibits a moderate asymmetry that might be traced back to the spin–phonon interactions, as in the case of CrI_3 .



INTRODUCTION

A well-known family of transition metal trihalides (TMTs) MX_3 ($X = \text{Cr}, \text{B}, \text{or I}$) have received a great deal of attention due to potential existence of two-dimensional (2D) ferromagnetism,^{1–6} which has been confirmed in CrI_3 .^{7,8} The similar crystal structure and magnetic properties of CrI_3 and VI_3 fostered a belief that the same might be found in the latter. In fact, magnetization measurements revealed the 2D ferromagnetic nature of VI_3 with a Currie temperature (T_c) of around 50 K.^{9,10} Contrary to a layer-dependent ferromagnetism in CrI_3 ,¹¹ the first-principles calculations predict that ferromagnetism in VI_3 persists down to a single layer,⁹ making it a suitable candidate for engineering 2D spintronic devices. Resistivity measurements showed VI_3 is an insulator with an optical band gap of ~ 0.6 eV.^{9,12}

Whereas laboratory X-ray diffraction studies reported three possible high-temperature VI_3 unit cell symmetries,^{9,12–14} high-resolution synchrotron X-ray diffraction confirmed a rhombohedral $R\bar{3}$ space group.¹⁰ A very recently published Raman spectroscopy study indicated that the VI_3 crystal structure can be described within the C_{2h} point group.¹⁵ All results agree on the existence of a phase transition at a temperature of 79 K. However, the subtle¹² structural changes below 79 K are still under debate.

The long-range magnetic order in ultrathin 2D van der Waals (vdW) crystals stems from strong uniaxial anisotropy, in contrast to materials with isotropic exchange interactions where order parameters are forbidden.^{16–18} 2D vdW magnetic materials are of interest both as examples of exotic magnetic order¹⁹ and for potential applications in spintronic technology.^{2,4,20,21}

Atomically thin flakes of CrCl_3 have a magnetic transition temperature that is different from that of bulk crystals possibly

due to the different crystal structure of the monolayer and ultrathin crystals when compared to bulk.^{22,23} Similar observations were made on CrI_3 monolayers.^{22,24,25} It has been proposed²³ that the second anomaly in heat capacity in bulk CrCl_3 arises due to regions close to the surface that host a different crystal structure when compared to bulk;^{26,27} however, due to the substantial mass fraction detected in heat capacity measurements, this could also reflect differences between the short-range order and long-range crystallographic order of Bragg planes. The short-range order is determined by the space group that is energetically favorable for a monolayer or a few layers, whereas the long-range crystallographic order is established over large packing lengths.

In this paper, we present an experimental Raman scattering study of the bulk VI_3 high-temperature structure, supported by density functional theory (DFT) calculations and the X-ray atomic pair distribution function (PDF) analysis. The comparison between the Raman experiment and DFT calculations for each of the previously reported space groups suggested that the high-temperature lattice vibrations of bulk VI_3 are consistent with a $P\bar{3}1c$ trigonal structure. Nine ($2A_{1g} + 7E_g$) of 12 observed peaks were assigned on the basis of factor group analysis (FGA) and DFT calculations. The PDF analysis indicated the coexistence of two crystallographic phases at two different interatomic distances, short-range ordered $P\bar{3}1c$ and

Received: July 12, 2020

long-range ordered $R\bar{3}$, as two segregated phases and/or as randomly distributed short-range ordered $P\bar{3}1c$ domains in the long-range ordered $R\bar{3}$ lattice. Raman data displayed a moderate asymmetry of the A_{1g}^3 phonon line. This behavior was attributed to the spin–phonon interaction, similar to the case for CrI_3 . The additional peaks in our spectra obey A_g selection rules and can be described in terms of overtones, as well as the A_{2g} silent modes “activated” by the symmetry breaking.

EXPERIMENTAL AND COMPUTATIONAL DETAILS

The preparation of single-crystal VI_3 samples used in this study is presented elsewhere.¹⁰ For the Raman scattering experiment, a Tri Vista 557 spectrometer was used in the backscattering micro-Raman configuration with a 1800/1800/2400 grooves/mm diffraction grating combination. A Coherent Ar^+/Kr^+ ion laser with a 514 nm line was used as an excitation source. Laser beam focusing was achieved through the microscope objective with 50 \times magnification. The direction of the incident (scattered) light coincides with the crystallographic c axis. The sample, cleaved in open air, was held inside a KONTI CryoVac continuous helium flow cryostat with a 0.5 mm thick window. Raman scattering measurements were performed under high vacuum (10^{-6} mbar). All of the obtained Raman spectra were corrected by the Bose factor. The spectrometer resolution is comparable to the Gaussian width of 1 cm^{-1} .

PDF and wide-angle X-ray scattering measurements were carried out in capillary transmission geometry using a PerkinElmer amorphous silicon area detector placed 206 and 983 mm downstream from the sample, respectively, at beamline 28-ID-1 (PDF) of National Synchrotron Light Source II at Brookhaven National Laboratory. The setup utilized a 74.3 keV ($\lambda = 0.1668\text{ \AA}$) X-ray beam.

Two-dimensional diffraction data were integrated using the Fit2D software package.²⁸ Data reduction was performed to obtain experimental PDFs ($Q_{\text{max}} = 26\text{ \AA}^{-1}$) using the xPDFsuite software package.²⁹ The Rietveld and PDF analyses were carried out using GSAS-II³⁰ and PDFgui³¹ software packages, respectively.

Density functional theory calculations were performed using the Quantum Espresso software package,³² employing the PBE exchange–correlation functional³³ and PAW pseudopotentials.^{34,35} All calculations are spin-polarized. The cutoff for wave functions and the charge density were set to 48 and 650 Ry, respectively. The k -points were sampled using the Monkhorst–Pack scheme, on a $6 \times 6 \times 6$ Γ -centered grid for $R\bar{3}$ and $C2/m$ structures and a $12 \times 12 \times 8$ grid for the $P\bar{3}1c$ structure. Optimization of the lattice parameters and atomic positions in the unit cell was performed until the interatomic forces were $<10^{-6}$ Ry/ \AA . To obtain more accurate lattice parameters, treatment of the van der Waals interactions is included using the Grimme-D2 correction. The correlation effects are treated with the Hubbard U correction (LDA+ U), using a rotationally invariant formulation implemented in QE,³⁶ where $U = 3.68\text{ eV}$. Band structure plots are calculated at 800 k -points on the chosen path over high-symmetry points. Phonon frequencies were calculated with the linear response method, as implemented in the -phonon part of Quantum Espresso.

RESULTS AND DISCUSSION

The first reported results for VI_3 , dating from the 1950s,^{37–39} indicated that VI_3 adopts a honeycomb layer-type BiI_3 structure described with space group $R\bar{3}$, which is a structure common in TMTs, also found in the low-temperature phase of CrI_3 .^{6,40}

There have been several proposed unit cell symmetries for VI_3 in the literature: $R\bar{3}$,^{12,13} $C2/m$,¹⁴ and $P\bar{3}1c$.⁹ Schematic representations of the $P\bar{3}1c$, $R\bar{3}$, and $C2/m$ crystal structures are depicted in Figure 1. The corresponding crystallographic unit cell parameters, previously reported, are listed in Table 1.

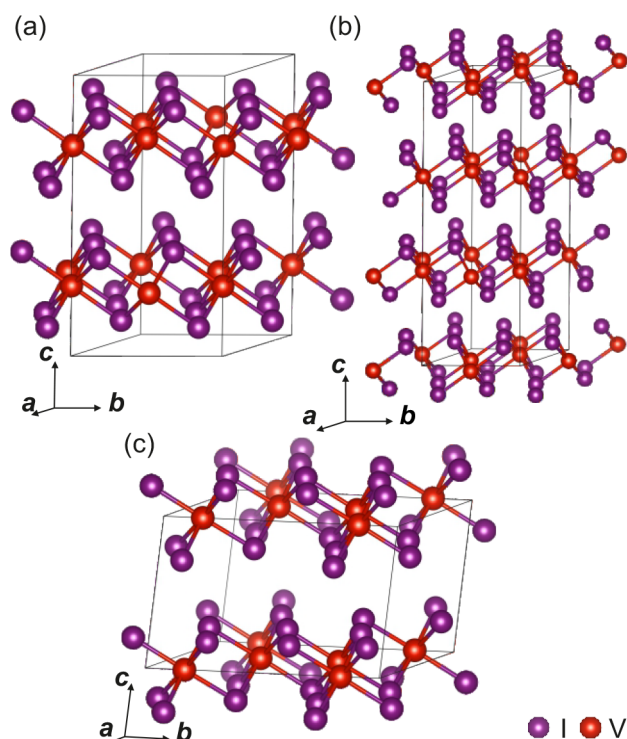


Figure 1. Schematic representation of the high-temperature (a) $P\bar{3}1c$, (b) $R\bar{3}$, and (c) $C2/m$ structures of VI_3 . Black solid lines represent unit cells.

Each of the suggested symmetries implies a different distribution of Raman active modes.

According to FGA, eight ($4A_g + 4E_g$), 11 ($3A_{1g} + 8E_g$), and 12 ($6A_g + 6B_g$) Raman active modes are expected to be observed in the light scattering experiment for $R\bar{3}$, $P\bar{3}1c$, and $C2/m$ crystal structures, respectively. Wyckoff positions, irreducible representations, and corresponding tensors of Raman active modes for each space group are listed in Table 2.

The first step in determining the crystal symmetry from the light scattering experiment is to compare the expected and observed Raman active modes, shown in Figure 2. The red solid line represents the spectrum measured in the parallel polarization configuration, whereas the blue line corresponds to the cross polarization configuration. Five of 12 observed peaks emerge only in parallel, whereas five peaks and a broad peak-like structure can be observed for both polarization configurations. The emergence of the 123.4 cm^{-1} peak in the cross polarization can be understood as a “leakage” of the A_{1g}^3 mode due to a possible finite c axis projection and/or the presence of defects.

Now the peaks that appear only for the parallel polarization configuration can be assigned as either A_{1g} or A_g symmetry modes, assuming the light polarization direction along the main crystal axis of the $C2/m$ structure for the later. On the basis of the FGA for possible symmetry group candidates, the remaining Raman active modes can be either of E_g or B_g symmetry. The selection rules (Table 2) do not allow observation of the B_g symmetry modes for the parallel polarization configuration. Consequently, the peaks that can be observed in both scattering channels were recognized as E_g modes. The absence of B_g modes in the Raman spectra rules out the possibility of the AlCl_3 type of structure (space group $C2/m$). Two possible remaining crystal symmetries ($R\bar{3}$ and

Table 1. Previously Reported Experimental and Calculated Unit Cell Parameters for $\bar{P}31c$, $\bar{R}3$, and $C2/m$ Structures of VI_3

	$\bar{P}31c$		$\bar{R}3$		$C2/m$	
	calcd	exp. ⁹	calcd	exp. ¹²	calcd	exp. ¹⁴
<i>a</i> (Å)	6.87	6.89(10)	6.69	6.89(3)	7.01	6.84(3)
<i>b</i> (Å)	6.87	6.89(10)	6.69	6.89(3)	12.14	11.83(6)
<i>c</i> (Å)	13.224	13.289(1)	19.81	19.81(9)	7.01	6.95(4)
α (deg)	90	90	90	90	90	90
β (deg)	90	90	90	90	109.05	108.68
γ (deg)	120	120	120	120	90	90
cell volume (Å ³)	559.62	547.74(10)	767.71	814.09(8)	563.33	533.66(36)

Table 2. Wyckoff Positions of Atoms and Their Contributions to the Γ -Point Phonons for the $\bar{R}3$, $C2/m$, and $\bar{P}31c$ Structures and the Raman Tensors for the Corresponding Space Groups

space group $\bar{P}31c$		space group $\bar{R}3$		space group $C2/m$	
atom	irreducible representation	atom	irreducible representation	atom	irreducible representation
V (2a)	$A_{2g} + A_{2u} + E_g + E_u$	V (3a)		V (4g)	$A_g + A_u + 2B_g + 2B_u$
V (2c)	$A_{2g} + A_{2u} + E_g + E_u$	V (6c)	$A_g + A_u + E_g + E_u$	I (4i)	$2A_g + A_u + B_g + 2B_u$
I (12i)	$3A_{1g} + 3A_{1u} + 3A_{2g} + 3A_{2u} + 6E_g + 6E_u$	I (18f)	$3A_g + 3A_u + 3E_g + 3E_u$	I (8j)	$3A_g + 3A_u + 3B_g + 3B_u$

$$A_{1g} = \begin{pmatrix} a & a & b \end{pmatrix}$$

$${}^1E_g = \begin{pmatrix} c & -c & d \\ -c & c & d \\ d & d & d \end{pmatrix} {}^2E_g = \begin{pmatrix} -c & -c & -d \\ -c & c & d \\ d & d & d \end{pmatrix}$$

$$A_g = \begin{pmatrix} a & a & b \end{pmatrix}$$

$${}^1E_g = \begin{pmatrix} c & d & e \\ d & -c & f \\ e & f & e \end{pmatrix} {}^2E_g = \begin{pmatrix} d & -c & -f \\ -c & -d & e \\ -f & e & e \end{pmatrix}$$

$$A_g = \begin{pmatrix} a & d \\ c & b \end{pmatrix}$$

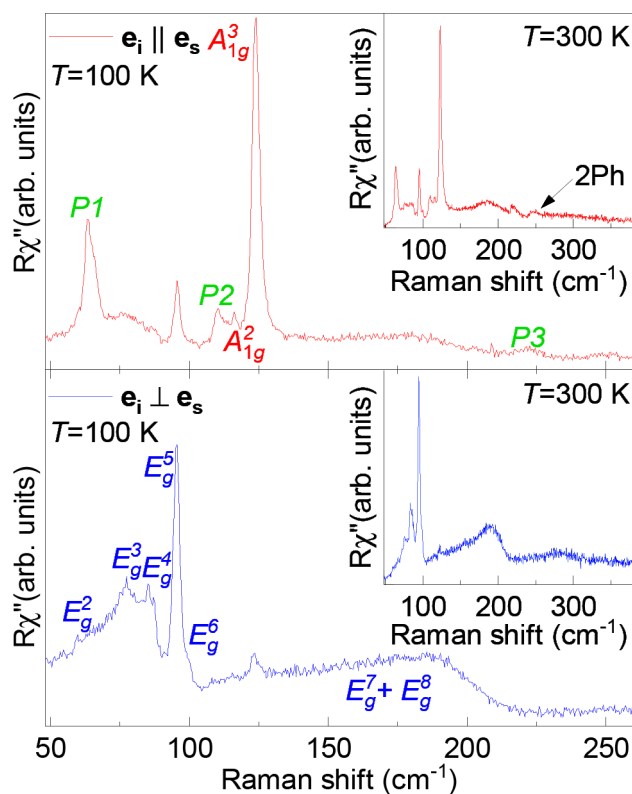
$$B_g = \begin{pmatrix} e & f \\ e & f \end{pmatrix}$$


Figure 2. Raman spectra of the high-temperature VI_3 single-crystal structure measured in parallel (red solid line) and cross (blue solid line) polarization configurations at 100 K. Peaks observed in both spectra were identified as E_g modes, whereas peaks observed only in the red spectrum were assigned as A_{1g} modes. Additional peaks that obey pure A_{1g} symmetry are marked as P1–P3.

$\bar{P}31c$) are difficult to single out on the basis of the Raman data symmetry analysis alone. To overcome this obstacle, the DFT method was applied for each of the suggested structures.

It was reported in the literature that $\bar{P}31c$ VI_3 can have two possible electronic states^{9,14,41–43} that both can be obtained using DFT+U calculations by varying the smearing and mixing parameters. This approach resulted in a Mott-insulator state having a lower energy making it the electronic ground state of VI_3 . However, the total energy difference of these two states is small and will not be mentioned further because it is outside of the scope of our analysis. For the sake of completeness, both sets of phonon energies obtained through DFT calculations for these electronic states of the $\bar{P}31c$ structure are listed in Table 3 together with the results for the $\bar{R}3$ and $C2/m$ space groups as well as the experimental results measured at 100 K.

Now one can see that, even though the Raman mode symmetries for the case of the $\bar{R}3$ crystal structure can describe our Raman spectra, there is a stronger mismatch in calculated and experimentally determined phonon energies when compared to the results obtained for the $\bar{P}31c$ structure. The deviation is largest for the calculated A_g^1 mode. The closest mode in energy, which obeys the same symmetry rules as the calculated A_g^1 , is a peak at ~ 64.1 cm^{-1} , yielding a deviation of $\sim 30\%$. Also, the calculated energy of the A_g^4 mode could not be identified within our spectrum, with the closest experimental A_g peaks being within 20%. Such deviation in theory and experiment, $>20\%$, indicates that the room-temperature phonon vibrations in VI_3 do not originate predominantly from the BiI_3 structure type either, leaving $\bar{P}31c$ as the only candidate. This indication is further reinforced by the inability to connect the experimentally observed E_g modes at ~ 77 and ~ 86 cm^{-1} with the $\bar{R}3$ -calculated modes.

Our experimental data (Table 3) are mostly supported by the phonon energies obtained for possible electronic states of

Table 3. Comparison between Calculated Values of Raman Active Phonon Energies for Insulating and Half-Metallic States of the $P\bar{3}1c$ Structure and Experimentally Obtained Values (left)^a and Phonon Symmetries and Calculated Phonon Energies for the $R\bar{3}$ and $C2/m$ Structures of VI_3 ^b

space group $P\bar{3}1c$				space group $R\bar{3}$		space group $C2/m$	
symmetry	calcd (cm^{-1})	calcd (cm^{-1})	exp. (cm^{-1})	symmetry	calcd (cm^{-1})	symmetry	calcd (cm^{-1})
E_g^1	17.2	15.2	—	E_g^1	45.2	A_g^1	58.1
A_{2g}^1 (silent)	35.0	56.8		E_g^2	69.9	B_g^1	60.0
E_g^2	62.2	61.6	59.8	A_g^1	99.3	A_g^2	82.7
A_{2g}^2 (silent)	69.4	72.3		E_g^3	99.8	B_g^2	82.9
E_g^3	74.1	75.9	77.2	A_g^2	105.1	A_g^3	85.7
A_{1g}^1	83.3	84.2	—	A_g^3	135.5	B_g^3	88.9
E_g^4	84.9	86.6	86.7	A_g^4	167.9	A_g^4	99.3
E_g^5	91.5	98.4	95.2	E_g^4	176.8	B_g^4	99.3
A_{2g}^3 (silent)	92.2	96.3				A_g^5	122.3
E_g^6	97.4	108.3	100.4			B_g^5	149.9
A_{1g}^2	113.2	119.3	116.8			B_g^6	161.0
A_{1g}^3	117.1	123.9	123.4			A_g^6	164.0
A_{2g}^4 (silent)	121.3	147.8					
E_g^7	132.2	151.9	^c				
E_g^8	149.4	166.9	^c				
A_{2g}^5 (silent)	185.9	212.1					

^aThe experimental values were determined at 100 K. The experimental uncertainty is 0.3 cm^{-1} . ^bAll calculations were performed at 0 K. ^cSee the text for an explanation.

the $P\bar{3}1c$ trigonal structure with deviations of around 10% and 15%. Nine of 11 Raman modes were singled out and identified, with E_g^1 being not observable in our experimental setup due to its low energy. The A_{1g}^1 mode might be missing due to its low intensity and/or the finite spectrometer resolution. The most striking was the observation of the broad feature at $\sim 180 \text{ cm}^{-1}$, persisting up to 300 K in both scattering channels. Whereas its line shape resembles those of the two-magnon type of excitation, we believe that scenario is unlikely for a ferromagnetic material. The energy region where the feature was observed may also suggest the possibility of a two-phonon type of excitation. However, their scattering cross sections are usually small and dominated by overtones, thus mostly observed for the parallel scattering configuration.⁴⁵ For example, such an excitation was observed at $\sim 250 \text{ cm}^{-1}$ (Figure 2). Finally, the observed feature also falls into the energy region where, as suggested by the numerical calculations, observation of the E_g^7 and E_g^8 modes is expected. We believe that it is actually a complex structure comprising E_g^7 and E_g^8 Raman modes, significantly broadened by the spin-phonon interaction, that is particularly strong on these phonon branches. The proximity of the two very broad, presumably asymmetric peaks hampers their precise assignment.

Closer inspection of other Raman peaks revealed that some of them also exhibit an asymmetric line shape. To further demonstrate this virtue, we have quantitatively analyzed the highest-intensity peak, A_{1g}^3 , using the symmetric Voigt line shape and convolution of a Fano profile and a Gaussian.^{44–46} The asymmetric line shape (with a Fano parameter of $|q| = 12.3$) gives a slightly better agreement with the experimental data, as depicted in Figure 3. Considering that the observed asymmetry in similar materials was shown to reflect the spin-phonon interaction,^{46,47} we propose it as a possible scenario in VI_3 , as well.

Our findings, based on the inelastic light scattering experiments, at first glance differ from those presented in ref 10. To resolve this discrepancy, we used synchrotron X-ray Rietveld and PDF analysis. Typically, the short-range order

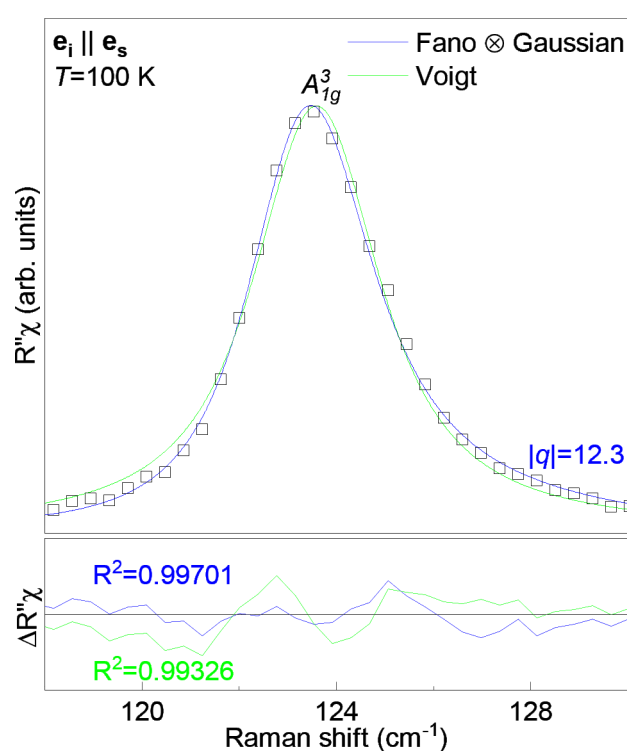


Figure 3. Quantitative analysis of the A_{1g}^3 mode. The blue solid line represents the line shape obtained as a convolution of the Fano line shape and the Gaussian, whereas the green one represents a Voigt profile fitted to experimental data (\square). For details, see refs 44 and 45.

(SRO) contributes to diffuse scattering under the long-range order (LRO) Bragg peaks when they coexist. Because the diffuse scattering is subtracted as part of the background in the Rietveld refinement, this method is more sensitive to the average structure of materials. In contrast, PDF analysis is performed on the sine Fourier transform of the properly corrected diffraction pattern, including both Bragg and diffuse

components. PDF is a real space function that provides a histogram of interatomic distances, which contain information regarding all length scales.^{48–51} The 1–10 and 11–30 Å PDF length scales are more sensitive to SRO and LRO, respectively. For the VI_3 system, the best Rietveld fit was obtained using the $\text{R}\bar{3}$ space group (Figure 4a), in agreement with that previously

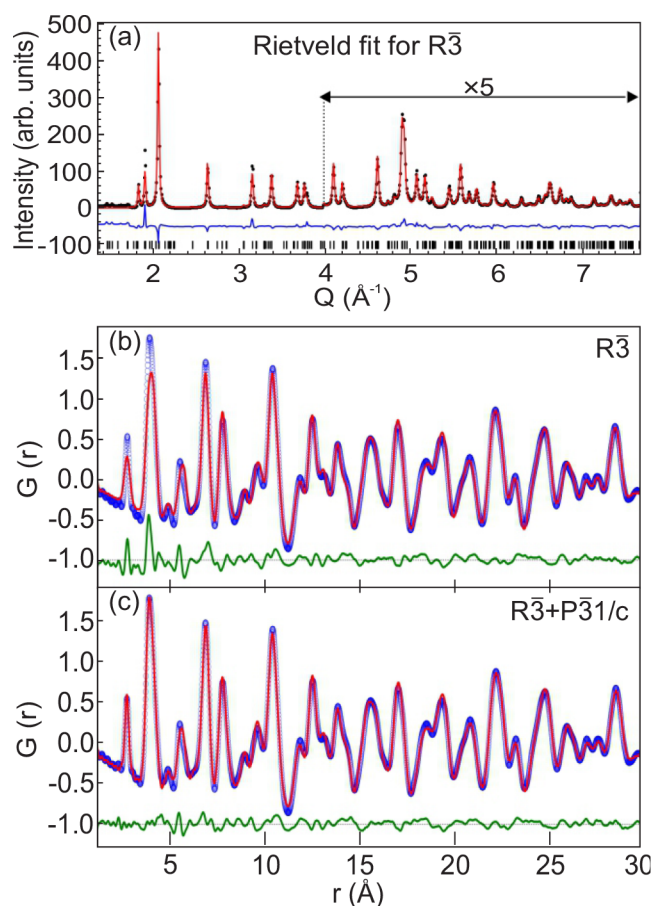


Figure 4. Best structural model fits to diffraction data. (a) Rietveld fit using the $\text{R}\bar{3}$ space group with black vertical bars indicating calculated peak positions. (b) PDF fit using the $\text{R}\bar{3}$ space group. (c) Two-phase PDF fit using $\text{R}\bar{3}$ and $\text{P}\bar{3}1\text{c}$ space groups to fit LRO and SRO, respectively. Black dots (XRD) and blue dots (PDF) represent experimental data, and red solid lines represent the model-based fits. The fit residues are shown at the bottom of each plot.

observed.¹⁰ Not surprisingly, LRO obtained from the Rietveld refinement showed a good agreement on the PDF length scale of 10–30 Å. However, the $\text{R}\bar{3}$ space group gave a poor fit on the length scale of 1.5–15 Å with refined $\delta 1$ to account for correlated motion (Figure 4b). In contrast, $\text{P}\bar{3}1\text{c}$ gave a better fit to SRO, but a poor fit to LRO. The best PDF fits were obtained by refining a weighted two-phase structural model containing ~25 wt % SRO $\text{P}\bar{3}1\text{c}$ and ~75 wt % LRO $\text{R}\bar{3}$ phases. The refined correlation length of the SRO is ~15–20 Å (Figure 4c). These results suggest two possible scenarios: (1) coexistence of two segregated phases, LRO $\text{R}\bar{3}$ and SRO $\text{P}\bar{3}1\text{c}$, and (2) randomly distributed short-range ordered $\text{P}\bar{3}1\text{c}$ domains in the long-range ordered $\text{R}\bar{3}$ lattice. A detailed structural analysis is required to pinpoint scenario 1 and/or 2, which is beyond the scope of this work.

In addition to the peaks already assigned to Γ -point Raman active phonons of the $\text{P}\bar{3}1\text{c}$ crystal structure (Table 2), three

additional peaks at 64.2 cm^{-1} (P1), 110.1 cm^{-1} (P2), and 220.6 cm^{-1} (P3) are observed (see Figure 2). According to the results of DFT, energies of these modes correspond well to those calculated for silent A_{2g}^2 , A_{2g}^3 , and A_{2g}^5 modes. Their observability in Raman data may come from the release of the symmetry selection rules by breaking of the (translation) symmetry as suggested by the PDF in both scenarios.^{52–55} However, as previously discussed, these peaks obey A_{1g} selection rules, indicating the possibility for them to be overtones in nature. In this less likely scenario, the phonon–phonon coupling is enhanced by the spin–phonon interaction and/or by the structural imperfections, thus enhancing the Raman scattering rate for the two-phonon processes.⁴⁵ Hence, the observed Raman modes reflect the symmetry of phonon vibrations related to the SRO.^{56,57} It is interesting to note that, besides a possible short-range crystallography that is different from the average, VI_3 might also feature short-range magnetic order above 79 K.¹⁴

CONCLUSION

In summary, room-temperature phonon vibrations of VI_3 stem from the $\text{P}\bar{3}1\text{c}$ symmetry of the unit cell. The PDF analysis suggested the coexistence of two phases, short-range ordered $\text{P}\bar{3}1\text{c}$ and long-range ordered $\text{R}\bar{3}$, as two segregated phases and/or as randomly distributed short-range ordered $\text{P}\bar{3}1\text{c}$ domains in the long-range ordered $\text{R}\bar{3}$ lattice. Nine of 12 observed peaks in the Raman spectra were assigned in agreement with $\text{P}\bar{3}1\text{c}$ symmetry calculations. Three additional peaks, which obey A_{1g} symmetry rules, could be explained as either overtones or as activated A_{2g} silent modes caused by a symmetry breaking. The asymmetry of one of the A_{1g} phonon modes, together with the anomalous behavior of E_g^7 and E_g^8 , indicates strong spin–phonon coupling, which has already been reported in similar 2D materials.^{46,58}

AUTHOR INFORMATION

Corresponding Author

Nenad Lazarević – Institute of Physics Belgrade, University of Belgrade, 11080 Belgrade, Serbia; orcid.org/0000-0001-6310-9511; Email: nenadl@ipb.ac.rs

Authors

Sanja Djurdjić Mijin – Institute of Physics Belgrade, University of Belgrade, 11080 Belgrade, Serbia

A. M. Milinda Abeykoon – National Synchrotron Light Source II, Brookhaven National Laboratory, Upton, New York 11973, United States

Andrijana Solajić – Institute of Physics Belgrade, University of Belgrade, 11080 Belgrade, Serbia

Ana Milosavljević – Institute of Physics Belgrade, University of Belgrade, 11080 Belgrade, Serbia

Jelena Pešić – Institute of Physics Belgrade, University of Belgrade, 11080 Belgrade, Serbia

Yu Liu – Condensed Matter Physics and Materials Science Department, Brookhaven National Laboratory, Upton, New York 11973-5000, United States; orcid.org/0000-0001-8886-2876

Cedomir Petrovic – Condensed Matter Physics and Materials Science Department, Brookhaven National Laboratory, Upton, New York 11973-5000, United States; orcid.org/0000-0001-6063-1881

Zoran V. Popović – Institute of Physics Belgrade, University of Belgrade, 11080 Belgrade, Serbia; Serbian Academy of Sciences and Arts, 11000 Belgrade, Serbia

Complete contact information is available at:
<https://pubs.acs.org/10.1021/acs.inorgchem.0c02060>

Notes

The authors declare no competing financial interest.

ACKNOWLEDGMENTS

The authors acknowledge funding provided by the Institute of Physics Belgrade, through a grant from the Ministry of Education, Science and Technological Development of the Republic of Serbia, Project F-134 of the Serbian Academy of Sciences and Arts, and the Science Fund of the Republic of Serbia, PROMIS, 6062656, StrainedFeSC. DFT calculations were performed using computational resources at Johannes Kepler University (Linz, Austria). Materials synthesis was supported by the U.S. DOE-BES, Division of Materials Science and Engineering, under Contract DE-SC0012704 (BNL). This research used beamline 28-ID-1 of National Synchrotron Light Source II, a U.S. DOE Office of Science User Facility operated for the DOE Office of Science by Brookhaven National Laboratory under Contract DE-S.


REFERENCES

- (1) Seyler, K. L.; Zhong, D.; Klein, D. R.; et al. Ligand-field helical luminescence in a 2D ferromagnetic insulator. *Nat. Phys.* **2018**, *14*, 277–281.
- (2) Klein, D. R.; MacNeill, D.; Lado, J. L.; Soriano, D.; Navarro-Moratalla, E.; Watanabe, K.; et al. Probing magnetism in 2D van der Waals crystalline insulators via electron tunneling. *Science* **2018**, *360*, 1218–1222.
- (3) Huang, B.; Clark, G.; Klein, D. R.; MacNeill, D.; Navarro-Moratalla, E.; Seyler, K. L.; et al. Electrical control of 2D magnetism in bilayer CrI₃. *Nat. Nanotechnol.* **2018**, *13*, 544–548.
- (4) Jiang, S.; Li, L.; Wang, Z.; Mak, K. F.; Shan, J. Controlling magnetism in 2D CrI₃ by electrostatic doping. *Nat. Nanotechnol.* **2018**, *13*, 549–553.
- (5) McGuire, M. A.; Clark, G.; KC, S.; Chance, W. M.; Jellison, G. E.; Cooper, V. R.; Xu, X.; Sales, B. C. Magnetic behavior and spin-lattice coupling in cleavable van der Waals layered CrCl₃ crystals. *Phys. Rev. Materials* **2017**, *1*, 014001.
- (6) Djurdjic-Mijin, S. D.; Solajić, A.; Pešić, J.; Šćepanović, M.; Liu, Y.; Baum, A.; et al. Lattice dynamics and phase transition in CrI₃ single crystals. *Phys. Rev. B: Condens. Matter Mater. Phys.* **2018**, *98*, 104307.
- (7) Thiel, L.; Wang, Z.; Tschudin, M.; Rohner, D.; Gutierrez-Lezama, I. G.; Ubrig, N.; et al. Probing magnetism in 2D materials at the nanoscale with single-spin microscopy. *Science* **2019**, *364*, 973–976.
- (8) Lin, G. T.; Luo, X.; Chen, F. C.; Yan, J.; Gao, J. J.; Sun, Y.; et al. Critical behavior of two-dimensional intrinsically ferromagnetic semiconductor CrI₃. *Appl. Phys. Lett.* **2018**, *112*, 072405.
- (9) Son, S.; Coak, M. J.; Lee, N.; Kim, J.; Kim, T. Y.; Hamidov, H.; et al. Bulk properties of the van der Waals hard ferromagnet VI₃. *Phys. Rev. B: Condens. Matter Mater. Phys.* **2019**, *99*, 041402.
- (10) Liu, Y.; Abeykoon, M.; Petrovic, C. Critical behavior and magnetocaloric effect in VI₃. *Phys. Rev. Research* **2020**, *2*, 013013.
- (11) Huang, B.; Clark, G.; Navarro-Moratalla, E.; Klein, D. R.; Cheng, R.; Seyler, K. L.; et al. Layer-dependent ferromagnetism in a van der Waals crystal down to the monolayer limit. *Nature* **2017**, *546*, 270–273.
- (12) Kong, T.; Stolze, K.; Timmons, E. I.; Tao, J.; Ni, D.; Guo, S.; et al. VI₃ – a New Layered Ferromagnetic Semiconductor. *Adv. Mater.* **2019**, *31*, 1808074.
- (13) Doležal, P.; Kratochvílová, M.; Holý, V.; Čermak, P.; Sechovský, V.; Dušek, M.; et al. Crystal structures and phase transitions of the van der Waals ferromagnet VI₃. *Phys. Rev. Materials* **2019**, *3*, 121401.
- (14) Tian, S.; Zhang, J.-F.; Li, C.; Ying, T.; Li, S.; Zhang, X.; et al. Ferromagnetic van der Waals Crystal VI₃. *J. Am. Chem. Soc.* **2019**, *141*, 5326–5333.
- (15) Wang, Y.-M.; Tian, S.-J.; Li, C.-H.; Jin, F.; Ji, J.-T.; Lei, H.-C.; Zhang, Q.-M. Raman scattering study of two-dimensional magnetic van der Waals compound VI₃. *Chin. Phys. B* **2020**, *29*, 056301.
- (16) Lee, I.; Utermohlen, F. G.; Weber, D.; Hwang, K.; Zhang, C.; van Tol, J.; Goldberger, J. E.; Trivedi, N.; Hammel, P. C. Fundamental Spin Interactions Underlying the Magnetic Anisotropy in the Kitaev Ferromagnet CrI₃. *Phys. Rev. Lett.* **2020**, *124*, 017201.
- (17) Xu, C.; Feng, J.; Xiang, H.; Bellaiche, L. Interplay between Kitaev interaction and single ion anisotropy in ferromagnetic CrI₃ and CrGeTe₃ monolayers. *npj Comput. Mater.* **2018**, *4*, 57.
- (18) Mermin, N. D.; Wagner, H. Absence of Ferromagnetism or Antiferromagnetism in One- or Two-Dimensional Isotropic Heisenberg Models. *Phys. Rev. Lett.* **1966**, *17*, 1133–1136.
- (19) Pershoguba, S. S.; Banerjee, S.; Lashley, J. C.; Park, J.; Ågren, H.; Aeppli, G.; Balatsky, A. V. Dirac Magnons in Honeycomb Ferromagnets. *Phys. Rev. X* **2018**, *8*, 011010.
- (20) Liu, J.; Shi, M.; Mo, P.; Lu, J. Electrical-field-induced magnetic Skyrmion ground state in a two-dimensional chromium tri-iodide ferromagnetic monolayer. *AIP Adv.* **2018**, *8*, 055316.
- (21) Jiang, S.; Li, L.; Wang, Z.; Shan, J.; Mak, K. Spin tunnel field-effect transistors based on two-dimensional van der Waals heterostructures. *Nature Electronics* **2019**, *2*, 159.
- (22) Klein, D. R.; MacNeill, D.; Song, Q.; Larson, D. T.; Fang, S.; Xu, M.; Ribeiro, R. A.; Canfield, P. C.; Kaxiras, E.; Comin, R.; Jarillo-Herrero, P. Enhancement of interlayer exchange in an ultrathin two-dimensional magnet. *Nat. Phys.* **2019**, *15*, 1255–1260.
- (23) Wang, Z.; Gibertini, M.; Dumcenco, D.; Taniguchi, T.; Watanabe, K.; Giannini, E.; Morpurgo, A. Determining the phase diagram of atomically thin layered antiferromagnet CrCl₃. *Nat. Nanotechnol.* **2019**, *14*, 1116.
- (24) Ubrig, N.; Wang, Z.; Teyssier, J.; Taniguchi, T.; Watanabe, K.; Giannini, E.; Morpurgo, A. F.; Gibertini, M. Low-temperature monoclinic layer stacking in atomically thin CrI₃ crystals. *2D Mater.* **2020**, *7*, 015007.
- (25) Sun, Z.; et al. Giant nonreciprocal second-harmonic generation from antiferromagnetic bilayer CrI₃. *Nature* **2019**, *572*, 497–501.
- (26) McGuire, M. A.; Clark, G.; KC, S.; Chance, W. M.; Jellison, G. E.; Cooper, V. R.; Xu, X.; Sales, B. C. Magnetic behavior and spin-lattice coupling in cleavable van der Waals layered CrCl₃ crystals. *Phys. Rev. Materials* **2017**, *1*, 014001.
- (27) Kuhlow, B. Magnetic Ordering in CrCl₃ at the Phase Transition. *physica status solidi (a)* **1982**, *72*, 161–168.
- (28) Hammersley, A. P.; Svensson, S. O.; Hanfland, M.; Fitch, A. N.; Hausermann, D. Two-dimensional detector software: From real detector to idealised image or two-theta scan. *High Pressure Res.* **1996**, *14*, 235–248.
- (29) Yang, X.; Juhas, P.; Farrow, C. L.; Billinge, S. J. L. *xPDFsuite: an end-to-end software solution for high throughput pair distribution function transformation, visualization and analysis*; 2014.
- (30) Toby, B. H.; Von Dreele, R. B. GSAS-II: the genesis of a modern open-source all purpose crystallography software package. *J. Appl. Crystallogr.* **2013**, *46*, 544–549.
- (31) Farrow, C. L.; Juhas, P.; Liu, J. W.; Bryndin, D.; Božin, E. S.; Bloch, J.; Proffen, T.; Billinge, S. J. L. PDFfit2 and PDFgui: computer programs for studying nanostructure in crystals. *J. Phys.: Condens. Matter* **2007**, *19*, 335219.
- (32) Giannozzi, P.; et al. QUANTUM ESPRESSO: a modular and open-source software project for quantum simulations of materials. *J. Phys.: Condens. Matter* **2009**, *21*, 395502.
- (33) Perdew, J. P.; Burke, K.; Ernzerhof, M. Generalized Gradient Approximation Made Simple. *Phys. Rev. Lett.* **1996**, *77*, 3865–3868.

- (34) Blöchl, P. E. Projector augmented-wave method. *Phys. Rev. B: Condens. Matter Mater. Phys.* **1994**, *50*, 17953–17979.
- (35) Kresse, G.; Joubert, D. From ultrasoft pseudopotentials to the projector augmented-wave method. *Phys. Rev. B: Condens. Matter Mater. Phys.* **1999**, *59*, 1758–1775.
- (36) Cococcioni, M.; de Gironcoli, S. Linear response approach to the calculation of the effective interaction parameters in the LDA + U method. *Phys. Rev. B: Condens. Matter Mater. Phys.* **2005**, *71*, 035105.
- (37) Juza, D.; Giegling, D.; Schäfer, H. Über die Vanadinjodide VJ₂ und VJ₃. *Z. Anorg. Allg. Chem.* **1969**, *366*, 121–129.
- (38) Berry, K. O.; Smardzewski, R. R.; McCarley, R. E. Vaporization reactions of vanadium iodides and evidence for gaseous vanadium-(IV) iodide. *Inorg. Chem.* **1969**, *8*, 1994–1997.
- (39) Klemm, W.; Krose, E. Die Kristallstrukturen von ScCl₃, TiCl₃ und VCl₃. *Z. Anorg. Chem.* **1947**, *253*, 218–225.
- (40) Liu, Y.; Petrovic, C. Three-dimensional magnetic critical behavior in CrI₃. *Phys. Rev. B: Condens. Matter Mater. Phys.* **2018**, *97*, 014420.
- (41) He, J.; Ma, S.; Lyu, P.; Nachtigall, P. Unusual Dirac half-metallicity with intrinsic ferromagnetism in vanadium trihalide monolayers. *J. Mater. Chem. C* **2016**, *4*, 2518–2526.
- (42) Wang, Y.-P.; Long, M.-Q. Electronic and magnetic properties of van der Waals ferromagnetic semiconductor VI₃. *Phys. Rev. B: Condens. Matter Mater. Phys.* **2020**, *101*, 024411.
- (43) Li, Y.; Liu, Y.; Wang, C.; Wang, J.; Xu, Y.; Duan, W. Electrically tunable valleytronics in quantum anomalous Hall insulating transition metal trihalides. *Phys. Rev. B: Condens. Matter Mater. Phys.* **2018**, *98*, 201407.
- (44) Lazarević, N.; Popović, Z. V.; Hu, R.; Petrovic, C. Evidence for electron-phonon interaction in Fe_{1-x}M_xSb₂ (M = Co and Cr 0 ≤ x ≤ 0.5) single crystals. *Phys. Rev. B: Condens. Matter Mater. Phys.* **2010**, *81*, 144302.
- (45) Baum, A.; Milosavljević, A.; Lazarević, N.; Radonjić, M. M.; Nikolić, B.; Mitschek, M.; Maranloo, Z. I.; Šćepanović, M.; Grujić-Brojčin, M.; Stojilović, N.; Opel, M.; Wang, A.; Petrovic, C.; Popović, Z. V.; Hackl, R. Phonon anomalies in FeS. *Phys. Rev. B: Condens. Matter Mater. Phys.* **2018**, *97*, 054306.
- (46) Milosavljević, A.; Solajic, A.; Pešić, J.; Liu, Y.; Petrovic, C.; Lazarević, N.; Popović, Z. V. Evidence of spin-phonon coupling in CrSiTe₃. *Phys. Rev. B: Condens. Matter Mater. Phys.* **2018**, *98*, 104306.
- (47) McCarty, K. F.; Radousky, H. B.; Hinks, D. G.; Zheng, Y.; Mitchell, A. W.; Folkerts, T. J.; Shelton, R. N. Electron-phonon coupling in superconducting Ba_{0.6}K_{0.4}BiO₃: A Raman scattering study. *Phys. Rev. B: Condens. Matter Mater. Phys.* **1989**, *40*, 2662–2665.
- (48) Proffen, T.; Page, K. L.; McLain, S. E.; Clausen, B.; Darling, T. W.; TenCate, J. A.; Lee, S.-Y.; Ustundag, E. Atomic pair distribution function analysis of materials containing crystalline and amorphous phases. *Z. Kristallogr.* **2005**, *220*, 1002–1008.
- (49) Bordet, P. Application of the pair distribution function analysis for the study of cultural heritage materials. *C. R. Phys.* **2018**, *19*, 561–574.
- (50) Bozin, E. S.; Yin, W. G.; Koch, R. J.; Abeykoon, M.; Hor, Y. S.; Zheng, H.; Lei, H. C.; Petrovic, C.; Mitchell, J. F.; Billinge, S. J. L. Local orbital degeneracy lifting as a precursor to an orbital-selective Peierls transition. *Nat. Commun.* **2019**, *10*, 3638.
- (51) Egami, T.; Billinge, S. J. L. *Underneath the Bragg Peaks: Structural Analysis of Complex Materials*; 2003; p 16.
- (52) Jin, F.; Lazarević, N.; Liu, C.; Ji, J.; Wang, Y.; He, S.; Lei, H.; Petrovic, C.; Yu, R.; Popović, Z. V.; Zhang, Q. Phonon anomalies and magnetic excitations in BaFe₂Se₂O. *Phys. Rev. B: Condens. Matter Mater. Phys.* **2019**, *99*, 144419.
- (53) Moskovits, M.; Dilella, D. Surface-enhanced Raman spectroscopy of benzene and benzene-d₆ adsorbed on silver. *J. Chem. Phys.* **1980**, *73*, 6068–6075.
- (54) Dubroka, A.; Humlíček, J.; Abrashev, M. V.; Popović, Z. V.; Sapiña, F.; Cantarero, A. Raman and infrared studies of La_{1-y}Sr_yMn_{1-x}M_xO₃ (M = Cr, Co, Cu, Zn, Sc or Ga): Oxygen disorder and local vibrational modes. *Phys. Rev. B: Condens. Matter Mater. Phys.* **2006**, *73*, 224401.
- (55) Souza Filho, A. G.; Faria, J. L. B.; Guedes, I.; Sasaki, J. M.; Freire, P. T. C.; Freire, V. N.; Mendes Filho, J.; Xavier, M. M.; Cabral, F. A. O.; de Araújo, J. H.; da Costa, J. A. P. Evidence of magnetic polaronic states in La_{0.70}Sr_{0.30}Mn_{1-x}Fe_xO₃ manganites. *Phys. Rev. B: Condens. Matter Mater. Phys.* **2003**, *67*, 052405.
- (56) Lekgoathi, M.; Kock, L. Effect of short and long range order on crystal structure interpretation: Raman and powder X-ray diffraction of LiPF₆. *Spectrochim. Acta, Part A* **2016**, *153*, 651–654.
- (57) Wolverton, C.; Zunger, A.; Lu, Z.-W. Long-versus short-range order in Ni₃V and Pd₃V alloys. *Phys. Rev. B: Condens. Matter Mater. Phys.* **1994**, *49*, 16058.
- (58) Webster, L.; Liang, L.; Yan, J.-A. Distinct spin-lattice and spin-phonon interactions in monolayer magnetic CrI₃. *Phys. Chem. Chem. Phys.* **2018**, *20*, 23546–23555.

RESEARCH ARTICLE

Vacancies and spin–phonon coupling in $\text{CrSi}_{0.8}\text{Ge}_{0.1}\text{Te}_3$

Ana Milosavljević¹  | Andrijana Šolajić¹ | Bojana Višić¹ | Marko Opačić¹ |
Jelena Pešić¹ | Yu Liu² | Cedomir Petrović² | Zoran V. Popović^{1,3} |
Nenad Lazarević¹

¹Institute of Physics Belgrade, University of Belgrade, Pregrevica 118, Belgrade, 11080, Serbia

²Condensed Matter Physics and Materials Science Department, Brookhaven National Laboratory, Upton, New York, 11973-5000, USA

³Serbian Academy of Sciences and Arts, Knez Mihailova 35, Belgrade, 11000, Serbia

Correspondence

Ana Milosavljević, Institute of Physics Belgrade, University of Belgrade, Pregrevica 118, 11080 Belgrade, Serbia.
Email: ana.milosavljevic@ipb.ac.rs

Funding information

Serbian Academy of Sciences and Arts, Grant/Award Number: F-134; Slovenian Research Agency, Grant/Award Number: P1-0099; Ministry of Education, Science and Technological Development of the Republic of Serbia U.S. DOE-BES, Division of Materials Science and Engineering, Grant/Award Number: DE-SC0012704

Abstract

We report temperature-dependent Raman scattering and magnetization studies of van der Waals ferromagnetic compound $\text{CrSi}_{0.8}\text{Ge}_{0.1}\text{Te}_3$. Magnetic susceptibility measurements revealed dominant ferromagnetic interactions below T_C which shift to the lower values due to the presence of vacancies. A Raman active mode, additional to the ones predicted by symmetry in the parent compounds, has been observed. This A_g symmetry mode most likely emerges as a consequence of the atomic vacancies on Si/Ge site. Presence of the strong spin–phonon coupling at temperature around 210 K is indicated by deviations from conventional phonon self-energy temperature dependence of all analysed modes.

KEYWORDS

magnetism, phonons, raman spectroscopy, van der Waals materials

1 | INTRODUCTION

Considerable progress has been made in the field of material science through developing new materials and revealing their properties in the last decade. Namely, in the recent years, large family of van der Waals materials with inherent magnetism became the focus of experimental and theoretical research, because they seem suitable for numerous technical applications.^[1–7] The family includes $\text{Fe}_{3-x}\text{GeTe}_2$ metallic materials with high magnetic transition temperature,^[8–10] semiconductors CrXTe_3 ($X = \text{Si, Ge, Sn}$) and CrX_3 ($X = \text{Cl, Br, I}$) monolayers^[2,11–13] and heterostructures.^[14]

CrSiTe_3 and CrGeTe_3 are ferromagnetic (FM) semiconductors with band gap of 0.4 and 0.7 eV and Curie temperatures (T_C) of 32 and 61 K, respectively.^[15–18] Twinning of CrSiTe_3 single crystals along c -axes was revealed by X-ray diffraction experiment as well as Cr^{3+} ions magnetic order.^[15] Recently, through high-resolution angle-resolved photoemission spectroscopy (ARPES), it was possible to identify full electronic structure near the Fermi level. Due to spin–orbit coupling, CrSiTe_3 is a Mott-type FM insulator.^[19] Electronic structure of CrGeTe_3 single crystals was also investigated by ARPES.^[20] It was shown that the low-lying valence bands are centred around the Γ point and are mainly formed from Te 5p orbitals.

Raman scattering studies of CrSiTe_3 reveal strong spin-lattice coupling in the paramagnetic phase^[15,21] as a consequence of a short-range magnetic order in this compound. In addition to renormalization of energies and linewidths of observed Raman active modes, coupling of doubly degenerate E_g mode with magnetic continuum was found.^[21] The coupling results in an asymmetric phonon line shape up to 180 K. Besides the splitting of two low-energy E_g modes in the magnetic phase of CrGeTe_3 and unconventional behaviour of phonon properties around transition temperature, experimental results indicate spin-phonon coupling effect with magnetic quasi-elastic scattering.^[22] Pressure-dependent Raman scattering study of CrGeTe_3 showed a decrease in bond length, the deviation of Cr-Te-Cr angle, and reduction of phase transition temperature.^[23]

Change of the carrier concentration plays an important role in the physics of semiconducting materials as it can lead to surprising physical properties. Very small variations in dopant concentrations can lead to structural modifications and considerable changes in magnetic transition temperature. Here, we report a Raman scattering and magnetization studies of $\text{CrSi}_{0.8}\text{Ge}_{0.1}\text{Te}_3$. Our scanning electron microscopy (SEM) measurements reveal 10% of Ge atoms concentration and 10% of vacancies. Vacancies induced a decrease in T_C was detected within magnetic susceptibility measurements. In the Raman scattering results, we identified three A_g and four E_g symmetry modes. Additional peak of the A_g symmetry is also observed in our spectra. This mode may be traced to vacancies and possible inhomogeneous distribution of Ge atoms substitution on Si atomic site at nano-scale. Energies of modes predicted by symmetry analysis are found between the experimental values of parent compounds CrSiTe_3 and CrGeTe_3 , reported previously in Milosavljević et al.^[21] The presence of the strong spin-phonon interaction at temperature around 210 K is indicated in small deviations from conventional temperature-dependent behaviour of the observed modes energies and linewidths, including additional one.

2 | EXPERIMENT AND NUMERICAL METHOD

$\text{CrSi}_{0.8}\text{Ge}_{0.1}\text{Te}_3$ single crystals were grown as described previously.^[24] Magnetic properties were measured in a Quantum Design MPMS-XL5 system.

SEM measurements were performed using FEI HeliosNanolab 650. This microscope is equipped with an Oxford Instruments energy dispersive spectroscopy (EDS) system with an X-max SSD detector operating at 20 kV. Measurements were performed on as-cleaved samples

deposited on a graphite tape. The elemental composition EDS mapping was obtained on crystals that appeared to be uniform for several tens of microns. The maps show the presence of Cr, Ge, Te and Si.

For Raman scattering experiment, Tri Vista 557 spectrometer was used in the subtractive backscattering micro-Raman configuration. The combination of gratings was 1800/1800/2400 grooves/mm and the entrance slit of 80 μm . Solid state laser with 532-nm line was used as an excitation source. In our scattering configuration, plane of incidence is ab -plane, where $|a|=|b|$ ($\angle(a,b)=120^\circ$), with incident (scattered) light propagation direction along c -axes. Samples were cleaved in the air before being placed in vacuum. All measurements were performed in high vacuum (10^{-6} mbar) using a KONTI CryoVac continuous Helium flow cryostat with 0.5-mm thick window. Laser beam focusing was achieved using microscope objective with $\times 50$ magnification. All spectra were corrected for Bose factor.

Spin-polarized density functional theory calculations were performed in Quantum Espresso software package,^[25] based on plane waves and pseudopotentials, using Perdew-Burke-Ernzerhof (PBE) exchange-correlation functional^[26] and projector augmented wave (PAW) pseudopotentials.^[27,28] The cutoff for wavefunctions and the charge density of 85 and 425 Ry were chosen, respectively. The k -point were sampled using the Monkhorst-Pack scheme, on $8 \times 8 \times 8$ Γ centred grid used for both structures. Optimization of the lattice parameters and atomic positions in unit cell was performed until the interatomic forces were minimized down to 10^{-6} Ry/Å. Treatment of the van der Waals interactions is included using the Grimme-D2 correction, in order to obtain the lattice parameters more accurately. Phonon wave numbers were calculated within the linear response method, as implemented in PHonon part of Quantum Espresso.

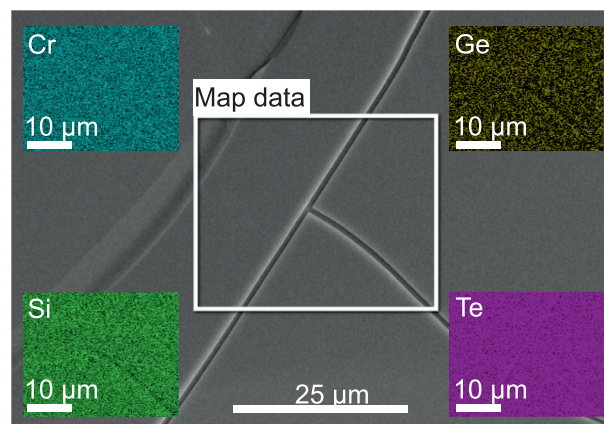


FIGURE 1 Energy dispersive spectroscopy (EDS) mapping on a $\text{CrSi}_{0.8}\text{Ge}_{0.1}\text{Te}_3$ single crystal [Colour figure can be viewed at wileyonlinelibrary.com]

3 | RESULTS AND DISCUSSION

In order to investigate uniformity and elemental composition of $\text{CrSi}_{0.8}\text{Ge}_{0.1}\text{Te}_3$ sample, SEM measurements were performed on as-cleaved crystals. EDS mapping presented in Figure 1 shows that the ratio of Cr:Si:Ge:Te (averaged over 10 measurements) is 1:0.8:0.1:3. This result reveals the presence of 10% Ge atomic vacancies in the sample.

Figure 2a,b presents the temperature dependence of zero-field cooling (ZFC) magnetic susceptibility $\chi(T) = M(T)/H$ measured in 1-kOe magnetic field applied parallel to a (a) and c (b) crystallographic axes. Curie–Weiss law $\chi = \frac{C}{T - \theta}$ fit at high temperatures yields Weiss temperatures $\theta_a = 61(2)$ K, $\theta_c = 70(2)$ K and high temperature paramagnetic moments $\mu_{\text{eff},a} = 4.14(2)\mu_B$ and $\mu_{\text{eff},c} = 3.91(2)\mu_B$ for $\text{CrSi}_{0.8}\text{Ge}_{0.1}\text{Te}_3$, consistent with dominant FM interactions below T_c and in line with the observed FM T_c and magnetic hysteresis loops.^[13,24] The approximate T_c value can be determined from the minima of the $d\chi/dT$ curves insets in Figure 2(a,b). It should be noted

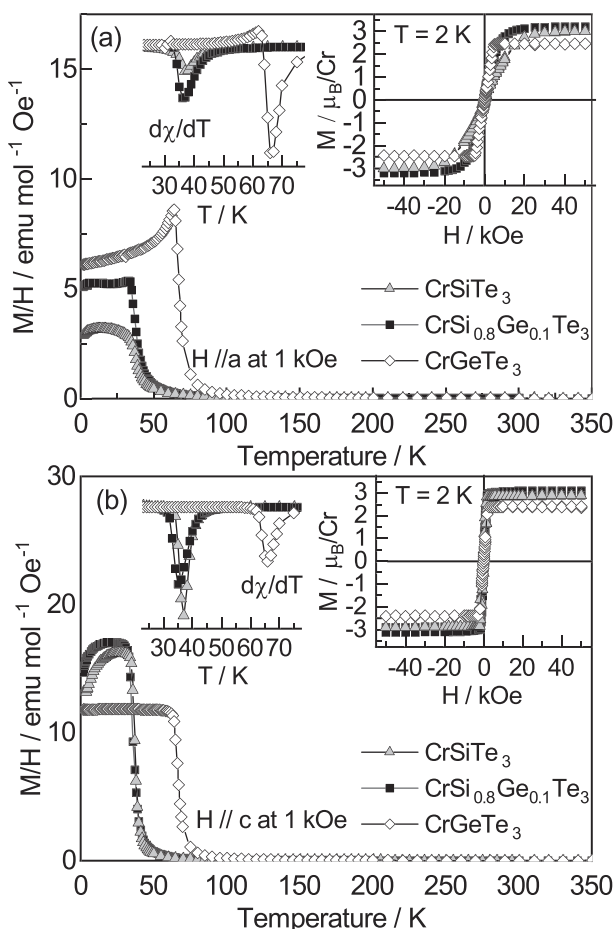


FIGURE 2 Temperature dependence of zero-field cooling (ZFC) $\chi = M/H$ for CrSiTe_3 , $\text{CrSi}_{0.8}\text{Ge}_{0.1}\text{Te}_3$ and CrGeTe_3 in 1-kOe magnetic field applied in-plane (a) and along the c -axis (b). Insets show transition temperatures of ferromagnetic orders ($d\chi/dT$) and magnetic hysteresis loops taken at 2 K

that, instead of monotonous rise, there is a weak but discernible shift to lower temperature in $d\chi/dT$ in $\text{CrSi}_{0.8}\text{Ge}_{0.1}\text{Te}_3$ when compared with CrSiTe_3 . This small reduction in FM transition temperature is likely induced by the presence of vacancies, as suggested by the EDS data. The presence of vacancies in this class of materials usually disarrange magnetic exchange due to disorder increment, which leads to the reduction of T_c .^[29]

Isostructural parent compounds CrSiTe_3 and CrGeTe_3 crystallize in the rhombohedral crystal structure, described with space group $R\bar{3}$ (C_{3i}^2).^[30] According to factor group analysis, five A_g and five double degenerate E_g symmetry modes are expected to be observed in the light scattering experiment. Detailed symmetry analysis, phonon mode distribution and selection rules for parent compounds (CrSiTe_3 and CrGeTe_3) can be found in Milosavljević et al.^[21] In our scattering configuration, the plane of incidence is ab plane, where $|a| = |b|$ ($\angle(a,b) = 120^\circ$) (inset in Figure 3), and the direction of incident (scattered) light propagation is along c -axes. According to the selection rules for this scattering configuration,^[21] all Raman active modes may be observed, having in mind that A_g symmetry modes can be detected only in parallel polarization configuration. The E_g symmetry modes are expected to appear in both the parallel and cross polarization configurations. Raman spectra of $\text{CrSi}_{0.8}\text{Ge}_{0.1}\text{Te}_3$, obtained by continuous change of the angle between polarization vectors of incident and

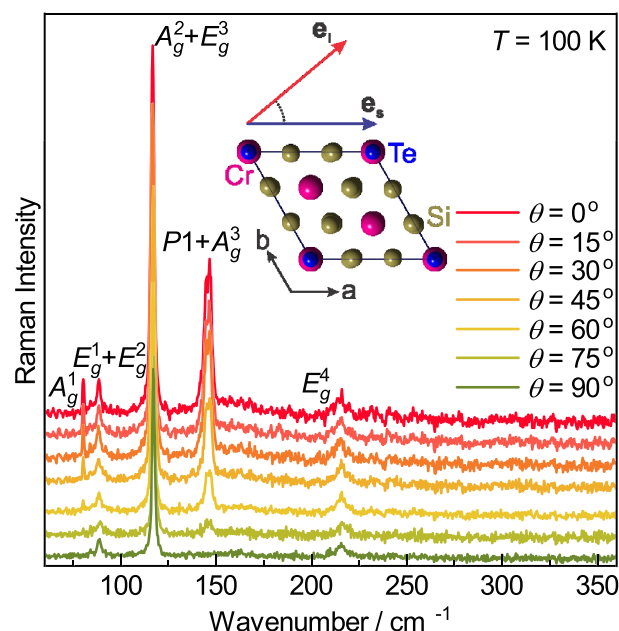


FIGURE 3 Raman spectra of $\text{CrSi}_{0.8}\text{Ge}_{0.1}\text{Te}_3$ single crystal, measured at 100 K, as a function of angle θ , between incident and scattered light polarization. Inset: schematic representation of the incident and scattered light polarization with respect to the crystal orientation [Colour figure can be viewed at wileyonlinelibrary.com]

scattered light, $\theta = \angle(\mathbf{e}_i, \mathbf{e}_s)$, ($0^\circ \leq \theta \leq 90^\circ$) at 100 K, are shown in Figure 3. It can be seen that by changing this angle, starting from $\theta = 0^\circ$, the intensities of the peaks at energies 80.2, 116.4 and 145.5 cm^{-1} continuously decrease and completely vanish for polarization angle of 90° . Therefore, these excitations obey pure A_g symmetry. On the other hand, the peaks at energies of 84.5, 88.3, 117.2 and 215.0 cm^{-1} are not influenced by change of polarization angle, so they can be identified as E_g symmetry modes.

Here, one should note that the feature observed at around 117 cm^{-1} in both scattering configurations is actually a two-peak structure comprising of 116.4 cm^{-1} A_g and 117.2 cm^{-1} E_g symmetry modes. Detailed analysis of the structure for two scattering configurations is presented in Figure A1 of Appendix. Furthermore, closer inspection of the data revealed that peak at energy of 145.5 cm^{-1} , which obeys pure A_g symmetry, is also composed of two modes, P1 (144.6 cm^{-1}) and A_g^3 (146.7 cm^{-1}), as shown in Figure A2 of Appendix.

Calculated optical phonon wavenumbers of the parent compounds, CrSiTe_3 and CrGeTe_3 , together with their experimental Raman active values as well as Raman mode energies of $\text{CrSi}_{0.8}\text{Ge}_{0.1}\text{Te}_3$, are compiled in Table 1. As expected, experimental values of $\text{CrSi}_{0.8}\text{Ge}_{0.1}\text{Te}_3$ Raman active modes are found between the values of the observed modes in parent compounds.^[21] Figure 4a shows compositional evolution of the peaks with highest

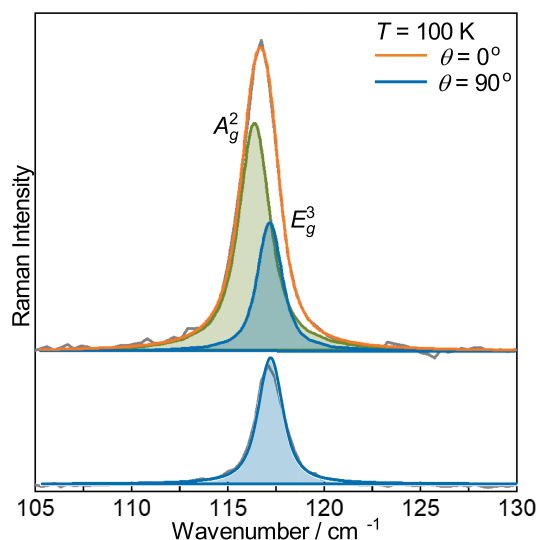


FIGURE A1 Decomposition of unresolved A_g^2 and E_g^3 symmetry modes obtained by simultaneous modelling in parallel and cross polarization configuration. Grey line represents the measured data, Voigt line of A_g^2 mode is shown by green, and blue lines represent the E_g^3 symmetry mode in parallel (upper panel) and cross (lower panel) polarization. The orange line is the superposition of these two lines [Colour figure can be viewed at [wileyonlinelibrary.com](#)]

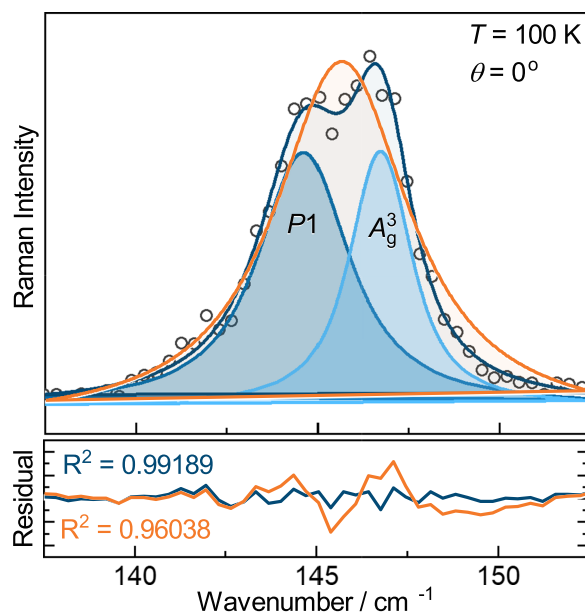


FIGURE A2 Decomposition of phonon mode in parallel scattering configuration on two A_g symmetry modes. Open circles represent the measured data and the blue one sum of two Voigt profile line shapes. Data modelled with one Voigt profile line shape (orange line) deviates significantly from measured data [Colour figure can be viewed at [wileyonlinelibrary.com](#)]

intensity, assigned as E_g^3 and A_g^3 symmetry modes in parent compounds. The E_g^3 mode energy changes almost linearly (Figure 4b), as a consequence of change in lattice parameters and “change of mass” effect. The observed energy shift is followed by doubling of the linewidth, dominantly induced by the significant crystalline disorder. The similar type of behaviour, with somewhat larger increase in the linewidth, was also observed for the A_g^3 symmetry mode. The most striking feature was the additional A_g symmetry mode (denoted as P1, see Figure A2 of the Appendix), observed in the doped sample. Generally, both the substitutional defects and vacancies may have similar impact on the Raman modes energy and linewidth. Here, the appearance of P1 peak can be understood as a consequence of the presence of vacancies on Si/Ge atomic site and their inharmonic distribution at nano-scale. The mode “splitting” is detected only for the A_g^3 but not for other observed modes, due to the fact that different nature of these vibrations results in different values of energy shifts. In the case of other modes, the difference between the shifts for corresponding domains is smaller than the spectral resolution of the instrument ($\sim 1.8 \text{ cm}^{-1}$), and therefore, the separate modes can not be resolved.

Figure 5 shows $\text{CrSi}_{0.8}\text{Ge}_{0.1}\text{Te}_3$ Raman scattering spectra measured at various temperatures. For clarity, spectra obtained for cross polarization configuration are

TABLE 1 Phonon symmetry, calculated ($T = 0$ K) and experimental ($T = 100$ K) Raman active phonon wavenumbers of parent compounds CrSiTe_3 and CrGeTe_3 .^[21] Experimental values for Raman active phonons of $\text{CrSi}_{0.8}\text{Ge}_{0.1}\text{Te}_3$ at 100 K are shown in the last column

Raman active modes					
Symmetry	Calculations		Experiment		
	CrSiTe_3	CrGeTe_3	CrSiTe_3	CrGeTe_3	$\text{CrSi}_{0.8}\text{Ge}_{0.1}\text{Te}_3$
A_g^1	88.2	84.2	—	—	80.2
E_g^1	93.5	82.0	88.9	83.5	84.5
E_g^2	96.9	90.8	—	—	88.3
E_g^3	118.3	114.2	118.2	112.2	117.2
A_g^2	122.0	105.9	—	—	116.4
A_g^3	148.0	134.8	147.4	137.9	146.7
A_g^4	208.7	200.3	—	—	—
E_g^4	219.5	209.6	217.2	217.5	215.0
E_g^5	357.4	229.8	—	—	—
A_g^5	508.9	290.7	—	296.6	—

Note: All values are given in cm^{-1} .

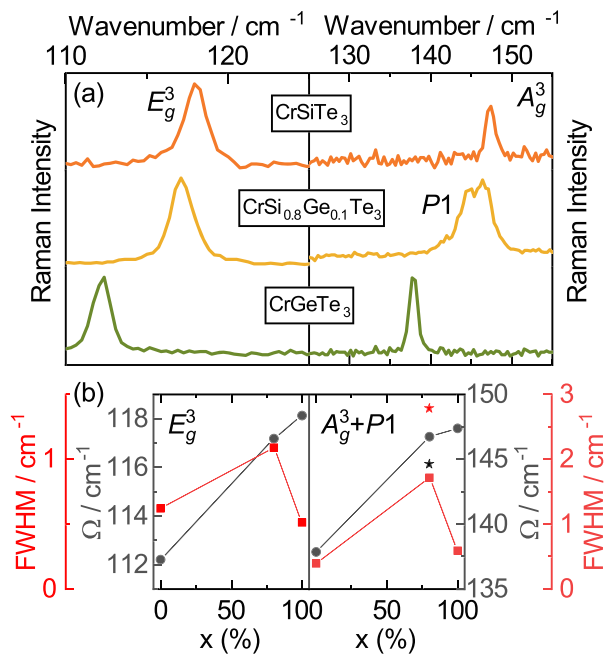


FIGURE 4 (a) Raman scattering spectra of E_g^3 and A_g^3 phonon modes of CrSiTe_3 (orange line), $\text{CrSi}_{0.8}\text{Ge}_{0.1}\text{Te}_3$ (yellow line) and CrGeTe_3 (green line) at $T = 100$ K measured in cross (left panel) and parallel (right panel) scattering configuration, respectively. (b) Energy (grey line) and linewidth (red line) of these two modes with respect to the percentage of Si atoms concentration. Energy and linewidth of $P1$ mode are marked with black and red star, respectively [Colour figure can be viewed at wileyonlinelibrary.com]

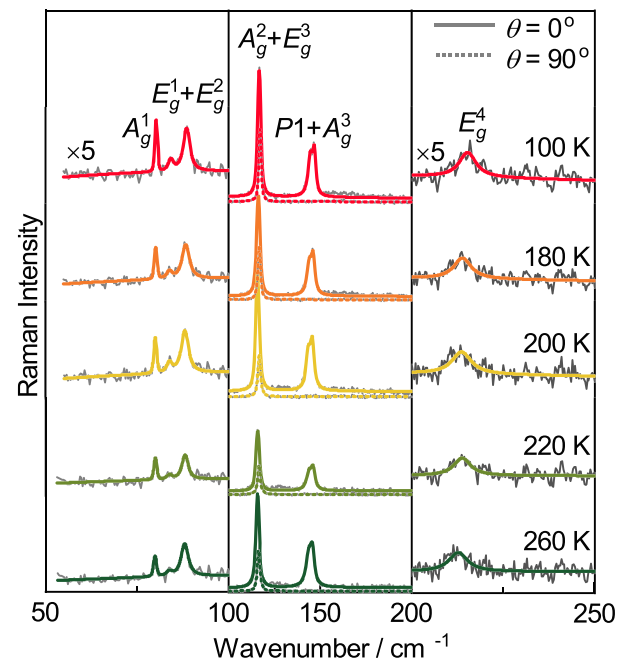


FIGURE 5 Raman spectra of $\text{CrSi}_{0.8}\text{Ge}_{0.1}\text{Te}_3$ single crystal measured at various temperatures. The spectra were analysed by using multiple Voigt peak functions and a single $\chi''_{\text{cont}} = a\Gamma\omega/(\Gamma^2 + \omega^2) + b\omega$ function, for parallel ($\theta = 0^\circ$, solid coloured lines) and cross ($\theta = 90^\circ$, dashed coloured lines) scattering configuration. For clarity, higher and lower energy ranges (left and right panel) are multiplied by the factor of five [Colour figure can be viewed at wileyonlinelibrary.com]

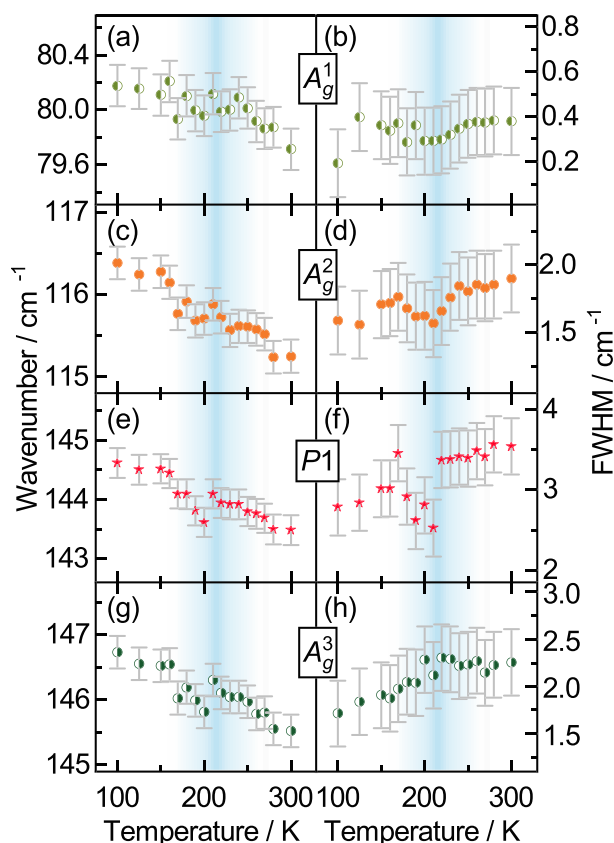


FIGURE 6 Energy and linewidth temperature dependence of A_g^1 (a,b), A_g^2 (c,d), $P1$ (e,f) and A_g^3 (g,h) Raman modes [Colour figure can be viewed at wileyonlinelibrary.com]

only shown for the mid-energy range. Temperature dependence of energies and linewidths of all the observed A_g symmetry modes, including $P1$, are presented in Figure 6. By heating the sample from 100 K to approximately 210 K, monotonous decrease in energy of all the A_g symmetry modes is present, dominantly driven by thermal expansion.^[31] In the temperature region around 210 K, these modes' energy exhibit small deviation, followed by a continuous decrease up to room temperature. In the same temperature region, deviation from expected anharmonic type of behaviour is observed for all the A_g symmetry modes linewidth. This effect is more pronounced for higher energy modes where the anharmonicity is expected to be higher. Similar response of analysed E_g symmetry modes is present and shown in Figure 7.

Concerning previously reported strong spin-phonon coupling in CrSiTe_3 ,^[15,21] which persists up to 180 K, we believe that this unconventional behaviour of energies and linewidths can be attributed to the coupling of the phonon modes to the spin system.^[32] Due to the doping and presence of vacancies, strong magnetic correlations in $\text{CrSi}_{0.8}\text{Ge}_{0.1}\text{Te}_3$ are sustained up to 210 K.

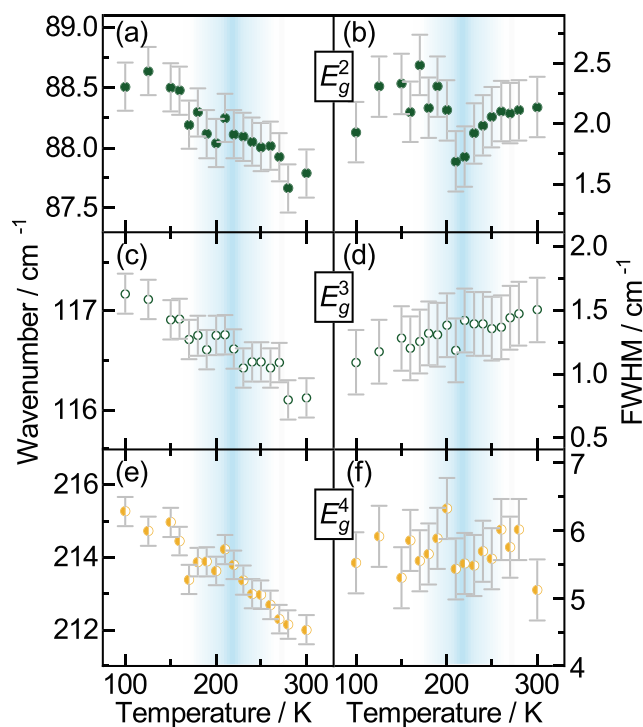


FIGURE 7 Energy and linewidth temperature dependence of E_g^2 (a,b), E_g^3 (c,d) and E_g^4 (e,f) symmetry modes [Colour figure can be viewed at wileyonlinelibrary.com]

4 | CONCLUSIONS

In summary, we presented temperature-dependent Raman scattering and magnetization studies of doped van der Waals ferromagnet $\text{CrSi}_{0.8}\text{Ge}_{0.1}\text{Te}_3$. SEM measurements revealed the presence of 10% vacancies on Si/Ge atomic site. As a consequence, magnetization measurements detected small but clear decrease in T_C . Seven out of 10 Raman active modes have been assigned in our Raman spectra. Temperature dependence of all the observed modes shows the persistence of magnetic correlations up to 210 K. In addition, the results revealed the appearance of the peak that obey pure A_g symmetry, which is attributed to the possible inhomogeneous distribution of Ge atoms and vacancies at nano-scale. This study provides an insight into the impact of doping and presence of vacancies on magnetic and lattice properties in this class of materials.

ACKNOWLEDGEMENTS

This work was supported by the Ministry of Education, Science and Technological Development of the Republic of Serbia and project no F-134 of the Serbian Academy of Sciences and Arts. DFT calculations were performed using computational resources at Johannes Kepler University, Linz, Austria. Electron microscopy was performed at Jozef Stefan Institute, Ljubljana, Slovenia,

under Slovenian Research Agency contract P1-0099 (B. V.). Work at BNL (crystal synthesis and magnetic characterization) was supported by the U.S. DOE-BES, Division of Materials Science and Engineering, under Contract No. DE-SC0012704.

ORCID

Ana Milosavljević  <https://orcid.org/0000-0002-8654-0475>

REFERENCES

- [1] F. Hellman, A. Hoffmann, Y. Tserkovnyak, G. S. Beach, E. E. Fullerton, C. Leighton, A. H. MacDonald, D. C. Ralph, D. A. Arena, H. A. Dürr, P. Fischer, *Rev. Mod. Phys.* **2017**, 89, 025006.
- [2] N. Sivadas, M. W. Daniels, R. H. Swendsen, S. Okamoto, D. Xiao, *Phys. Rev. B* **2015**, 91, 235425.
- [3] K. S. Novoselov, A. K. Geim, S. V. Morozov, D. Jiang, Y. Zhang, S. V. Dubonos, I. V. Grigorieva, A. A. Firsov, *Science* **2004**, 306(5696), 666.
- [4] Q. H. Wang, K. Kalantar-Zadeh, A. Kis, J. N. Coleman, M. S. Strano, *Nat. Nanotechnol.* **2012**, 7, 699.
- [5] G. Cheng, L. Lin, L. Zhenglu, J. Huiwen, S. Alex, X. Yang, C. Ting, B. Wei, W. Chenzhe, W. Yuan, Z. Q. Qiu, R. J. Cava, G. L. Steven, X. Jing, Z. Xiang, *Nature* **2017**, 546, 265.
- [6] B. Huang Bevin, G. Clark, E. Navarro-Moratalla, D. R. Klein, R. Cheng, K. L. Seyler, D. Zhong, E. Schmidgall, M. A. McGuire, D. H. Cobden, W. Yao, *Nature* **2017**, 546, 270.
- [7] K. S. Burch, D. Mandrus, J.-G. Park, *Nature* **2018**, 563 (7729), 47.
- [8] J.-X. Zhu, M. Janoschek, D. Chaves, S. J. C. Cezar, T. Durakiewicz, F. Ronning, Y. Sassa, M. Mansson, B. L. Scott, N. Wakeham, E. D. Bauer, J. D. Thompson, *Phys. Rev. B* **2016**, 93, 144404.
- [9] B. Chen, J. H. Yang, H. D. Wang, M. Imai, H. Ohta, C. Michioka, K. Yoshimura, M. H. Fang, *J. Phys. Soc. Japan* **2013**, 82(12), 124711.
- [10] A. Milosavljević, A. Šolajić, S. Djurdjic-Mijin, J. Pešić, B. Višić, Y. Liu, C. Petrovic, N. Lazarević, Z. V. Popović, *Phys. Rev. B* **2019**, 99, 214304.
- [11] M. A. McGuire, H. Dixit, V. R. Cooper, B. C. Sales, *Chem. Mat.* **2015**, 27(2), 612.
- [12] H. L. Zhuang, Y. Xie, P. R. C. Kent, P. Ganesh, *Phys. Rev. B* **2015**, 92, 035407.
- [13] G. T. Lin, H. L. Zhuang, X. Luo, B. J. Liu, F. C. Chen, J. Yan, Y. Sun, J. Zhou, W. J. Lu, P. Tong, Z. G. Sheng, *Phys. Rev. B* **2017**, 95, 245212.
- [14] M. Gibertini, M. Koperski, A. F. Morpurgo, K. S. Novoselov, *Nat. Nanotech.* **2019**, 14(5), 408.
- [15] L. D. Casto, A. J. Clune, M. O. Yokosuk, J. L. Musfeldt, T. J. Williams, H. L. Zhuang, M.-W. Lin, K. Xiao, R. G. Hennig, B. C. Sales, J.-Q. Yan, D. Mandrus, *APL Mat.* **2015**, 3(4), 041515.
- [16] X. Zhang, Y. Zhao, Q. Song, S. Jia, J. Shi, W. Han, *JJpn. J. Appl. Phys.* **2016**, 55(3), 033001.
- [17] B. Siberchicot, S. Jobic, V. Carteaux, P. Gressier, G. Ouvrard, *Phys. J. Chem.* **1996**, 100(14), 5863.
- [18] V. Carteaux, F. Moussa, M. Spiesser, *EPL* **1995**, 29(3), 251.
- [19] J. Zhang, X. Cai, W. Xia, A. Liang, J. Huang, C. Wang, L. Yang, H. Yuan, Y. Chen, S. Zhang, Y. Guo, *Phys. Rev. Lett.* **2019**, 123, 047203.
- [20] Y. F. Li, W. Wang, W. Guo, C. Y. Gu, H. Y. Sun, L. He, J. Zhou, Z. B. Gu, Y. F. Nie, X. Q. Pan, *Phys. Rev. B* **2018**, 98, 125127.
- [21] A. Milosavljević, A. Šolajić, J. Pešić, Y. Liu, C. Petrovic, N. Lazarević, Z. V. Popović, *Phys. Rev. B* **2018**, 98, 104306.
- [22] Y. Tian, M. J. Gray, H. Ji, R. J. Cava, K. S. Burch, *2D Mater.* **2016**, 3(2), 025035.
- [23] Y. Sun, R. C. Xiao, G. T. Lin, R. R. Zhang, L. S. Ling, Z. W. Ma, X. Luo, W. J. Lu, Y. P. Sun, Z. G. Sheng, *Appl. Phys. Lett.* **2018**, 112(7), 072409.
- [24] Y. Liu, C. Petrovic, *Phys. Rev. Mater.* **2019**, 3, 014001.
- [25] P. Giannozzi, S. Baroni, N. Bonini, M. Calandra, R. Car, C. Cavazzoni, D. Ceresoli, G. L. Chiarotti, M. Cococcioni, I. Dabo, A. Dal Corso, *J. Phys. Condens. Matter* **2009**, 21(39), 395502.
- [26] J. P. Perdew, K. Burke, M. Ernzerhof, *Phys. Rev. Lett.* **1996**, 77, 3865.
- [27] P. E. Blöchl, *Phys. Rev. B* **1994**, 50, 17953.
- [28] G. Kresse, D. Joubert, *Phys. Rev. B* **1999**, 59, 1758.
- [29] F. A. May, S. Calder, C. Cantoni, H. Cao, M. A. McGuire, *Phys. Rev. B* **2016**, 93, 014411.
- [30] R. E. Marsh, *J. Solid State Chem.* **1988**, 77(1), 190.
- [31] M. Opačić, N. Lazarević, M. Šćepanović, H. Ryu, H. Lei, C. Petrovic, Z. V. Popović, *J. Phys. Condens. Matter.*, 48(27), 485701.
- [32] F. Feng, N. Lazarević, C. Liu, J. Ji, Y. Wang, S. He, H. Lei, C. Petrovic, R. Yu, Z. V. Popović, Q. Zhang, *Phys. Rev. B* **2019**, 99, 144419.

How to cite this article: Milosavljević A, Šolajić A, Višić B, et al. Vacancies and spin-phonon coupling in CrSi_{0.8}Ge_{0.1}Te₃. *J Raman Spectrosc.* 2020;1–8. <https://doi.org/10.1002/jrs.5962>

APPENDIX: A DECOMPOSITION OF UNRESOLVED MODES

Analysing the spectra of CrSi_{0.8}Ge_{0.1}Te₃ single crystal, in different polarization configurations (Figure 3), in the energy range around 117 cm⁻¹, becomes clear that lower energy part completely disappears in cross polarization configuration, whereas higher energy part persists. Enlarged part of this energy region is shown in Figure A1, in parallel and cross polarization configuration at temperature of 100 K. After simultaneous modelling of these spectra becomes clear that they consist of the A_g² and E_g³ modes, at energies 116.4 and 117.2 cm⁻¹, respectively. This is completely supported with theoretical calculations presented in Table 1.

On the other hand, existence of P_1 is not predicted by theoretical calculations, as Raman active peak. Only closer inspection and detailed analysis, presented in

Figure A2, shows that much better agreement with experimental results gives modelling as a superposition of two Voigt lines.

Lattice dynamics and phase transitions in $\text{Fe}_{3-x}\text{GeTe}_2$

A. Milosavljević,¹ A. Šolajić,¹ S. Djurdjić-Mijin,¹ J. Pešić,¹ B. Višić,¹ Yu Liu (刘育),² C. Petrovic,²
N. Lazarević,¹ and Z. V. Popović^{1,3}

¹*Center for Solid State Physics and New Materials, Institute of Physics Belgrade,
University of Belgrade, Pregrevica 118, 11080 Belgrade, Serbia*

²*Condensed Matter Physics and Materials Science Department, Brookhaven National Laboratory, Upton, New York 11973-5000, USA*

³*Serbian Academy of Sciences and Arts, Knez Mihailova 35, 11000 Belgrade, Serbia*



(Received 23 April 2019; published 17 June 2019)

We present Raman spectroscopy measurements of the van der Waals bonded ferromagnet $\text{Fe}_{3-x}\text{GeTe}_2$, together with lattice dynamics. Four out of eight Raman active modes are observed and assigned, in agreement with numerical calculations. The energies and linewidths of the observed modes display an unconventional temperature dependence at about 150 and 220 K, followed by the nonmonotonic evolution of the Raman continuum. Whereas the former can be related to the magnetic phase transition, the origin of the latter anomaly remains an open question.

DOI: [10.1103/PhysRevB.99.214304](https://doi.org/10.1103/PhysRevB.99.214304)

I. INTRODUCTION

A novel class of magnetism hosting van der Waals bonded materials has recently become of great interest, since the materials are suitable candidates for numbers of technical applications [1–5]. Whereas CrXTe_3 ($X = \text{Si, Ge, Sn}$) and CrX_3 ($X = \text{Cl, Br, I}$) classes maintain low phase transition temperatures [1,6–9] even in a monolayer regime [10], $\text{Fe}_{3-x}\text{GeTe}_2$ has a high bulk transition temperature, between 220 and 230 K [11,12], making it a promising applicant.

The $\text{Fe}_{3-x}\text{GeTe}_2$ crystal structure consists of Fe_{3-x}Ge sublayers stacked between two sheets of Te atoms, and a van der Waals gap between neighboring Te layers [13,14]. Although the structure contains two different types of Fe atoms, it is revealed that vacancies take place only in the Fe2 sites [13,15].

Neutron diffraction, thermodynamic and transport measurements, and Mössbauer spectroscopy were used to analyze the magnetic and functional properties of $\text{Fe}_{3-x}\text{GeTe}_2$, with an Fe atom deficiency of $x \approx 0.1$ and $T_C = 225$ K. It is revealed that at a temperature of 1.5 K, magnetic moments of $1.95(5)\mu_B$ and $1.56(4)\mu_B$ are directed along the easy magnetic c axes [16]. In chemical vapor transport (CVT) grown Fe_3GeTe_2 single crystals, besides the ferromagnetic (FM)-paramagnetic (PM) transition at a temperature of 214 K, FM layers order antiferromagnetically at 152 K [17]. Close to a ferromagnetic transition temperature of 230 K, a possible Kondo lattice behavior, i.e., coupling of traveling electrons and periodically localized spins, is indicated at $T_K = 190 \pm 20$ K, which is in good agreement with theoretical predictions of 222 K [18].

Lattice parameters, as well as the magnetic transition temperature, vary with Fe ion concentration. Lattice parameters a and c follow the opposite trend, whereas the Curie temperature T_C decreases with an increase of Fe ion concentration [15]. For flux-grown crystals, the critical behavior was investigated by bulk dc magnetization around the ferromagnetic phase transition temperature of 152 K [13]. The anomalous Hall effect was also studied, where a significant amount of defects produces bad metallic behavior [19].

Theoretical calculations predict a dynamical stability of Fe_3GeTe_2 single-layer, uniaxial magnetocrystalline anisotropy that originates from spin-orbit coupling [20]. Recently, anomalous Hall effect measurements on single-crystalline metallic Fe_3GeTe_2 nanoflakes with different thicknesses are reported, with a T_C near 200 K and strong perpendicular magnetic anisotropy [21].

We report $\text{Fe}_{3-x}\text{GeTe}_2$ single-crystal lattice dynamic calculations, together with Raman spectroscopy measurements. Four out of eight Raman active modes were observed and assigned. Phonon energies are in a good agreement with theoretical predictions. Analyzed phonon energies and linewidths reveal fingerprint of a ferromagnetic phase transition at a temperature around 150 K. Moreover, discontinuities in the phonon properties are found at temperatures around 220 K. Consistently, in the same temperature range, the Raman continuum displays nonmonotonic behavior.

II. EXPERIMENT AND NUMERICAL METHOD

$\text{Fe}_{3-x}\text{GeTe}_2$ single crystals were grown by the self-flux method as previously described [13]. Samples for scanning electron microscopy (SEM) were cleaved and deposited on graphite tape. Energy dispersive spectroscopy (EDS) maps were collected using a FEI Helios NanoLab 650 instrument equipped with an Oxford Instruments EDS system, equipped with an X-max SSD detector operating at 20 kV. The surface of the as-cleaved $\text{Fe}_{3-x}\text{GeTe}_2$ crystal appears to be uniform for several tens of microns in both directions, as shown in Fig. 4 of Appendix A. Additionally, the elemental composition maps of Fe, Ge, and Te show a distinctive homogeneity of all the three elements (Fig. 5 of Appendix A).

For Raman scattering experiments, a Tri Vista 557 spectrometer was used in the backscattering micro-Raman configuration. As an excitation source, a solid state laser with a 532 nm line was used. In our scattering configuration, the plane of incidence is the ab plane, where $|a| = |b|$ ($\angle(a, b) = 120^\circ$), with the incident (scattered) light propagation direction

TABLE I. Top panel: The type of atoms, Wyckoff positions, each site's contribution to the phonons in the Γ point, and corresponding Raman tensors for the $P6_3/mmc$ space group of $\text{Fe}_{3-x}\text{GeTe}_2$. Bottom panel: Phonon symmetry, calculated optical Raman active phonon frequencies (in cm^{-1}) for the magnetic (M) phase, and experimental values for Raman active phonons at 80 K.

Space group $P6_3/mmc$ (No. 194)			
Fe1 (4e)			$A_{1g} + E_{1g} + E_{2g} + A_{2u} + E_{1u}$
Fe2 (2c)			$E_{2g} + A_{2u} + E_{1u}$
Ge (2d)			$E_{2g} + A_{2u} + E_{1u}$
Te (2c)			$A_{1g} + E_{1g} + E_{2g} + A_{2u} + E_{1u}$
Raman tensors			
$A_{1g} = \begin{pmatrix} a & 0 & 0 \\ 0 & a & 0 \\ 0 & 0 & b \end{pmatrix}$	$E_{1g} = \begin{pmatrix} 0 & 0 & -c \\ 0 & 0 & c \\ -c & c & 0 \end{pmatrix}$	$E_{2g} = \begin{pmatrix} d & -d & 0 \\ -d & -d & 0 \\ 0 & 0 & 0 \end{pmatrix}$	
Raman active modes			
Symmetry	Calculations (M)	Experiment (M)	
E_{2g}^1	50.2		
E_{1g}^1	70.3		
E_{2g}^2	122.2	89.2	
A_{1g}^1	137.2	121.1	
E_{1g}^2	209.5		
E_{2g}^3	228.6	214.8	
A_{1g}^2	233.4	239.6	
E_{2g}^4	334.3		

along the c axes. Samples were cleaved in the air, right before being placed in the vacuum. All the measurements were performed in the high vacuum (10^{-6} mbar) using a KONTE CryoVac continuous helium flow cryostat with a 0.5 mm thick window. To achieve laser beam focusing, a microscope objective with $\times 50$ magnification was used. A Bose factor correction of all spectra was performed. More details can be found in Appendix C.

Density functional theory (DFT) calculations were performed with the QUANTUM ESPRESSO (QE) software package [22]. We used the projector augmented-wave (PAW) pseudopotentials [23,24] with the Perdew-Burke-Ernzerhof (PBE) exchange-correlation functional [25]. The electron wave function and charge density cutoffs of 64 and 782 Ry were chosen, respectively. The k points were sampled using the Monkhorst-Pack scheme, with an $8 \times 8 \times 4$ Γ -centered grid. Both magnetic and nonmagnetic calculations were performed, using the experimentally obtained lattice parameters and the calculated values obtained by relaxing the theoretically proposed structure. In order to obtain the lattice parameters accurately, a treatment of the van der Waals interactions is introduced. The van der Waals interaction was included in all calculations using the Grimme-D2 correction [26]. Phonon frequencies in the Γ point are calculated within the linear response method implemented in QE.

III. RESULTS AND DISCUSSION

$\text{Fe}_{3-x}\text{GeTe}_2$ crystallizes in a hexagonal crystal structure, described with the $P6_3/mmc$ (D_{6h}^4) space group. The atom type, site symmetry, each site's contribution to the phonons

in the Γ point, and corresponding Raman tensors for the $P6_3/mmc$ space group are presented in Table I.

Calculated displacement patterns of Raman active modes, which can be observed in our scattering configuration, are presented in Fig. 1(a). Since the Raman tensor of the E_{1g} mode contains only the z component (Table I), by selection rules, it cannot be detected when measuring from the ab plane in the backscattering configuration. Whereas A_{1g} modes include vibrations of Fe and Te ions along the c axis, E_{2g} modes include in-plane vibrations of all four atoms. The Raman spectra of $\text{Fe}_{3-x}\text{GeTe}_2$ in the magnetic phase (M), at 80 K, and nonmagnetic phase (NM), at 280 K, in a parallel scattering configuration ($\mathbf{e}_i \parallel \mathbf{e}_s$), are presented in Fig. 1 (b). As it can be seen, four peaks at 89.2, 121.1, 214.8, and 239.6 cm^{-1} can be clearly observed at 80 K. According to numerical calculations (see Table I), peaks at 89.2 and 239.6 cm^{-1} correspond to two out of four E_{2g} modes, whereas peaks at 121.1 and 239.6 cm^{-1} can be assigned as two A_{1g} symmetry modes. One should note that numerical calculations performed by using experimentally obtained lattice parameters in the magnetic phase yield a better agreement with experimental values. This is not surprising since the calculations are performed for the stoichiometric compound as opposed to the nonstoichiometry of the sample. Furthermore, it is known that lattice parameters strongly depend on the Fe atom deficiency [15]. All calculated Raman and infrared phonon frequencies, for the magnetic and nonmagnetic phase of $\text{Fe}_{3-x}\text{GeTe}_2$, using relaxed and experimental lattice parameters, together with experimentally observed Raman active modes, are summarized in Table II of Appendix D.

After assigning all observed modes we focused on their temperature evolution. Having in mind finite instrumental

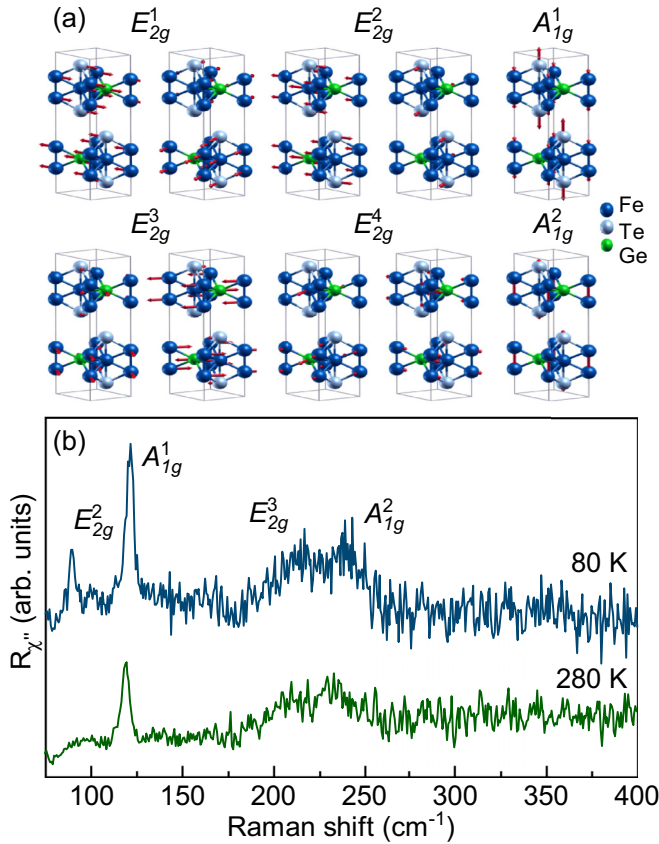


FIG. 1. (a) Displacement patterns of A_{1g} and E_{2g} symmetry modes. (b) Raman spectra of Fe_{3-x}GeTe₂ single crystal measured at different temperatures in a parallel polarization configuration.

broadening, the Voigt line shape was used for the data analysis [27,28]. The modeling procedure is described in detail in Appendix B and presented in Fig. 6. Figure 2 shows the temperature evolution of the energy and linewidth of the A_{1g}^1 , E_{2g}^3 , and A_{1g}^2 modes between 80 and 300 K. Upon heating the sample, both the energy and linewidth of A_{1g}^1 and A_{1g}^2 symmetry modes exhibit a small but sudden discontinuity at about 150 K [Figs. 2(a) and 2(e)]. An apparent discontinuity in energy of all analyzed Raman modes is again present at temperatures around 220 K. In the same temperature range the linewidths of these Raman modes show a clear deviation from the standard anharmonic behavior [27–31].

Apart from the anomalies in the phonon spectra, a closer inspection of the temperature-dependent Raman spectra measured in the parallel polarization configuration reveals a pronounced evolution of the Raman continuum [Fig. 3(a)]. For the analysis we have used a simple model including a damped Lorentzian and linear term, $\chi''_{\text{cont}} \propto a\Gamma\omega/(\omega^2 + \Gamma^2) + b\omega$ [32], where a , b , and Γ are temperature-dependent parameters. Figure 3(b) summarizes the results of the analysis with the linear term omitted (most likely originating from a luminescence). At approximately the same temperatures, where phonon properties exhibit discontinuities, the continuum temperature dependence manifests nonmonotonic behavior. The maximum positions of the curve were obtained by integrating

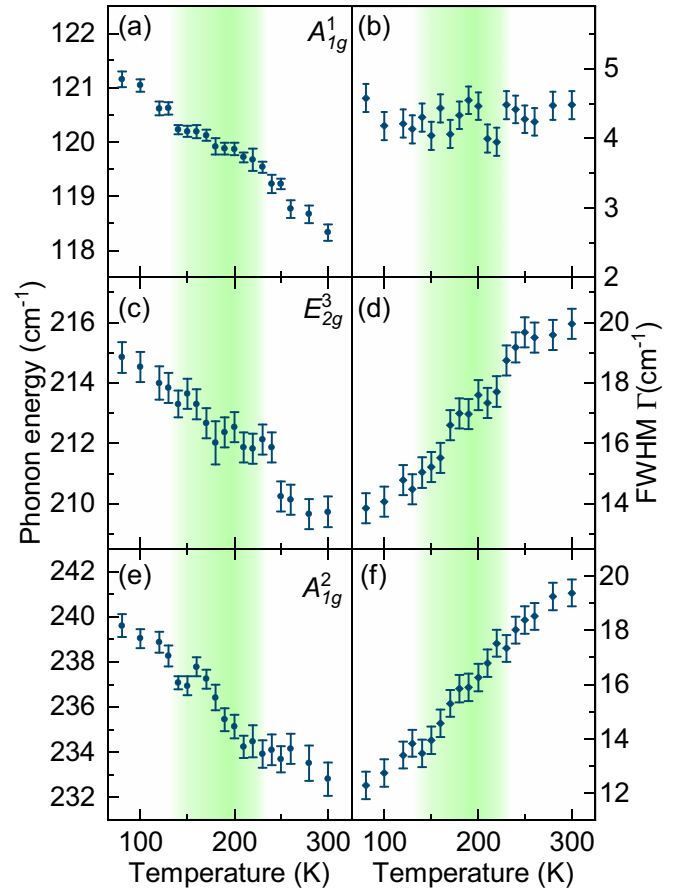


FIG. 2. Energy and linewidth temperature dependence of A_{1g}^1 [(a) and (b)], E_{2g}^3 [(c) and (d)], and A_{1g}^2 [(e) and (f)] phonon modes in Fe_{3-x}GeTe₂.

those shown in Fig. 3(b). The inset of Fig. 3(b) shows the temperature evolution of their displacements. This analysis confirms the presence of discontinuities in the electronic continuum at temperatures around 150 and 220 K, which leaves a trace in the phonon behavior around these temperatures (Fig. 2). While we do not have evidence for the Kondo effect in the Fe_{3-x}GeTe₂ crystals we measured, a modification of the electronic background at FM ordering due to localization or the Kondo effect cannot be excluded.

The temperature evolutions of the phonon self-energies and the continuum observed in the Raman spectra of Fe_{3-x}GeTe₂ suggest the presence of phase transition(s). Magnetization measurements of the samples were performed as described in Ref. [13], revealing a FM-PM transition at 150 K. Thus, the discontinuity in the observed phonon properties around this temperature can be traced back to the weak to moderate spin-phonon coupling. The question remains open regarding the anomaly observed at about 220 K. As previously reported, the Curie temperature of the Fe_{3-x}GeTe₂ single crystals grown by the CVT method is between 220 and 230 K [11,12,14], varying with the vacancy concentration, i.e., a decrease in the vacancy content will result an increment of T_C [15]. On the other hand, the Fe_{3-x}GeTe₂ crystals grown by the self-flux method usually have a lower Curie temperature, since the

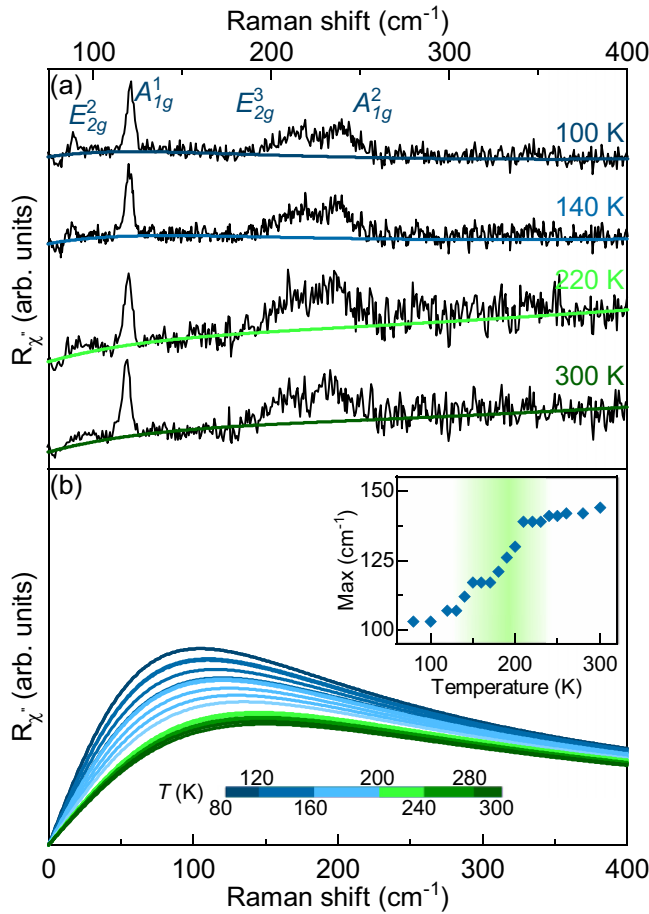


FIG. 3. (a) Raman spectra of $\text{Fe}_{3-x}\text{GeTe}_2$ at four temperatures measured in a parallel polarization configuration. Solid lines represent the theoretical fit to the experimental data. (b) Temperature evolution of the electronic continuum after omitting the linear term. Inset: Displacement of the maximum of fitted curves.

vacancy content is higher [13,15]. Crystals used in the Raman scattering experiment presented here were grown by the self-flux method with a Fe vacancy content of $x \approx 0.36$ [13]. This is in good agreement with our EDS results of $x = 0.4 \pm 0.1$, giving rise to the FM-PM transition at 150 K. Nevertheless,

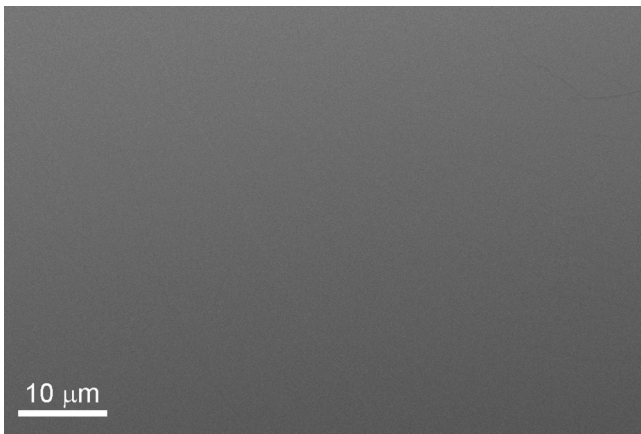


FIG. 4. SEM image of a $\text{Fe}_{3-x}\text{GeTe}_2$ single crystal.

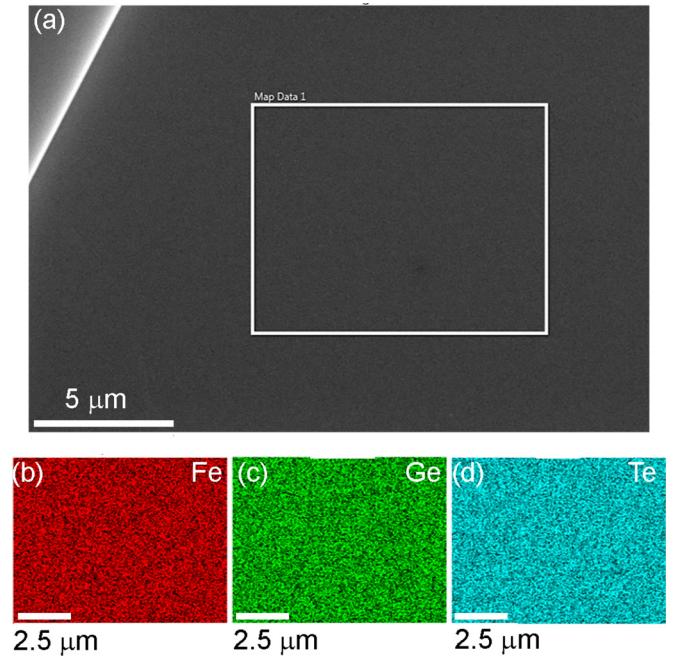


FIG. 5. EDS mapping on a $\text{Fe}_{3-x}\text{GeTe}_2$ single crystal. (a) Secondary electron image of the crystal with the mapping performed within the rectangle. (b)–(d) Associated EDS maps for Fe, Ge, and Te, respectively.

an inhomogeneous distribution of vacancies may result the formation of vacancy depleted “islands” which in turn would result in an anomaly at 220 K similar to the one observed in our Raman data. However, the EDS data (see Fig. 5) do not support this possibility. At this point we can only speculate that while the long-range order temperature is shifted to a lower temperature by the introduction of vacancies, short-range correlations may develop at 220 K.

IV. CONCLUSION

We have studied the lattice dynamics of flux-grown $\text{Fe}_{3-x}\text{GeTe}_2$ single crystals by means of Raman spectroscopy and DFT. Four out of eight Raman active modes, two A_{1g} and two E_{2g} , have been observed and assigned. DFT calculations are in good agreement with experimental results. The temperature dependence of the A_{1g}^1 , E_{2g}^3 , and A_{1g}^2 mode properties reveals a clear fingerprint of spin-phonon coupling, at a temperature of around 150 K. Furthermore, the anomalous behavior in the energies and linewidths of the observed phonon modes is present in the Raman spectra at temperatures around 220 K with the discontinuity also present in the electronic continuum. Its origin still remains an open question, and requires further analysis.

ACKNOWLEDGMENTS

The work was supported by the Serbian Ministry of Education, Science and Technological Development under Projects No. III45018 and No. OI171005. DFT calculations were performed using computational resources at Johannes Kepler University, Linz, Austria. Materials synthesis was supported

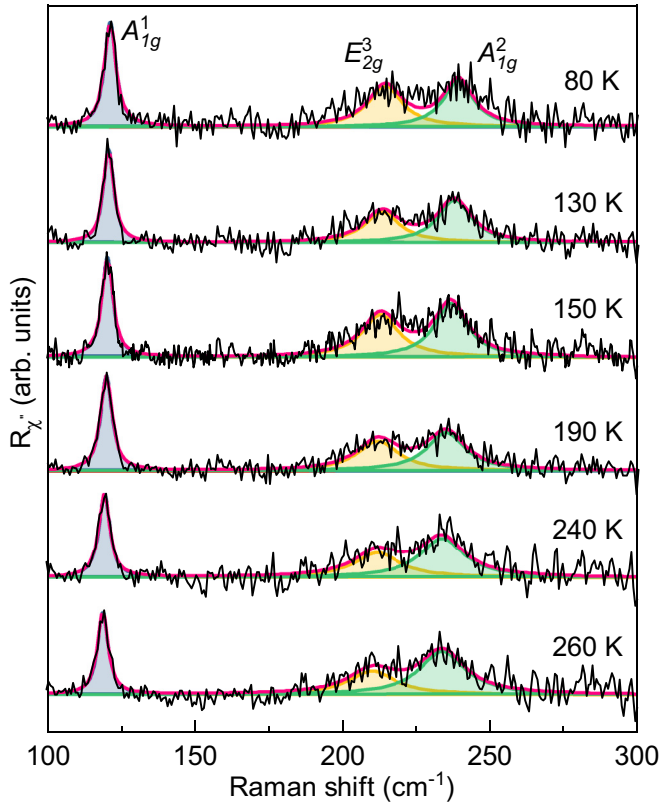


FIG. 6. Modeled Raman spectra of $\text{Fe}_{3-x}\text{GeTe}_2$ single crystal, after subtracting continuum contributions, obtained at various temperatures. For experimental data modeling, the Voigt line shape was used.

by the US Department of Energy, Office of Basic Energy Sciences as part of the Computation Material Science Program (Y.L. and C.P.). Electron microscopy was performed at Jozef Stefan Institute, Ljubljana, Slovenia under Slovenian Research Agency Contract No. P1-0099 (B.V.). This work has received funding from the European Union's Horizon 2020 research and innovation program under the Marie Skłodowska-Curie Grant Agreement No. 645658 (DAFNEOX Project).

APPENDIX A: ELECTRON MICROSCOPY

In order to examine the uniformity of $\text{Fe}_{3-x}\text{GeTe}_2$, Scanning electron microscopy (SEM) was performed on as-cleaved crystals. It can be seen from Fig. 4 that the crystals maintain uniformity for several tens of microns. Furthermore, the elemental composition was obtained using EDS mapping, as shown in Fig. 5. The atomic percentage, averaged over ten measurements, is 47%, 17%, and 36% ($\pm 2\%$) for Fe, Ge, and Te, respectively, with the vacancy content $x = 0.4 \pm 0.1$. The maps associated with the selected elements appear homogeneous, as they are all present uniformly with no apparent islands or vacancies.

APPENDIX B: DATA MODELING

In order to obtain the temperature dependence of the energies and linewidths of the observed $\text{Fe}_{3-x}\text{GeTe}_2$ phonon modes, the Raman continuum, shown in colored lines in

TABLE II. Top panel: Comparison of calculated energies of Raman active phonons using relaxed (R) and experimental [non-relaxed (NR)] lattice parameters for the magnetic (M) and nonmagnetic phase (NM), given in cm^{-1} . Obtained experimental values in the magnetic phase at a temperature of 80 K are given in the last column. Bottom panel: Comparison of calculated energies of infrared optical phonons of $\text{Fe}_{3-x}\text{GeTe}_2$.

Raman active modes					
Sym.	Calculations				Experiment (M)
	NM-R	M-R	NM-NR	M-NR	
E_{2g}^1	28.4	49.6	33.9	50.2	
E_{1g}^1	79.2	70.2	71.7	70.3	
E_{2g}^2	115.5	121.0	100.0	122.2	89.2
A_{1g}^1	151.7	139.2	131.7	137.2	121.1
E_{1g}^2	225.5	206.0	194.3	209.5	
E_{2g}^3	238.0	232.6	204.9	228.6	214.8
A_{1g}^2	272.0	262.6	235.7	233.4	239.6
E_{2g}^4	362.0	337.6	315.4	334.7	
Infrared active modes					
A_{2u}^1	70.7	96.6	73.5	92.7	
E_{1u}^1	112.5	121.2	89.4	121.6	
A_{2u}^2	206.0	162.5	183.1	153.7	
E_{1u}^2	226.4	233.6	192.1	231.3	
A_{2u}^3	271.8	248.6	240.8	241.0	
E_{1u}^3	361.1	336.6	314.7	334.7	

Fig. 3(a), was subtracted for simplicity from the raw Raman susceptibility data (black line). The spectra obtained after the subtraction procedure are presented in Fig. 6 (black line) for various temperatures. Because of the finite resolution of the spectrometer and the fact that line shapes of all the observed phonons are symmetric, the Voigt line shape ($\Gamma_G = 0.8 \text{ cm}^{-1}$) was used for data modeling. Blue, yellow, and green lines in Fig. 6 represent fitting curves for A_{1g}^1 , E_{2g}^3 , and A_{1g}^2 phonon modes, respectively, whereas the overall spectral shape is shown in the red line.

APPENDIX C: EXPERIMENTAL DETAILS

Before being placed in a vacuum and being cleaved, the sample was glued to a copper plate with GE varnish in order to achieve good thermal conductivity and prevent strain effects. Silver paste, as a material with high thermal conductivity, was used to attach the copper plate with the sample to the cryostat. The laser beam spot, focused through an Olympus long-range objective of $\times 50$ magnification, was approximately $6 \mu\text{m}$ in size, with a power less than 1 mW at the sample surface. A TriVista 557 triple spectrometer was used in the subtractive mode, with a diffraction grating combination of 1800/1800/2400 grooves/mm and the entrance and second intermediate slit set to $80 \mu\text{m}$, in order to enhance stray light rejection and attain good resolution.

APPENDIX D: CALCULATIONS

In Table II the results of DFT calculations are presented for magnetic (M) and nonmagnetic (NM) relaxed and experimental lattice parameters. For comparison, the

experimental results are shown in the last column. Since the lattice parameters strongly depend on the Fe atom deficiency, the best agreement with experimental results gives the magnetic nonrelaxed solution.

- [1] N. Sivadas, M. W. Daniels, R. H. Swendsen, S. Okamoto, and D. Xiao, Magnetic ground state of semiconducting transition-metal trichalcogenide monolayers, *Phys. Rev. B* **91**, 235425 (2015).
- [2] K. S. Novoselov, A. K. Geim, S. V. Morozov, D. Jiang, Y. Zhang, S. V. Dubonos, I. V. Grigorieva, and A. A. Firsov, Electric field effect in atomically thin carbon films, *Science* **306**, 666 (2004).
- [3] Q. H. Wang, K. Kalantar-Zadeh, A. Kis, J. N. Coleman, and M. S. Strano, Electronics and optoelectronics of two-dimensional transition metal dichalcogenides, *Nat. Nanotechnol.* **7**, 699 (2012).
- [4] C. Gong, L. Li, Z. Li, H. Ji, A. Stern, Y. Xia, T. Cao, W. Bao, C. Wang, Y. Wang, Z. Q. Qiu, R. J. Cava, S. G. Louie, J. Xia, and X. Zhang, Discovery of intrinsic ferromagnetism in two-dimensional van der Waals crystals, *Nature (London)* **546**, 265 (2017).
- [5] B. Huang, G. Clark, E. Navarro-Moratalla, D. R. Klein, R. Cheng, K. L. Seyler, D. Zhong, E. Schmidgall, M. A. McGuire, D. H. Cobden, W. Yao, D. Xiao, P. Jarillo-Herrero, and X. Xu, Layer-dependent ferromagnetism in a van der Waals crystal down to the monolayer limit, *Nature (London)* **546**, 270 (2017).
- [6] M. A. McGuire, H. Dixit, V. R. Cooper, and B. C. Sales, Coupling of crystal structure and magnetism in the layered, ferromagnetic insulator CrI_3 , *Chem. Mater.* **27**, 612 (2015).
- [7] H. L. Zhuang, Y. Xie, P. R. C. Kent, and P. Ganesh, Computational discovery of ferromagnetic semiconducting single-layer CrSnTe_3 , *Phys. Rev. B* **92**, 035407 (2015).
- [8] G. T. Lin, H. L. Zhuang, X. Luo, B. J. Liu, F. C. Chen, J. Yan, Y. Sun, J. Zhou, W. J. Lu, P. Tong, Z. G. Sheng, Z. Qu, W. H. Song, X. B. Zhu, and Y. P. Sun, Tricritical behavior of the two-dimensional intrinsically ferromagnetic semiconductor CrGeTe_3 , *Phys. Rev. B* **95**, 245212 (2017).
- [9] L. D. Casto, A. J. Clune, M. O. Yokosuk, J. L. Musfeldt, T. J. Williams, H. L. Zhuang, M.-W. Lin, K. Xiao, R. G. Hennig, B. C. Sales, J.-Q. Yan, and D. Mandrus, Strong spin-lattice coupling in CrSiTe_3 , *APL Mater.* **3**, 041515 (2015).
- [10] M.-W. Lin, H. L. Zhuang, J. Yan, T. Z. Ward, A. A. Puretzy, C. M. Rouleau, Z. Gai, L. Liang, V. Meunier, B. G. Sumpter, P. Ganesh, P. R. C. Kent, D. B. Geohegan, D. G. Mandrus, and K. Xiao, Ultrathin nanosheets of CrSiTe_3 : A semiconducting two-dimensional ferromagnetic material, *J. Mater. Chem. C* **4**, 315 (2016).
- [11] J.-X. Zhu, M. Janoschek, D. S. Chaves, J. C. Cezar, T. Durakiewicz, F. Ronning, Y. Sassa, M. Mansson, B. L. Scott, N. Wakeham, E. D. Bauer, and J. D. Thompson, Electronic correlation and magnetism in the ferromagnetic metal Fe_3GeTe_2 , *Phys. Rev. B* **93**, 144404 (2016).
- [12] B. Chen, J. H. Yang, H. D. Wang, M. Imai, H. Ohta, C. Michioka, K. Yoshimura, and M. H. Fang, Magnetic properties of layered itinerant electron ferromagnet Fe_3GeTe_2 , *J. Phys. Soc. Jpn.* **82**, 124711 (2013).
- [13] Y. Liu, V. N. Ivanovski, and C. Petrovic, Critical behavior of the van der Waals bonded ferromagnet $\text{Fe}_{3-x}\text{GeTe}_2$, *Phys. Rev. B* **96**, 144429 (2017).
- [14] H.-J. Deiseroth, K. Aleksandrov, C. Reiner, L. Kienle, and R. K. Kremer, Fe_3GeTe_2 and Ni_3GeTe_2 - Two new layered transition-metal compounds: Crystal structures, HRTEM investigations, and magnetic and electrical properties, *Eur. J. Inorg. Chem.* **2006**, 1561 (2006).
- [15] A. F. May, S. Calder, C. Cantoni, H. Cao, and M. A. McGuire, Magnetic structure and phase stability of the van der Waals bonded ferromagnet $\text{Fe}_{3-x}\text{GeTe}_2$, *Phys. Rev. B* **93**, 014411 (2016).
- [16] V. Yu. Verchenko, A. A. Tsirlin, A. V. Sobolev, I. A. Presniakov, and A. V. Shevelkov, Ferromagnetic order, strong magnetocrystalline anisotropy, and magnetocaloric effect in the layered telluride $\text{Fe}_{3-\delta}\text{GeTe}_2$, *Inorg. Chem.* **54**, 8598 (2015).
- [17] J. Yi, H. Zhuang, Q. Zou, Z. Wu, G. Cao, S. Tang, S. A. Calder, P. R. C. Kent, D. Mandrus, and Z. Gai, Competing antiferromagnetism in a quasi-2D itinerant ferromagnet: Fe_3GeTe_2 , *2D Mater.* **4**, 011005 (2016).
- [18] Y. Zhang, H. Lu, X. Zhu, S. Tan, W. Feng, Q. Liu, W. Zhang, Q. Chen, Y. Liu, X. Luo, D. Xie, L. Luo, Z. Zhang, and X. Lai, Emergence of Kondo lattice behavior in a van der Waals itinerant ferromagnet, Fe_3GeTe_2 , *Sci. Adv.* **4**, eaao6791 (2018).
- [19] Y. Liu, E. Stavitski, K. Attenkofer, and C. Petrovic, Anomalous Hall effect in the van der Waals bonded ferromagnet $\text{Fe}_{3-x}\text{GeTe}_2$, *Phys. Rev. B* **97**, 165415 (2018).
- [20] H. L. Zhuang, P. R. C. Kent, and R. G. Hennig, Strong anisotropy and magnetostriction in the two-dimensional Stoner ferromagnet Fe_3GeTe_2 , *Phys. Rev. B* **93**, 134407 (2016).
- [21] C. Tan, J. Lee, S.-G. Jung, T. Park, S. Albarakati, J. Partridge, M. R. Field, D. G. McCulloch, L. Wang, and C. Lee, Hard magnetic properties in nanoflake van der Waals Fe_3GeTe_2 , *Nat. Commun.* **9**, 1554 (2018).
- [22] P. Giannozzi *et al.*, QUANTUM ESPRESSO: A modular and open-source software project for quantum simulations of materials, *J. Phys.: Condens. Matter* **21**, 395502 (2009).
- [23] P. E. Blöchl, Projector augmented-wave method, *Phys. Rev. B* **50**, 17953 (1994).
- [24] G. Kresse and D. Joubert, From ultrasoft pseudopotentials to the projector augmented-wave method, *Phys. Rev. B* **59**, 1758 (1999).
- [25] J. P. Perdew, K. Burke, and M. Ernzerhof, Generalized Gradient Approximation Made Simple, *Phys. Rev. Lett.* **77**, 3865 (1996).
- [26] S. Grimme, Semiempirical GGA-type density functional constructed with a long-range dispersion correction, *J. Comput. Chem.* **27**, 1787 (2006).
- [27] A. Milosavljević, A. Šolajić, J. Pešić, Y. Liu, C. Petrovic, N. Lazarević, and Z. V. Popović, Evidence of spin-phonon coupling in CrSiTe_3 , *Phys. Rev. B* **98**, 104306 (2018).
- [28] A. Baum, A. Milosavljević, N. Lazarević, M. M. Radonjić, B. Nikolić, M. Mitschek, Z. I. Maranloo, M. Šćepanović, M. Grujić-Brožćin, N. Stojilović, M. Opel, A. Wang,

- C. Petrovic, Z. V. Popović, and R. Hackl, Phonon anomalies in FeS, *Phys. Rev. B* **97**, 054306 (2018).
- [29] M. Opačić, N. Lazarević, M. M. Radonjić, M. Šćepanović, H. Ryu, A. Wang, D. Tanasković, C. Petrovic, and Z. V. Popović, Raman spectroscopy of $K_xK_{2-y}Se_2$ single crystals near the ferromagnet–paramagnet transition, *J. Phys.: Condens. Matter* **28**, 485401 (2016).
- [30] Z. V. Popović, N. Lazarević, S. Bogdanović, M. M. Radonjić, D. Tanasković, R. Hu, H. Lei, and C. Petrovic, Signatures of the spin-phonon coupling in $Fe_{1+y}Te_{1-x}Se_x$ alloys, *Solid State Commun.* **193**, 51 (2014).
- [31] Z. V. Popović, M. Šćepanović, N. Lazarević, M. Opačić, M. M. Radonjić, D. Tanasković, H. Lei, and C. Petrovic, Lattice dynamics of $BaFe_2X_3$ ($X = S, Se$) compounds, *Phys. Rev. B* **91**, 064303 (2015).
- [32] T. P. Devereaux and R. Hackl, Inelastic light scattering from correlated electrons, *Rev. Mod. Phys.* **79**, 175 (2007).



Self-assembled line network in BiFeO₃ thin films

B. Colson^a, V. Fuentes^a, Z. Konstantinović^{b,*}, D. Colson^c, A. Forget^c, N. Lazarević^b,
M. Šćepanović^b, Z.V. Popović^b, C. Frontera^a, Ll. Balcells^a, B. Martínez^a, A. Pomar^a

^a Institut de Ciència de Materials de Barcelona, ICMA-B-CSIC, Campus UAB, 08193 Bellaterra, Spain

^b Center for Solid State Physics and New Materials, Institute of Physics Belgrade, Pregrevica 118, University of Belgrade, Serbia

^c SPEC, CEA, CNRS UMR 3680, Université Paris-Saclay, 91191 Gif sur Yvette Cedex, France

ARTICLE INFO

Keywords:

Multiferroic thin films
Long-range ordered nanostructures
Growth kinetic
Mixed phase nanodomains

ABSTRACT

In this work we report on the controlled fabrication of a self-assembled line network in highly epitaxial BiFeO₃ thin films on top of LaAlO₃ in the kinetically limited grown region by RF sputtering. As previously shown in the case of manganite thin films, the remarkable degree of ordering is achieved using vicinal substrates with well-defined step-terrace morphology. Nanostructured BiFeO₃ thin films show mixed-phase morphology. Besides typical formation following (100) and (010) axes, some mixed phase nanodomains are detected also in-between the regular line network. These particular microstructures open a playground for future applications in multi-ferroic nanomaterials.

1. Introduction

Bismuth ferrite BiFeO₃ (BFO) is a very active research domain due to environment friendly room-temperature multiferroic character with wide range of potential applications, from the low-power spintronic to optical devices [1,2]. The very large electrical polarization [3,4], coupling between the polarization and magnetic easy plane [5–7] and its strong sensitivity on the epitaxial strain are crucial parameters for applications and for understanding their fundamental properties in general [8,9]. The control over the ferroelectric polarization through the structural strain and the miscut angle of underlying substrates rapidly gain interest [10], additionally enhanced with the discovery of mixed phase nanodomains [9,11–13]. In addition, it has been recently shown that the kinetic growth conditions allow synthesizing high quality films with selective ferroelectric domains [14].

Self-organization of long-range ordered nanostructures of transition metal oxide thin films is of major relevance for both, the study of enhanced or novel physical properties at the nanoscale (from enhanced magneto-resistive properties to unexpected interfacial effects) and for developing a new generation of devices [15,16]. This bottom-up nanostructural approach presents an alternative to the more conventional top-down lithography-based methods with numerous advantages ranging from rapid preparation of low-cost and large surface oxide nanostructures to the formation of nanoobjects with size and densities beyond actual possibilities [17]. Finally, ferroelectric BFO thin films crystallize in the very similar rhombohedral structure as previously

studied LSMO thin films [15,17] and open a huge playground for the formation of nanostructured networks at the surface.

In this paper, we report on the formation of regular nanostructures in ferroelectric BFO thin films grown on top of LaAlO₃ (LAO) substrates by RF sputtering. The nanostructuration of BFO thin films is directly induced by structural and morphological features of the underlying substrate (lattice parameter inducing strain conditions on the one side and step-terrace morphology and chemical affinity on the other side). In addition to regular network, stripe-like features are detected and analyzed by X-ray, Raman and AFM spectroscopy.

2. Experimental

BFO thin films were grown by RF magnetron sputtering on top of LaAlO₃ (0 0 1) substrates under an oxygen partial pressure of 0.19 Pa using commercial stoichiometric target (Kurt J. Lesker Company). Growth conditions (growth rate of F ~ 0.03 ML/s and high growth temperature) were adjusted to promote self-organized surface nanostructures in the kinetic growth regime, i.e. far away from thermodynamic relaxation mechanisms, that have been previously studied in detail in GeSi semiconductors [18]. By a fine tuning of the growth kinetic pathway, the surface diffusion was reduced (but not completely suppressed), taking advantage of the unusual misfit strain relaxation in presence of stepped substrate [17]. Substrates were previously washed in milliQ water and thermally treated at 1000 °C to assure the presence of terrace-step morphology with unit cell height. The thickness value, *t*,

* Corresponding author.

E-mail address: zorica.konstantinovic@ipb.ac.rs (Z. Konstantinović).

<https://doi.org/10.1016/j.jmmm.2020.166898>

Received 16 October 2019; Received in revised form 6 April 2020; Accepted 14 April 2020

Available online 15 April 2020

0304-8853/ © 2020 Elsevier B.V. All rights reserved.

of the different BFO/LAO films presented in this study is in the range of $40 \text{ nm} < t < 50 \text{ nm}$.

The surface morphology of the films was studied using Atomic Force Microscopy (AFM) and Scanning Electron Microscopy (SEM). AFM images were obtained in a MFP3D Asylum AFM while SEM images were obtained with a QUANTA FEI 200 FEG-ESEM. The crystal structure was characterized by X-ray diffraction (XRD) and reflectivity techniques (XRR) using a Siemens D5000 diffractometers with $K\alpha$ -Cu radiation.

Magnetic characterization was performed at room temperature (in-plane configuration $H \parallel (100)$ and out-of-plane configuration $H \perp (100)$) with a superconducting quantum interference device magnetometer (Quantum Design). In order to estimate the magnetization of the film, the diamagnetic background of substrates was subtracted (estimated from negative slope of $M(H)$ at high magnetic field, $10000 < H < 50000 \text{ Oe}$).

Raman scattering measurements were performed using a Jobin Yvon T64000 Raman system in μ -Raman configuration. A Coherent VerdiG solid state laser with 532 nm line was used as an excitation source. Laser beam focusing was accomplished by a microscope objective with $\times 50$ magnification.

3. Results and discussion

BiFeO_3 presents, at room temperature, a rhombohedral structure in bulk form (lattice constant $a_{\text{bulk}} = 3.964 \text{ \AA}$) [3,5]. In thin films, structural and functional properties of this multiferroic compound can be drastically modified due to presence of the structural strain induced by the selected substrate [19]. Particularly, the epitaxial growth of BFO on top of LAO substrate induces huge compressive in-plane strain, which allows stabilizing the tetragonal phase, correlated with theoretically predicted giant ferroelectric polarization [20]. In this study, the films were grown under large compressive strain of $\varepsilon = (a_{\text{LAO}} - a_{\text{BFO}})/a_{\text{BFO}} = -4.62\%$, giving rise to a significantly larger perpendicular cell parameter compared to bulk counterpart (see below).

Fig. 1 shows the formation of the long range ordered line network on top of the BFO surface during crystal growth. Fast Fourier Transform (FFT) (Fig. 1(b)) of topographic AFM image (Fig. 1(a)) indicate long-range order of grooves along one specific direction (see two high intensity dots in circles) with a separation around $1/k \sim 150 \text{ nm}$. Two

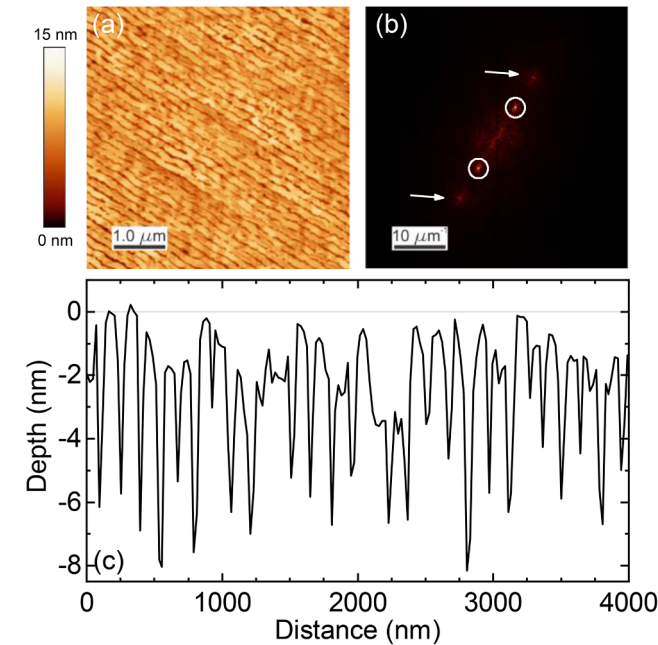


Fig. 1. (a) Topographic AFM image ($4 \times 4 \mu\text{m}^2$) of BiFeO_3 film (thickness, $t = 45 \text{ nm}$) grown on top of LAO and (b) corresponding Fast Fourier Transform (c) Typical line profile of regular grooves.

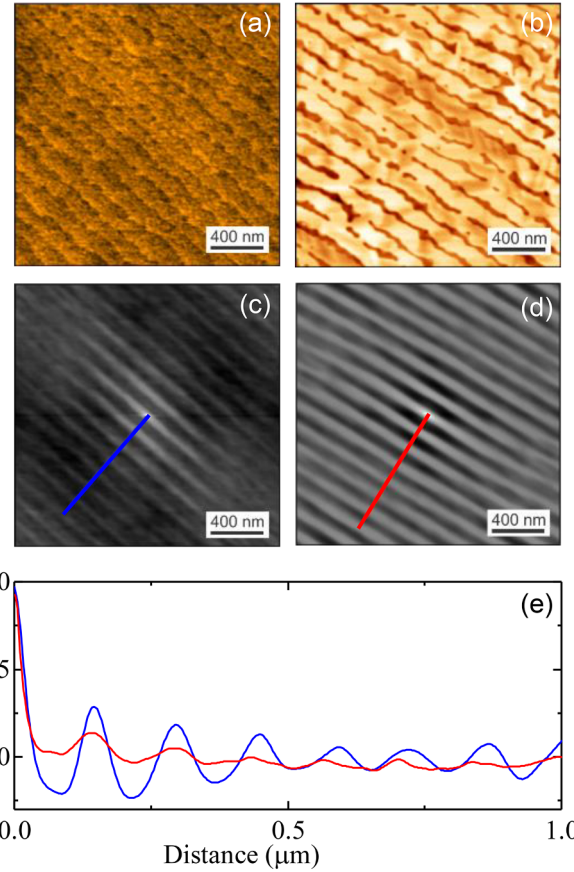


Fig. 2. (a) Topographic AFM images ($2 \times 2 \mu\text{m}^2$) of (a) LaAlO_3 substrate ($\alpha \sim 0.155^\circ$) and (b) BiFeO_3 film (thickness, $t = 45 \text{ nm}$) grown on top of it. The corresponding height-height correlation functions of the topographic surfaces are shown in (c) and (d) respectively. (e) Corresponding profile lines of LAO (blue) and of BFO (red).

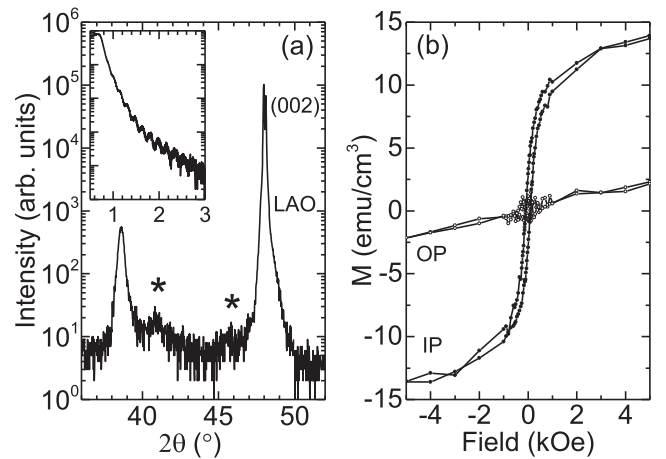


Fig. 3. (a) θ - 2θ XRD scans of the $(0 0 2)$ reflections for BFO/LAO thin film. In the inset, corresponding XRR data with thickness values of 45 nm. (b) Magnetization versus field corrected with the diamagnetic slope for the in-plane (IP) and out-of-plane field (OP) at room temperature.

additional dots (see arrows) are also visible (doubled distance in k space) in possible correlation with the formation of the polarization nano-domains (see below). The regular lines, i.e. grooves have typical depth of around $6 \pm 2 \text{ nm}$ (Fig. 1(c)).

In order to further clarify the structural arrangement of the regular lines the topography of BFO thin films (Fig. 2(b)) is compared directly

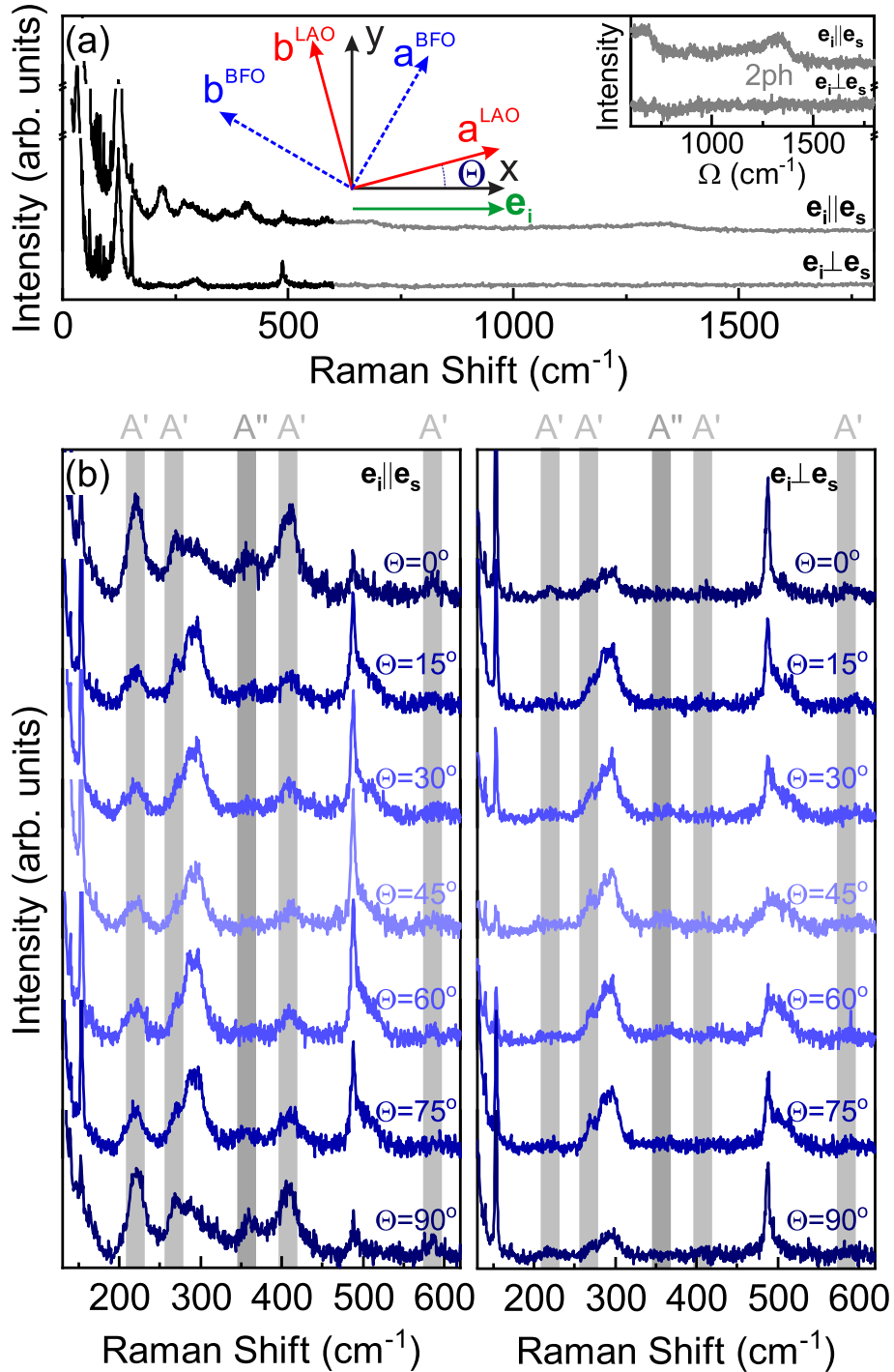


Fig. 4. (a) Raman spectra measured in parallel and cross polarization configurations for $\Theta = 0^\circ$. xy is the laboratory system at room temperature. Black and grey lines represent spectra obtained with binning 1 and 2 respectively. Inset: High energy region of the BFO/LAO Raman spectra. (b) BFO/LAO Raman spectra measured in parallel and cross polarization configurations for various sample orientations.

with the topography of the underlying LAO substrate (Fig. 2(a)). The corresponding height-height autocorrelation functions are shown in Fig. 2(c) for LAO and (d) for BFO topography. The regular line pattern is visible at the overall surface in both cases, also as non-vanishing oscillations in the corresponding profile perpendicular to lines. A clear correlation between the two patterns is evident from the corresponding profile lines in Fig. 2(e), demonstrating a typical separation between ordered nanostructured lines of $l \sim 140$ nm, in agreement with the underlying terrace-step morphology of the LAO substrate with a miscut angle of $\alpha \sim 0.155^\circ$.

The structural properties have been investigated by θ -2 θ X-ray diffraction (XRD), Fig. 3(a) shows scans around (0 0 2) LAO reflection. The strongest peak in Fig. 3(a) corresponds to the LAO substrate ($2\theta = 48.05^\circ$ with lattice parameter of $c = 3.787$ Å). Besides this, a dominant peak ($2\theta = 38.62^\circ$) and two small intensity peaks are also detected ($2\theta = 40.87^\circ$ and $2\theta = 45.74^\circ$, see stars in Fig. 3(a)). Dominant peak corresponds to an out-of-plane parameter of $c_{\text{perp}} = 4.66(2)$ Å, much larger than the pseudocubic cell parameter of bulk BFO and it is associated with hyper strained tetragonal phase.

The position of the two small peaks suggests the presence of two

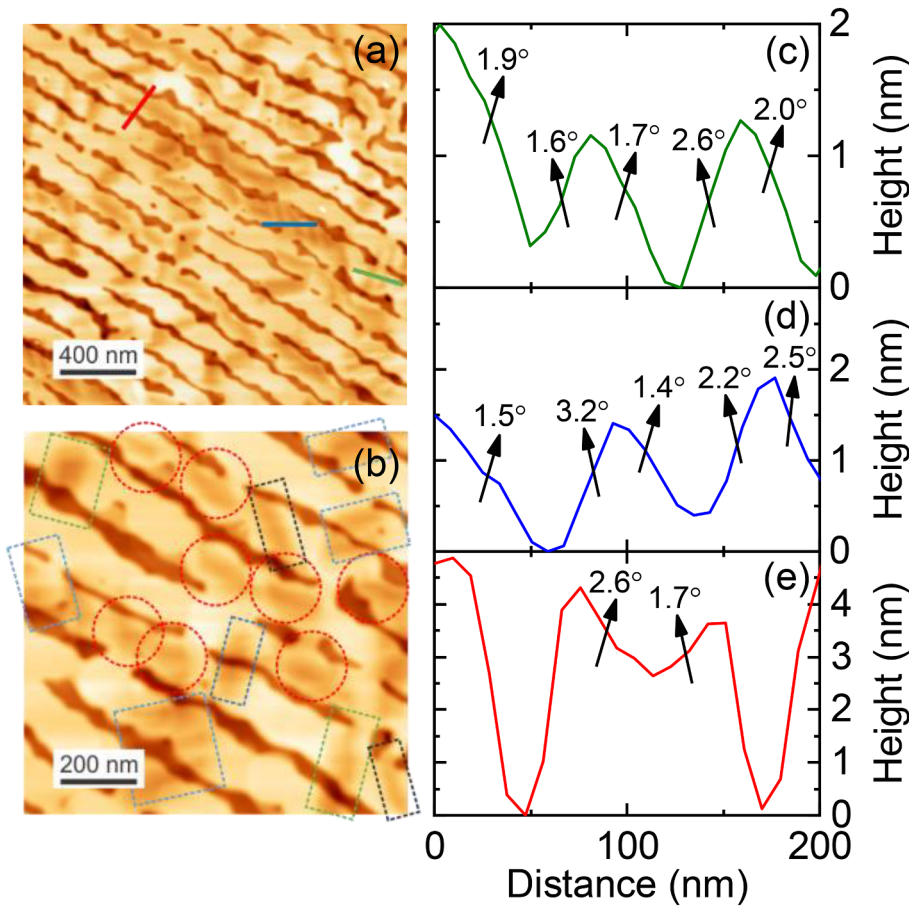


Fig. 5. The formation of nanodomains in the presence of regular line network. (a) AFM topography ($2 \times 2 \mu\text{m}^2$) with profile lines. (b) Small area AFM topography ($1 \times 1 \mu\text{m}^2$) with different orientation of detected nanodomains (expected orientation in blue and green rectangles and new nanodomains induced by line network in red circles). (c)-(e) Profile lines of nanodomains from (a).

additional phases with out-of-plane parameters in the order of $c_{\text{perp1}} = 4.41(6) \text{ \AA}$ and $c_{\text{perp2}} = 3.96(7) \text{ \AA}$, which are ascribed to the intermediate monoclinic structure and the rhombohedral phase respectively. While the intermediate monoclinic phase is associated to the formation of nanodomains [9,12] the rhombohedral phase is the residue of the bulk counterpart phase [3]. Thickness value of the BFO/LAO film ($t \sim 45 \text{ nm}$) is determined from XRR curve (inset of Fig. 3(a)). No magnetic impurity phases are detected, in agreement with the weak ferromagnetic moment measured at room-temperature (Fig. 3(b)).

Raman spectra of BFO film with ordered connected pits morphology are shown in Fig. 4. Due to the fact that the film thickness is much smaller than the penetration depth of the beam, significant contribution from the LAO substrate is clearly observable in the BFO/LAO Raman spectra (Fig. 4(a)). For the purpose of probing the crystal structure of the BFO film, Raman spectra were collected for different sample orientation (as presented in Fig. 4) in two polarization configurations.

Detailed analysis of the Raman intensity angular dependence [21] taking into account the twinning effects, indicates that Raman features observed at about 227, 273, 417 and 587 cm^{-1} correspond to the A' symmetry modes, whereas peak at 368 cm^{-1} correspond to A'' symmetry mode of the monoclinic Cc crystal structure. These findings are in accordance with the density-functional calculations predicting that BFO structure under strain values higher than 4% become tetragonal-like with larger c/a ratio [22]. According to the first principles calculations, this structure has Cc symmetry with the base centered unit cell containing four formula units, for which the factor group analysis predicts the existence of $13A' + 14A''$ Raman-active phonon modes [22]. Note that, a large number of modes ascribed to the Cc structure have been experimentally observed in the low-temperature Raman spectra of BiFeO_3 films commensurately grown on LaAlO_3 substrates and subjected to $\sim 4.4\%$ compressive strain, wherein it was indicated that 13

most intense modes (including those at 237, 282, 415, and 605 cm^{-1}) could be referred to the A' symmetry [23]. However, Himcinschi et al. [23] suggested that the modes at 225, 263 and 367 cm^{-1} in the Raman spectrum of highly strained BiFeO_3 epitaxial films deposited on LaAlO_3 may correspond to A'' symmetry mode of the Cc monoclinic structure [23]. Therefore, there is no doubt that BFO/LAO film whose Raman spectra are shown in Fig. 4 has Cc structure, but small differences in the positions of the identified modes in comparison with those referred in the literature [23] indicate that the structure of the film investigated here is monoclinically distorted in a specific way.

More details of the formation of the mixed-phase structures in the middle of the regular network line can be obtained from AFM topography shown in Fig. 5. The thin strip-line patterns could be visualized in Fig. 5(a), known in literature as asymmetric “saw-tooth” surface structure and identified as intimated mixture between highly distorted monoclinic phase (monoclinic version of highly tetragonal phase with $c/a = 1.23$), detected by Raman scattering in Fig. 4 and an intermediate monoclinic phase ($c/a = 1.17$), detected as small peak by XRD in Fig. 3(a). The profile line of these strip-like patterns can be found in Fig. 5(c)-(e). Typical strip-like patterns, disoriented around $\sim 1^\circ$ from the in-plane (100) and (010) axes, could be seen in green and blue squares in Fig. 5(b). Corresponding AFM profile line indicate that they are tilted away from the surface normal for about $2.5\text{--}3^\circ$ (intermediate monoclinic phase) and $1.5\text{--}2^\circ$ (highly distorted monoclinic phase), in agreement with previous reports [9,12]. The typical height difference between different phases (around 3 nm) [9,24] is not always observed, as strongly perturbed with formation of regular grooved (for more details see Fig. S1 in supplementary material). In addition, the stripe-like formation could be observed also in our case between regular line-network and disoriented around $\sim 150^\circ$ from the in-plane (100) axes (red circles in Fig. 5(b)) with very similar profile line (Fig. 5(e)).

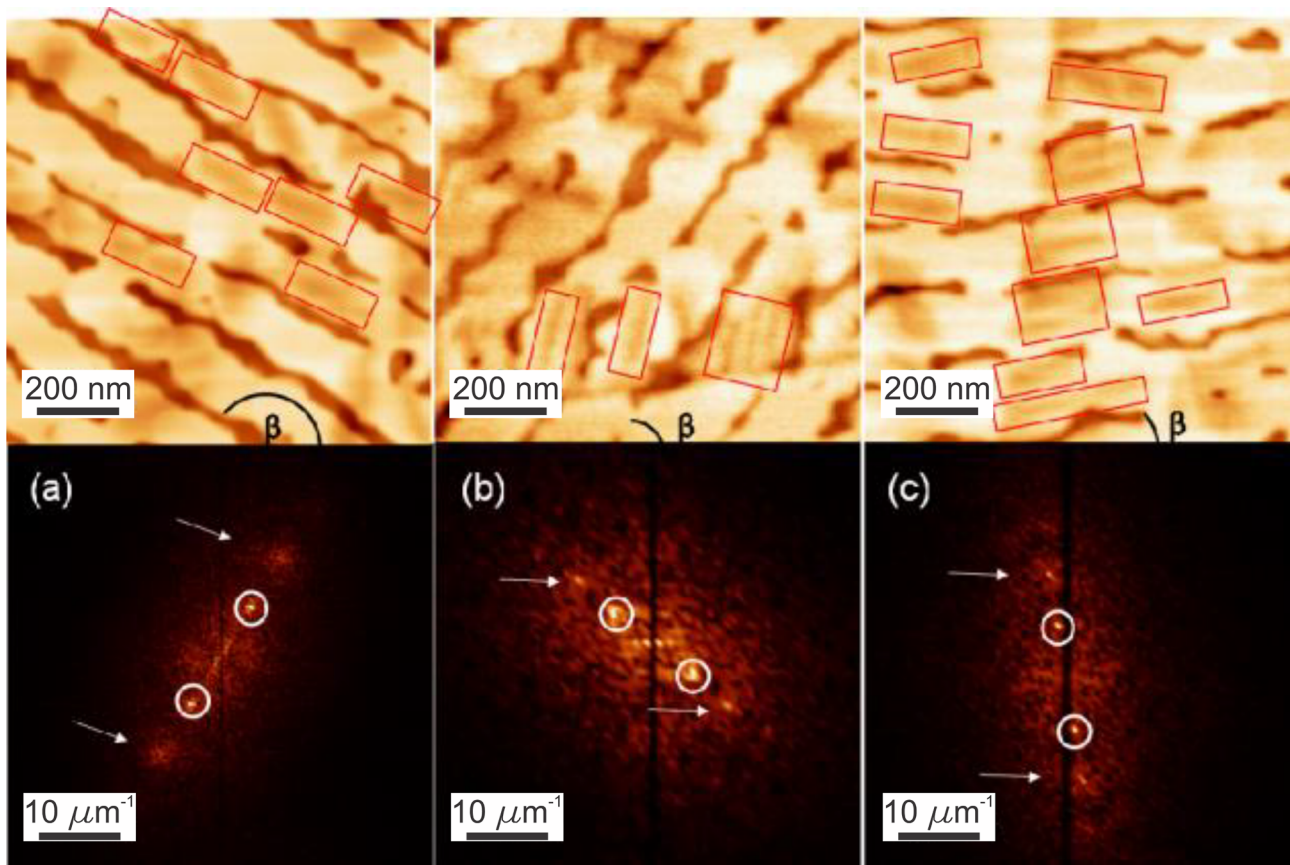


Fig. 6. AFM of BFO films grown on the top of LAO with similar miscut angle ($0.12^\circ < \alpha < 0.16^\circ$) with different orientation of nanostructured lines respected to $[1\ 0\ 0]$ direction (a) $\beta \sim 150^\circ$, (b) 52° and (c) 6° . The corresponding FFT images are given below.

Finally, the formation of the mixed-phase structures in the middle of the regular network is followed for different network orientations respected to $[100]$ direction. In Fig. 6, AFM topography with corresponding Fast Fourier Transform is shown for BFO thin films grown on LAO with similar terrace width but with different orientation respected to substrate edges ($6^\circ < \beta < 150^\circ$). FFT of topographic images indicate the long-range order coming from formation of groove network (two high intensity dots in circles in all cases). In addition, as mentioned before, two additional points (see arrows) are visible at doubled distance in k space, suggesting the presence of additional structures in-between the regular line network. In all cases, the presence of “saw-tooth” surface structures in between the grooves could be identified in the corresponding AFM topography (see red rectangles and Fig. S1 in supplementary). Noticeably, in the case of network line slightly disoriented from the in-plane (100) axes ($\beta \sim 6^\circ$), the nano-domains form more easily in-between the grooves (see Fig. 6(c)) as it is closer to their spontaneous configuration [9,12,24].

4. Conclusion

In summary, a regular nanostructured network is grown on the surface of BFO films, in close correlation with the step-terraces morphology of the underlying LAO substrate (miscut angle $0.12^\circ < \alpha < 0.16^\circ$). Raman scattering detected the dominant contribution from the monoclinic version of highly strained tetragonal phase. XRD spectra also indicate the presence of additional polymorphs, rhombohedral and intermediate monoclinic phases. The stripe-like patterns, formed by intimate mixture between two monoclinic polymorphs, are visualized by AFM topography. Beside typical formation following (100) and (010) axes, some stripe-like patterns are also detected in-between the regular line network. Finally, the observed self-nanostructuring of the BFO surface

opens a playground for tailoring structural polymorphs with strong potential interest for future applications in multiferroic nanomaterials.

5. Author statement

B. Colson: thin film preparation and characterization, Z. Konstantinović: design and leading the research, manuscript preparation, D. Colson, A. Forget: ferroelectric properties, N. Lazarević, M. Šćepanović, Z. V. Popović: Raman measurements, V. Fuentes, C. Frontera: X-ray diffraction characterization, D. Colson, L.I. Balcells, B. Martinez, A. Pomar: Reviewing and editing manuscript.

Declaration of Competing Interest

The authors declare that they have no known competing financial interests or personal relationships that could have appeared to influence the work reported in this paper.

Acknowledgements

This work has received funding from the European Union’s Horizon 2020 research and innovation under the Marie Skłodowska-Curie grant agreement No. 645658 (DAFNEOX Project). A.P., V. F. and Z.K. thank Sensor-INFIZ (Serbia) for the cooperation provided during their respective secondments. E. P.-M. acknowledge financial support from the Spanish Ministry of Economy and Competitiveness through the “Severo Ochoa” Programme for Centres of Excellence in R&D (SEV-2015- 0496), and project MAT2015-71664 and SPINCURIOX (RTI2018-099960-B-I00). N. L., M. S., Z. K. and Z.V.P. acknowledge the support of the Serbian Ministry of Education, Science and Technological Development (Projects No III45018).

Appendix A. Supplementary data

Supplementary data to this article can be found online at <https://doi.org/10.1016/j.jmmm.2020.166898>.

References

- [1] G. Catalan, J.F. Scott, Physics and applications of bismuth ferrite, *Adv. Mater.* 21 (2009) 2463.
- [2] D. Sando, A. Barthelemy, M. Bibes, BiFeO₃ epitaxial thin films and devices: past, present and future, *J. Phys.: Condens. Matter* 26 (2014) 473201.
- [3] D. Lebeugle, D. Colson, A. Forget, M. Viret, P. Bonville, J.F. Marucco, S. Fusil, Room temperature coexistence of large electric polarization and magnetic order in BiFeO₃ single crystals, *Phys. Rev. B* 76 (2007) 024116.
- [4] D. Lebeugle, D. Colson, A. Forget, M. Viret, Very large spontaneous electric polarization in BiFeO₃ single crystals at room temperature and its evolution under cycling fields, *Appl. Phys. Lett.* 91 (2007) 022907.
- [5] D. Lebeugle, D. Colson, A. Forget, M. Viret, A.M. Bataille, A. Gukasov, Electric Field-Induced Spin Flop in BiFeO₃ single crystals at room temperature, *Phys. Rev. Lett.* 100 (2008) 227602.
- [6] T. Zhao, A. Scholl, F. Zavaliche, K. Lee, M. Barry, A. Doran, M.P. Cruz, Y.H. Chu, C. Ederer, N.A. Spaldin, R.R. Das, D.M. Kim, S.H. Baek, C.B. Eom, R. Ramesh, Electrical control of antiferromagnetic domains in multiferroic BiFeO₃ films at room temperature, *Nature Mater.* 5 (2006) 823.
- [7] S. Lee, W. Ratcliff, S.W. Cheong, V. Kiryukhin, Electric field control of the magnetic state in BiFeO₃ single crystals, *Appl. Phys. Lett.* 92 (2006) 192906.
- [8] C. Ederer, N.A. Spaldin, Effect of epitaxial strain on the spontaneous polarization of thin film ferroelectrics, *Phys. Rev. Lett.* 95 (2005) 257601.
- [9] A.R. Damodaran, J.C. Agar, S. Pandya, Z. Chen, L. Dedon, R. Xu, B. Apgar, S. Saremi, L.W. Martin, New modalities of strain-control of ferroelectric thin films, *J. Phys.: Condens. Matter* 28 (2016) 263001.
- [10] Y.-H. Chu, M.P. Cruz, C.-H. Yang, L.W. Martin, P.-L. Yang, J.-X. Zhang, K. Lee, P. Yu, L.-Q. Chen, R. Ramesh, Domain control in multiferroic BiFeO₃ through substrate vicinity, *Adv. Mater.* 19 (2007) 2662.
- [11] J.X. Zhang, Q. He, M. Trassin, W. Luo, D. Yi, M.D. Rossell, P. Yu, L. You, C.H. Wang, C.Y. Kuo, J.T. Heron, Z. Hu, R.J. Zeches, H.J. Lin, A. Tanaka, C.T. Chen, L.H. Tjeng, Y.-H. Chu, R. Ramesh, Microscopic origin of the giant ferroelectric polarization in tetragonal-like BiFeO₃, *Phys. Rev. Lett.* 107 (2011) 147602.
- [12] L. You, Z. Chen, X. Zou, H. Ding, W. Chen, L. Chen, G. Yuan, J. Wang, Characterization and manipulation of mixed phase nanodomains in highly strained BiFeO₃ thin films, *ACS Nano* 6 (2012) 5388.
- [13] A. Kumar, S. Denev, R.J. Zeches, E. Vlahos, N.J. Podraza, A. Melville, D.G. Schlom, R. Ramesh, V. Gopalan, Probing mixed tetragonal/rhombohedral-like monoclinic phases in strained, bismuth ferrite films by optical second harmonic generation, *Appl. Phys. Lett.* 97 (2010) 112903; J. Seidel, M. Trassin, Y. Zhang, P. Maksymovych, T. Uhlig, P. Milde, D. Köhler, A.P. Baddorf, S.V. Kalinin, L.M. Eng, X. Pan, R. Ramesh, Electronic properties of isosymmetric phase boundaries in highly strained Ca-doped BiFeO₃, *Adv. Mater.* 26 (2014) 4376.
- [14] A. Solmaz, M. Huijben, G. Koster, R. Egoavil, N. Gauquelin, G. Van Tendeloo, J. Verbeeck, B. Noheda, G. Rijnders, Domain selectivity in BiFeO₃ thin films by modified substrate termination, *Adv. Funct. Mater.* 26 (2016) 2882.
- [15] Z. Konstantinovic, J. Santiso, L.I. Balcells, B. Martinez, Strain-driven self-assembled network of antidots in complex oxide thin films, *Small* 5 (2009) 265.
- [16] Y. Zhao, Z. Yin, X. Zhang, Z. Fu, J. Wu, Formation and local conduction of nanospots in BiFeO₃ epitaxial films, *J. Mater. Chem. C* 3 (2015) 11250.
- [17] Z. Konstantinovic, F. Sandiumenge, J. Santiso, L.I. Balcells, B. Martinez, Self-assembled pit arrays as templates for the integration of Au nanocrystals in oxide surfaces, *Nanoscale* 5 (2013) 1001.
- [18] J.L. Grey, R. Hull, C.-H. Lam, P. Sutter, J. Means, J.A. Floro, Beyond the hetero-epitaxial quantum dot: self-assembling complex nanostructures controlled by strain and growth kinetics, *Phys. Rev. B* 72 (2005) 155323.
- [19] H. Bea, B. Dupe, S. Fusil, R. Mattana, E. Jacquet, B. Warot-Fonrose, F. Wilhelm, A. Rogalev, S. Petit, V. Cros, A. Anane, F. Petroff, K. Bouzehouane, G. Geneste, B. Dkhil, S. Lisenkov, I. Ponomareva, L. Bellaiche, M. Bibes, A. Barthelemy, Evidence for room-temperature multiferroicity in a compound with a giant axial ratio, *Phys. Rev. Lett.* 102 (2009) 217603.
- [20] B. Colson, «Elaboration et caractérisation de films minces de BiFeO₃ nanostructurés», DUT Mesures Physiques, IUT d'Orsay, Université Paris-Sud, 2016.
- [21] D.R. Palai, H. Schmid, J.F. Scott, R.S. Katiyar, Raman spectroscopy of single-domain multiferroic BiFeO₃, *Phys. Rev. B – Condens. Matter Mater. Phys.* 81 (2010) 064110.
- [22] J. Hatt, N.A. Spaldin, C. Ederer, Strain-induced isosymmetric phase transition in BiFeO₃, *Phys. Rev. B – Condens. Matter Mater. Phys.* 81 (2010) 054109.
- [23] C. Himcinschi, A. Bhatnagar, A. Talkenberger, M. Barchuk, D.R.T. Zahn, D. Rafaja, J. Kortus, M. Alexe, Optical properties of epitaxial BiFeO₃ thin films grown on LaAlO₃, *Appl. Phys. Lett.* 106 (2015) 012908.
- [24] R.J. Zeches, M.D. Rossell, J.X. Zhang, A.J. Hatt, Q. He, C.-H. Yang, A. Kumar, C.H. Wang, A. Melville, C. Adamo, G. Sheng, Y.-H. Chu, J.F. Ihlefeld, R. Erni, C. Ederer, V. Gopalan, L.Q. Chen, D.G. Schlom, N.A. Spaldin, L.W. Martin, R. Ramesh, A strain-driven morphotropic phase boundary in BiFeO₃, *Science* 326 (2009) 977.

Temperature-Dependent Raman Study of Nanostructured and Multifunctional Materials

Maja Šćepanović,* Mirjana Grujić-Brojčin, Nenad Lazarević, and Zoran V. Popović

The scope of this paper is temperature dependence of Raman spectra in several nanocrystalline materials and iron-based single-crystals. The Raman results presented and analyzed here are related to TiO_2 nanopowders (with dominant anatase and brookite phase) and $\text{Zn}_x\text{Cd}_{1-x}\text{Se}$ single layers measured at different temperatures. Temperature-dependent Raman spectra of iron-based sulphides and selenides (BaFe_2S_3 and BaFe_2Se_3), as well as alkali-doped iron selenides ($\text{K}_x\text{Fe}_{2-y}\text{Se}_2$ and $\text{K}_{0.8}\text{Fe}_{1.8}\text{Co}_{0.2}\text{Se}_2$) are also analyzed. A physical model, including thermal expansion as well as three- and four-phonon anharmonic effects, is used to quantitatively analyze temperature evolution of the characteristic Raman mode self-energies for the materials of interest. It is demonstrated how this model can be used as a tool for predicting the temperature of structural and phase transitions, with critical scrutiny of its limitations.

spin ladders, spin dimers, etc.).^[5] The temperature dependent Raman spectra of iron-based sulphides and selenides (BaFe_2S_3 and BaFe_2Se_3 , belonging to the family of the iron-based $S=2$ two-leg spin-ladder compounds),^[5] together with alkali-doped iron selenides (superconducting $\text{K}_x\text{Fe}_{2-y}\text{Se}_2$ and non-superconducting $\text{K}_{0.8}\text{Fe}_{1.8}\text{Co}_{0.2}\text{Se}_2$)^[6] are analyzed. A physical model, including thermal expansion, as well as three- and four-phonon anharmonic effects, is used to quantitatively analyze experimentally obtained temperature dependence of energy and linewidth of the Raman modes characteristic for investigated materials. We have shown that this simplified model could be successfully used to predict the temperature of microstructural phase transitions, but its limitations have also been indicated.

1. Introduction

Variable-temperature Raman scattering measurements provide great assistance in the analysis of structural, electronic, and magnetic properties, as well as phase transitions, in large number of materials currently in the focus of modern research in condensed matter physics. Two important classes of materials are in the scope of the present paper – nanomaterials and iron-based compounds. Temperature-dependent Raman spectra of nanomaterials is a significant source of information on their thermal stability and other properties (such as phase composition, nanocrystallite size distribution, strain, defects, and non-stoichiometry) strongly depended on the temperature and affecting the shape, shift, and linewidth of characteristic Raman modes.^[1–4] The obtained Raman results are related to titanium dioxide (TiO_2) nanopowders (with dominant anatase or brookite phase) and $\text{Zn}_x\text{Cd}_{1-x}\text{Se}$ single layers. In addition the influence of the antiferromagnetic order, ferromagnetism, and magnetic fluctuations on the Raman scattering spectra of several iron-based compounds measured in wide temperature range were also analyzed. These materials may have not only superconducting but also low-dimensional magnetic properties (forming spin chains,

2. Theoretical Background

Lattice vibrations are strongly related to crystalline, thermodynamical, and transport properties of materials, including phase stability at finite temperatures, lattice thermal conductivity, and superconducting critical temperature of phonon-mediated superconductors.^[7] In order to interpret experimental vibrational spectra some computational methods based on density functional theory have been developed. These methods use the first-principles calculations of phonons and other related properties, but it appears that their performance is always limited by chosen approximations and assumptions. The harmonic approximation, assuming independent phonons, is usually adopted in calculations of phonon properties at low temperatures; it is a method of choice when describing the phonon spectra of the metals and insulators, valid and useful for obtaining phonon dispersion curves and studying phase stability. However, harmonic approximation is not successful in describing phonon behavior at high temperatures, where phonon-phonon interactions must be considered, together with properties related to the lattice anharmonicity (thermal expansion, lattice thermal conductivity, temperature, and volume dependences of phonon frequencies). The anharmonic effects can be successfully treated by the many-body perturbation theory.^[8,9] However, this theory seems to be inadequate, when the cubic and higher-order anharmonic terms of the phonon energies are larger than the harmonic one, or when the harmonic solution shows dynamical instability. In order to overcome these limitations, some advanced methods have been

Dr. M. Šćepanović, Dr. M. Grujić-Brojčin, Dr. N. Lazarević,
Prof. Z. V. Popović
Center for Solid State Physics and New Materials
Institute of Physics
University of Belgrade
Pregrevica 118, 11080 Belgrade, Serbia
E-mail: maja@ipb.ac.rs

DOI: 10.1002/pssa.201800763

developed, such as the self-consistent phonon theory,^[10] or ab-initio molecular dynamics method,^[11,12] both treating anharmonic effects in solids nonperturbatively.^[7] However, all these calculations require significant computer resources, rapidly increasing with the size of the system. This may be the reason why the first-principles calculations of phonons are usually performed at low temperatures, and the results related to the temperature dependence of phonon properties are, to the best of our knowledge, still unavailable for materials studied here.

The analysis of experimentally obtained temperature dependence of phonon frequency and lifetime in the materials presented in this paper includes quasiharmonic and anharmonic contribution to the lattice potential, which both contribute to nonharmonic lattice dynamics. The phonon modes in the quasiharmonic model behave harmonically with infinite lifetimes, but their frequencies are influenced by the effects of lattice volume on the interatomic potential,^[13] whereas explicit anharmonicity originates from phonon-phonon interactions increasing with temperature.

Frequency shift and broadening of phonon mode can be described as real and imaginary part of phonon self-energy^[6,14,15]:

$$\Sigma_i(T) = \Delta_i(T) + i\Gamma_i(T) \quad (1)$$

where $\Delta_i(T)$ corresponds to the energy of i -th Raman mode and $\Gamma_i(T)$ to its linewidth, defined as inverse value of phonon lifetime τ . Temperature dependence of Raman shift can be defined by the real part of self-energy:

$$\omega_i(T) = \omega_{0,i} + \Delta_i(T) \quad (2)$$

where $\omega_{0,i}$ is temperature independent contribution to phonon mode energy. Temperature dependent term may be written as

$$\Delta_i(T) = \Delta_i^V + \Delta_i^A \quad (3)$$

The first term, Δ_i^V , corresponds to the frequency shift from the volume thermal expansion or quasiharmonicity, and can be expressed as

$$\Delta_i^V = -\omega_{0,i} \left(e^{-\gamma_i \int_0^T \alpha_V(T') dT'} - 1 \right) \quad (4)$$

with Grüneisen parameter γ_i of given mode and volume thermal expansion coefficient $\alpha_V(T)$ of investigated material.^[15] The Grüneisen model assumes that the Grüneisen parameter correlates the temperature dependence of vibrational frequencies with the unit cell volume. At constant pressure the Grüneisen constant is defined by

$$\gamma_i = \left. \frac{\partial \ln \omega_i}{\partial \ln V} \right|_P = - \frac{1}{\alpha_V} \left. \frac{\partial \ln \omega_i}{\partial T} \right|_P \quad (5)$$

where ω_i is the frequency of i -th vibrational mode, V the unit cell volume and α_V the volumetric thermal expansion given by

$$\alpha_V = \left. \frac{1}{V} \frac{\partial V}{\partial T} \right|_P \quad (6)$$



Maja Šćepanović received her PhD from the School of Electrical Engineering, University of Belgrade. She is employed as a Research Professor at the Center for Solid State Physics and New Materials, Institute of Physics Belgrade. She has contributed greatly to the understanding of a number of problems in the experimental study

and simulation of intense ns laser pulse-matter interaction, Raman, infrared and photoluminescence spectroscopy, and spectroscopic ellipsometry. In recent years, she has been primarily concerned with the experimental and theoretical studies, as well as development of numerical models, related to the investigation of nanostructured and iron-based related materials.



Mirjana Grujić-Brojčin, PhD (School of Electrical Engineering, University of Belgrade). Employed, as a Research Professor at the Center for Solid State Physics and New Materials, Institute of Physics Belgrade. She is engaged in experimental study and development of numerical models in Raman, infrared and photoluminescence

spectroscopy, and spectroscopic ellipsometry of nanomaterials. In recent years she has been involved in application of spectroscopic techniques in Cultural Heritage.



Nenad Lazarević is Research Associate professor employed at the Center for Solid State Physics and Materials, Institute of Physics, University of Belgrade. His main research interest is focused on optical spectroscopy of strongly correlated electron systems with particular emphasis on Raman spectroscopy. In the last years, his

activities were mostly focused on the iron-based superconductors and related materials. Other activities include work on devising new experimental setups for Raman spectroscopy.

Hence, when the temperature dependence of vibrational modes is known, the Grüneisen parameter (which varies significantly from one mode to the other) can be determined from the known thermal expansion (or vice-versa).

The second term, Δ_i^A , in the Equation (3) describes the frequency shift caused by the anharmonic phonon-phonon coupling, that is, the explicit anharmonicity or pure temperature

effect. The anharmonic decay of phonons includes the leading, three-phonon and four-phonon processes, cubic $\Delta_i^{(3)}$ and quartic $\Delta_i^{(4)}$ components of the anharmonicity term Δ_i^A and it should be determined for each Raman mode. The explicit anharmonicity for frequency shift may be simplified by the model proposed by Klemens^[16] and extended by Balkanski et al.^[17] where phonon-phonon interactions include only overtone processes (one optical phonon at the Γ point decays into two or three phonons of equal energy on the same branch), specifying the contributions of three-phonon and four-phonon processes to the frequency shift in the following form^[17]:

$$\Delta_i^A = \Delta_i^{(3)} + \Delta_i^{(4)} = C_i \left(1 + \frac{2}{e^{\frac{\hbar\omega_i}{2k_B T}} - 1} \right) + D_i \left(1 + \frac{3}{e^{\frac{\hbar\omega_i}{3k_B T}} - 1} + \frac{3}{\left(\frac{\hbar\omega_i}{e^{3k_B T} - 1} \right)^2} \right) \quad (7)$$

where C_i and D_i are so-called anharmonic constants. It should be noted that the parameters which exist in the simplified Klemens model are treated as independent, which is not quite physically correct. In general, the exact interdependence of these parameters is very hard to determine. In order to obtain the relationship between the parameters, when the anharmonic effect can be defined only by three phonon processes, the model of a damped oscillator is adopted,^[15] and phonon-phonon scattering contribution to energy of Raman mode is represented as:

$$\Delta_i^A = C_i \left(1 + \frac{4\lambda_{ph-ph,i}}{\frac{\hbar\omega_i}{e^{2k_B T} - 1}} \right) \quad (8)$$

with phonon-phonon interaction constant λ_{ph-ph} introduced as fitting parameter to represent phonon-phonon coupling strength.

Unlike the phonon energy, the phonon linewidth is not affected by the thermal expansion of crystal lattice. Two main contributions to the phonon linewidth are the anharmonic decay of the phonons and the perturbation of the crystal translational symmetry, due to the presence of impurities and defects. According to Klemens model, temperature dependence of Raman mode linewidth can be described by

$$\Gamma_i(T) = \Gamma_{0,i} + A_i \left(1 + \frac{2}{e^{\frac{\hbar\omega_i}{2k_B T}} - 1} \right) + B_i \left(1 + \frac{3}{e^{\frac{\hbar\omega_i}{3k_B T}} - 1} + \frac{3}{\left(e^{\frac{\hbar\omega_i}{3k_B T}} - 1 \right)^2} \right) \quad (9)$$

where $\Gamma_{0,i}$ is the temperature-independent linewidth, which originates mainly from the presence of impurities and defect (nonstoichiometry), whereas A_i and B_i are the three- and four-phonon anharmonic constants, respectively. According to the model of a damped oscillator, if four-phonon processes turned out to be negligible, Raman mode linewidth could be written as^[15]:

$$\Gamma_i(T) = \Gamma_{0,i} \left(1 + \frac{2\lambda_{ph-ph,i}}{\frac{\hbar\omega_i}{e^{2k_B T}} - 1} \right) \quad (10)$$

with $\Gamma_{0,i}$ as anharmonic constant, which could be related to the phonon-phonon interaction constant λ_{ph-ph} and the anharmonic parameter C_i from relation (8), given as^[15]:

$$C_i = \frac{\Gamma_{0,i}^2}{2\omega_{0,i}} \quad (11)$$

It should be noted that more general calculations, including asymmetric decay channels, result in a better agreement with experiment, especially in some semiconductors.^[15]

3. Temperature-Dependent Raman Spectra of Nanomaterials

The Raman scattering provides important information on the nature of the solid on a scale of few lattice constants. Therefore, this technique can be used to study the correlation between the change in vibrational properties on one, and structural and/or morphological changes in nanostructured material on the other side.

The Raman spectra of nanocrystalline materials are usually simulated by phenomenological phonon confinement model (PCM).^[18,19] In this model several independent factors, like phonon confinement, strain, non-homogeneity of the size distribution, defects, and variations in phonon relaxation with crystallite size decreasing, contribute to the changes in the position and linewidth of calculated Raman mode.^[18–21] Due to the crystallite size decrease, the phonons are confined and optical phonons over the entire Brillouin zone (BZ) contribute to the first-order Raman spectra. The Raman intensity $I(\omega)$ for crystallite size L , according to Richter et al.^[22] and Campbell and Fauchet,^[23] is presented as a superposition of weighted Lorentzian contributions over the whole BZ, by the equation^[3,4,18–23]:

$$I(\omega) = \sum_{i=1}^m \int_0^\infty \rho(L) dL \left(\int_{BZ} \frac{\exp\left(\frac{-q^2 L^2}{8\beta}\right) d^3 q}{[\omega - (\omega_i(q) + \Delta\omega_i(q, L, T))]^2 + \left(\frac{\Gamma_{0i}(T)}{2}\right)^2} \right) \quad (12)$$

where $\rho(L)$ defines crystallite size distribution, q is expressed in units of π/a_L (a_L – effective unit cell parameter), β – strength of confinement (varies from $\beta = 1$ in the Richter's confinement model to $\beta = 2\pi^2$ in the Campbell's confinement model, depending on the confinement boundary conditions in different nanomaterials), $\omega_i(q)$ – phonon dispersion, $\Gamma_{0i}(T)$ – the intrinsic linewidth of Raman mode dependent on temperature T , as well as nonstoichiometry, disorder, and defects state.

The change of the lattice parameters (lattice volume) with nanocrystallite size decrease is registered in nanomaterials due to effect of microstrain and may affect the Raman mode position. The influence of strain on Raman shift $\Delta\omega_i(q, T, L)$ of particular mode is included into PCM through the term given by^[4,20,24]:

$$\Delta\omega_i(q, T, L) = -\gamma_i\omega_i(q, T) \frac{V(L)}{V_0} \quad (13)$$

The unit cell volume variation of nanocrystallite size L can be written as

$$V(L) = V_0 \pm \Delta V(L) \quad (14)$$

where signs “+” and “−” correspond to tensile and compressive strain, respectively.

3.1. TiO₂ Based Nanomaterials

Titanium dioxide is material of great importance in modern materials science. It is probably the most characterised oxide in different areas, such as defect chemistry, phase transitions, surface structure, surface chemistry, optical properties, and electronic structure.^[2] Also, it is widely used nowadays, with a variety of achieved and potential applications: as a pigment, in photocatalysis, as electron transport layer in solar cells, as self-cleaning material, etc.^[25] Only three of TiO₂ several polymorphs (rutile, anatase, and brookite) are considered to be its naturally occurring phases. Although extensively studied during past decades, there are still some unresolved questions related to vibrational and thermal properties of these phases, especially those originated from their nanocrystalline structure.

3.1.1. Anatase Nanocrystalline Powders

The Raman spectroscopy of nanocrystalline anatase (the TiO₂ phase most commonly synthesized at ambient conditions), has been established as a very sensitive tool for detecting nanostructural changes in this material, associated with phonon confinement effect, non-stoichiometry, internal stress/surface tension effects and/or the anharmonicity effects due to temperature variations.^[1–4]

In this review we present our experimental results related to the temperature dependence of the most intense anatase E_g Raman mode, taken from laser-synthesized and commercial anatase nanopowder samples, published in our earlier papers.^[1,2] The interpretation of these results is slightly modified here, in accordance with recent experimental and theoretical findings related to the variation of nanostructural properties of anatase with temperature.^[26–30]

The results of a detailed study of the most intense E_g mode in the Raman spectra of anatase nanopowder synthesized by laser-induced pyrolysis, with crystallite size about 12.3 nm, are presented in the **Figure 1**. The spectra in the temperature range from 25 to 300 K were taken in closed cryostat coupled with Jobin Yvon U1000 macro-Raman system. Other spectra were obtained in the same Raman system, but under conditions of local heating of the sample due to laser radiation, with the temperature estimation based on the intensity ratio between the Stokes and anti-Stokes Raman spectra.^[1]

As can be seen from the Figure 1a, very good agreement between the experimental and calculated spectra of anatase

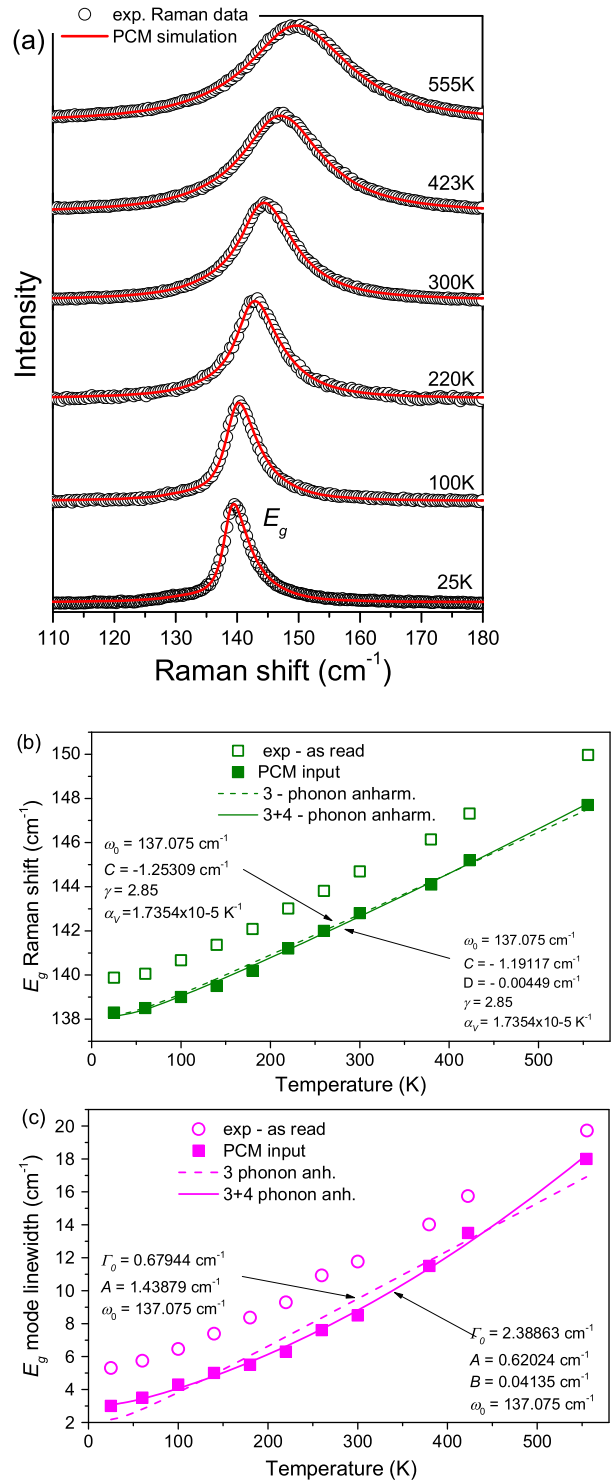


Figure 1. a) The Raman spectra of laser-synthesized TiO₂ nanopowder measured at different temperatures (circles) simulated by PCM (lines). Temperature dependence of the E_g Raman (b) shift and (c) linewidth fitted by three- (dashed lines) and four-phonon (full lines) anharmonic model with the corresponding parameters specified in the figures.

nanopowder has been obtained at all given temperatures, by using the PCM (Equation (12)) with anisotropic dispersion relations^[31] and temperature dependent parameters.^[1] It has also been demonstrated that the frequency shift (Figure 1b) and mode broadening (Figure 1c) of the E_g Raman mode were induced by both phonon confinement due to the nanocrystalline size and effect of heating. In order to analyze only heating effects on E_g Raman shift and linewidth, their as-read experimental values (shown with open symbols in the Figure 1b and c) have been corrected to exclude the effects of phonon confinement. Thereafter the corresponding temperature dependences of the E_g Raman shift and linewidth (closed symbols in Figures 1b and c) were fitted according to the Equations (7) and (9), respectively. The obtained results show that the contribution of explicit anharmonicity overpowers the effect of quasiharmonicity in the E_g frequency shift. Namely, the volume thermal expansion due to the heating, in combination with the positive value of Grüneisen parameter for E_g mode, should lead to a decreasing in E_g Raman frequency with temperature, contrary to experimental observation. It also has been shown that the curves (full line) corresponding to the contributions of both three- and four-phonon processes were better matched to the experimental results, than those calculated with the assumption of three-phonon processes only (dashed line). This effect is particularly pronounced in linewidth temperature dependence of E_g Raman mode.

Raman spectra of commercial anatase TiO_2 nanocrystals (Aldrich 637254, 99.7%) with a declared average crystallite size of about 5 nm were measured in the temperature range from 22 to 900 °C using Linkam TS 1500 heating stage coupled with Jobin Yvon T64000 micro-Raman system.^[2] The temperature dependences of Raman shift and broadening of the lowest frequency E_g mode were analyzed by using PCM and anharmonic model. Comparison between experimental spectra and those calculated by PCM (Equation (12)) at several chosen temperatures is shown in the Figure 2a. In this case PCM included not only the effects of phonon confinement and nonstoichiometry, but also the strain. Namely, recently published results have revealed that the strain in anatase particles varied with temperature^[26,27,29,30]: at some medium-high temperatures, the strain could be released, but at high temperatures, close to the transformations from anatase to rutile phase, the strain could strengthen again. Also, in situ x-ray diffraction study of the anatase microstructure evolution as a function of temperature has confirmed that anatase nanoparticle size increased with temperature. But it should be pointed out that the temperature at which the particles size begin to increase depends on their initial size,^[32] and that for smaller anatase nanoparticles the increase starts at higher temperature. This was the reason for modification of our previous calculations by including the strain in PCM, which led to the increase of calculated temperature at which the anatase nanoparticles begin to grow from previously estimated 500 °C to currently specified 600 °C.^[2] Different calculated results are the consequence of following assumption: the discrepancy of experimental temperature dependences of E_g Raman shift and linewidth from those predicted by anharmonic model (Equations (7) and (9)), observed at about 500 °C, originates from strain relaxation, and nanoparticle growth starts at higher temperatures (about 600 °C). Also, nanoparticles growth with temperature, estimated

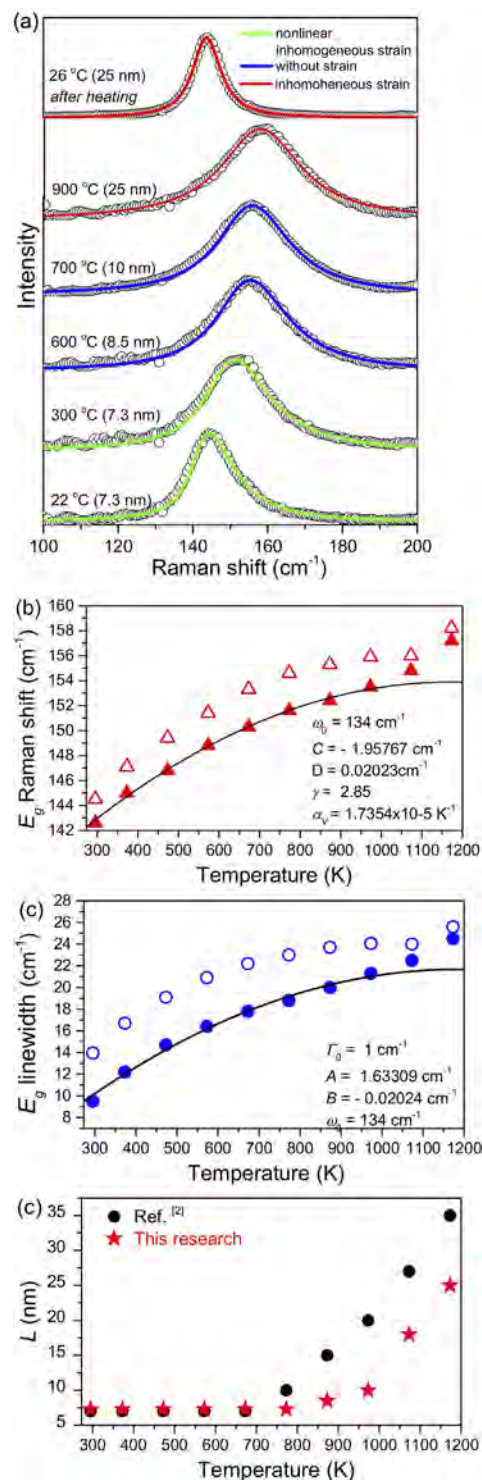


Figure 2. a) The Raman spectra of commercial anatase TiO_2 nanopowder measured at different temperatures (circles) simulated by PCM (lines). Temperature dependence of the E_g Raman (b) shift and (c) linewidth fitted by four-phonon anharmonic model (full lines) with the corresponding parameters specified in the figures. d) Nanocrystallite size L estimated by using PCM with (circles) and without (asterisks) included strain.

by using PCM with strain effect, is less steep than that obtained with strain effect neglected,^[2] which is much more consistent with the published XRD results for very small anatase nanoparticles.^[32] Note that we assume anatase nanocrystallites to obey a log-normal size distribution with average crystallite size of about 7 nm, previously estimated by the procedure based on the low frequency Raman scattering measurements.^[2]

3.1.2. Brookite Nanocrystalline Powders

Unlike the anatase phase, the variation of Raman spectra of TiO₂ brookite phase with temperature has not yet been reported, to the best of our knowledge. The Raman spectra of hydrothermally synthesized spindle-like brookite nanoparticles with mean crystallite size of ≈ 33 nm (according to XRD results^[33]) were measured in the temperature range from 80 to 860 K using Linkam THMS 600 heating stage coupled with Jobin Yvon T64000 micro-Raman system. The Raman spectra of brookite taken at several temperatures are shown in the **Figure 3a**. It can be seen that a great number of observed modes, characteristic for this orthorhombic structure (36 Raman active modes are expected according to symmetry considerations),^[34] broadens and shifts towards lower frequencies with the temperature increase. The temperature dependence of Raman shift (squares) and linewidth (circles) of the most intensive brookite A_{1g} mode, collected from experimental spectra is presented in the **Figure 3b**. The PCM has not been used to analyze the spectra of brookite nanopowder, because of relatively large mean crystallite size, as well as quite flat phonon dispersion curves theoretically predicted for this brookite Raman mode.^[35] Even the application of the anharmonic model in this analysis is not simple, due to lack of experimental and calculated data on the brookite thermal expansion coefficients, as well as the pressure dependence of brookite vibrational properties, needed for determination of mode Grüneisen parameter. Therefore, the value of volume thermal expansion coefficient for brookite is assumed in the range limited by expansion coefficients of anatase and rutile, as indicated by published experimental results related to polyhedral thermal expansion in these TiO₂ polymorphs.^[36] The value of Grüneisen parameter is taken as fitting parameter in the calculation of quasi-harmonic contribution to A_{1g} Raman shift according to Equations (4). The curves calculated as described above start to deviate from experimental temperature dependence of A_{1g} Raman shift on temperature already at 450 K, whereas the discrepancy of the values predicted according to Equation (9) from experimental linewidth appears above 600 K. The experimental A_{1g} linewidth at higher temperatures, narrower than predicted by the model, can be explained by the strain relaxation and increase of the brookite crystallite size with temperature. Note that gradual increase of brookite crystallite size due to thermal treatment of TiO₂ nanopowders has been documented in the literature.^[37] The comparison between brookite Raman spectra measured at 80 K, before and after heating the sample at 873 K (**Figure 3a**), indicates that some modes become better defined, narrower, and shifted to lower frequencies after the thermal treatment, thus supporting the assumptions of defect relaxation and partial consolidation of small particles into larger. On the other hand, the deviation of

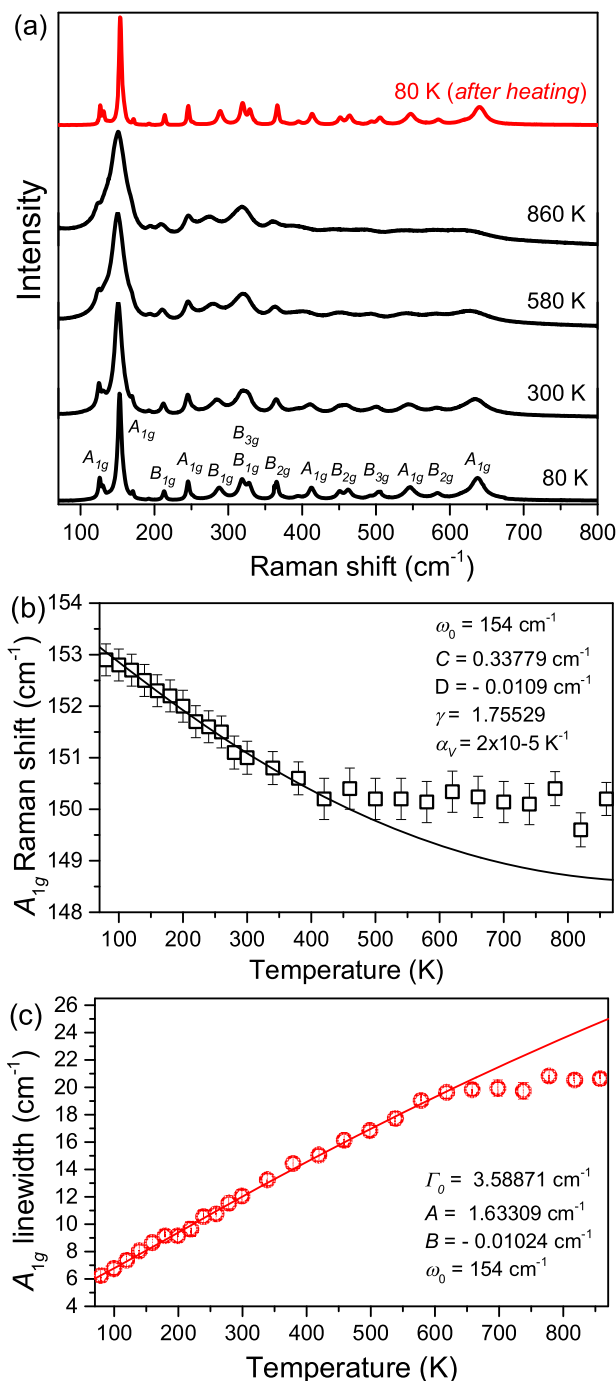


Figure 3. a) The Raman spectra of brookite TiO₂ nanopowder measured at different temperatures with characteristic modes assigned. Temperature dependence of the A_{1g} Raman mode (b) shift and (c) linewidth; experimental as read values (symbols) are fitted by four-phonon (full lines) anharmonic model with the corresponding parameters specified in the figures.

temperature dependence of A_{1g} Raman shift from those predicted by model, could be not only a consequence of microstructural changes in brookite nanopowder due to heating, but also a result of the changes in the thermal properties of

brookite with temperature. These changes are not taken into account because, despite some indications, precise data about these phenomena still are not available.

3.2. $\text{Zn}_x\text{Cd}_{1-x}\text{Se}$ Single Layers

The examination of vibrational properties of $\text{Zn}_{1-x}\text{Cd}_x\text{Se}$ is a matter of special interest due to structural phase transition observed in this material with variation of composition x and temperature.^[38] There are also the strong indications that vibration properties of thin layers are not identical to those for bulk $\text{Zn}_{1-x}\text{Cd}_x\text{Se}$ mixed crystal.^[39] The Raman spectra of microcrystalline $\text{Zn}_x\text{Cd}_{1-x}\text{Se}$ single layer (with composition $x = 0.59$ and thickness of 400 nm), prepared by thermal vacuum evaporation, through alloying of ultrathin ZnSe and CdSe films with equivalent thickness,^[40] were measured in the temperature range from 20 to 600 °C using Linkam THMS 600 heating stage coupled with Jobin Yvon T64000 micro-Raman system. Some of these spectra, obtained with 514.5 nm line of mixed Ar/Kr laser, are presented in the Figure 4a. The temperature dependences of Raman shift and linewidth of the most intensive Raman mode, ascribed to the scattering from 1LO phonons of the $\text{Zn}_x\text{Cd}_{1-x}\text{Se}$,^[38,41,42] are shown in the Figure 4b for chosen temperatures. We have decided to analyze temperature dependence of 1LO mode because of the change of the LO-phonon spectrum versus crystal composition, which has been described as one-mode type. On the other side, the TO-phonon dependence appeared to be much more complicated, with rather anomalous features in the line shape and mode frequency versus crystal composition, as well as the temperature, due to the anharmonic coupling between TO-mode and two-phonon states.^[42] To simulate this dependence by the model described in Section 2, values for thermal expansion coefficient and Grüneisen parameter have been taken from recently calculated pressure and temperature dependence of $\text{Zn}_{0.5}\text{Cd}_{0.5}\text{Se}$ thermodynamic properties.^[43] It is obvious that at the temperatures higher than 700 K, there are some discrepancies between experimentally obtained values and those predicted by the model, more pronounced for the mode frequencies. Such discrepancies are most probably the consequence of the change in the film composition at higher temperatures. Namely, it is well known that frequency of 1LO Raman mode of $\text{Zn}_x\text{Cd}_{1-x}\text{Se}$ increases with the increase in composition x , which arises here due to the evaporation of Cd at higher temperatures.^[41]

4. Temperature Dependence of Raman Spectra of Iron-Based Materials

The discovery of superconductivity in iron-based materials has attracted a great attention of the solid state community. During the last decade many new classes of iron-based materials with reach phase diagrams have been reported, featuring a variety of the (competing) phases,^[44] and their phonon properties have been extensively studied by using temperature-dependent Raman spectroscopy.^[5,6,45–64] In order to demonstrate the ability of inelastic light scattering to probe a number of structural and/or magnetic properties of iron-based materials, an overview of some published results is presented.^[5,6] The Raman scattering experiments shown here were performed in backscattering micro-Raman configuration using 514.5 nm line

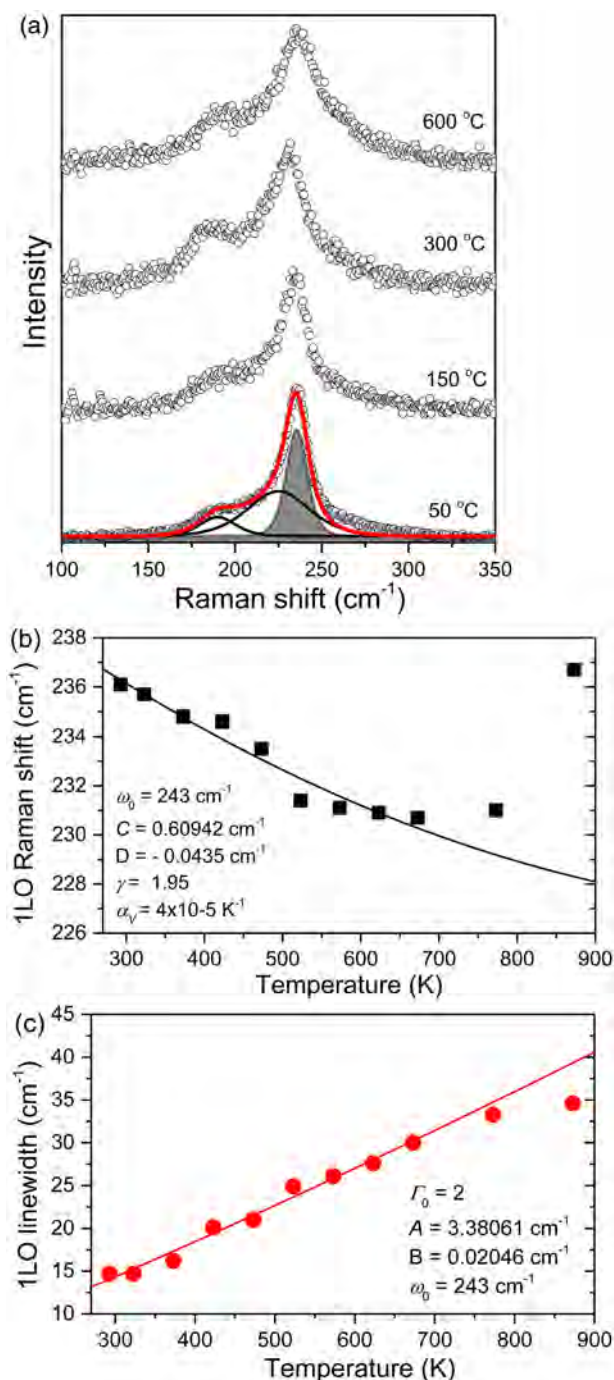


Figure 4. a) Experimental Raman spectra of $\text{Zn}_x\text{Cd}_{1-x}\text{Se}$ single layers measured at different temperatures; Lorentzian fit correspond to the 1LO mode of $\text{Zn}_x\text{Cd}_{1-x}\text{Se}$ is pointed out. Temperature dependence of the 1LO Raman mode (b) shift and (c) linewidth; symbols represent as-read experimental values, whereas full lines correspond to the results calculated by model described in the text with the parameters specified in the figures.

of an Ar^+/Kr^+ mixed laser. Low-temperature measurements were taken using KONTE CryoVac continuous flow cryostat coupled with JY T64000 or TriVista 557 Raman systems, whereas the Raman scattering measurements at higher

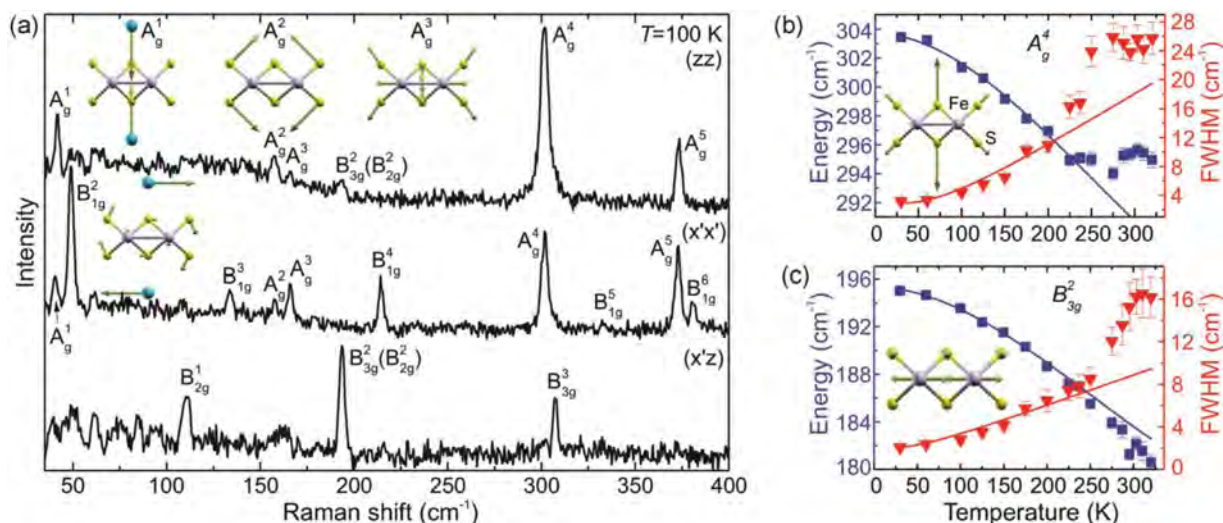


Figure 5. a) The polarized Raman scattering spectra of BaFe₂S₃ single crystal measured at 100 K. Insets: the normal modes of the A_g¹, A_g², A_g³, and B_{2g}¹ vibrations. x = [110], y = [110], and z = [001]. Experimental values (symbols) and calculated temperature dependence (solid lines) of the energies and broadenings of (b) A_g⁴ and (c) B_{2g}² Raman modes of BaFe₂S₃, with the normal modes of corresponding vibrations graphically represented in the insets. Reproduced with permission.^[5] Copyright 2015, American Physical Society.

temperatures were done using a Linkam THMS600 heating stage.

4.1. Temperature-Dependent Raman Spectra of BaFe₂S₃ and BaFe₂Se₃

The crystal structures of the BaFe₂S₃ and BaFe₂Se₃, representatives of the iron-based S = 2 two-leg spin-ladder compound

family, are isomorphic, but not isostructural.^[5] They can be described as alternate stacking of Fe-S(Se) layers and Ba cations along the crystallographic *a* axis (*b* axis), whereas in the Fe-S(Se) plane, only one-dimensional (1D) double chains of edge-shared [FeS(Se)]₄ tetrahedra propagate along these axes.

The BaFe₂S₃ is a quasi-one-dimensional semiconductor with orthorhombic crystal symmetry, with space group *Cmcm* and Z = 4. Based on the factor group analysis, the 18 Raman active modes are expected to be registered in the spectra of single-

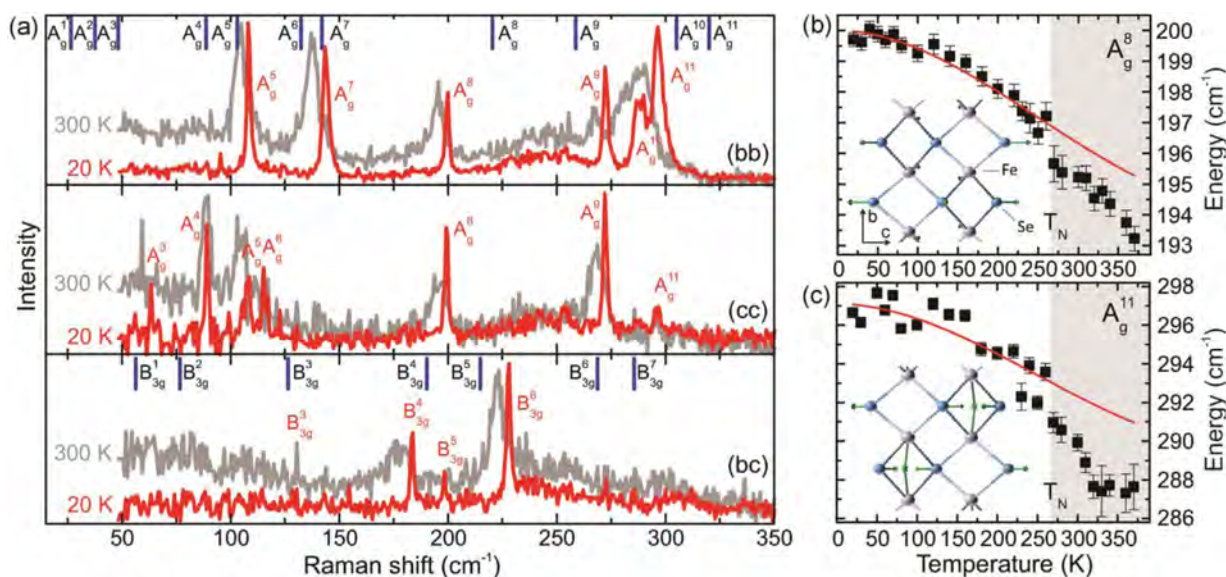


Figure 6. a) The x(yy)x, x(zz)x, and x(yz)x polarized Raman scattering spectra of BaFe₂Se₃ single crystals measured at room temperature and at 20 K. Vertical bars are calculated values of the A_g⁸ and the B_{2g}³ symmetry Raman active vibrations. Experimental values (symbols) and calculated temperature dependence (solid lines) of BaFe₂Se₃ (b) A_g⁸ and (c) A_g¹¹ Raman mode energies with normal modes of corresponding vibrations graphically represented in the insets. Reproduced with permission.^[5] Copyright 2015, American Physical Society.

crystal with (110) orientation.^[5] Most of these modes are observed in polarized Raman scattering spectra of BaFe₂S₃ investigated here (Figure 5a).

Experimental values and temperature dependence of the energy and broadening of A_g^4 and B_{3g}^2 Raman modes of BaFe₂S₃, calculated by Equations (3), (4), (8) and (10), are shown in the Figures 5b and c, respectively. The change in the slope of temperature dependence of these modes linewidth (energy), as well as deviations of simulated anharmonic behavior from experimental values, is observed at about 275 K. This could be related to the spin and charge, because of a hump in the inverse molar magnetic susceptibility, and a change of slope of the electrical resistivity temperature dependence, which have been observed in BaFe₂S₃ at similar temperature.

The antiferromagnetic ordering of spins within the ladder legs could change from short-range to the long-range state, without 3D antiferromagnetic spin ordering (the Néel state) of the whole BaFe₂S₃ crystal, followed by the change of electronic structure, which could explain the abrupt increase of the resistivity at this temperature. Note that 3D-antiferromagnetic phase transition is registered in many of iron-based spin-ladder materials at about 260 K.

The BaFe₂Se₃ also has an orthorhombic structure (*Pmna*) with unit cell consisting of four formula units containing 24 atoms. However, unlike the BaFe₂S₃, there is an alternation of the Fe–Fe distances along the chain direction in BaFe₂Se₃. The 36 Raman active modes are predicted in the BaFe₂Se₃ spectra by the factor

group analysis, but only modes of A_g and B_{3g} symmetry are observed in the spectra measured from the (100) plane of the sample (the crystallographic *a* axis is perpendicular to the plane of the single crystal), as shown in the Figure 6a.

The energies of A_g^8 and A_g^{11} Raman modes of BaFe₂Se₃ change abruptly at temperatures below $T_N = 255$ K, when this compound becomes antiferromagnetically long-range ordered (Figure 6b and c, respectively). It appears that the spin-phonon (magnetoelastic) coupling is responsible for Raman mode energy change in the antiferromagnetic phase, due to significant local lattice distortion (Fe atom displacement along the *b* axis of ≈ 0.001 nm) driven by the magnetic order. Moreover, local displacements in the Fe atoms at T_N have a significant impact on the electronic structure due to rearrangement of electrons near the Fermi level, and, consequently, the change in the phonon energy and broadening.

4.2. Temperature-Dependent Raman Spectra of Superconducting $K_x\text{Fe}_{2-y}\text{Se}_2$ and Non-Superconducting $K_{0.8}\text{Fe}_{1.8}\text{Co}_{0.2}\text{Se}_2$

According to the selection rules, two Raman modes in the spectra of $K_x\text{Fe}_{2-y}\text{Se}_2$ can be ascribed to high symmetry (*I4/mmm*), whereas 18 phonon modes could originate from low-symmetry (*I4/m*) phase, out of which 16 has been observed in this phase-separated sample.^[6,50] Polarized Raman scattering

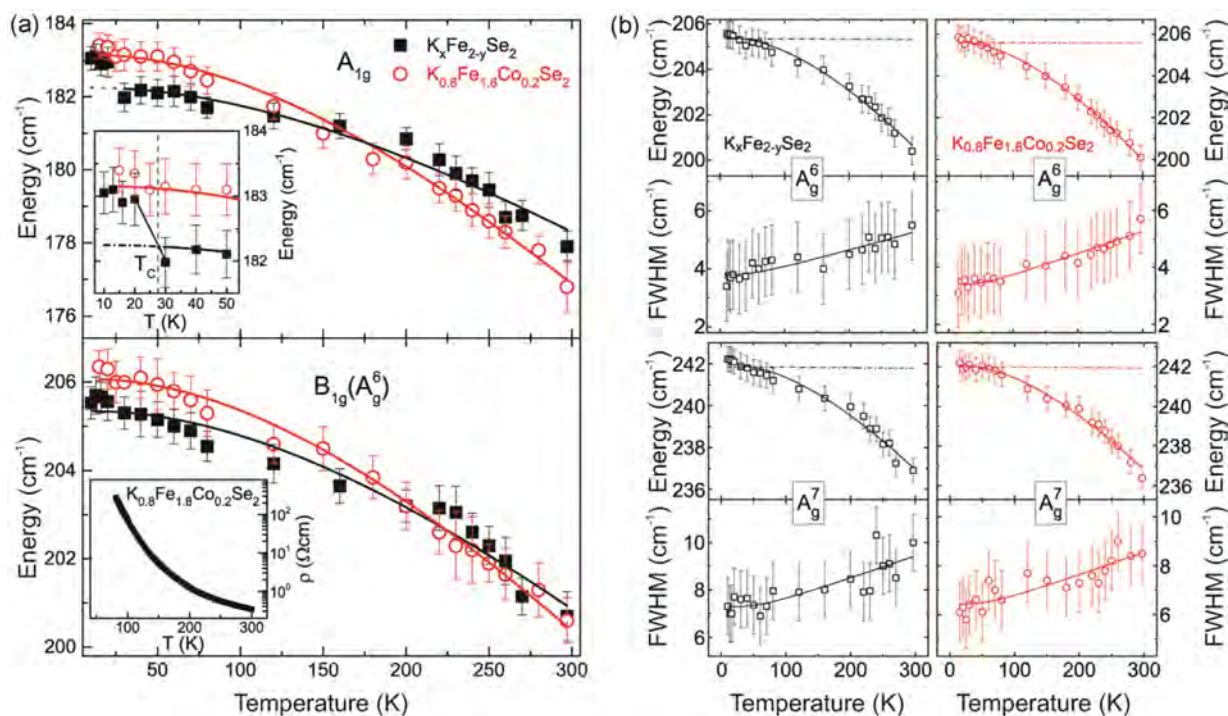


Figure 7. a) Temperature dependence of the energy for the A_{1g} and $B_{1g}(A_g^6)$ Raman modes of $K_x\text{Fe}_{2-y}\text{Se}_2$ and $K_{0.8}\text{Fe}_{1.8}\text{Co}_{0.2}\text{Se}_2$ single crystals. Upper inset: Enlarged view of the dependence of the A_{1g} mode energy on temperature in a low-temperature region near T_C for $K_x\text{Fe}_{2-y}\text{Se}_2$. Lower inset: the temperature dependence of the electrical resistivity for $K_{0.8}\text{Fe}_{1.8}\text{Co}_{0.2}\text{Se}_2$ shows the nonmetallic behaviour of this single crystal. b) Temperature dependence of energy and linewidth for some A_g modes of $K_x\text{Fe}_{2-y}\text{Se}_2$ (left panel) and $K_{0.8}\text{Fe}_{1.8}\text{Co}_{0.2}\text{Se}_2$ (right panel). Solid lines take into account only the volume contribution to the phonon mode energy. Reproduced with permission.^[6] Copyright 2015, IOP Publishing.

spectra of $\text{K}_{0.8}\text{Fe}_{1.8}\text{Co}_{0.2}\text{Se}_2$ single crystals, measured from the (001) plane of the sample at various temperatures, have shown that the energies of Raman active phonons are close to the energies of the corresponding modes in $\text{K}_x\text{Fe}_{2-y}\text{Se}_2$. The same number of Raman modes observed in both compounds, with similar corresponding energies, suggests that phase separation is also present in $\text{K}_{0.8}\text{Fe}_{1.8}\text{Co}_{0.2}\text{Se}_2$, and that doping of a $\text{K}_x\text{Fe}_{2-y}\text{Se}_2$ single crystal with a small amount of Co does not have a significant impact on the phonon spectrum in the normal state.^[6]

The temperature dependences of A_{1g} and $B_{1g}(A_g^6)$ modes of $\text{K}_x\text{Fe}_{2-y}\text{Se}_2$ and $\text{K}_{0.8}\text{Fe}_{1.8}\text{Co}_{0.2}\text{Se}_2$ single crystals are shown in the Figure 7a. These dependences are analyzed using Equation (3) with Δ_i^V therm only, knowing that the calculated values of parameters C_i in the anharmonic term Δ_i^A are negligible. The temperature dependence of the $B_{1g}(A_g^6)$ mode energy in both samples in the whole temperature range under investigation is well described by the proposed model. However, A_{1g} mode energy is well fitted by this model only in the case of non-superconducting Co-doped sample, whereas an abrupt change in A_{1g} mode energy around T_C in the superconducting sample is observed. It may be concluded that the hardening of A_{1g} mode around T_C (observed for superconducting sample and absent for non-superconducting one; see the inset in the Figure 7a) is caused by the superconductivity induced phonon renormalization. Note that sudden change in the energy near T_C is registered only for the mode corresponding to vibration of high-symmetry ($I4/mmm$) phase in the superconducting $\text{K}_x\text{Fe}_{2-y}\text{Se}_2$ and could be related to the rearrangement of the electronic states to which this mode couples, as the superconducting gap opens.

On the other side, the temperature dependence of the Raman energy and linewidth of A_g^6 and A_g^7 modes (Figure 7b), registered in the spectra of $\text{K}_x\text{Fe}_{2-y}\text{Se}_2$ and $\text{K}_{0.8}\text{Fe}_{1.8}\text{Co}_{0.2}\text{Se}_2$ single crystals, and ascribed to non-superconducting low-symmetry phase ($I4/m$), are well described by the proposed lattice anharmonic model only with the contribution of the lattice thermal expansion.

5. Conclusion

The results presented in this paper have shown how temperature-dependent Raman scattering measurements could be used to analyze the variation of structural, morphological, compositional, electronic, and/or magnetic material properties with the temperature. It was demonstrated that physical model, including quasi-harmonic and anharmonic contributions, used to quantitatively analyze experimentally obtained temperature dependence of energy and linewidth of the characteristic Raman modes, could serve as predictive tool for determining the temperatures at which significant changes occur in studied materials. Temperature-dependent Raman spectra of nanomaterials have given information about their thermal stability and allowed tracking changes in phase composition, nanocrystallite size, strain and non-stoichiometry with temperature. In addition to thermal expansion and three-phonon anharmonic contribution, usually the four-phonon anharmonic contribution must be included in order to describe the temperature dependence of the shift and linewidth of Raman modes in nanomaterials.

However, it should be noted that, although this approach provides good fits to experimental Raman data of investigated nanomaterials, some results may not have a complete physical meaning, due to oversimplified approximations (too large cubic anharmonicity in comparison to the quartic, a negative fitting parameter for the quartic anharmonicity in some cases, which is unreasonable). However, if asymmetric phonon decays and four phonon processes turn out to be negligible, the Klemens model provides a reasonable fit to the Raman shift and linewidth of all studied phonons in iron-based single crystals, making this model very convenient for investigated iron-based materials. Thermal expansion and three-phonon anharmonic contributions are usually sufficient to describe temperature dependence of shift and linewidth of Raman modes characteristic for iron-based materials, whereas deviation of experimental values from those predicted by the model has indicated structural and phase transitions and has allowed determining the temperature at which they occurred. The influence of antiferromagnetic order, ferromagnetism, and magnetic fluctuations on the Raman scattering spectra of iron-based compounds depending on temperature can show, not only superconducting, but also a low-dimensional magnetic properties of these materials.

Acknowledgements

This work was financially supported by the Ministry of Education, Science and Technological Development, Republic of Serbia, under the Project No. III45018. We would like to express our very great appreciation to dr Diana Nesheva (Institute of Solid State Physics, Bulgarian Academy of Sciences), dr Cedomir Petrovic (Condensed Matter Physics & Materials Science Department Brookhaven National Laboratory), and dr Nataša Tomić (Institute of Physics, University of Belgrade), who provided us with valuable sample materials and participated in discussing experimental results. The assistance provided by dr Marko Opačić (Institute of Physics, University of Belgrade) is always greatly appreciated.

Conflict of Interest

The authors declare no conflict of interest.

Keywords

iron-based compounds, nanomaterials, quasi-harmonic and anharmonic effects, Raman spectra

Received: September 30, 2018

Revised: January 21, 2019

Published online:

- [1] M. J. Šćepanović, M. Grujić-Brojčin, Z. D. Dohčević-Mitrović, Z. V. Popović, *Appl. Phys. A* **2007**, 86, 365.
- [2] M. J. Šćepanović, M. Grujić-Brojčin, Z. D. Dohčević-Mitrović, Z. V. Popović, *Sci. Sinter.* **2009**, 41, 67.
- [3] M. Šćepanović, M. Grujić-Brojčin, Z. Dohčević-Mitrović, Z. V. Popović, *J. Phys. Conf. Ser.* **2010**, 253, 012015.
- [4] M. Grujić-Brojčin, M. J. Šćepanović, Z. D. Dohčević-Mitrović, Z. V. Popović, *Acta Phys. Pol. A* **2009**, 116, 51.

- [5] Z. V. Popović, M. Šćepanović, N. Lazarević, M. Opačić, M. M. Radonjić, D. Tanasković, H. Lei, C. Petrovic, *Phys. Rev. B* **2015**, 91, 064303.
- [6] M. Opačić, N. Lazarević, M. Šćepanović, H. Ryu, H. Lei, C. Petrovic, Z. V. Popović, *J. Phys. —Condens. Mat.* **2015**, 27, 485701.
- [7] T. Tadano, S. Tsuneyuki, *J. Phys. Soc. Jpn.* **2018**, 87, 041015.
- [8] A. A. Maradudin, R. F. Wallis, *Phys. Rev.* **1960**, 120, 442; A. A. Maradudin, P. A. Flinn, R. A. Coldwell-Horsfall, *Ann. Phys-New York* **1961**, 15, 337; A. A. Maradudin, P. A. Flinn, R. A. Coldwell-Horsfall, *Ann. Phys-New York* **1961**, 15, 360; A. A. Maradudin, I. P. Ipatova, *J. Math. Phys.* **1968**, 9, 525.
- [9] I. P. Ipatova, A. A. Maradudin, R. F. Wallis, *Phys. Rev.* **1967**, 155, 882.
- [10] I. Errea, M. Calandra, F. Mauri, *Phys. Rev. B* **2014**, 89, 064302.
- [11] T. Sun, D.-B. Zhang, R. M. Wentzcovitch, *Phys. Rev. B* **2014**, 89, 094109.
- [12] T. Lan, X. Tang, B. Fultz, *Phys. Rev. B* **2012**, 85, 094305; T. Lan, C. W. Li, O. Hellman, D. S. Kim, J. A. Munoz, H. Smith, D. L. Abernathy, B. Fultz, *Phys. Rev. B* **2015**, 92, 054304; T. Lan, Z. Zhu, *Adv. Cond. Matter Phys.* **2016**, 2714592.
- [13] Z. Zhao, J. Elwood, M. A. Carpenter, *J. Phys. Chem. C* **2015**, 119, 23094.
- [14] J. Menéndez, M. Cardona, *Phys. Rev. B* **1984**, 29, 2051.
- [15] H.-M. Eiter, P. Jaschke, R. Hackl, A. Bauer, M. Gangl, C. Pfleiderer, *Phys. Rev. B* **2014**, 90, 024411.
- [16] P. G. Klemens, *Phys. Rev.* **1966**, 148, 845.
- [17] M. Balkanski, R. F. Wallis, E. Haro, *Phys. Rev. B* **1983**, 28, 1928.
- [18] A. K. Arora, M. Rajalakshmi, T. R. Ravindran, V. Sivasubramanian, *J. Raman Spectrosc.* **2007**, 38, 604.
- [19] M. Fernandez-Garcia, A. Martinez-Arias, J. C. Hanson, J. A. Rodriguez, *Chem. Rev.* **2004**, 104, 4063.
- [20] J. E. Spanier, R. D. Robinson, F. Zhang, S.-W. Chan, I. P. Herman, *Phys. Rev. B* **2001**, 64, 245407.
- [21] S. Kelly, F. H. Pollak, M. Tomkiewicz, *J. Phys. Chem. B* **1997**, 101, 2730.
- [22] H. Richter, Z. P. Wang, L. Ley, *Solid State Commun.* **1981**, 39, 625.
- [23] I. I. Campbell, P. M. Fauchet, *Solid State Commun.* **1986**, 58, 739.
- [24] K.-R. Zhu, M.-S. Zhang, Q. Chen, Z. Yin, *Phys. Lett. A* **2005**, 340, 220.
- [25] A. C. Breeson, G. Sankar, G. K. Liang Goh, R. G. Palgrave, *Phys. Chem. Chem. Phys.* **2016**, 18, 24722.
- [26] H. M. Moghaddam, S. Nasirian, *Nanosci. Methods* **2012**, 1, 201.
- [27] B. Choudhury, A. Choudhury, *Int Nano Lett* **2013**, 3, 55.
- [28] W. Naffouti, T. B. Nasr, H. Meradji, N. Kamoun-Turki, *J. Electron. Mater.* **2016**, 45, 5096.
- [29] M. K. Hossain, M. F. Pervez, M. N. H. Mia, S. Tayyaba, M. J. Uddin, R. Ahamed, R. A. Khan, M. Hoq, M. A. Khan, F. Ahmed, *Mater. Sci. —Poland* **2017**, 35, 868.
- [30] A. Verma, A. K. Yadav, N. Khatun, S. Kumar, C.-M. Tseng, S. Biring, S. Sen, *J. Mater. Sci.: Mater. Electron* **2017**, 28, 19017.
- [31] M. Mikami, S. Nakamura, O. Kitao, H. Arakawa, *Phys. Rev. B* **2002**, 66, 1552131.
- [32] S. Patra, C. Davoisne, H. Bouyanfif, D. Foix, F. Sauvage, *Sci. Rep. —UK* **2016**, 5, 10928.
- [33] N. Tomić, M. Grujić-Brojčin, N. Finčur, B. Abramović, B. Simović, J. Krstić, B. Matović, M. Šćepanović, *Mater. Chem. Phys.* **2015**, 163, 518.
- [34] M. N. Iliev, V. G. Hadjiev, A. P. Litvinchuk, *Vib. Spectrosc.* **2013**, 64, 148.
- [35] E. Shojaei, M. Abbasnejad, M. Saeedian, M. R. Mohammadzadeh, *Phys. Rev. B* **2011**, 83, 174302.
- [36] E. P. Meagher, G. A. Lager, *Can. Mineral.* **1979**, 17, 77.
- [37] N. S. Allen, N. Mahdjoub, V. Vishnyakov, P. J. Kelly, R. J. Kriek, *Polym. Degrad. Stabil.* **2018**, 150, 31.
- [38] L. K. Vodopyanov, E. A. Vinogradov, V. S. Vinogradov, I. V. Kucherenko, B. N. Mavrin, N. N. Novikova, P. V. Shapkin, *phys. stat. sol. (c)* **2004**, 1, 3162.
- [39] L. K. Vodopyanov, *J. Alloy Compd.* **2004**, 371, 72.
- [40] D. Nesheva, Z. Aneva, M. J. Šćepanović, I. Bineva, Z. Levi, Z. V. Popović, B. Pejova, *J. Phys. Conf. Ser.* **2010**, 253, 012035.
- [41] D. Nesheva, Z. Aneva, M. J. Šćepanović, Z. Levi, I. Iordanova, Z. V. Popovic, *J. Phys. D: Appl. Phys.* **2011**, 44, 415305.
- [42] M. Y. Valakh, M. P. Lisitsa, G. S. Pekar, G. N. Polysskii, V. I. Sidorenko, A. M. Yaremko, *Phys. Stat. Sol. (b)* **1982**, 113, 635.
- [43] N. ul Aarifeen, A. Afaq, *Mater. Res. Express* **2017**, 4, 095901.
- [44] G. R. Stewart, *Rev. Mod. Phys.* **2011**, 83, 1589.
- [45] Z. V. Popović, M. Šćepanović, N. Lazarević, M. M. Radonjić, D. Tanasković, H. Lei, C. Petrovic, *Phys. Rev. B* **2014**, 89, 014301.
- [46] Z. V. Popović, N. Lazarević, S. Bogdanović, M. M. Radonjić, D. Tanasković, R. Hu, H. Lei, C. Petrovic, *Solid State Commun.* **2014**, 193, 51.
- [47] N. Lazarević, M. Radonjić, M. Šćepanović, H. Lei, D. Tanasković, C. Petrovic, Z. V. Popović, *Phys. Rev. B* **2013**, 87, 144305.
- [48] N. Lazarević, H. Lei, C. Petrovic, Z. V. Popović, *Phys. Rev. B* **2011**, 84, 214305.
- [49] N. Lazarević, M. M. Radonjić, D. Tanasković, R. Hu, C. Petrovic, Z. V. Popović, *J. Phys.: Condens. Matter* **2012**, 24, 255402.
- [50] N. Lazarević, M. Abeykoon, P. W. Stephens, H. Lei, E. S. Bozin, C. Petrovic, Z. V. Popović, *Phys. Rev. B* **2012**, 86, 054503.
- [51] R. Hu, H. Lei, C. Petrovic, *Solid State Commun.* **2014**, 193, 51.
- [52] M. R. Opačić, N. Ž. Lazarević, *J. Serb. Chem. Soc.* **2017**, 82, 1.
- [53] M. Opačić, N. Lazarević, D. Tanasković, M. M. Radonjić, A. Milosavljević, Y. Ma, C. Petrovic, Z. V. Popović, *Phys. Rev. B* **2017**, 96, 174303.
- [54] A. Baum, Ying Li, M. Tomić, N. Lazarević, D. Jost, F. Löffler, B. Muschler, T. Böhm, J.-H. Chu, I. R. Fisher, R. Valentí, I. I. Mazin, R. Hackl, *Phys. Rev. B* **2018**, 98, 075113.
- [55] A. Baum, A. Milosavljević, N. Lazarević, M. M. Radonjić, B. Nikolić, M. Mitschek, Z. Inanloo Maranloo, M. Šćepanović, M. Grujić-Brojčin, N. Grujić-Brojčin, M. Opel, Aifeng Wang, C. Petrovic, Z. V. Popović, R. Hackl, *Phys. Rev. B* **2018**, 97, 054306.
- [56] A. P. Litvinchuk, V. G. Hadjiev, M. N. Iliev, Bing Lv, A. M. Guloy, C. W. Chu, *Phys. Rev. B* **2008**, 78, 060503(R).
- [57] V. Gnezdilov, Y. G. Pashkevich, P. Lemmens, D. Wulferding, T. Shevtsova, A. Gusev, D. Chareev, A. Vasiliev, *Phys. Rev. B* **2013**, 87, 144508.
- [58] V. Gnezdilov, Yu. Pashkevich, P. Lemmens, A. Gusev, K. Lamonova, T. Shevtsova, I. Vitebskiy, O. Afanasiev, S. Gnatchenko, V. Tsurkan, J. Deisenhofer, A. Loidl, *Phys. Rev. B* **2011**, 83, 245127.
- [59] L. Chauvière, Y. Gallais, M. Cazayous, A. Sacuto, M. A. Méasson, D. Colson, A. Forget, *Phys. Rev. B* **2009**, 80, 094504.
- [60] Y. Gallais, A. Sacuto, M. Cazayous, P. Cheng, L. Fang, H. H. Wen, *Phys. Rev. B* **2008**, 78, 132509.
- [61] A. M. Zhang, K. Liu, J. H. Xiao, J. B. He, D. M. Wang, G. F. Chen, B. Normand, Q. M. Zhang, *Phys. Rev. B* **2012**, 85, 024518.
- [62] T.-L. Xia, D. Hou, S. C. Zhao, A. M. Zhang, G. F. Chen, J. L. Luo, N. L. Wang, J. H. Wei, Z.-Y. Lu, Q. M. Zhang, *Phys. Rev. B* **2009**, 79, 140510(R).
- [63] A. Ignatov, A. Kumar, P. Lubik, R. H. Yuan, W. T. Guo, N. L. Wang, K. Rabe, G. Blumberg, *Phys. Rev. B* **2012**, 86, 134107.
- [64] Y. J. Um, A. Subedi, P. Toulemonde, A. Y. Ganin, L. Boeri, M. Rahlenbeck, Y. Liu, C. T. Lin, S. J. E. Carlsson, A. Sulpice, M. J. Rosseinsky, B. Keimer, M. Le Tacon, *Phys. Rev. B* **2012**, 85, 064519.



Influence of chemical fixation process on primary mesenchymal stem cells evidenced by Raman spectroscopy

J.J. Lazarević^a, U. Ralević^a, T. Kukolj^b, D. Bugarski^b, N. Lazarević^{a,*}, B. Bugarski^c, Z.V. Popović^{a,d}

^aCenter for Solid State Physics and New Materials, Institute of Physics Belgrade, University of Belgrade, Pregrevica 118, Belgrade 11080, Serbia

^bLaboratory for Experimental Hematology and Stem Cells, Institute for Medical Research, University of Belgrade, Belgrade 11000, Serbia

^cDepartment of Chemical Engineering, Faculty of Technology and Metallurgy, University of Belgrade, Karnegijeva 4, Belgrade 11060, Serbia

^dSerbian Academy of Sciences and Arts, Knez Mihailova 35, Belgrade 11000, Serbia

ARTICLE INFO

Article history:

Received 7 December 2018

Received in revised form 6 March 2019

Accepted 6 March 2019

Available online 9 March 2019

Keywords:

Raman spectroscopy

Stem cells

Chemical fixation

ABSTRACT

In investigation of (patho)physiological processes, cells represent frequently used analyte as an exceptional source of information. However, spectroscopic analysis of live cells is still very seldom in clinics, as well as in research studies. Among others, the reasons are long acquisition time during which autolysis process is activated, necessity of specified technical equipment, and inability to perform analysis in a moment of sample preparation. Hence, an optimal method of preserving cells in the existing state is of extreme importance, having in mind that selection of fixative is cell lineage dependent. In this study, two commonly used chemical fixatives, formaldehyde and methanol, are used for preserving primary mesenchymal stem cells extracted from periodontal ligament, which are valuable cell source for reconstructive dentistry. By means of Raman spectroscopy, cell samples were probed and the impact of these fixatives on their Raman response was analyzed and compared. Different chemical mechanisms are the core processes of formaldehyde and methanol fixation and certain Raman bands are shifted and/or of changed intensity when Raman spectra of cells fixed in that manner are compared. In order to get clearer picture, comprehensive statistical analysis was performed.

© 2019 Elsevier B.V. All rights reserved.

1. Introduction

Mesenchymal stem cells (MSCs) are heterogenous group of adult stem cells originally discovered in bone marrow, but present in all tissues and organs, with the purpose to keep tissue homeostasis, regeneration and renewal. These acts are performed not only through multipotent differentiation potential (toward chondrogenic, adipogenic, and osteogenic lineages), but also through their ability to modulate immune response (directly or indirectly) [1–5]. Although MSCs possess common cellular features, it is overall accepted that these cells still exhibit variable regenerative capacity due to different tissue origin, donor diversity, and variations in culture conditions [6,7]. Human MSCs investigated in this study originate from periodontal ligament, a fibrous, cellular, and vascular soft connective tissue. The main role of periodontal ligament is to anchor tooth to the alveolar bone, maintain mineralisation level and alleviate mechanical forces associated with the process of mastication [8–10]. Previously, it was demonstrated that human periodontal ligament

stem cells (hPDLSCs) investigated in this experiment fulfill criteria for MSCs identification and characterization, set by The International Society for Cell Therapy (ISCT) [11,12]. Minimal criteria for characterization of human MSCs, set by ISCT, include plastic adhesion, with expression of CD73, CD90, CD105 surface markers and lack of hematopoietic markers CD34–, CD45–, CD14–, CD79α–, HLA-DR–; and multilineage differentiation potential into osteoblasts, adipocytes, and chondroblasts [13]. However, MSCs nature, including hPDLSCs, is still elusive. Therefore, the exploration of hPDLSCs, as a cell source for reconstructive dentistry, is of great importance for the novel therapeutic strategies related to recovery of periodontium and curing dental defects [14].

Taking into account the heterogeneity of MSCs, it is crucial for these cells to be adequately characterized during the lifespan, before further manipulation. Although many techniques are available in this field, including mass spectroscopy, flow cytometry, and immunocytochemistry, most of them are destructive, invasive, time consuming or require expensive cell-specific labels [15,16]. However, a light scattering technique, Raman spectroscopy, is able to overrun these issues due to its unique properties: it is non-invasive, non-destructive, fast, label-free, and complex sample preparation is not required. It operates with low sample volume even in aqueous

* Corresponding author.

E-mail address: nenadl@ipb.ac.rs (N. Lazarević).

solutions and provide a plenty of biochemical information as an outcome. Raman spectroscopy is a type of vibrational spectroscopy, based on Raman effect [17], in which an inelastically scattered component of the visible light bears the information of the analyte. Raman scattering experiment results in vibrational spectrum, a fingerprint of a sample, which carries the information about chemical composition and structure of a sample, on a submolecular level. Typically, it comprises vibrational modes of the highest Raman scattering cross section [16, 18–20].

Spectroscopic analysis of live cells is still very seldom, both in clinical and research conditions, particularly due to the longevity of the processes, when autolysis is inevitable. On the other hand, it is not always possible to investigate a sample in a moment of acquiring. The crucial and fundamental step in cell biology, for obtaining sensitive and reproducible results, is a process called fixation, which maintain the localization of biomolecules. It is used for preserving a cell in a physiological state, by preventing cell shrinkage or swelling caused by osmotic pressure initiated with air-drying, as well as autolysis by activating lysosomal enzymes, which includes denaturation of proteins, dephosphorylation of mononucleotides, phospholipids and proteins, chromatin compaction, nuclear fragmentation, and cytoplasmic condensation and fragmentation [21]. However, it is known that selection of a fixative is very much dependent on a cell nature when it comes to Raman spectroscopy and can significantly distort experimental data [22]. In the past decade, investigations of different fixatives' influence on Raman spectra of numerous cell lineages were reported, with an aim to clarify the best option for each cell lineage. One of the studies investigated the effect of formaldehyde and ethanol fixation on CARS (Coherent Anti-Stokes Raman Spectroscopy) signal of proteins and lipids in different cellular compartments of glial and neuronal cells, concluding that formaldehyde fixation is preferable method of preservation of these cells [22]. Also, the effect of chemical fixation procedures on the Raman spectra of normal and leukemia cells was characterized [23]. When compared to the spectra of unfixed cells, the fixed cell spectra showed changes in the intensity of specific Raman markers, and latter statistical analysis suggested that methanol provokes greater changes in Raman spectra when compared to paraformaldehyde. Further, micro-Raman spectroscopy was employed for chemical fixation mechanism study in three cell lines (normal skin, normal bronchial epithelium, and lung adenocarcinoma) [24]. Nucleic acid degradation, protein denaturation, and lipid leaching was observed with all fixatives (formalin, Carnoy's fixative, and methanol-acetic acid) and for all cell lines, but to varying degrees. Also, the authors suggested that formalin best preserves cellular integrity and gives the closest spectral content to that in live cells. The next study monitored the impact of fixation by formalin, desiccation, and air-drying on *in vitro* cell culture lines [25]. The results indicate that the choice of fixation methodology significantly influences the quality and reproducibility of the resulting spectral data. Formalin showed inconsistency in sample preservation and a loss of signal intensity, while air-drying appears to be inconsistent in terms of spectral reproducibility. Desiccation showed good spectral reproducibility and good signal-to-noise ratio [25].

Although numerous Raman studies of fixative process' spectral influence have been performed [22–25], according to our knowledge, no such research has been performed on primary mesenchymal stem cells originating from periodontal ligament. We used micro-Raman spectroscopy in order to probe fixed hPDLSCs and investigate the effects of two most frequently used chemical fixatives which have different chemical mechanisms of preservation (formaldehyde and methanol), and then compared those effects. Formaldehyde reacts extensively with amino groups to form methylene bridges and cross-links molecules, which alters, but stabilizes them [26]. Further, formaldehyde does not appear to perturb tertiary structure very much. On the other hand, methanol replaces water in cell environment, disrupts hydrophobic and hydrogen bonding, and

consequently alters tertiary structure of proteins [27,28]. Although fixation substantially alters composition and appearance, it is possible to produce consistent chemical and physical properties by selection of suitable preparation conditions. Nevertheless, standardization of Raman spectroscopy regarding fixative selection could provide valuable additional information in many biological tests that require cell fixation and also indicate the existence of fine differences in the fixative effect that are necessary to be taken into consideration during standard biological protocols.

2. Experiment

2.1. Isolation and Cultivation of Human Periodontal Ligament Stem Cells

After getting the informed consent from healthy patients (age 18), subjected to the procedure of tooth extraction for orthodontic reasons, at the Department of Oral Surgery of the Faculty of Dental Medicine, the University of Belgrade, human periodontal ligament tissues from normal impacted third molars were collected. Immediately after, tissues were placed in sterile cell culturing conditions. As previously reported [11], human PDLSCs were isolated, characterized and expanded. For hPDLSCs isolation, periodontal tissues were carefully detached from the mid-third of the root surface, cut into small pieces and placed in a 25 cm² flask with Dulbecco's modified Eagle's medium (DMEM; Sigma-Aldrich St. Louis, MO, USA) supplemented with 10% fetal bovine serum (FBS; Capricorn-Scientific, Germany), 100 U/ml penicillin and 100 mg/ml streptomycin (Gibco, Thermo Fisher Scientific, USA). Standard cultivation conditions included 37 °C temperature, humidified atmosphere containing 5% CO₂, while medium was exchanged two times per week. After reaching 80% to 90% confluence, cells were detached regularly in growth medium (GM-DMEM with 10% FBS) using 0.05% trypsin with 1 mM EDTA (Gibco, Thermo Fisher Scientific, USA). In order to demonstrate the universality of experimental results for MSCs, cells from third and sixth passages were used, divided into two batches. Moreover, hPDLSCs were characterized based on immunophenotype and multipotent differentiation potential toward osteogenic, chondrogenic and adipogenic lineages as it has been described before [11]. All treatments were performed according to the approved ethical guidelines set by Ethics Committee of the Faculty of Dental Medicine, University of Belgrade and Declaration of Helsinki.

2.2. Sample Preparation

For the Raman experiment, hPDLSCs were seeded on rounded CaF₂ slides in 24-well plate (5 × 10³ cells per slide) and cultivated in GM in standard cultivation conditions during 24 h. Following the adhesion, hPDLSCs were washed with saline buffer and fixed with 3.7% formaldehyde or methanol for 10 min at room temperature. Right before Raman spectroscopy was performed, samples were washed with distilled water.

2.3. μ -Raman Spectroscopy

In most of the cases, the Raman spectroscopy independently probes single vibrations within a molecule or a crystal, but in a complex biological systems composed of various types of macromolecules, only vibrational bands consisting of numerous vibrations of the same type, rather than a single vibration, could be distinguished. Consequently, the changes of biological system composition may result with a change of certain Raman bands line-shapes and/or intensities.

The Raman scattering experiment was performed using NTegra Spectra from NTMDT. The 532 nm line of a semiconductor laser was used as an excitation source. The laser power was set to 2 mW

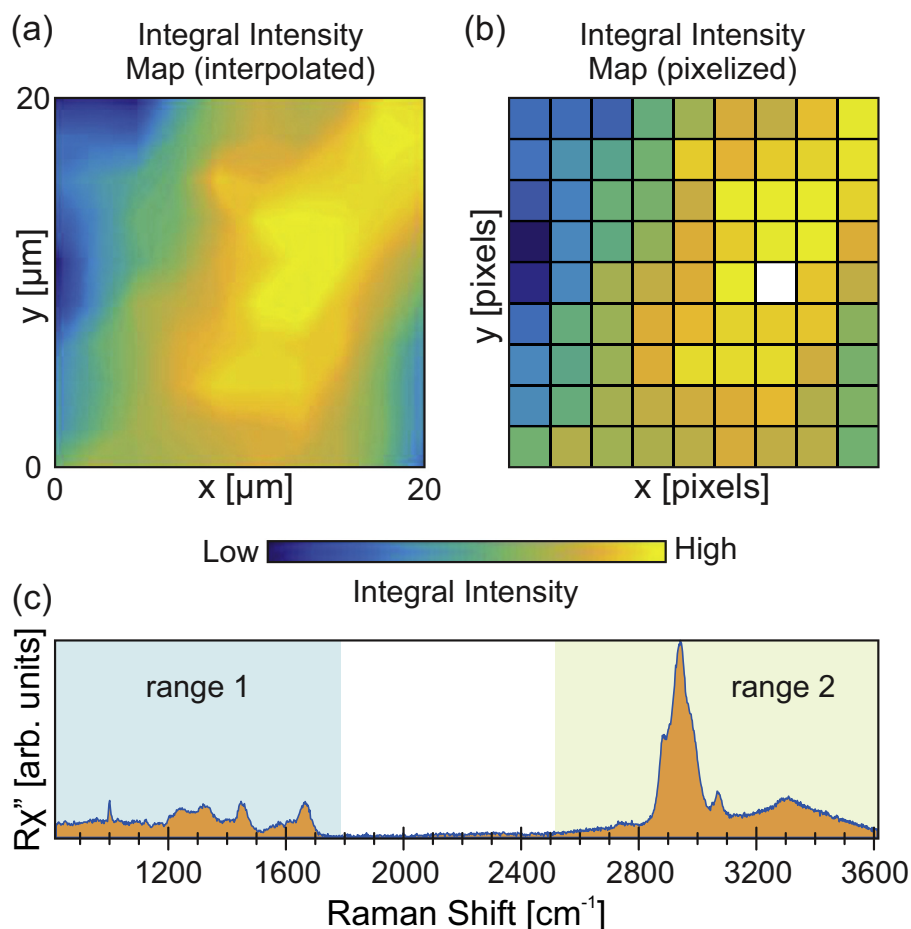


Fig. 1. A single PDLSC Raman (a) interpolated integral intensity map, and (b) pixelized integral intensity map. (c) Human PDLSC Raman scattering spectrum acquired on a pixel marked in white.

and focused on the area of about $1\ \mu\text{m}$, in order to provide a reasonable Raman intensity for a 60 s long acquisition. Under these conditions, the sample associated Raman bands, acquired sequentially at the same position, were found to be stable in terms of both the band intensity and spectral position. In other words, no visible laser induced modifications of the cells were observed upon repeating the signal acquisition for a few times at any of the acquisition points.

Due to very complex inner structure of a cell, there may be small variations in Raman spectra for the data collected at different positions. Consequently, suitable methodology must be applied in order to achieve the needed level of sample representation. In other words, the applied method has to be robust. Here, two batches of cells treated with methanol and formaldehyde were examined by spatially mapping the Raman scattering signal on 20 cells per batch. The spectra were collected at 10×10 or 11×11 matrices of spatial points separated by a distance larger than the estimated focus diameter of $\approx 1\ \mu\text{m}$. The distance between adjacent spatial points, or the spatial resolution, was varied between $2\ \mu\text{m}$ and $3\ \mu\text{m}$ depending on the cell size. The example of an interpolated spectral map of a single methanol fixed cell is presented in Fig. 1(a). Fig. 1(b) shows the same map with the actual pixels omitting the interpolation for clarity. The x and y represent spatial coordinates in which a spectrum is acquired. The intensity of a pixel, labeled white in Fig. 1(b), is obtained by integrating the Raman spectra collected at that pixel. The value of the integral is equal to the area below the acquired signal as illustrated by shaded (orange) area below the typical hPDLSC

Raman spectra in Fig. 1(c). It is characterized by clearly visible Raman bands in two spectral regions marked in Fig. 1(c). The first spectral region spans from $800\ \text{cm}^{-1}$ to $1770\ \text{cm}^{-1}$, whereas the second starts at $2500\ \text{cm}^{-1}$ and ends at $3600\ \text{cm}^{-1}$.

2.4. Data Processing and Analysis

In addition to typical PDLSCs Raman spectra [Fig. 1(c)], a few (in total) significantly different spectra, having an extremely high

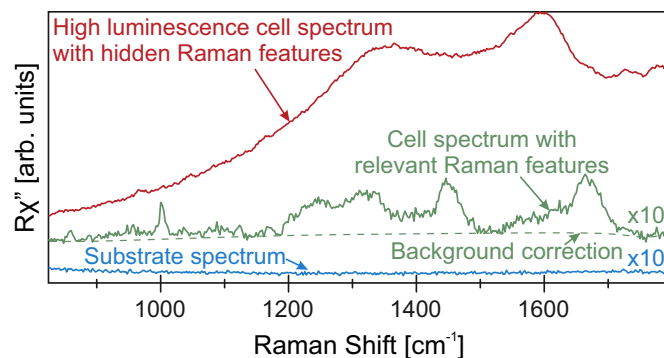


Fig. 2. A typical PDLSCs, substrate, and high luminescence points Raman spectra in the range from $800\ \text{cm}^{-1}$ to $1800\ \text{cm}^{-1}$, depicting spectral selection and preprocessing.

luminescence contribution, were observed as well. The example of such a spectrum truncated to the spectral region from 800 cm^{-1} to 1770 cm^{-1} is shown in Fig. 2. Clearly, extremely strong luminescence masks the relevant Raman bands, making them misleading. Consequently, the high luminescence spectra were omitted from the analysis. The relevant Raman spectra were preprocessed before further manipulation. In the initial step, the background, modelled as a polynomial function of the fourth degree, was subtracted (see Fig. 2). Upon background removal, the spectra were normalized to the value of the integral intensity, calculated within the considered spectral region and then subjected to the analysis.

Besides the direct comparison of the Raman spectra of the cells fixed with formaldehyde and methanol, a multivariate statistical method, principal component analysis (PCA), was applied [15,18,29,30]. Thereby, the dimensionality of the experimental data set is reduced, by transforming to a new set of variables, the principal components, which are uncorrelated and ordered in a way that the first few retain most of the variation present in all of the original variables [31]. The outcome of this analysis is distinct grouping of Raman spectra based on their mutual features [18,29].

3. Results and Discussion

Regarding biological background of our samples, it is well known that primary mesenchymal stem cell cultures represent heterogenic cellular populations, thus the intrinsic heterogeneity of primary cells should be taken into consideration. Moreover, cellular features of

these cells are highly prone to modifications during standard cultivation process [32,33]. Therefore, in order to get reproducible results, we analyzed cells from different passages (passage 3 in Batch 1 and passage 6 in Batch 2).

It is known that the effect of fixation process is cell type and fixative dependent [25]. Different chemical mechanisms may result in variations of the respective Raman spectra. Whereas depletion of certain component will result in reduction of corresponding Raman bands' intensities, various perturbations of the electronic cloud will lead to the changes of bands energy and linewidth. The second does not exclude the possibility of variations of the Raman intensities since the change in electronic structure may impact probability of the inelastic light scattering processes. In our data, the most pronounced changes are occurring in two spectral regions [Fig. 1], ranging from 800 cm^{-1} to 1770 cm^{-1} and from 2500 cm^{-1} to 3600 cm^{-1} . In the statistical treatment, these regions were analyzed independently due to the intrinsic imperfections of the spectrometer.

In Fig. 3, 2D Raman spectra map, averaged spectra, their difference and PCA of Batch 1 and Batch 2 of formaldehyde and methanol fixed PDLSCs, are presented respectively, for spectral region between 800 cm^{-1} and 1770 cm^{-1} . Closer inspection of formaldehyde and methanol fixed PDLSCs 2D Raman spectra map [Fig. 3(a) and (c)] already reveals significant difference between two groups. Relative change of intensity and/or energy shift can be clearly observed for multiple Raman bands. This is even more evident in the difference of formaldehyde and methanol fixed PDLSCs average Raman spectra [Fig. 3(a) and (c)]. It can be seen that phenylalanine peaks at 1002 cm^{-1} and 1030 cm^{-1} are of higher intensity in methanol fixed PDLSCs Raman spectra compared to formaldehyde fixed ones.

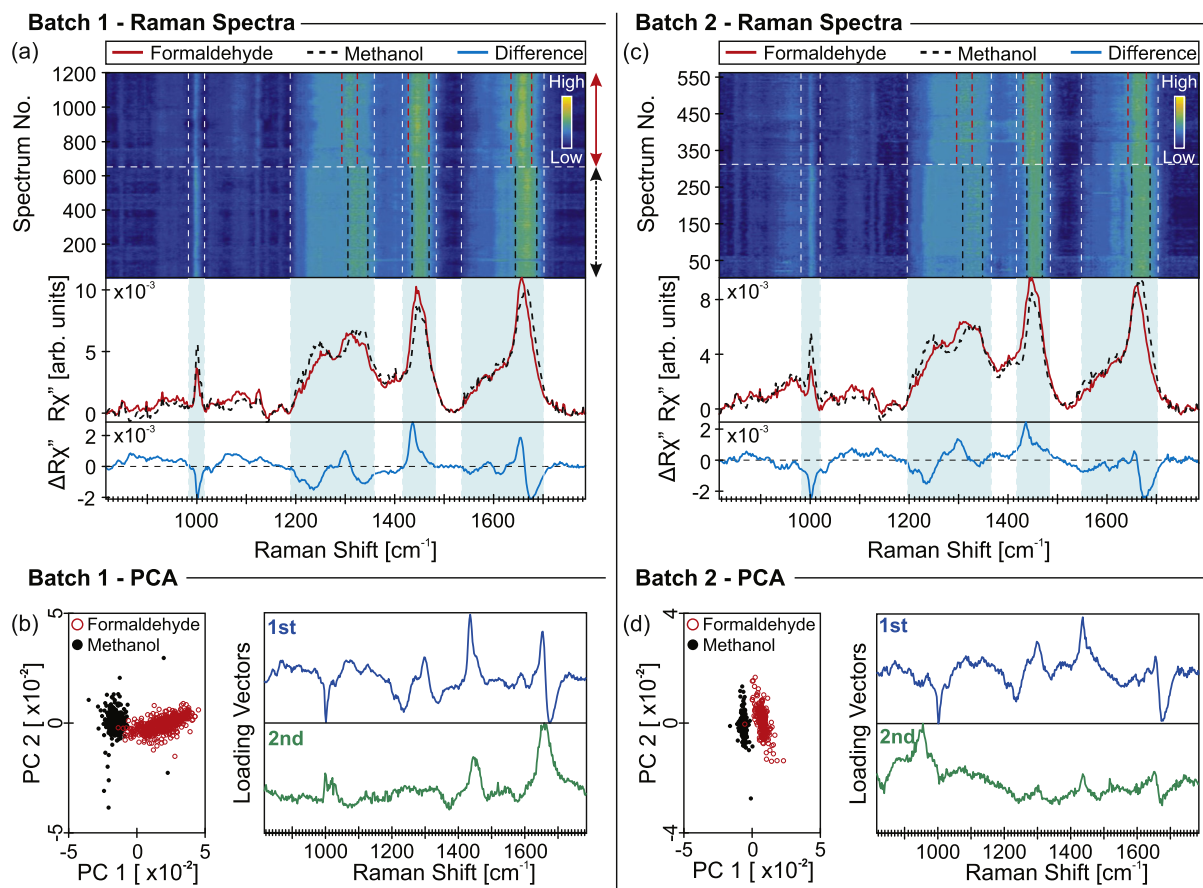


Fig. 3. 2D Raman spectra map obtained from PDLSCs (see Supplementary information), fixed with formaldehyde and methanol, their mean spectra, as well as their difference for the spectral region from 800 cm^{-1} to 1770 cm^{-1} ; PCA score plots calculated for these two groups of cells, and PCA loading vectors for (a)–(b) Batch 1 and (c)–(d) Batch 2, respectively. Percentage of variance PC1–PC2: for Batch 1 19.85%–5.76%; for Batch 2 17.95%–7.43%.

The DNA bands at 1095 cm^{-1} , 1130 cm^{-1} , and 1330 cm^{-1} are of higher intensity in formaldehyde fixed PDLSCs spectra whereas the band at about 1330 cm^{-1} is also slightly shifted. Amide III band at about 1260 cm^{-1} is significantly shifted and of higher intensity in methanol fixed spectra. When it comes to lipid band at 1450 cm^{-1} , it is of noticeable higher intensity and shifted in formaldehyde fixed spectra, as well as the Amide I band at about 1660 cm^{-1} .

The observed behaviour is consistent with the biochemical picture in which the protein content is larger in methanol fixed cells. This is evidenced by more pronounced phenylalanine peak. On the other hand, the secondary structure is more preserved in formaldehyde fixed samples (Amide I band). Modification of native proteins by formaldehyde does not perturb the secondary structure very much. Lipid content is maintained greatly in formaldehyde fixed sample, which is in a good agreement with the literature, due to methanol-caused leaching of lipids through deteriorated cell membrane. As a consequence of cross-linking mechanism of fixation, DNA level is maintained in greater moiety in formaldehyde fixed PDLSCs Raman spectrum [27,28,34].

Spectra of averaged formaldehyde and methanol fixed PDLSCs spectra, and their difference spectrum, from Batch 2 are given in Fig. 3(c). The only observable difference, in comparison to Batch 1, is lower intensity of Amide I band at 1660 cm^{-1} in formaldehyde fixed PDLSCs Raman spectrum, relative to methanol fixed PDLSCs spectrum.

The same procedure is repeated for spectral region from 2500 cm^{-1} to 3600 cm^{-1} . In Fig. 4, 2D Raman spectra map, averaged

spectra, their difference, and PCA of Batch 1 and Batch 2 of formaldehyde and methanol fixed PDLSCs, are presented respectively. Again, formaldehyde and methanol fixed PDLSCs Raman spectra are compared in this spectral region which reflects protein, lipid, and water content. In Fig. 4(a) and (c), it is observable from averaged spectra of difference that the bands at 2860 cm^{-1} and 2890 cm^{-1} , are more intense in formaldehyde fixed PDLSCs Raman spectra. These two bands present CH_2 and CH_3 symmetric stretch in lipids and proteins [35]. Raman band at 2940 cm^{-1} is assigned to CH vibrations in lipids and proteins and is more pronounced in methanol fixed PDLSCs Raman spectra. This confirms above-mentioned statements that formaldehyde better maintains the level of lipids with regard to methanol. On the other hand, methanol keeps protein levels.

Further, PCA is applied for the treatment of the spectral data, and the outcome is presented in Figs. 3 (b), (d) and 4(b), (d) for Batch 1 and Batch 2, respectively. Analyzing PCA score plots, clear assemblage of cells fixed with the same fixative is observable and, as expected, in all cases, PC1 is the component that makes the difference [Figs. 3(b), (d), and 4(b), (d)]. Only a few overlapping points have been observed due to the heterogeneity of the samples and/or variable signal-to-noise ratio. For illustration, PC2s and corresponding loading vectors are also presented. They represent intra- and inter-cellular variations, within the group of cells fixed with the same fixative. PC1 loading vectors are consistent with discrepancies directly observable in Raman spectra of differences, as discussed above. This is not surprising, having in mind the nature of this principal component and the algorithms applied.

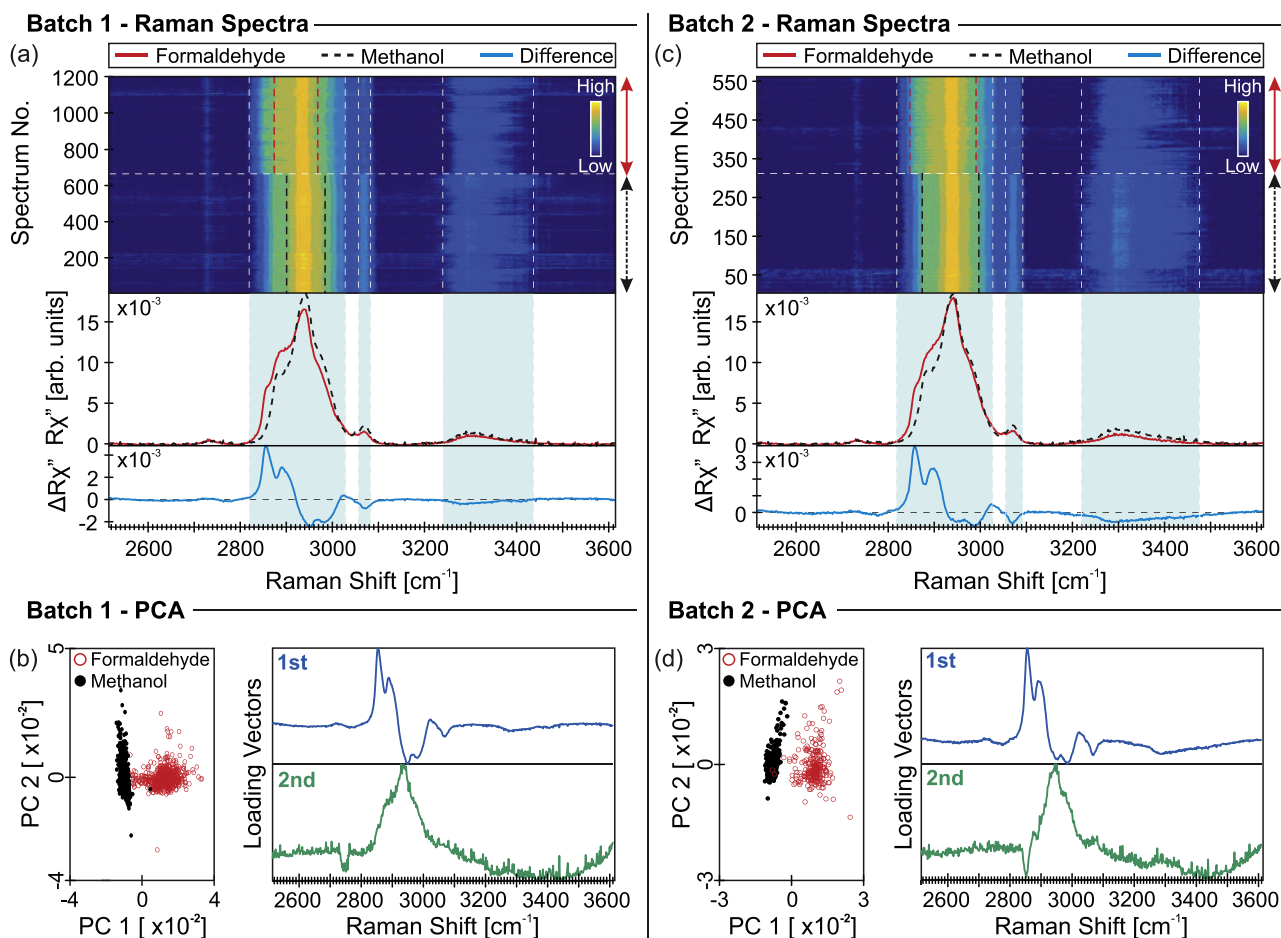


Fig. 4. 2D Raman spectra map obtained from PDLSCs (see Supplementary information), fixed with formaldehyde and methanol, their mean spectra, as well as their difference for spectral region from 2500 cm^{-1} to 3600 cm^{-1} ; PCA score plots calculated for these two groups of cells, and PCA loading vectors for (a)–(b) Batch 1 and (c)–(d) Batch 2, respectively. Percentage of variance PC1–PC2: for Batch 1 64.09%–12.59%; for Batch 2 60.08%–14.64%.

Closer inspection of PCA score plots [Figs. 3(b), (d), and 4(b), (d)] reveals greater spread along PC1 for Batch 1, in particular for the spectral region from 800 cm^{-1} to 1770 cm^{-1} of formaldehyde fixed cells. This is most likely a consequence of heterogeneity of these primary cells. Depending on the nature of the inter-/intracellular variations, fixation process may enhance and/or suppress their Raman spectra signatures [22–26]. Detailed comparison between batches for both fixatives is presented in the Supplementary information.

4. Conclusion

Fixatives cause dramatic changes for all cell types but to varying extent. It is crucial to have a clear idea of what is expected from the sample when choosing the fixative agent. Preservation of cells by formaldehyde and methanol treatment represents standard procedures in most laboratory protocols. In this study, we investigated the effects of these two chemicals on Raman spectra of primary cell lineage, PDLSCs. Both procedures provided quantitatively and qualitatively close Raman spectra that can be considered as fingerprint spectra for this cell lineage. Through the direct comparison of the Raman spectra, as well as the statistical treatment, subtle differences have been observed between two groups that can be traced back to the variations in lipid and protein content. Consequently, when choosing the fixation method, the purpose of investigation has to be kept in mind. When it comes to Raman spectroscopy of hPDLSCs, both formaldehyde and methanol are acceptable choices, but with unlike sensitivity for tracing different biochemical composition.

Acknowledgments

We gratefully acknowledge M. Miletić and M. Andrić for supplying the periodontal ligament tissue. This work was supported by the Ministry of Education, Science, and Technological Development of the Republic of Serbia under Projects Nos. III46010, III45018, ON175062, and OI171005.

Appendix A. Supplementary Data

Supplementary data to this article can be found online at <https://doi.org/10.1016/j.saa.2019.03.012>.

References

- [1] M. Gazdic, V. Volarevic, N. Arsenijevic, M. Stojkovic, Mesenchymal stem cells: a friend or foe in immune-mediated diseases, *Stem Cell Rev. Rep.* 11 (2) (2015) 280–287.
- [2] Y. Sato, H. Araki, J. Kato, K. Nakamura, Y. Kawano, M. Kobune, T. Sato, K. Miyaniishi, T. Takayama, M. Takahashi, et al. Human mesenchymal stem cells xenografted directly to rat liver are differentiated into human hepatocytes without fusion, *Blood* 106 (2) (2005) 756–763.
- [3] R.O. Oreffo, C. Cooper, C. Mason, M. Clements, Mesenchymal stem cells, *Stem Cell Rev.* 1 (2) (2005) 169–178.
- [4] A.R. Williams, J.M. Hare, Mesenchymal stem cells biology, pathophysiology, translational findings, and therapeutic implications for cardiac disease, *Circ. Res.* 109 (8) (2011) 923–940.
- [5] J. Lazarević, T. Kukolj, D. Bugarski, N. Lazarević, B. Bugarski, Z. Popović, Probing primary mesenchymal stem cells differentiation status by micro-Raman spectroscopy, *Spectrochim. Acta A Mol. Biomol. Spectrosc.* 213, 384–390.
- [6] R. Hass, C. Kasper, S. Böhm, R. Jacobs, Different populations and sources of human mesenchymal stem cells (msc): a comparison of adult and neonatal tissue-derived msc, *Cell Commun. Signal* 9 (1) (2011) 12.
- [7] D.G. Phinney, Functional heterogeneity of mesenchymal stem cells: implications for cell therapy, *J. Cell. Biochem.* 113 (9) (2012) 2806–2812.
- [8] I.C. Gay, S. Chen, M. MacDougall, Isolation and characterization of multipotent human periodontal ligament stem cells, *Orthod. Craniofacial Res.* 10 (3) (2007) 149–160.
- [9] S. Ivanovski, S. Gronthos, S. Shi, P. Bartold, Stem cells in the periodontal ligament, *Oral Dis.* 12 (4) (2006) 358–363.
- [10] M. Shimono, T. Ishikawa, H. Ishikawa, H. Matsuzaki, S. Hashimoto, T. Muramatsu, K. Shima, K.I. Matsuzaka, T. Inoue, Regulatory mechanisms of periodontal regeneration, *Microsc. Res. Tech.* 60 (5) (2003) 491–502.
- [11] A. Miletić, S. Mojsilović, I. Okić-Djordjević, T. Kukolj, A. Jauković, J. Santibanez, G. Jovčić, D. Bugarski, Mesenchymal stem cells isolated from human periodontal ligament, *Arch. Biol. Sci.* 66 (1) (2014) 261–271.
- [12] T. Kukolj, D. Trivanović, I.O. Djordjević, J. Mojsilović, J. Krstić, H. Obradović, S. Janković, J.F. Santibanez, A. Jauković, D. Bugarski, Lipopolysaccharide can modify differentiation and immunomodulatory potential of periodontal ligament stem cells via ERK1, 2 signaling, *J. Cell. Physiol.* 233 (1) (2018) 447–462.
- [13] A. Klimczak, U. Kozłowska, Mesenchymal stromal cells and tissue-specific progenitor cells: their role in tissue homeostasis, *Stem Cells Int.* 2016 (2016) 1–11.
- [14] H. Egusa, W. Sonoyama, M. Nishimura, I. Atsuta, K. Akiyama, Stem cells in dentistry—part II: clinical applications, *J. Prosthodont. Res.* 56 (4) (2012) 229–248.
- [15] A. Downes, R. Mouras, A. Elfick, Optical spectroscopy for noninvasive monitoring of stem cell differentiation, *BioMed Res. Int.* 2010 (2010) 1–10.
- [16] A. Downes, R. Mouras, P. Bagnaninchi, A. Elfick, Raman spectroscopy and CARS microscopy of stem cells and their derivatives, *J. Raman Spectrosc.* 42 (10) (2011) 1864–1870.
- [17] C.V. Raman, K.S. Krishnan, A new type of secondary radiation, *Nature* 121 (3048) (1928) 501.
- [18] J.W. Chan, D.K. Lieu, Label-free biochemical characterization of stem cells using vibrational spectroscopy, *J. Biophotonics* 2 (11) (2009) 656–668.
- [19] A.F. Palonpon, J. Ando, H. Yamakoshi, K. Dodo, M. Sodeoka, S. Kawata, K. Fujita, Raman and SERS microscopy for molecular imaging of live cells, *Nat. Protoc.* 8 (4) (2013) 677–692.
- [20] I. Nottingher, I. Bisson, A.E. Bishop, W.L. Randle, J.M. Polak, L.L. Hench, In situ spectral monitoring of mRNA translation in embryonic stem cells during differentiation in vitro, *Anal. Chem.* 76 (11) (2004) 3185–3193.
- [21] F. Lyng, E. Gazi, P. Gardner, Preparation of Tissues and Cells for Infrared and Raman Spectroscopy and Imaging, *Biomedical Applications of Synchrotron Infrared Microspectroscopy: A Practical Approach*, Royal Society of Chemistry, Cambridge, 2010, 147–191.
- [22] S.M. Levchenko, X. Peng, L. Liu, J. Qu, The impact of cell fixation on CARS signal intensity in neuronal and glial cell lines, *J. Biophotonics* (2018) e201800203.
- [23] J.W. Chan, D.S. Taylor, D.L. Thompson, The effect of cell fixation on the discrimination of normal and leukemia cells with laser tweezers Raman spectroscopy, *Biopolymers Original Res. Biomol.* 91 (2) (2009) 132–139.
- [24] A.D. Meade, C. Clarke, F. Draux, G.D. Sockalingum, M. Manfait, F.M. Lyng, H.J. Byrne, Studies of chemical fixation effects in human cell lines using Raman microspectroscopy, *Anal. Bioanal. Chem.* 396 (5) (2010) 1781–1791.
- [25] M.M. Mariani, P. Lampen, J. Popp, B.R. Wood, V. Deckert, Impact of fixation on in vitro cell culture lines monitored with Raman spectroscopy, *Analyst* 134 (6) (2009) 1154–1161.
- [26] E.A. Hoffman, B.L. Frey, L.M. Smith, D.T. Auble, Formaldehyde crosslinking: a tool for the study of chromatin complexes, *J. Biol. Chem.* (2015) jbc-R115.
- [27] M. Noguchi, J.S. Furuya, T. Takeuchi, S. Hirohashi, Modified formalin and methanol fixation methods for molecular biological and morphological analyses, *Pathol. Int.* 47 (10) (1997) 685–691.
- [28] J. Shaham, Y. Bomstein, A. Meltzer, Z. Kaufman, E. Palma, J. Ribak, DNA-protein crosslinks, a biomarker of exposure to formaldehyde in vitro and in vivo studies, *Carcinogenesis* 17 (1) (1996) 121–126.
- [29] T. Ichimura, K.F. Liang-da Chiu, S. Kawata, T.M. Watanabe, T. Yanagida, H. Fujita, Visualizing cell state transition using Raman spectroscopy, *PLoS One* 9 (1) (2014) 1–8.
- [30] E. Brauchle, K. Schenke-Layland, Raman spectroscopy in biomedicine—non-invasive in vitro analysis of cells and extracellular matrix components in tissues, *Biotechnol. J.* 8 (3) (2013) 288–297.
- [31] I. Jolliffe, Principal component analysis, *International Encyclopedia of Statistical Science*, Springer, 2011, pp. 1094–1096.
- [32] W. Wagner, P. Horn, M. Castoldi, A. Diehlmann, S. Bork, R. Saffrich, V. Benes, J. Blake, S. Pfister, V. Eckstein, et al. Replicative senescence of mesenchymal stem cells: a continuous and organized process, *PLoS One* 3 (5) (2008) e2213.
- [33] Y.H.K. Yang, C.R. Ogando, C.W. See, T.Y. Chang, G.A. Barabino, Changes in phenotype and differentiation potential of human mesenchymal stem cells aging in vitro, *Stem Cell Res. Ther.* 9 (1) (2018) 131.
- [34] E. Gazi, J. Dwyer, N.P. Lockyer, J. Miyan, P. Gardner, C. Hart, M. Brown, N.W. Clarke, Fixation protocols for subcellular imaging by synchrotron-based Fourier transform infrared microspectroscopy, *Biopolymers Original Res. Biomol.* 77 (1) (2005) 18–30.
- [35] A.C.S. Talari, Z. Movasaghi, S. Rehman, I.U. Rehman, Raman spectroscopy of biological tissues, *Appl. Spectrosc. Rev.* 50 (1) (2015) 46–111.



Probing primary mesenchymal stem cells differentiation status by micro-Raman spectroscopy

J.J. Lazarević^a, T. Kukolj^b, D. Bugarski^b, N. Lazarević^{a,*}, B. Bugarski^c, Z.V. Popović^{a,d}

^aCenter for Solid State Physics and New Materials, Institute of Physics Belgrade, University of Belgrade, Pregrevica 118, Belgrade 11080, Serbia

^bLaboratory for Experimental Hematology and Stem Cells, Institute for Medical Research, University of Belgrade, Belgrade 11000, Serbia

^cDepartment of Chemical Engineering, Faculty of Technology and Metallurgy, University of Belgrade, Karnegijeva 4, Belgrade 11060, Serbia

^dSerbian Academy of Sciences and Arts, Knez Mihailova 35, Belgrade 11000, Serbia

ARTICLE INFO

Article history:

Received 17 September 2018

Accepted 21 January 2019

Available online 29 January 2019

Keywords:

Raman spectroscopy

Stem cells

Differentiation

ABSTRACT

We have employed micro-Raman spectroscopy to get insight into intrinsic biomolecular profile of individual mesenchymal stem cell isolated from periodontal ligament. Furthermore, these cells were stimulated towards adipogenic, chondrogenic, and osteogenic lineages and their status of differentiation was assessed using micro-Raman spectroscopy. In both cases, glass coverslips were used as substrates, due to their wide availability and cost effectiveness. In all sample groups, the same type of behavior was observed, manifested as changes in Raman spectra: the increase of relative intensity of protein/lipid bands and decrease of nucleic acid bands. Comprehensive statistical analysis in the form of principal component analysis was performed, which revealed noticeable grouping of cells with the similar features. Despite the inhomogeneity of primary stem cells and their differentiated lineages, we demonstrated that micro-Raman spectroscopy is sufficient for distinguishing cells' status, which can be valuable for medical and clinical application.

© 2019 Published by Elsevier B.V.

1. Introduction

In the era of regenerative medicine development, stem cells are in the center of attention, bringing hope for treating conditions and diseases presently incurable. In general, these expectations arise from unique qualities of these cells, which include self-renewal and multilineage differentiation potential *in vitro*. When it comes to potential clinical application of stem cells, from the aspect of differentiation capacity, embryonic stem cells (ESCs) and induced pluripotent stem cells (iPSCs) provide the greatest possibilities. However, it is well documented that both ESCs and iPSCs can form teratoma which directly restricts their therapeutic application. On the other hand, considering relatively simple isolation procedures, without ethical issues that follow manipulation of ESCs, mesenchymal stem cells (MSCs) have advantage over ESCs and iPSCs. Therefore, MSCs are promising agents in cell therapy and tissue engineering [1,2]. More than forty years ago, MSCs were discovered in bone marrow, but today it is known that this heterogeneous population of cells resides in tissues and organs throughout the adult organism, where their primary role

is maintenance of tissue regeneration and tissue homeostasis [3,4]. According to The International Society for Cellular Therapy, minimal criteria for characterisation of human MSCs are plastic adhesion with expression of CD73, CD90, and CD105 surface markers and lack of hematopoietic markers CD34-, CD45-, CD14-, CD79α-, HLA-DR-, and multilineage differentiation potential into osteoblasts, adipocytes, and chondroblasts [5]. Even though MSCs possess common cellular features, it is generally accepted that, due to tissue origin, donor age, culture conditions, these cells exhibit variable regenerative capacity [6,7]. Along with differentiation potential, an important part in considering MSCs as possible new therapeutic agents is their ability of immune response modulation (directly, through cell-to-cell contact or indirectly, by secretion of soluble factors) [8]. Originally, it was reported that MSCs can alter immune response in hypoinnogenic manner, but their role in immunity is still the subject of extensive research [9].

Within regenerative dentistry, there is a great interest in development of novel therapeutic strategies related to the recovery of periodontium. As tooth supportive tissue, periodontium is directly responsible for appropriate incorporation of synthetic implants which today represents one of the main methods of medical treatment for curing dental defects. However, damaged periodontal tissue has limited capacity for regeneration and is often influenced by inflammation that can severely hamper periodontal structure,

* Corresponding author.

E-mail address: nenadl@ipb.ac.rs.

disabling implantation and tooth restoration. Periodontal ligament is a soft connective tissue which anchors tooth to the alveolar bone. Hence, the exploration of human periodontal ligament stem cells (hPDLSCs), as potential cell source for reconstructive dentistry, strongly contributes to the improvement of periodontal therapies [10–12]. Previously is demonstrated that PDLSCs fulfill criteria for MSCs identification and characterisation [13,14], set by International Society for Cellular Therapy [5,15]. Keeping in mind that the origin tissue of PDLSCs is periodontal ligament and that the main role of cells within this tissue is maintenance of mineralization level [16,17], it is expected for PDLSCs to be more osteogenic than adipogenic committed when compared to MSCs derived from other sources [18,19].

Regarding heterogeneity of MSCs, carefully performed characterisation of these cells and thoroughly monitored process of their differentiation, before further manipulation, is of great significance for their usage [20]. Various techniques are available in this field, such as immunocytochemistry, flow cytometry, mass spectrometry or gene expression analyses. However, these methods mostly imply disruption of cell integrity and, at the same time, they can be time consuming and require expensive biomarkers for each cell type [21]. Destructiveness comes out as the dominant drawback of these techniques. This gives rise to a need for non-invasive, non-destructive and fast technique, which would be able to monitor stem cells behavior, including differentiation process [20,21]. Owing to its features, Raman spectroscopy appears to be a promising candidate. Regarding clinical applicability, no sample preparation or a minimal preparation, is important feature of Raman spectroscopy. It is also suitable for measurements in aqueous solutions. The outcome of Raman scattering measurement is a vibrational spectrum in which macromolecules, such as proteins, nucleic acids, carbohydrates, and lipids, are presented with the most pronounced vibration modes of different chemical bonds. Interactions of molecules are also visible. Accordingly, Raman spectrum is a fingerprint of the analysed sample. In past decade, the interest in performing this type of analysis on stem cells is well documented [21–30].

Currently, advanced Raman setups are used in biomedical researches [31]. Most of the studies in the field of stem cells biology were performed with more experimentally demanding Raman spectroscopy experiments, such as Coherent anti-Stokes Raman spectroscopy (CARS), Raman tweezers, Tip enhanced Raman spectroscopy (TERS), or Surface enhanced Raman spectroscopy (SARS), due to their higher sensitivity. As far as we know, great number of these studies were focused on live murine and human ESCs [22–26], and spectral mapping of live and apoptotic ESCs [27], but the interest in mesenchymal stem cells is also noticeable [28,29,21]. One of the Raman studies on MSCs was performed to characterise the Raman spectra of bone marrow-derived MSCs and to study the effect of different inducers on their differentiation towards osteogenic lineage [30]. Further, Raman spectroscopy was assessed as the analytical tool which could be used for characterisation and identification of rhesus monkey mesenchymal stem cells from different age groups (fetal to juvenile) [32]. Moreover, Raman spectroscopy was used to map the distribution of different biomolecules within two types of stem cells: adult human bone marrow-derived MSCs and human ESCs, and to identify Raman spectral characteristics which distinguish genetically abnormal and transformed stem cell from normal ones [33]. Another study was dedicated to viability transitions detection of umbilical cord mesenchymal stem cells (hUC-MSCs) by micro-Raman spectroscopy, where the authors proposed that the viability of hUC-MSCs can be described with three peaks of certain energies [28].

Although numerous Raman studies of different stem cell lineages have been performed [22–26], it is still unclear whether Raman spectroscopy can unambiguously distinguish differentiation status of primary stem cells such as hPDLSCs. In order to

address this matter, Raman scattering study of undifferentiated and differentiated hPDLSCs (osteogenic, chondrogenic, and adipogenic cells) has been performed. To assure multilineage mesenchymal differentiation capacity of hPDLSCs, standard biological detection of adipogenesis, chondrogenesis, and osteogenesis was conducted.

In general, the widespread applicability of this technique demands simplicity of the experimental setup and the availability of used substrates. In medicine, the most commonly used substrates are made of glass, which may be challenging for Raman spectroscopy, due to contributions to the sample spectrum. Besides limiting the spectral region that can be probed in the light scattering experiment it also hinders signal to noise ratio. The aim of this work was to determine the analytical ability of micro-Raman spectroscopy in commonly available experimental configuration, in order to assess differentiation status of hPDLSCs, with minimal sample processing, on glass substrates. Direct comparison of the primary hPDLSCs and differentiated hPDLSCs Raman spectra, as well as statistical analysis, revealed clear distinction between these groups. This approach could vastly simplify diagnostics and promote clinical application of MSCs.

2. Experiment

2.1. Isolation and Cultivation of Human Periodontal Ligament Stem Cells

Human PDLSCs were isolated from normal impacted third molars, as described elsewhere [14]. In brief, following the informed consent, tissues were collected from healthy patients aging 18–25 years, subjected to the procedure of tooth extraction for orthodontic reasons, at the Department of Oral Surgery of the Faculty of Dental Medicine, the University of Belgrade. All treatments were performed according to the approved ethical guidelines set by Ethics Committee of the Faculty of Dental Medicine, the University of Belgrade and Declaration of Helsinki. Directly after tooth extraction, periodontal tissues were carefully detached from the mid-third of the root surface, minced into small pieces and placed in a 25 cm² flask with Dulbecco's modified Eagle's medium (DMEM; PAA Laboratories, Pasching, Austria) supplemented with 10% fetal bovine serum (FBS; PAA Laboratories), 100 U/ml penicillin and 100 µg/ml streptomycin (PAA Laboratories), and cultured at 37 °C in a humidified atmosphere containing 5% CO₂, with medium exchange every third day. When the 80% to 90% confluence was reached, the cells were passaged regularly in growth medium (GM-DMEM with 10% FBS) using 0.05% trypsin with 1 mM EDTA (PAA Laboratories) and for this study cells from third to sixth passages were used. Further on, considering the minimal criteria for characterisation of MSC [5] immunophenotype of hPDLSCs and their multipotent differentiation capacity towards osteogenic, chondrogenic, and adipogenic lineages were confirmed as previously reported [14].

2.2. Sample Preparation

For Raman measurements, hPDLSCs were seeded on rounded glass coverslips in 24-well plate (2×10^4 cells per well) and grown in standard cultivation conditions. Simultaneously, cells were seeded in 24-well plate (2×10^4 cells per well) to follow differentiation by regular *in vitro* staining. When the confluence was reached, cells were induced to differentiate into osteogenic, chondrogenic and adipogenic lineages by specific differentiation medium. Osteogenic differentiation medium contained DMEM supplemented with 5% FBS, 100 U/ml penicillin/streptomycin, 50 µM ascorbic acid-2-phosphate and 10 mM β -glycerophosphate (both from Sigma-Aldrich). Chondrogenic medium contained DMEM with 5% FBS, 2 ng/ml of transforming growth

factor- β 1 (TGF- β ; R&D Systems, Minneapolis, MN, USA), 50 μ M ascorbic acid-2-phosphate, 10 nM dexamethasone, 100 U/ml penicillin/streptomycin. Adipogenic medium contained 5% FBS in DMEM, 100 U/ml penicillin/streptomycin, 100 μ g/ml isobutyl-methyl xanthine (IBMX; Sigma-Aldrich), 1 μ M dexamethasone and 10 μ g/ml insulin (Sigma-Aldrich). With regular medium exchange, osteogenesis and chondrogenesis were evaluated after three weeks of cultivation, whereas adipogenesis was induced during four weeks. As for the control samples, cells were cultivated in GM with 5% FBS during the corresponding time. After this period, hPDLSCs were washed with saline buffer, fixed with methanol for 10 min at room temperature and washed with distilled water just before Raman spectroscopy was performed. Standard *in vitro* examination of differentiation process was performed after cells had been fixed and stained with specific dye. Intracellular lipid droplets were observed by Oil Red O (Merck Chemicals, Darmstadt, Germany) staining, while Safranin O confirmed cartilage-specific proteoglycan formation. Alizarin red was used to visualize calcium deposition and mineralization of extracellular matrix (see Fig. 1). Optical microscope with digital camera was used for cell morphology analysis and imaging.

2.3. μ -Raman Spectroscopy

Raman scattering measurements were performed using TriVista 557 Raman system in backscattering μ -Raman configuration. As an excitation source, 532 nm laser line of the Coherent VerdiG laser was used. The focusing on the sample was achieved by using $\times 100$ microscope objective, $NA = 0.80$. The laser spot diameter in our experimental configuration was $\approx 4 \mu$ m. In order to avoid any possible sample damage and/or temperature related effect, the laser power at the sample plain was kept at low levels, ≈ 1 mW. Acquisition time was 900 s. More details on Raman scattering experiment can be found in the Section S1 of the Supplementary Information.

From the aspects of vibrational spectroscopy, which can independently probe a single vibration within a molecule or a crystal, biological samples consisting of various types of macro-molecules, represent rather complicated systems. In these systems, only vibrational bands, consisting of numerous vibrations of the same type, can be taken into consideration, rather than a single vibration. Consequently, the changes of biological system (e.g. single cell) composition, may result in a change of certain Raman bands intensities.

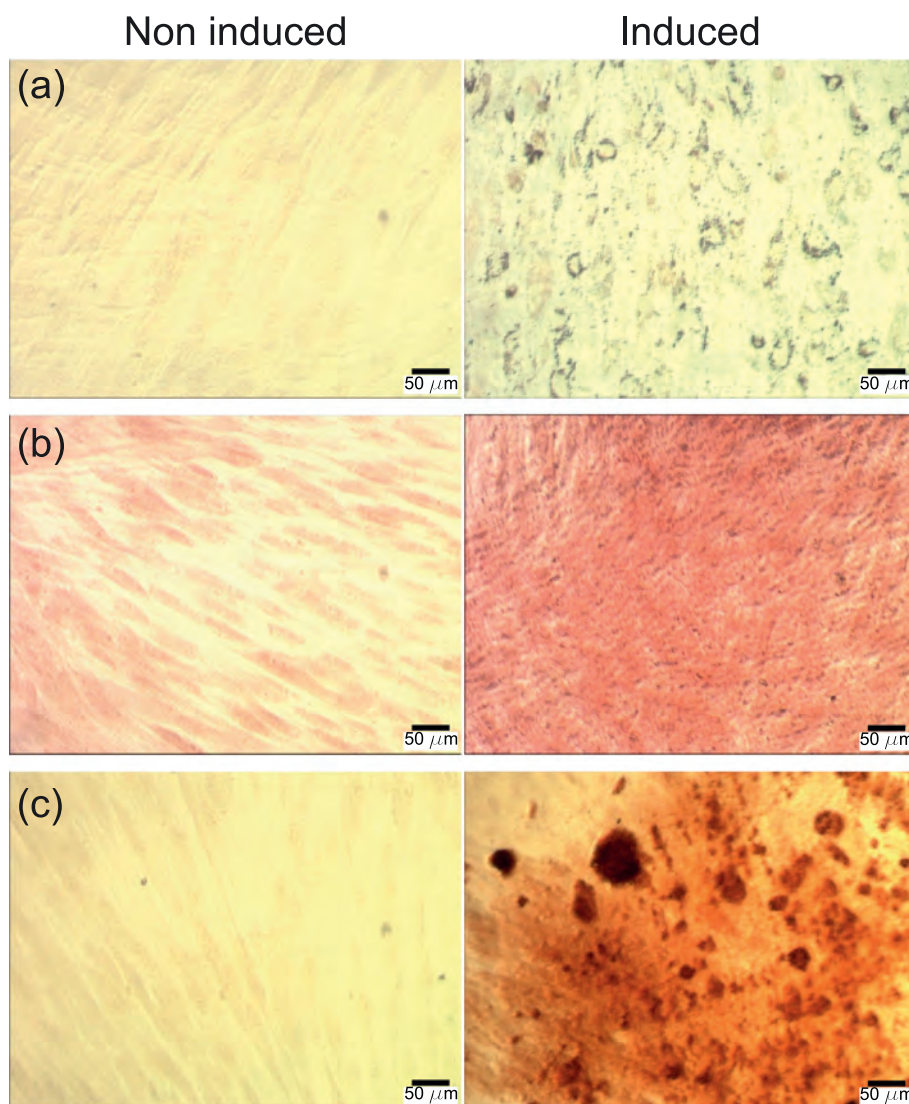


Fig. 1. Multilineage differentiation potential of hPDLSCs. (a) Oil Red O staining showed presence of intracytoplasmatic lipid droplets confirming adipogenic differentiation. (b) Chondrogenic differentiation was demonstrated by positive staining of proteoglycans with Safranin O. (c) Positive Alizarin red staining of extracellular matrix mineralization confirmed osteogenic differentiation.

It should be taken into account that when probing a single cell, due to its complex inner structure, there might be small variations in Raman spectra for the data collected at different positions. To obtain single spectra representative for each of the cells, recorded spectra were averaged. The preliminary experiment involved investigation of 54 cells of Batch 1. For every cell lineage, 9 hPDLSCs and 9 differentiated cells were analysed by probing each cell at 10 randomly chosen positions. The results of the analysis performed on the full set of data as well as on the sub-set including three random positions, revealed no qualitative difference. This implies that for our experimental configuration and for the samples under investigation, three randomly chosen positions are sufficient to make qualitative conclusions. Having in mind statistical treatment of the results, a total of 1080 spectra from 360 cells were recorded and analysed in the main experiment.

2.4. Data Processing and Analysis

Prior to the analysis, all Raman spectra were processed by subtracting the contributions from substrate (see Fig. 2 (a)), as well as biological fluorescence. No spectral smoothing of the samples spectra has been performed. On the other hand, the substrate spectrum was obtained separately with greater acquisition time and statistics and post-processed by Savitzky–Golay filter. Right inset on Fig. 2 (a) compares the substrate and the mean of 540 hPDLSCs Raman spectra. Significantly smaller noise level of the (glass) substrate spectrum indicates absence of its contribution to hPDLSCs spectra statistics. Due to the substantial increase of the substrate spectral weight at lower energies, our analysis was limited to the region above 1000 cm^{-1} .

The absolute value of Raman intensity is not usually a reliable quantity. Even small variations in the experimental conditions may

produce the “artificial” variations of Raman intensity. In order to exclude this possible uncertainty, all spectra were normalised onto the peak at about 1660 cm^{-1} , which is present with high intensity in all obtained spectra.

Besides the direct comparison of spectra obtained from stem cells and differentiated cells, a multivariate statistical method, principal component analysis (PCA), was employed [40,20,25,22]. The main goal of PCA is to reduce the effective dimensionality of the experimental data set by determining the orthonormal basis of loading vectors in a way that the greatest variance is projected onto the first coordinate, the second greatest variance is projected onto the second coordinate, and so on. The outcome of this analysis is clear grouping of Raman spectra according to their mutual features. Prior to performing PCA, the spectral data were subtracted by the mean spectrum and divided by its standard deviation [40,22].

3. Results and Discussion

To get insight on how hPDLSCs differentiation status reflects on Raman spectra, three sets of Raman experiments were performed. The samples were set in two batches. For every lineage, spectra were obtained for 30 hPDLSCs and 30 differentiated cells (hPDLSC grown in standard cultivation medium for the corresponding time for each differentiation). The spectrum of every cell was measured three times on each of three randomly chosen positions within the cell in order to incorporate possible variations within a single cell and test the approach sufficiency for observing the difference between cell lineages.

Fig. 2 (b) shows Raman spectrum of hPDLSCs obtained by averaging spectra of all control samples. The main contribution to the hPDLSCs Raman spectrum for the region under consideration comes from nucleic acids, proteins and lipids [24,28,41,23,37–39]. Spectral features of nucleic acids originate from the individual purine and pyrimidine bases (adenine, thymine, guanine, cytosine, and uracil), as well as from backbone structure of DNA and RNA, whereas protein spectral features include contributions from aromatic amino acids (phenylalanine, tryptophan, and tyrosine), amide groups of secondary protein structures (α -helices, β -sheets, and random coils), and various vibrations of carbon atoms bonded with nitrogen and/or other carbon atoms [38]. Different vibrations within the hydrocarbon chain (e.g. C—C stretching, CH_2 and CH_3 scissoring and twisting) present specific features of lipids in Raman spectra [35]. Principally, various contributions may overlap, making the determination of the potential changes in Raman spectra of undifferentiated and differentiated hPDLSCs a formidable task. As can be seen from Fig. 2 (b), numerous vibrational bands have been observed in hPDLSCs Raman spectrum. The most pronounced bands are assigned according to the literature [24,28,41,23, 34–39] and summarized in Table 1.

Fig. 3 (a)–(c) shows averaged hPDLSCs Raman spectra of control samples, differentiated cells (adipocytes, chondroblasts, and osteoblasts, respectively) of both batches, as well as corresponding pairs' differences. Although the overall spectral features in these pairs of spectra look almost the same, after the subtraction, the difference is more pronounced. General conclusion, consistent with the literature data [22,25], is that relative intensities (with regard to 1660 cm^{-1} peak structure intensity) of nucleic acids and proteins, are able to distinguish stem cells from more mature cells. In the case of adipogenic differentiation, a slight decrease of the relative intensity of the band at 1100 cm^{-1} and increase of the relative intensity of peaks at about 1353 cm^{-1} , 1447 cm^{-1} , and 1590 cm^{-1} (see Fig. 3 (a)) is observed. According to Table 1, this might be understood as slight reduction of nucleic acids and enhancement of proteins and lipids. On the other hand, the possible increase of the band at 1735 cm^{-1} , assigned to lipids (esters), is absent. Explanation for this lies in the fact that these cells do not originate from

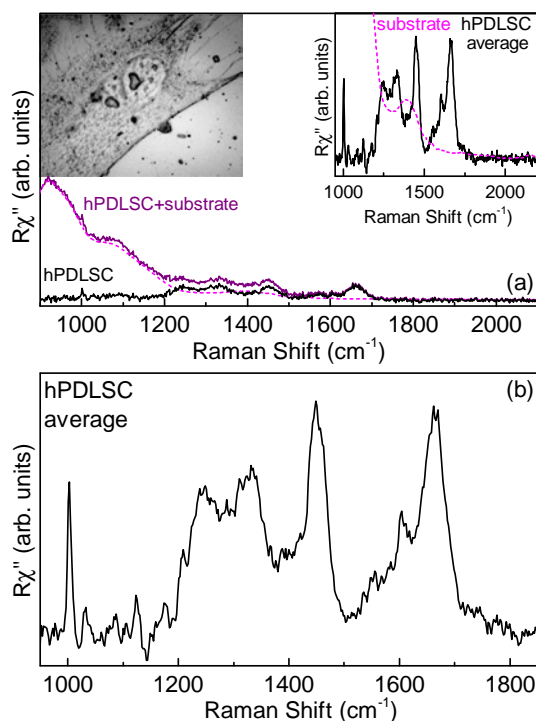


Fig. 2. (a) Raman scattering spectra of hPDLSCs on glass, glass substrate and their difference. Left inset: Image of hPDLSCs. Right inset: Comparison between the substrate and the mean of 540 hPDLSCs Raman spectra. (b) The mean of 540 hPDLSCs Raman spectra.

Table 1

Vibrations in hPDLSCs and their energies noticed in Raman spectrum. (A) adenine, (U) uracil, (C) cytosine, (T) thymine, (G) guanine, (Phe) phenylalanine, (Trp) tryptophan, (Tyr) tyrosine, (vib) vibration, (bg) bending, (br) breathing, (bk) backbone, (def) deformation, (tw) twist, (sym) symmetric, (asym) asymmetric, and (str) stretch [28,23,34–39].

Energy (cm ⁻¹)	Assignment
1004	Phe
1032	Phe
1061	C—N and C—C str
1080	PO ₂ ⁻ sym str
1085	C—O str
1105	PO ₂ ⁻ str (sym)
1130	C—N and C—C asym str
1155	C—C and C—N str of proteins
1165	C—O str, COH bg
1172	G ring str
1178	CH ben Tyr
1209	C—C ₆ H ₅ str, Phe, Trp
1228	Asym phosphate str
1250	T, amide III _β
1260	N—H and C—H bg (amide III/distorted)
1265	Amide III _α
1315	G, CH def.
1332	DNA purine bases (CH ₃ CH ₂ wagging mode of polynucleotide chain)
1450	CH ₂ str def of methylene group in lipids
1456	CH def.
1556	Amide II
1604	Phe, Tyr
1654	Amide I, α helix
1670	Amide I, β sheet

adipose tissue [18,19]. When it comes to the case of chondrogenic differentiation, higher relative intensities of the peaks at 1065 cm⁻¹, 1250–1450 cm⁻¹, and 1630 cm⁻¹ are exhibited (Fig. 3 (b)). These

changes arise from higher content of proteins and proteoglycans [42,43]. Regarding the osteogenic differentiation, spectral changes between hPDLSCs and their differentiated pairs (Fig. 3 (c)) originate from the lower relative intensities of the bands in the region from 1170 cm⁻¹ to 1220 cm⁻¹ and from 1450 cm⁻¹ to 1490 cm⁻¹, and higher relative intensities at about 1045 cm⁻¹, 1070 cm⁻¹, and 1600 cm⁻¹. These changes are caused by decrease in amino acids and likely lipids, and increase in carbonates and phosphates, as expected. This decrease of the band intensity in the region that most likely correspond to lipids, might be understood as a change in proteins to lipids ratio. Typical spectral marker for this type of cells is hydroxyapatite, but due to spectral interference from the substrate (glass), it is out of spectral range of interest in this study [43]. Consistently observed spectral changes during the differentiation process (the increase of protein bands and decrease of nucleic acid bands in differentiated cells) are in accordance with the literature [22,25]. The possible explanation for this behavior is that, as cells differentiate, they gradually begin to use up the pool of mRNA to support the synthesis of new, cell lineage specific proteins [22].

Although the direct comparison between hPDLSCs and their differentiated lineages Raman spectra gave us means to distinguish cell differentiation status, it is demanding and require detailed analysis of the spectra. However, if we utilize the Raman spectra as characteristic fingerprints of the cells under investigation, PCA can be employed for pattern recognition and grouping. Fig. S1 of the Supplementary information summarizes loading vectors for the main PCs. It is noticeable that a certain loading vector or their linear combination fully describe corresponding difference spectra shown in Fig. 3 (a)–(c). Consequently, the same conclusions can be made as in previous paragraph. Fig. 3 (d)–(f) shows score plots calculated independently using PCA for three groups of control hPDLSCs samples and their differentiated lineages'

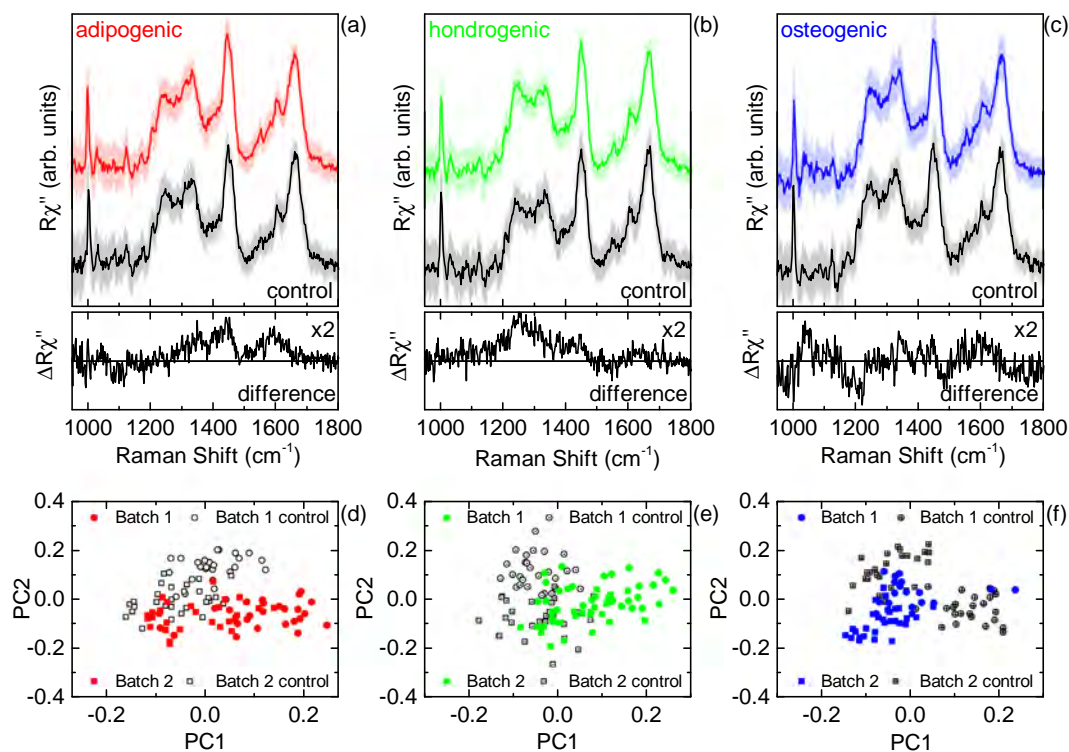


Fig. 3. (a)–(c) Averaged Raman spectra (black lines) of hPDLSCs (control samples), differentiated hPDLSCs (adipogenic, chondrogenic, and osteogenic lineages) and difference spectrum between these two groups of cells. Standard deviation for each lineage and control group is presented with the colored areas. (d)–(f) Score plots calculated independently using PCA for three groups of control hPDLSCs and differentiated hPDLSCs Raman spectra.

Raman spectra. In all three cases, two groups can be observed, with each grouping corresponding to a particular cell lineage. Furthermore, within each grouping, sub-groupings are noticed, indicating variations and inhomogeneity between the batches. In fact, this is not surprising since these are primary cells and the higher level of inhomogeneity is expected. In the following paragraphs, the attention will be focused on the analysis within the batches.

Fig. 4 summarizes adipogenic, chondrogenic, and osteogenic lineages score plots for Batches 1 and 2. Although the separation between data point groupings can be observed for both batches, it is more pronounced for Batch 1. Most likely, this is a consequence of higher inhomogeneity within the Batch 2.

In the next step, we wanted to test whether the same approach can be used to distinguish different types of differentiated cells (adipocytes, chondroblasts, and osteoblasts). For this purpose, the data from all three sets of experiments had been combined and PCA performed, for both batches. The obtained score plots are presented in Fig. 5. Shaded areas represent 1σ 2D confidence level. Remarkably, very good grouping of the different cell lineages has been observed for Batch 1. Less separation of different cell groups was observed for Batch 2, in agreement with the results presented in Fig. 4. Additionally, PCA indicates the variations within hPDLSCs (in particular for Batch 2) although this was not so obvious in direct comparison. When PCA was applied on hPDLSCs from all three control groups and compared with differentiated hPDLSCs data, it could be noticed that even though small variations are present, control hPDLSCs retain characteristics of stem cells, suggesting these cell populations are not homogeneous. Keeping that in mind, spectral analyses of hPDLSCs are in accordance with data obtained by traditional MSCs characterisation methods that also emphasize heterogeneity of MSCs population. As being primary cells, cellular diversity of MSCs is a result of isolation methods and culture conditions. Further, the absence of unique MSCs biomarkers makes these cells still highly difficult for molecular identification

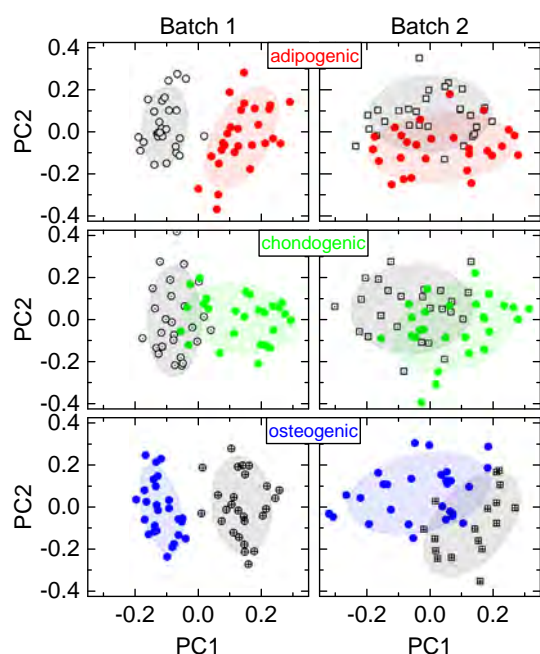


Fig. 4. Score plots calculated independently using PCA for three groups of control (black) and differentiated (adipogenic, chondrogenic, and osteogenic lineages) hPDLSCs samples Raman spectra in two batches. Shaded areas represent 1σ 2D confidence level.

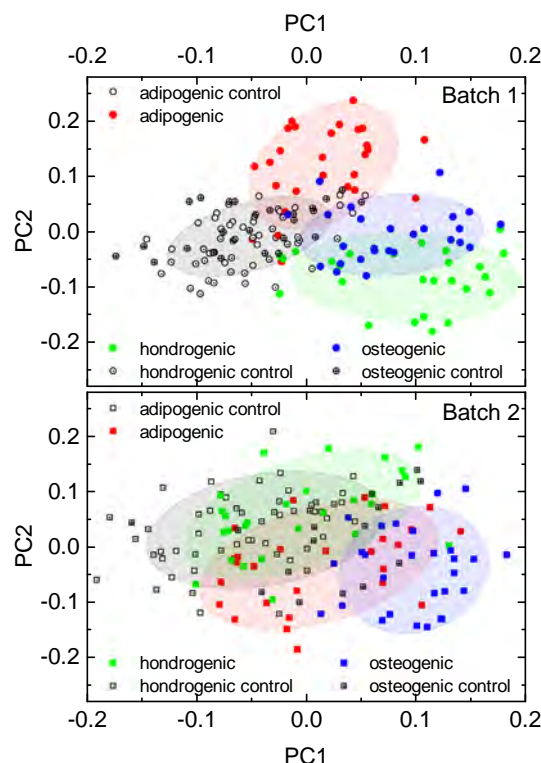


Fig. 5. PCA performed on all obtained Raman spectra of four groups of cells including nondifferentiated hPDLSCs (control) and differentiated hPDLSCs (osteogenic, chondrogenic and adipogenic lineages) for different batches. Shaded areas represent 1σ 2D confidence level.

and characterisation [5,44]. Thus, our results suggest the possibility of the Raman spectroscopy application in characterisation of MSCs.

4. Conclusion

In this study, the applicability of micro-Raman spectroscopy for probing primary hPDLSCs differentiation status on glass substrate was demonstrated. In direct comparison of hPDLSCs and differentiated cells Raman spectra, the difference in the relative intensities of certain marker bands has been observed. Additionally, statistical analysis of fingerprint Raman spectra of the cells using PCA, revealed distinct groupings based on the similar features. This gives a possibility of devising the procedure not only for fast and simple detection of different mesenchymal stem cell lineages, but also for the variations within. Furthermore, due to minimal preparation requirements and independency on the reagents that are necessary in standard biological techniques, Raman spectroscopy can be used as an additional method in MSCs characterisation. From the standpoint of MSCs utilization in biomedicine, simplification of the procedures in cell identification could significantly facilitate research in the field of stem cell biology.

Acknowledgments

We gratefully acknowledge M. Milić and M. Andrić for supplying the periodontal ligament tissue and Dr. N. Paunović for constructive discussions on the subject. This work was supported by the Ministry of Education, Science, and Technological Development of the Republic of Serbia, Serbia under Projects No. III46010, III45018, and ON175062.

Appendix A. Supplementary data

Supplementary data to this article can be found online at <https://doi.org/10.1016/j.saa.2019.01.069>.

References

- [1] X. Wei, X. Yang, Z. p. Han, F. f. Qu, L. Shao, Y. f. Shi, Mesenchymal stem cells: a new trend for cell therapy, *Acta Pharmacol. Sin.* 34 (6) (2013) 747–754.
- [2] D. Howard, L.D. Buttery, K.M. Shakesheff, S.J. Roberts, Tissue engineering: strategies, stem cells and scaffolds, *J. Anat.* 213 (1) (2008) 66–72.
- [3] Y. Sato, H. Araki, J. Kato, K. Nakamura, Y. Kawano, M. Kobune, T. Sato, K. Miyaniishi, T. Takayama, M. Takahashi, et al. Human mesenchymal stem cells xenografted directly to rat liver are differentiated into human hepatocytes without fusion, *Blood* 106 (2) (2005) 756–763.
- [4] C. Toma, M.F. Pittenger, K.S. Cahill, B.J. Byrne, P.D. Kessler, Human mesenchymal stem cells differentiate to a cardiomyocyte phenotype in the adult murine heart, *Circulation* 105 (1) (2002) 93–98.
- [5] M. Dominici, K. Le Blanc, I. Mueller, I. Slaper-Cortenbach, F. Marini, D. Krause, R. Deans, A. Keating, D. Prockop, E. Horwitz, Minimal criteria for defining multipotent mesenchymal stromal cells. The International Society for Cellular Therapy position statement, *Cytotherapy* 8 (4) (2006) 315–317.
- [6] R. Hass, C. Kasper, S. Böhm, R. Jacobs, D. Populations, Sources of human mesenchymal stem cells (msc). A comparison of adult and neonatal tissue-derived msc, *Cell Commun. Signal* 9 (1) (2011) 12.
- [7] D.G. Phinney, Functional heterogeneity of mesenchymal stem cells: implications for cell therapy, *J. Cell. Biochem.* 113 (9) (2012) 2806–2812.
- [8] M. Gazdic, V. Volarevic, N. Arsenijevic, M. Stojkovic, Mesenchymal stem cells: a friend or foe in immune-mediated diseases, *Stem Cell Rev. Rep.* 11 (2) (2015) 280–287.
- [9] R. Abdi, P. Fiorina, C.N. Adra, M. Atkinson, M.H. Sayegh, Immunomodulation by mesenchymal stem cells: a potential therapeutic strategy for type 1 diabetes, *Diabetes* 57 (7) (2008) 1759–1767.
- [10] S. Shi, P. Bartold, M. Miura, B. Seo, P. Robey, S. Gronthos, The efficacy of mesenchymal stem cells to regenerate and repair dental structures, *Orthod. Craniofac. Res.* 8 (3) (2005) 191–199.
- [11] E.A.A. Neel, W. Chrzanowski, V.M. Salih, H.W. Kim, J.C. Knowles, Tissue engineering in dentistry, *J. Dent.* 42 (8) (2014) 915–928.
- [12] H. Egusa, W. Sonoyama, M. Nishimura, I. Atsuta, K. Akiyama, Stem cells in dentistry-part ii: clinical applications, *J. Prosthodont. Res.* 56 (4) (2012) 229–248.
- [13] T. Kukolj, D. Trivanović, I.O. Djordjević, S. Mojsilović, J. Krstić, H. Obradović, S. Janković, J.F. Santibanez, A. Jauković, D. Bugarski, Lipopolysaccharide can modify differentiation and immunomodulatory potential of periodontal ligament stem cells via erk1,2 signaling, *J. Cell. Physiol.* 233 (1) (2018) 447–462.
- [14] M. Miletić, S. Mojsilović, I. Okić-Djordjević, T. Kukolj, A. Jauković, J. Santibanez, G. Jovčić, D. Bugarski, Mesenchymal stem cells isolated from human periodontal ligament, *Arch. Biol. Sci.* 66 (1) (2014) 261–271.
- [15] A. Klimczak, U. Kozłowska, Mesenchymal stromal cells and tissue-specific progenitor cells: their role in tissue homeostasis, *Stem Cells Int.* 2016 (2016) 1–11.
- [16] M. Shimono, T. Ishikawa, H. Ishikawa, H. Matsuzaki, S. Hashimoto, T. Muramatsu, K. Shima, K.I. Matsuzaka, T. Inoue, Regulatory mechanisms of periodontal regeneration, *Microsc. Res. Tech.* 60 (5) (2003) 491–502.
- [17] A. Nanci, D.D. Bosshardt, Structure of periodontal tissues in health and disease, *Periodontol.* 2000 40 (1) (2006) 11–28.
- [18] T. Iwata, M. Yamato, Z. Zhang, S. Mukobata, K. Washio, T. Ando, J. Feijen, T. Okano, I. Ishikawa, Validation of human periodontal ligament-derived cells as a reliable source for cytotherapeutic use, *J. Clin. Periodontol.* 37 (12) (2010) 1088–1099.
- [19] D. Trivanović, A. Jauković, B. Popović, J. Krstić, S. Mojsilović, I. Okić-Djordjević, T. Kukolj, H. Obradović, J.F. Santibanez, D. Bugarski, Mesenchymal stem cells of different origin: comparative evaluation of proliferative capacity, telomere length and pluripotency marker expression, *Life Sci.* 141 (2015) 61–73.
- [20] A. Downes, R. Mouras, A. Elfick, Optical spectroscopy for noninvasive monitoring of stem cell differentiation, *Biomed. Res. Int.* 2010 (2010) 1–10.
- [21] A. Downes, R. Mouras, P. Bagnaninchi, A. Elfick, Raman spectroscopy and cars microscopy of stem cells and their derivatives, *J. Raman Spectrosc.* 42 (10) (2011) 1864–1870.
- [22] J.W. Chan, D.K. Lieu, Label-free biochemical characterization of stem cells using vibrational spectroscopy, *J. Biophotonics* 2 (11) (2009) 656–668.
- [23] I. Nottingher, I. Bisson, A.E. Bishop, W.L. Randle, J.M. Polak, L.L. Hensch, In situ spectral monitoring of mrna translation in embryonic stem cells during differentiation in vitro, *Anal. Chem.* 76 (11) (2004) 3185–3193.
- [24] C. Aksoy, F. Severcan, Role of vibrational spectroscopy in stem cell research, *J. Spectrosc.* 27 (3) (2012) 167–184.
- [25] E. Brauchle, K. Schenke-Layland, Raman spectroscopy in biomedicine-non-invasive in vitro analysis of cells and extracellular matrix components in tissues, *Biotechnol. J.* 8 (3) (2013) 288–297.
- [26] H.G. Schulze, S.O. Konorov, N.J. Caron, J.M. Piret, M.W. Blades, R.F. Turner, Assessing differentiation status of human embryonic stem cells noninvasively using Raman microspectroscopy, *Anal. Chem.* 82 (12) (2010) 5020–5027.
- [27] A. Ghita, F.C. Pascut, V. Sottile, C. Denning, I. Nottingher, Applications of Raman micro-spectroscopy to stem cell technology: label-free molecular discrimination and monitoring cell differentiation, *EPJ Techniques Instrum.* 2 (1) (2015) 1–14.
- [28] H. Bai, P. Chen, H. Fang, L. Lin, G. Tang, G. Mu, W. Gong, Z. Liu, H. Wu, H. Zhao, et al. Detecting viability transitions of umbilical cord mesenchymal stem cells by Raman micro-spectroscopy, *Laser Phys. Lett.* 8 (1) (2011) 78–84.
- [29] H.K. Chiang, F.Y. Peng, S.C. Hung, Y.C. Feng, In situ Raman spectroscopic monitoring of hydroxyapatite as human mesenchymal stem cells differentiate into osteoblasts, *J. Raman Spectrosc.* 40 (5) (2009) 546–549.
- [30] E. Azrad, D. Zahor, R. Vago, Z. Nevo, R. Doron, D. Robinson, L.A. Gheber, S. Rosenwaks, I. Bar, Probing the effect of an extract of elk velvet antler powder on mesenchymal stem cells using Raman microspectroscopy: enhanced differentiation toward osteogenic fate, *J. Raman Spectrosc.* 37 (4) (2006) 480–486.
- [31] C. Krafft, J. Popp, The many facets of Raman spectroscopy for biomedical analysis, *Anal. Bioanal. Chem.* 407 (3) (2015) 699–717.
- [32] B.S. Kim, C.C.I. Lee, J.E. Christensen, T.R. Huser, J.W. Chan, A.F. Tarantal, Growth, differentiation, and biochemical signatures of rhesus monkey mesenchymal stem cells, *Stem Cells Dev.* 17 (1) (2008) 185–198.
- [33] L. Harkness, S.M. Novikov, J. Beermann, S.I. Bozhevolnyi, M. Kassem, Identification of abnormal stem cells using Raman spectroscopy, *Stem Cells Dev.* 21 (12) (2012) 2152–2159.
- [34] A. Rygula, K. Majzner, K.M. Marzec, A. Kaczor, M. Pilarczyk, M. Baranska, Raman spectroscopy of proteins: a review, *J. Raman Spectrosc.* 44 (8) (2013) 1061–1076.
- [35] K. Czamara, K. Majzner, M. Pacia, K. Kochan, A. Kaczor, M. Baranska, Raman spectroscopy of lipids: a review, *J. Raman Spectrosc.* 46 (1) (2015) 4–20.
- [36] K. Maquelin, C. Kirschner, L.-P. Choo-Smith, N. van den Braak, H. Endtz, D. Naumann, G. Puppels, Identification of medically relevant microorganisms by vibrational spectroscopy, *J. Microbiol. Methods* 51 (3) (2002) 255–271.
- [37] G. Clemens, J.R. Hands, K.M. Dorling, M.J. Baker, Vibrational spectroscopic methods for cytology and cellular research, *Analyst* 139 (18) (2014) 4411–4444.
- [38] Q. Matthews, A. Jirasek, J. Lum, X. Duan, A.G. Brolo, Variability in Raman spectra of single human tumor cells cultured in vitro: correlation with cell cycle and culture confluency, *Appl. Spectrosc.* 64 (8) (2010) 871–887.
- [39] Z. Movasaghi, S. Rehman, I.U. Rehman, Raman spectroscopy of biological tissues, *Appl. Spectrosc. Rev.* 42 (5) (2007) 493–541.
- [40] T. Ichimura, K.F. Liang-da Chiu, S. Kawata, T.M. Watanabe, T. Yanagida, H. Fujita, Visualizing cell state transition using Raman spectroscopy, *PLoS one* 9 (1) (2014) 1–8.
- [41] E. Brauchle, S. Noor, E. Holtorf, C. Garbe, K. Schenke-Layland, C. Busch, Raman spectroscopy as an analytical tool for melanoma research, *Clin. Exp. Dermatol.* 39 (5) (2014) 636–645.
- [42] M. Pudlas, E. Brauchle, T.J. Klein, D.W. Huttmacher, K. Schenke-Layland, Non-invasive identification of proteoglycans and chondrocyte differentiation state by Raman microspectroscopy, *J. Biophotonics* 6 (2) (2013) 205–211.
- [43] G.S. Mandair, M.D. Morris, Contributions of Raman spectroscopy to the understanding of bone strength, *BoneKey Reports* 4 (620) (2015) 1–8.
- [44] J. Kobolak, A. Dinnyes, A. Memic, A. Khademhosseini, A. Mobasher, Mesenchymal stem cells: identification, phenotypic characterization, biological properties and potential for regenerative medicine through biomaterial micro-engineering of their niche, *Methods* 99 (2016) 62–68.



**XVII INTERNATIONAL WORKSHOP ON
Vortex Matter in Superconductors**
Antwerp, Belgium
20-25 May, 2019

ABSTRACT BOOK



This conference is organized within the framework of

[EU-COST](#) Action CA16218:

*Nanoscale Coherent Hybrid Devices for Superconducting
Quantum Technologies*



**NANOSCALE COHERENT
HYBRID DEVICES
FOR SUPERCONDUCTING
QUANTUM TECHNOLOGIES**

Frustration and fluctuations in FeSe: A Raman scattering study

Nenad LAZAREVIĆ¹, Andreas BAUM^{2,3}, Harrison N RUIZ⁴, Yao WANG^{4,6,10}, Thomas BÖHM^{2,3,11}, R Hosseinian AHANGHAMEJHAD^{2,3,12}, Peter ADELMANN⁷, Thomas WOLF⁷, Zoran V POPOVIĆ^{1,8}, Brian MORITZ⁴, Thomas P DEVEREAUX^{4,9}, Rudi HACKL²

¹Center for Solid State Physics and New Materials, Institute of Physics Belgrade, University of Belgrade, Pregrevica 118, 11080 Belgrade, Serbia.

²Walther Meissner Institut, Bayerische Akademie der Wissenschaften, 85748 Garching, Germany.

³Fakultät für Physik E23, Technische Universität München, 85748 Garching, Germany.

⁴Stanford Institute for Materials and Energy Sciences, SLAC National Accelerator Laboratory, 2575 Sand Hill Road, Menlo Park, CA 94025, USA.

⁵Department of Physics, Stanford University, Stanford, CA 94305, USA.

⁶Department of Applied Physics, Stanford University, Stanford, CA 94305, USA.

⁷Karlsruher Institut für Technologie, Institut für Festkörperphysik, 76021 Karlsruhe, Germany.

⁸Serbian Academy of Sciences and Arts, Knez Mihailova 35, 11000 Belgrade, Serbia.

⁹Geballe Laboratory for Advanced Materials, Stanford University, Stanford, CA 94305, USA.

¹⁰Present address: Lyman Laboratory 336, Harvard University, 17 Oxford St. Cambridge, 02138 MA, USA.

¹¹Present address: TNG Technology Consulting GmbH, Beta-Straße, 85774 Unterföhring, Germany.

¹²Present address: School of Solar and Advanced Renewable Energy, Department of Physics and Astronomy, University of Toledo, Toledo, OH 43606, USA.

FeSe, the simplest of the iron based superconductors, is a puzzling material. As opposed to the related iron pnictides and FeTe, no long range magnetic order is found down to lowest temperatures. Here, we use Raman scattering as a function of temperature and polarization to probe charge and spin dynamics in FeSe. In agreement with numerical simulations of a spin-1 Heisenberg model several peaks in all Raman active symmetries can be assigned to spin excitations. The dominating feature is a peak in B_{1g} symmetry around 500 cm⁻¹ which shows distinct temperature dependence. Further comparison of the simulations to neutron scattering data furnishes evidence for FeSe hosting nearly frustrated stripe order of local spins.

References

- [1] A. Baum, H. N. Ruiz, N. Lazarević, Yao Wang, T. Böhm, R. Hosseinian Ahangharnejhad, P. Adelman, T. Wolf, Z. V. Popović, B. Moritz, T. P. Devereaux & R. Hackl, *Communications Physics* **2**, 14 (2019).
- [2] H. Ruiz, Yao Wang, B. Moritz, A. Baum, R. Hackl & T. P. Devereaux, *Phys. Rev. B* **99**, 125130 (2019).

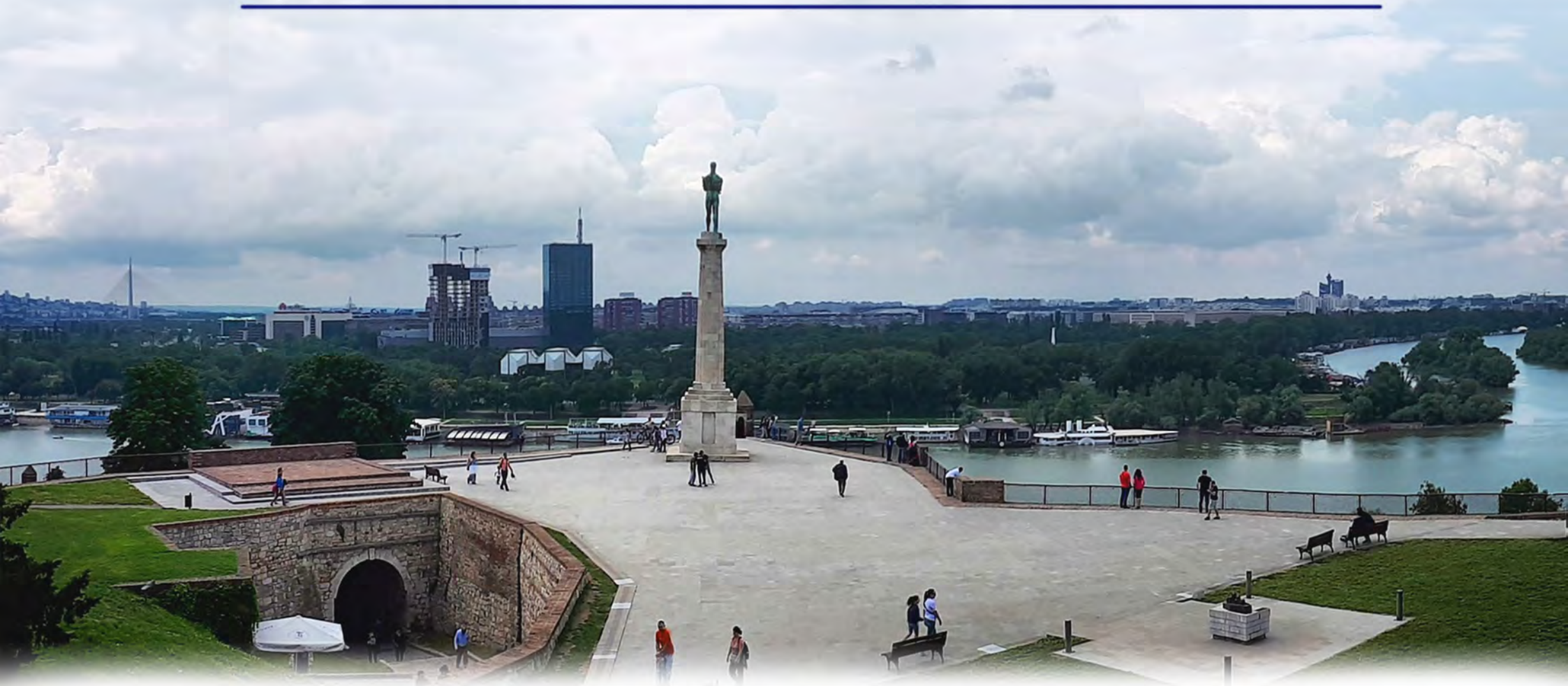
E-mail: nenad.lazarevic@ipb.ac.rs



<http://www.sfkm.ac.rs/>

The 20th Symposium on Condensed Matter Physics

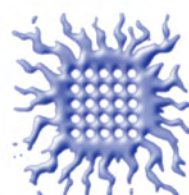
BOOK OF ABSTRACTS



University of Belgrade,
Faculty of Physics



Institute of Physics Belgrade



Vinca Institute
of Nuclear Sciences



Serbian Academy
of Sciences and Arts



Ministry of Education, Science and
Technological Development,
Republic of Serbia

Nematic Fluctuations In Iron Based Systems

A. Baum^{ab}, F. Kretzschmar^{ab}, D. Jost^{ab}, T. Böhm^{ab}, L. Peis^{ab},
U. Karahasanović^c, B. Muschler^{ab}, J. Schmalian^c, S. Caprara^d, M. Grilli^d,
C. Di Castro^d, J. G. Analytis^e, J.-H. Chu^e, I. R. Fisher^e, P. Gegenwart^f,
J. Maiwald^f, R. Hosseinian Ahangharnejhad^{ab}, P. Adelmann^c, T. Wolf^c,
N. Lazarević^g, Z. Popović^{gh} and R. Hackl^a

^aWalther Meissner Institut, Bayerische Akademie der Wissenschaften, Garching

^bFakultät für Physik E23, Technische Universität München

^cKarlsruhe Institute of Technology (KIT)

^dDepartment of Physics, University of Rome "Sapienza"

^eSIMES, SLAC National Accelerator Laboratory, and Geballe Laboratory for Advanced Materials
& Department of Applied Physics, Stanford University

^fExperimentalphysik VI, Universität Augsburg

^gCenter for Solid State Physics and New Materials, Institute of Physics, University of Belgrade

^hSerbian Academy of Sciences and Arts, Belgrade

Abstract. The origin and interplay of nematicity, magnetism, and superconductivity in iron based materials are still a subject of current research. The fluctuations which precede the ordered phases provide an additional probe for these phenomena. Using Raman spectroscopy we study fluctuations in $\text{Ba}(\text{Fe}_{1-x}\text{Co}_x)_2\text{As}_2$ ($x = 0-0.051$) as a function of temperature, symmetry, and doping. Our results provide evidence for critical spin fluctuations, suggesting a spin driven mechanism of the nematic and magnetic order. We discuss similarities with related systems such as EuFe_2As_2 and FeSe .

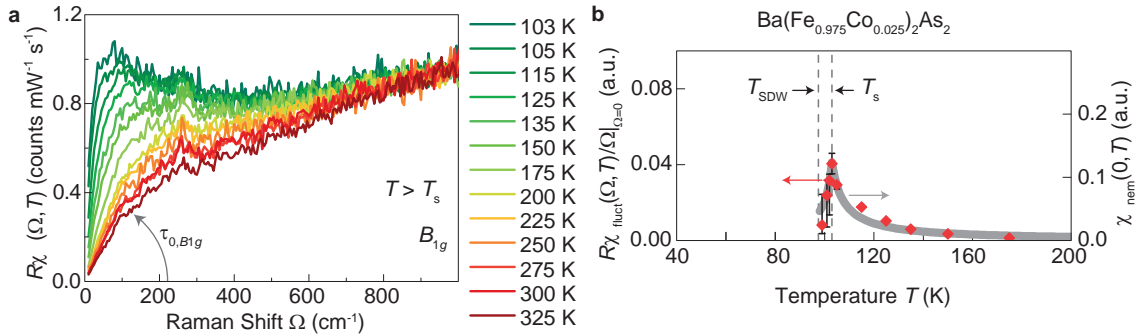


FIGURE 1. Fluctuations in $\text{Ba}(\text{Fe}_{0.975}\text{Co}_{0.025})_2\text{As}_2$. **a** Due to the response from fluctuations above the structural phase transition at $T_s \approx 103\text{ K}$ the spectral weight at low energies and the initial slope $\tau_{0,B1g}$ increase upon cooling. **b** The initial slope (red diamonds) exhibits a maximum at T_s , but the fluctuations only vanish at the magnetic ordering temperature T_{SDW} . The maximum is reflected in the temperature dependence of the electronic nematic susceptibility $\chi_{\text{nem}}^{\text{el}}$ (grey) when the fluctuations couple to the lattice.

REFERENCES

1. Kretzschmar *et al.*, *Nat. Phys.* **12**, 560-563 (2016)

The vibrational properties of CrI₃ single crystals

S. Djurdjic-Mijin,¹ A. Šolajić,¹ J. Pešić,¹ M. Šćepanović,¹ Y. Liu,² A. Baum,^{3,4} C. Petrovic,² N. Lazarević,¹ and Z. V. Popović^{1,5}

¹Center for Solid State Physics and New Materials, Institute of Physics Belgrade, University of Belgrade, Pregrevica 118, 11080 Belgrade, Serbia

²Condensed Matter Physics and Materials Science Department, Brookhaven National Laboratory, Upton, New York 11973-5000, USA

³Walther Meissner Institut, Bayerische Akademie der Wissenschaften, 85748 Garching, Germany

⁴Fakultät für Physik E23, Technische Universität München, 85748 Garching, Germany

⁵Serbian Academy of Sciences and Arts, Knez Mihailova 35, 11000 Belgrade, Serbia

Abstract. CrI₃ is a two-dimensional layered material and a ferromagnetic [1] with Curie temperature of 61K [1,2] and first order phase transition that occurs at 220K [3,4]. This class of materials has recently gained a lot of attention due to numerous potential applications. Here we represent our work consisting of both experimental and theoretical Raman scattering study of CrI₃ lattice dynamics. Based on our results we can distinguish two different phases for CrI₃ with monoclinic (*C2/m*) being the high-temperature and rhombohedral (*R3*) phase being the low-temperature phase. Abrupt changes to the spectra were found at the first order phase transition which was located at $T_s \approx 180$ K, lower than in previous studies. In contrast to the prior reports we found no sign of phase coexistence over temperature range exceeding 5 K [5].

REFERENCES

- [1] E. Navarro-Moratalla, B. Huang, G. Clark *et al.*, Layer dependent ferromagnetism in a van der Waals crystal down to the monolayer limit, *Nature (London)* **546**, 270 (2017).
- [2] J. F. Dillon, Jr. and C. E. Olson, Magnetization, resonance, and optical properties of the ferromagnet CrI₃, *J. Appl. Phys.* **36**, 1259 (1965).
- [3] M. A. McGuire, H. Dixit, V. R. Cooper, and B. C. Sales, Coupling of crystal structure and magnetism in the layered, ferromagnetic insulator CrI₃, *Chem. Mater.* **27**, 612 (2015).
- [4] D. T. Larson and E. Kaxiras, Raman Spectrum of CrI₃: An *ab initio* study, *Phys. Rev. B* **98**, 085406 (2018).
- [5] S. Djurdjic-Mijin, A. Šolajić, J. Pešić, M. Šćepanović, Y. Liu, A. Baum, C. Petrovic, N. Lazarević, and Z. V. Popović, Lattice dynamics and phase transition in CrI₃ single crystals, *Phys. Rev. B* **98**, 104307 (2018.)

Nanostructured BiFeO₃ thin films

B. Colson^a, V. Fuentes^a, Z. Konstantinovic^b, C. Frontera^a, D. Colson^c, A. Forget^c,
N. Lazarevic^b, M. Scepanovic^b, Z. V. Popovic^b, Ll. Balcells^a, B. Martinez^a, A. Pomar^a

^aICMAB-CSIC, Campus UAB, 08193 Bellaterra, Spain

^bCSSPNM, Institute of Physics Belgrade, University of Belgrade, Serbia

^cSPEC/IRASMIS/ DSM, CEA-Saclay, Gif-sur Yvette, France

Abstract. Well defined structures at nanometric scale of multiferroic materials present an increasing interest due to their unique physical properties and potential applications. Fabrication of artificial nanostructures requires sophisticated technology and has been recognized as a hard-attainable issue. For these reasons the fabrication of ordered nanostructures, via spontaneous self-organization, is a topic of major relevance. Complex oxide thin films are often elastically strained and this lattice strain can, in some cases, select preferential growth modes leading to the appearance of different self-organized morphologies. In this work we report on the controlled fabrication of a self-assembled network of nanostructures (pits and grooves) in highly epitaxial BiFeO₃ thin films. As previously shown in the case of manganite thin films [1-2], the remarkable degree of ordering is achieved using vicinal substrates with well-defined step-terrace morphology. Nanostructured BiFeO₃ thin films show mixed-phase morphology, exhibiting the giant ferroelectric polarization close to the theoretical limit. These particular microstructures open a huge playground for future applications in multiferroic nanomaterials.

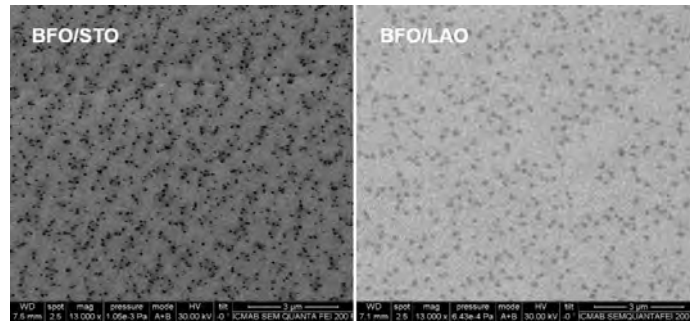


FIGURE 1. Scanning Electron Microscopy of nanostructured BiFeO₃ films grown on top of SrTiO₃ and LaAlO₃ substrates.

REFERENCES

1. Z. Konstantinovic et al., Small 5, 265 (2009)
2. Z. Konstantinovic et al., Nanoscale, 5, 1001 (2013).

Raman Spectroscopy Study of Primary Mesenchymal Stem Cells

J. J. Lazarević^a, T. Kukolj^b, U. Ralević^a, D. Bugarski^b, N. Lazarević^a, B. Bugarski^c, and Z.V. Popović^{a,d}

^a*Center for Solid State Physics and New Materials, Institute of Physics Belgrade, University of Belgrade, Pregrevica 118, Belgrade 11080, Serbia*

^b*Laboratory for Experimental Hematology and Stem Cells, Institute for Medical Research, University of Belgrade, Belgrade, Serbia*

^c*Department of Chemical Engineering, Faculty of Technology and Metallurgy, University of Belgrade, Karnegijeva 4, Belgrade 11060, Serbia*

^d*Serbian Academy of Science and Arts, Knez Mihailova 35, Belgrade 11000, Serbia*

Abstract. Cells possess specific dynamic biochemical structure and by analyzing (inter)molecular vibrations with Raman spectroscopy, correlation between biochemical composition to specific cell lineages is established, as well as to disorders of their physiologic state. In regenerative medicine and tissue engineering, mesenchymal stem cells, as adult stem cells, are of crucial importance, due to self-renewal, multi-lineage differentiation potential and undemanding isolation procedure. These cells are widespread in the adult organism and no ethical issues are related to their isolation. However, they need to be well characterized and purified before further application, having in mind their intrinsic heterogeneity. Raman spectroscopy was used for analyzing the influence of two most frequently used chemical fixatives, methanol and formaldehyde, on Raman spectra of primary mesenchymal stem cells isolated from periodontal ligament. Further, this vibrational spectroscopy technique was applied for probing differentiation status of these cells, after stimulating towards chondrogenic, adipogenic, and osteogenic lineages.

REFERENCES

1. Lazarević J.J., Kukolj T., Bugarski D., Lazarević N., Bugarski B., and Popović Z.V., *Spectrochim Acta A Mol Biomol Spectrosc.* **213**, 384-390 (2019).
2. Lazarević J.J., Ralević U., Kukolj T., Bugarski D., Lazarević N., Bugarski B., and Popović, Z.V., *Spectrochim Acta A Mol Biomol Spectrosc.* **216**, 173-178 (2019).

Frustrated Spin Order and Fluctuations in FeSe: A Raman Scattering Study

N. Lazarević^a, A. Baum^{b,c}, H. N. Ruiz^{d,e}, Yao Wang^{d,f,j}, T. Böhm^{b,c,k}, R. H. Ahanghamejhad^{b,c,l}, P. Adelmann^g, T. Wolf^g, Z. V. Popović^{a,h}, B. Moritz^d, T. P. Devereaux^{d,i}, R. Hackl^b

^aCenter for Solid State Physics and New Materials, Institute of Physics Belgrade, University of Belgrade, Pregrevica 118, 11080 Belgrade, Serbia.

^bWalther Meissner Institut, Bayerische Akademie der Wissenschaften, 85748 Garching, Germany.

^cFakultät für Physik E23, Technische Universität München, 85748 Garching, Germany.

^dStanford Institute for Materials and Energy Sciences, SLAC National Accelerator Laboratory, 2575 Sand Hill Road, Menlo Park, CA 94025, USA.

^eDepartment of Physics, Stanford University, Stanford, CA 94305, USA.

^fDepartment of Applied Physics, Stanford University, Stanford, CA 94305, USA.

^gKarlsruher Institut für Technologie, Institut für Festkörperphysik, 76021 Karlsruhe, Germany.

^hSerbian Academy of Sciences and Arts, Knez Mihailova 35, 11000 Belgrade, Serbia.

ⁱGeballe Laboratory for Advanced Materials, Stanford University, Stanford, CA 94305, USA.

^jPresent address: Lyman Laboratory 336, Harvard University, 17 Oxford St. Cambridge, 02138 MA, USA.

^kPresent address: TNG Technology Consulting GmbH, Beta-Straße, 85774 Unterföhring, Germany.

^lPresent address: School of Solar and Advanced Renewable Energy, Department of Physics and Astronomy, University of Toledo, Toledo, OH 43606, USA.

Abstract. FeSe is the simplest and yet the most controversial member of the iron based superconductors whose charge and spin dynamics may hold key information on the physics of high temperature superconductors. As opposed to the related iron pnictides and FeTe, no long range magnetic order is found down to lowest temperatures. Here, we present the results of the inelastic light scattering experiments on FeSe as a function of temperature and polarization. In agreement with numerical simulations of a spin-1 Heisenberg model, several peaks in all Raman active symmetries can be assigned to spin excitations. The dominating feature is a peak in B_{1g} symmetry around 500 cm⁻¹ which shows distinct temperature dependence. Further comparison of the simulations to neutron scattering data furnishes evidence for FeSe hosting nearly frustrated stripe order of local spins.

REFERENCES

1. A. Baum, H. N. Ruiz, N. Lazarević, Yao Wang, T. Böhm, R. Hosseinian Ahanghamejhad, P. Adelmann, T. Wolf, Z. V. Popović, B. Moritz, T. P. Devereaux & R. Hackl, *Communications Physics* **2**, 14 (2019).
2. H. Ruiz, Yao Wang, B. Moritz, A. Baum, R. Hackl & T. P. Devereaux, *Phys. Rev. B* **99**, 125130 (2019).

Lattice dynamics and phonon anomalies in FeS

A. Baum^{a,b}, A. Milosavljević^c, N. Lazarević^c, M.M. Radonjić^d, B. Nikolić^e, M. Mitschek^{a,b}, Z. Inanloo Maranloo^a, M. Šćepanović^c, M. Grujić – Brojčin^c, N. Stojilović^f, M. Opel^a, Aifeng Wang^g, C. Petrovic^g, Z.V. Popović^{c,h} and R. Hackl^a

^aWalther Meissner Institut, Bayerische Akademie der Wissenschaften, 85748 Garching, Germany

^bFakultät für Physik E23, Technische Universität München, 85748 Garching, Germany

^cCenter for Solid State Physics and New Materials, Institute of Physics Belgrade, University of Belgrade, Pregrevica 118, 11080 Belgrade, Serbia

^dScientific Computing Laboratory, Center for the Study of Complex Systems, Institute of Physics Belgrade, University of Belgrade, Pregrevica 118, 11080 Belgrade, Serbia

^eFaculty of Physics, University of Belgrade, Studentski trg 12, Belgrade, Serbia

^fDepartment of Physics and Astronomy, University of Wisconsin Oshkosh, Oshkosh, Wisconsin 54901, USA

^gCondensed Matter Physics and Materials Science Department, Brookhaven National Laboratory, Upton, New York 11973-5000, USA

^hSerbian Academy of Sciences and Arts, Knez Mihailova 35, 11000 Belgrade, Serbia

Abstract. Crystal structure, magnetic ordering and nematic phase are closely interrelated in the iron-based superconductors. Although isostructural and isoelectronic, properties of 11 chalcogenides, FeSe, FeTe and FeS, differ significantly. Whereas FeSe undergoes a nematic and structural phase transition at 90 K, together with superconductivity below 9 K, and no traces of long-range magnetic ordering, FeTe is not superconducting but exhibits magnetostructural phase transition at temperature of 67 K. The last member of the family, FeS, have a superconducting transition at 5 K, and remains tetragonal down to lowest temperatures.

Here, we present results of Raman scattering experiment on tetragonal FeS, and analysis of vibrational properties close to potential instabilities [1]. Besides A_{1g} and B_{1g} modes assignment, which is in a good agreement with DFT calculations, third peak within a gap of calculated phonon density of states can be identified as a result of second order scattering process. Both, selection rules for two-phonon processes, based on modified group projector technique and energy are in a good agreement with the experiment. A fourth mode, close to A_{1g} could originate from either defect-induced scattering or second order scattering as well. The temperature dependence of all four modes is governed by the contraction of the lattice, with anomalies at 50 K and below 20 K. The anomaly observed at 20 K has a correspondence with previously reported results of short-range magnetic ordering. The presence of two-phonon scattering indicates strong phonon-phonon scattering, which is likely to originate from an electron-phonon interaction being enhanced in comparison to other pnictides and chalcogenides.

REFERENCES

1. A. Baum, A. Milosavljević, N. Lazarević, M. M. Radonjić, B. Nikolić, M. Mitschek, Z. I. Maranloo, M. Šćepanović, M. Grujić-Brojčin, N. Stojilović, M. Opel, A. Wang, C. Petrovic, Z.V. Popović, and R. Hackl, Phonon anomalies in FeS, *Phys.Rev.B* **97**, 054306 (2018).

Lattice dynamics and phase transitions in $\text{Fe}_{3-x}\text{GeTe}_2$

A. Milosavljević^a, A. Šolajić^a, S. Djurdjić Mijin^a, J. Pešić^a, B. Višić^a, Y. Liu^b, C. Petrovic^b, N. Lazarević^a and Z. V. Popović^c

^aCenter for Solid State Physics and New Materials, Institute of Physics Belgrade, University of Belgrade, Pregrevica 118, 11080 Belgrade, Serbia

^bCondensed Matter Physics and Materials Science Department, Brookhaven National Laboratory, Upton, New York 11973-5000, USA

^cCenter for Solid State Physics and New Materials, Institute of Physics Belgrade, University of Belgrade, Pregrevica 118, 11080 Belgrade, Serbia and Serbian Academy of Sciences and Arts, Knez Mihailova 35, 11000 Belgrade, Serbia

Abstract. A new class of magnetic van der Waals bonded materials has recently become of great interest, as a suitable candidates for various applications. Whereas CrXTe_3 ($X = \text{Si, Ge, Sn}$) and CrX_3 ($X = \text{Cl, Br, I}$) classes maintain low phase transition temperatures even in a monolayer regime, $\text{Fe}_{3-x}\text{GeTe}_2$ has a high bulk transition temperature, between 220 and 230 K, making it a promising applicant.

Here we present DFT calculations of lattice dynamics and Raman spectroscopy measurements of the van der Waals bonded ferromagnet $\text{Fe}_{3-x}\text{GeTe}_2$ [1]. Four out of eight Raman active modes are observed and assigned, in agreement with numerical calculations. The energies and linewidths of the observed modes display an unconventional temperature dependence at about 150 and 220 K, followed by the nonmonotonic evolution of the Raman continuum. Whereas the former can be related to the magnetic phase transition, the origin of the latter anomaly remains an open question.

REFERENCES

1. A. Milosavljević, A. Šolajić, S. Djurdjić-Mijin, J. Pešić, B. Višić, Yu Liu, C. Petrovic, N. Lazarević, and Z. V. Popović. "Lattice dynamics and phase transitions in $\text{Fe}_{3-x}\text{GeTe}_2$." *Physical Review B* 99, no. 21 (2019): 214304.